Technische Universität München
Institut für Energietechnik

Lehrstuhl für Thermodynamik

Numerical Simulation of Deflagration-to-Detonation Transition on Industry Scale

Josef Haßlberger

Vollständiger Abdruck der von der Fakultät für Maschinenwesen der Technischen Universität München zur Erlangung des akademischen Grades eines

DOKTOR – INGENIEURS

genehmigten Dissertation.

Vorsitzender:
    Prof. Dr.-Ing. Michael Zäh
Prüfer der Dissertation:
    1. Prof. Dr.-Ing. Thomas Sattelmayer
    2. Prof. Jennifer Wen, Ph.D.
       University of Warwick, Coventry, UK

Vorwort

Die vorliegende Arbeit entstand am Lehrstuhl für Thermodynamik der Technischen Universität München während meiner Tätigkeit als wissenschaftlicher Mitarbeiter. Sie wurde durch das Bundesministerium für Wirtschaft und Energie über die Gesellschaft für Reaktorsicherheit gefördert.

Mein besonderer Dank gilt meinem Doktorvater Prof. Dr.-Ing. Thomas Sattelmayer für das in mich gesetzte Vertrauen, die gewährten wissenschaftlichen Freiheiten und die Übernahme des Hauptreferats. Prof. Jennifer Wen, Ph.D., danke ich für die freundliche Übernahme des Koreferats und Prof. Dr.-Ing. Michael Zäh für die Übernahme des Prüfungsvorsitzes.

Für die äußerst lehrreiche Zusammenarbeit auf dem Gebiet der Explosionsforschung danke ich Dr.-Ing. Lorenz Böck, Peter Katzy und Dr.-Ing. Florian Ettner. Dr.-Ing. Konrad Makowka und Dr.-Ing. Johannes Weinzierl danke ich ebenfalls für die zahlreichen fachlichen Diskussionen. Allen ehemaligen Studenten sei für ihre tatkräftige Unterstützung gedankt, wobei ich Sebastian Ketterl und Thomas Kaiser besonders hervorheben möchte. Für die angenehme Atmosphäre am Lehrstuhl danke ich der Brotzeit- und Fußballgruppe sowie allen anderen aktuellen und ehemaligen Mitarbeitern.

Zu guter Letzt gebührt der größte Dank meinen Eltern für die bedingungslose Unterstützung während meiner langen Ausbildungszeit.

München, im August 2017

Josef Haßlberger

Kurzfassung

Im Rahmen eines durch das Bundesministerium für Wirtschaft und Energie (BMWi) geförderten Forschungsprojekts wurde ein CFD-Verbrennungslöser für nukleare Sicherheitsanalysen weiterentwickelt. Ziel ist die Vorhersage von Wasserstoffexplosionen auf voller Industrieskala wie beim Kernschmelzunfall in Fukushima-Daiichi. Ein besonderes Augenmerk liegt dabei auf dem folgenschweren Deflagrations-Detonations-Übergang (engl. DDT). Unabhängig von der spezifischen Motivation dieser Arbeit kann die Methode ebenso auf andere potentiell gefährliche Situationen mit unbeabsichtigter Wasserstofffreisetzung in die umgebende Luft angewandt werden. Als Beispiele wären die chemische und Prozessindustrie zu nennen.

Entgegen dem Stand der Wissenschaft und Technik bei der Modellierung großskaliger Explosionen wird der gesamte Verbrennungsprozess mit einem einzigen Löser berechnet. Die Verwendung empirischer Kriterien für den Übergang zwischen Verbrennungsregimes wird gezielt vermieden. Das Mehrphänomen- und Mehrskalenproblem bringt eine Reihe von Herausforderungen mit sich, denen mit speziellen numerischen Techniken begegnet wird. Ein zentrales Element stellt das entwickelte hybride Flammen-Tracking Stoß-Capturing Verfahren zur Reduzierung der Gitterabhängigkeit dar. Dabei wird die Flamme als reaktive Diskontinuität betrachtet und mit einer geometrischen Volume-of-Fluid Methode propagiert. Gleichzeitig werden gasdynamische Diskontinuitäten, insbesondere Stöße, mit einem approximativen Riemannlöser bestimmt. Eine adaptive Netzverfeinerung wird zusätzlich zur Reduzierung des Gesamtrechenaufwands eingesetzt. Entsprechend der hochgradig instationären Natur von Explosionen wird die räumliche Auflösung lokal angepasst.

Aufgrund ihrer großskaligen Abmessungen werden die größten je in geschlossenen Räumen durchgeführten DDT-Versuche in der RUT-Anlage (Kurchatov Institut, nahe Moskau) zur Validierung des numerischen Modells herangezogen. Die untersuchten Gemischzusammensetzungen liegen in der Nähe des sicherheitsrelevanten unteren Detonationslimits, welches experimentell zu 12,5 % Wasserstoff in Luft bestimmt wurde. Wie die Simulationen zeigen, ist das Verfahren in der Lage, die grundlegenden Phänomene der Flammenbeschleunigung und des DDT in teilversperrten Kanälen abzubilden – auch auf zwangsweise unteraufgelösten Gittern. Die Qualität der DDT-Vorhersage hängt vom zugrundeliegenden Mechanismus ab. Im Gegensatz zur erfolgreichen Simulation des DDT durch Stoßfokussierung ist die Vorhersage des DDT in der Nähe der turbulenten Flammenzone weniger zuverlässig. Fundamentale Sicherheitscharakteristika, wie die Detonationsausbreitungsgeschwindigkeit samt zugehöriger Drucklasten, werden durch das Verfahren zufriedenstellend wiedergegeben.

Um der Motivation der Arbeit gerecht zu werden, wird der entwickelte Löser abschließend auf voller Reaktorskala angewandt. Der modellierte Leichtwasserreaktor vom Konvoi-Typ stellt eine standardisierte Bauform deutscher Druckwasserreaktoren dar. Massiv parallelisierte Rechnungen werden dazu auf dem SuperMUC-Höchstleistungsrechner durchgeführt. Die untersuchten hypothetischen DDT-Szenarien in global mageren Wasserstoff-Luft Gemischen zeigen eine hochgradig dreidimensionale Flammenausbreitung im Sicherheitsbehälter. Erwartungsgemäß kann eine starke Sensitivität des Explosionsprozesses bezüglich der Gemischzusammensetzung beobachtet werden. Weiterhin

werden die Charakteristika typischer transienter Drucklasten an verschiedenen Positionen im Sicherheitsbehälter analysiert. Ein weiterer Schritt in Richtung deterministischer DDT-Simulationen auf voller Reaktorskala wurde damit vollzogen.

Abschließend werden einige Ideen zur zielgerichteten Weiterentwicklung des Lösers (hinsichtlich nuklearer Sicherheitsanalysen) vorgestellt: Erweiterung des Wasserstoff-Luft Gemisches um Wasserdampf und Kohlenstoffmonoxid, Berücksichtigung des Effekts unauflösbarer kleiner Hindernisse mittels des Konzepts verteilter Porositäten, Verbesserung der Subgittermodellierung intrinsischer Flammeninstabilitäten und Erhöhung der Parallelisierungseffizienz durch dynamische Lastverteilung.

Abstract

In the framework of a research project funded by the German Federal Ministry of Economic Affairs and Energy (BMWi), a CFD combustion solver has been extended for the purpose of nuclear safety analysis. The methodology aims at the prediction of *industry-scale* hydrogen explosions like in the Fukushima-Daiichi core meltdown accident, with a particular focus on the hazardous Deflagration-to-Detonation Transition (DDT) phenomenon. Independent of the specific nuclear safety motivation of this work, the methodology can equally be applied to other potentially hazardous situations involving accidental release of hydrogen in air, e.g. in chemical and process industry.

Contrary to the state-of-the-art in large-scale explosion modeling, the entire combustion process is computed within a single solver framework. The usage of empirical combustion regime transition criteria is deliberately avoided. The multi-physics multi-scale problem poses several challenges which are met by special numerical techniques. As a key element, the developed hybrid flame-tracking shock-capturing scheme reduces grid dependency by treating the flame as a reactive discontinuity which is propagated by a geometrical Volume-of-Fluid method. At the same time, gas-dynamic discontinuities, especially shocks, are calculated by an approximate Riemann solver. Adaptive mesh refinement is additionally implemented to reduce overall computational cost. Spatial resolution is locally adapted according to the highly unsteady evolution of explosions.

For the validation of the numerical model, the largest ever conducted indoor DDT experiments in the RUT facility (Kurchatov Institute, Moscow region) are chosen because of their industry-scale geometrical dimensions. Investigated DDT mixtures are close to the safety-relevant lower detonation limit which was measured at 12.5 % of hydrogen in air. As the simulations show, the methodology is generally able to capture the essential phenomena behind flame acceleration and DDT in obstructed channels, even on necessarily under-resolved meshes. The quality of DDT predictions itself depends on the underlying mechanism. In contrast to successful simulations of DDT by shock focusing, prediction of DDT in the vicinity of the turbulent flame brush is less reliable. The code accurately reproduces key safety characteristics such as the detonation propagation velocity and associated pressure loads.

Following the motivation of this work, the developed solver is finally applied to a full-scale Konvoi-type light water reactor, i.e. a standardized German pressurized water reactor design. Massively parallelized computations are executed on the SuperMUC high performance cluster. Hypothetical DDT scenarios in globally lean hydrogen-air mixtures demonstrate a highly three-dimensional behavior of flame propagation in the containment. As expected, a strong sensitivity of the explosion process on mixture composition is observed. Further analysis concerns the characteristics of typical transient pressure loads at different positions in the containment. A step towards deterministic DDT simulations on full reactor scale has been made.

Finally, several ideas are presented to further enhance the solvers capabilities (with respect to nuclear safety analysis): extending the hydrogen-air mixture by steam and carbon monoxide, including the effect of unresolvable small obstacles via the distributed porosity concept, improving the sub-grid modeling of intrinsic flame instabilities and increasing the solver's parallel efficiency by dynamic load balancing.

Contents

List of Figures

List of Tables

Nomenclature

Latin letters

A	Area	m^2
a	Speed of sound	m/s
a	Thermal diffusivity	m^2/s
C	Offset	m
c	Specific heat capacity	J/(kg K)
c	Reaction progress	-
D	Detonation velocity	m/s
D	Diffusion coefficient	m^2/s
D	Diameter	m
d	Diameter	m
E	Error	-
e	Specific internal energy	J/kg
F	Blending function	-
F	Convective flux	m^3/s
f	Mixture fraction	-
f	Inherently serial part of the solver	-
G	Quenching factor	-
g	Gravitational acceleration	m/s^2
g	Quenching rate	1/s
H	Heaviside step function	-
h	Specific enthalpy	J/kg
h	Height	m
k	Specific turbulent kinetic energy	J/kg
L	Geometrical scale	m
l	Length scale	m
m	Mass	kg
m	Face normal	-
N	Count variable	-
n	Count variable	-
n	Front normal	-
p	Pressure	N/m^2
Q	Dimensionless heat	-
q	Specific heat	J/kg
q	Diffusive flux	W/m^2
R	Specific gas constant	J/(kg K)
R	Radius	m

r	Radial coordinate	m
S	Burning velocity	m/s
S	Parallel speedup	-
s	Spacing	m
T	Temperature	K
t	Time	s
u	Flow velocity	m/s
v	Flame velocity	m/s
V	Volume	m^3
X	Mole fraction	-
x	Cartesian coordinate	m
Y	Mass fraction	-
y	Cartesian coordinate	m
z	Cartesian coordinate	m

Greek letters

α	Volume fraction	-
β	Flux ratio	-
Γ	Pseudo diffusivity	kg/(m s)
δ_{ij}	Kronecker delta	-
ϵ	Tolerance	-
ε	Dissipation rate of k	J/(kg s)
Θ	Switch factor	-
θ	Thermicity	1/s
ϑ	Phase indicator	-
κ	Isentropic coefficient	-
λ	Heat conductivity	W/(m K)
λ	Detonation cell width	m
μ	Dynamic viscosity	kg/(m s)
ν	Kinematic viscosity	m^2/s
Ξ	Flame wrinkling factor	-
ρ	Density	kg/m^3
σ	Expansion ratio	-
σ	Standard deviation	-
σ	Strain rate	1/s
τ	Viscous stress	N/m^2
τ	Auto-ignition precursor	-
τ	Time scale	s
Φ	Stream function	m^2/s
Φ	Normalized equivalence ratio	-
ϕ	Equivalence ratio	-
ϕ	Signed distance	m
ϕ	General variable	
ψ	General variable	
Ω	Computational domain	
ω	Reaction rate	kg/(m^3 s)
ω	Angular (eddy) frequency	1/s

Superscripts

$'$	Fluctuation (Reynolds decomposition)
$'$	Projected
$''$	Fluctuation (Favre decomposition)
$*$	Modified
0	Initial
c	Based on c-field
f	Formation
NAG	Node-Averaged Gauss
s	Sensible

Subscripts

0	Initial
0	Axis
1	Pre-reaction
2	Post-reaction
A	Phase A
B	Phase B
b	Burned
CJ	Chapman-Jouguet
c	Cloud
cr	Critical
eff	Effective
eq	Equilibrium
exo	Exothermic
F	Flame
f	Face
fl	Flamelet
fn	Face neighbor
fp	Face point
gr	Grid
H_2	Hydrogen molecule
H	Hydrogen atom
id	Identification
ign	Ignition
it	Iteration
k	Specific turbulent kinetic energy
L	Laminar
L	Left
lim	Limit
max	Maximum
min	Minimum
N_2	Nitrogen
O_2	Oxygen
p	Point
p	Isobaric

prod	Products
R	Right
r	Resolved
re	Redistribution
ref	Reference
S	Sutherland
S	Shock
s	Surface-averaged
sp	Species
T	Taylor
T	Turbulent
T	Truncated
t	Total
u	Unburned
v	Isochoric
vN	von Neumann
vol	Volumetric
Γ	Face of the truncated polyhedron
δ	Heat release zone
η	Kolmogorov
ω	Eddy frequency
$\perp$	Orthogonally projected

Dimensionless numbers

CFL	Courant-Friedrichs-Lewy
Da	Damköhler
Ka	Karlovitz
Le	Lewis
Ma	Mach
Pr	Prandtl
Re	Reynolds
Sc	Schmidt

Abbreviations

2D	Two-Dimensional
3D	Three-Dimensional
AICC	Adiabatic Isochoric Complete Combustion
ALE	Arbitrary-Lagrangian-Eulerian
AMR	Adaptive Mesh Refinement
BML	Bray-Moss-Libby
BMWi	Bundesministerium für Wirtschaft und Energie
BVM	Burning Velocity Model
BWR	Boiling Water Reactor
CAD	Computer Aided Design
CFD	Computational Fluid Dynamics
CJ	Chapman-Jouguet

CLSMoF	Coupled Level-Set Moment-of-Fluid
CLSVoF	Coupled Level-Set Volume-of-Fluid
CPU	Central Processing Unit
DDT	Deflagration-to-Detonation Transition
DNS	Direct Numerical Simulation
DSD	Detonation Shock Dynamics
EBU	Eddy Break-Up
EDC	Eddy Dissipation Concept
EDM	Eddy Dissipation Model
EPR	European Presurized Reactor or Evolutionary Power Reactor
FA	Flame Acceleration
FEM	Finite Element Method
FDM	Finite Difference Method
FLOPS	Floating-point Operations Per Second
FSD	Flame Surface Density
FVM	Finite Volume Method
GraVent	Gradient and Venting
GRS	Gesellschaft für Anlagen- und Reaktorsicherheit or Global Research for Safety
HLLC	Harten-Lax-van Leer with Contact
IAEA	International Atomic Energy Agency
IGES	Initial Graphics Exchange Specification
ILDM	Intrinsic Low-Dimensional Manifolds
ISP	International Standard Problem
KIT	Karlsruhe Institute of Technology
KWU	Kraftwerk Union
LES	Large Eddy Simulation
LOCA	Loss-Of-Coolant Accident
LOFW	Loss-Of-Feed Water
LP	Lumped Parameter
LS	Level-Set
MCCI	Molten Corium Concrete Interaction
MoF	Moment-of-Fluid
MPI	Message Passing Interface
NAG	Node-Averaged Gauss
NASA	National Aeronautics and Space Administration
NIST	National Institute of Standards and Technology
OpenFOAM	Open Field Operation And Manipulation
PAR	Passive Auto-catalytic Recombiner
PaSR	Partially Stirred Reactor
PCFSC	Piecewise Constant Flux Surface Calculation
PDF	Probability Density Function
PIR	Patterned Interface Reconstruction
PISO	Pressure Implicit with Splitting of Operators
PLIC	Piecewise Linear Interface Calculation
PSA	Probabilistic Safety Analysis
PWR	Presurized Water Reactor
SBO	Station Black-Out

SIMPLE	Semi-Implicit Method for Pressure Linked Equations
SLIC	Simple Line Interface Calculation
SST	Shear Stress Transport
STEP	Standard for the Exchange of Product model data
STL	Stereo Lithographic surface
SWACER	Shock Wave Amplification by Coherent Energy Release
TFC	Turbulent Flame-speed Closure
TNT	Tri-Nitro-Toluene
TUM	Technische Universität München
TVD	Total Variation Diminishing
URANS	Unsteady Reynolds-Averaged Navier-Stokes
VoF	Volume-of-Fluid
WENO	Weighted Essentially Non-Oscillatory
ZND	Zeldovich-von Neumann-Döring

1 Introduction

Climate change is one of the century's biggest challenges. According to scientific calculations, there is 50 % chance that temperature rise until 2100 will be between 2.7 and 3.7 degrees Celsius. In the 2015 Paris emissions conference, nations worldwide agreed to limit temperature rise to two degrees Celsius. It is clear that such a goal can only be achieved by an energy system that emits considerably less carbon dioxide, one of the primary greenhouse gases in Earth's atmosphere besides water vapor, methane, nitrous oxide and ozone. Since there is currently a carbon dioxide level of approximately 400 parts per million (ppm) in the atmosphere, the plan is to stabilize concentration at 450 ppm. It was decided to take measures until 2030 to adapt the current energy system to this new situation [262].

Unfortunately, renewable technologies are subject to environmental influences and thus not qualified for a constant base-load energy supply. One way to circumvent the dilemma is via the Power-to-Gas concept. In doing so, water electrolysis is applied to produce hydrogen from excess power. Until the hydrogen is needed again to regain power, e.g. via gas-turbine combustion, it has to be stored. The existing natural gas infrastructure can be reutilized for this purpose which is one of the striking advantages of this concept. If necessary, hydrogen can be converted into methane by using carbon dioxide. Also in mobile applications, i.e. vehicles, hydrogen is continuously being discussed as a carbon-free energy carrying substance. In any case, the leakage issue is an undesired companion that must not be dismissed. Accidentally released hydrogen from storage systems can mix with ambient air and form a flammable cloud in a wide stoichiometry spectrum, which poses a significant risk. Under adverse conditions (ignition source, geometrical confinement), a hazardous high-speed combustion wave, i.e. explosion, can develop, entailing fatal consequences for infrastructure and human beings.

Another possibility to meet carbon emission goals is to maintain or even increase the percentage of nuclear power. In fact, the International Atomic Energy Agency (IAEA) does expect nuclear power to expand worldwide until 2030 because of the steady augmentation of reactors in Asia and the Middle East [24]. Nuclear energy seems to undergo a renaissance as carbon-neutral green energy. Risks by climate change and risks by nuclear energy have to be traded off against each other.

China announced to build six new power plants each year in the next ten years. In the same time frame, new nuclear reactors are planned in 14 EU countries, of which only half might actually be built. Once the mentioned 60 new power plants are in operation, the share of nuclear power in China will only be around 10 %. Compared to current shares around 20 % in the USA, more than 70 % in Europe's leading nuclear nation France and almost 30 % in Asia's leading nuclear nation South Korea, even higher Chinese shares might be expected in the long term. It can be concluded that China will take over technological leadership and dictate standards accordingly. Not only because of the impressive number of new reactors in China, but also because of the competitive cost-performance ratio

making Chinese technology attractive to Western states. The first new European power plant after a ten year break is already being built by a French-Chinese syndicate. The facts in this section are adopted from [240].

The German decision to radically quit nuclear energy has not led to similar efforts in other countries so far. More power plants than ever are currently being constructed worldwide. Remarkably, Japan holds on to nuclear energy, too. Not even its (direct) European neighbors could by convinced by Germany's exit plans. Quite the contrary, France, England, Poland and the Czech Republic extend their nuclear capabilities [271]. Nuclear safety therefore remains an urgent German topic in a collective European context. Radioactive fallout does not stop spreading across borderlines.

Also thanks to a strong anti-nuclear community, safety standards were among the highest in Germany. Germany now lost its role as an opinion maker. Only at the forefront of technology and as a lead exporter, it would have been possible to influence the development in Europe and maybe worldwide. Power plants of the newest generation will instead be developed and constructed by China, where anti-nuclear community is still in its infancy. Even Bill Gates recently moved research of his TerraPower nuclear project to Beijing [240].

Because of the potentially devastating consequences, nuclear safety is maybe the strongest motivation to foster research in the field of hydrogen risk analysis. Two major reactor accidents involving massive hydrogen release due to a (partial) core-meltdown are known to the public: the 1979 Three Mile Island accident in Harrisburg (USA) and the 2011 accident in Fukushima-Daiichi (Japan). While only a mild deflagration occurred in Harrisburg, severe explosions were observed in Fukushima. Probably not because of a low hydrogen amount but because of oxygen starvation, the Harrisburg plant escaped serious consequences [221]. The situation in the 1986 Chernobyl accident (former USSR) is less unambiguous. At least the first devastating blast was rather a thermodynamically-driven steam explosion than a chemically-driven hydrogen explosion [22, 130].

1.1 Nuclear safety analysis chain

A systematic methodology for hydrogen analysis in severe nuclear reactor accidents is depicted in flowchart 1.1. Its description mainly follows Breitung et al. [40] and Breitung and Royl [39].

The first step is to specify the *plant design* which has several implications on later stages of the analysis. Especially the core size and type of light-water reactor, Boiling Water Reactor (BWR) or Pressurized Water Reactor (PWR), is important since it determines e.g. the free containment volume, the pre-accident atmosphere (inertized or not) and the total amount of hydrogen and steam that can be produced. Regarding Computational Fluid Dynamics (CFD) methods, this step provides the necessary mathematical boundary conditions to arrive at a unique solution of the general field equations. Flowpaths are heavily depending on the complex three-dimensional geometry.

Depending on the manufacturer of nuclear power plants, different *mitigation systems* are employed to control hydrogen behavior. Glow or spark plug igniters can be used to initiate combustion of the mixture as long as fuel concentrations are comparably low and consequences are not severe. Passive Auto-catalytic Recombiners (PAR) are a popular al-
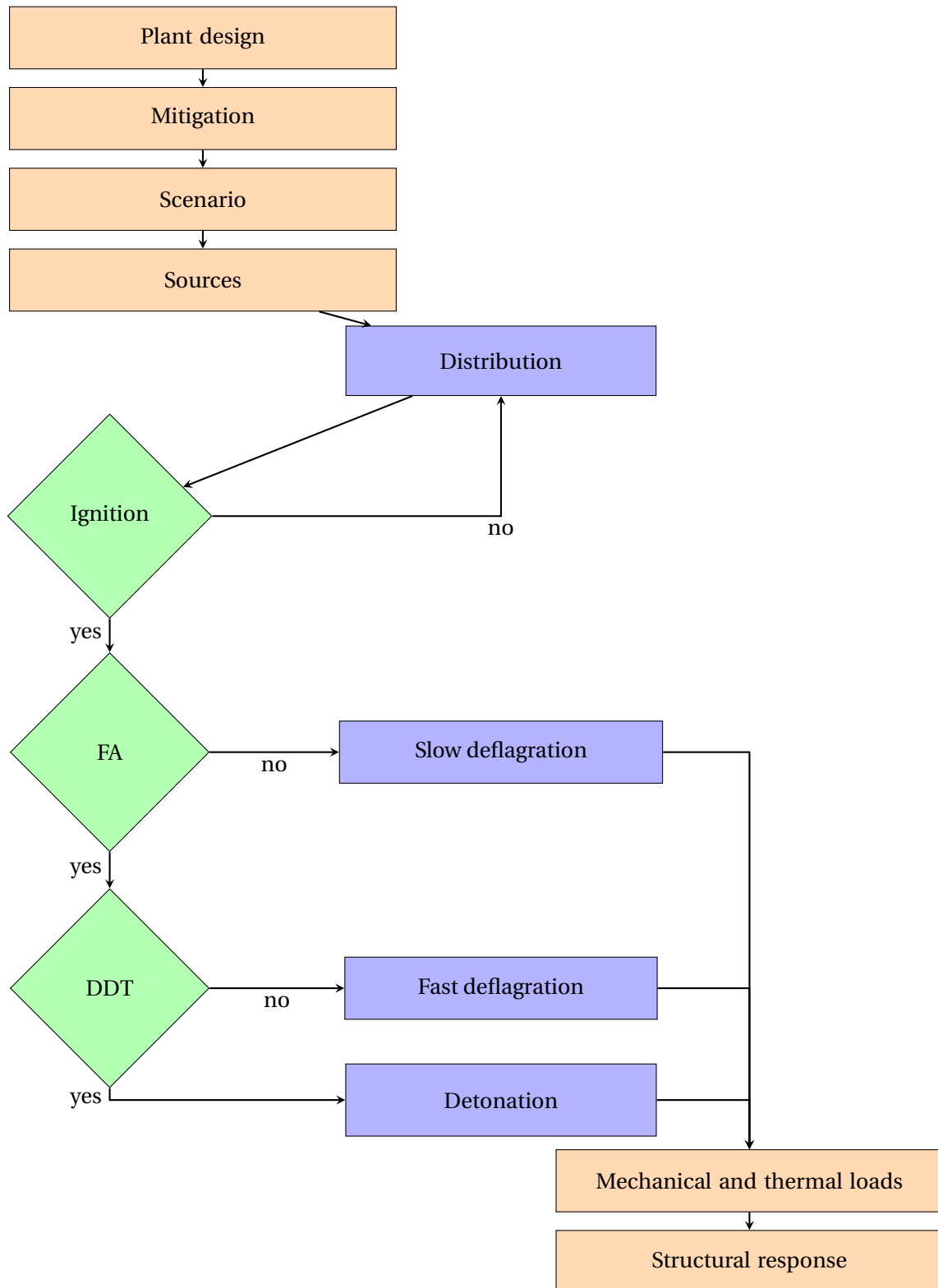
Figure 1.1: Nuclear safety analysis chain according to [39]

ternative to oxidate the hydrogen below ignition temperature. However, PAR are known to act as unintended ignition sources under adverse conditions. Corresponding models are available in most Lumped Parameter (LP) codes but cannot be considered a standard in current CFD codes.

Due to generally large event trees, detailed analysis of all *accident scenarios* is impossible. The most serious scenarios do not necessarily occur at high probability – and vice versa. Probabilistic Safety Analysis (PSA) is applied which denotes the investigation of accident events that occur at non-negligible probability and that can potentially lead to the failure of safety-critical system functions. Hence, only scenarios with a relevant contribution to the core damage frequency are studied in detail. The primary purpose of PSA is to assure a well-balanced safety concept by identifying weak points and deriving countermeasures. Frequently analyzed initiating events involving possible core-meltdown are the Loss-Of-Coolant Accident (LOCA; assuming either a small, medium or large loop break), Station Black-Out (SBO) and Loss-Of-Feed Water (LOFW) accident. The sequence of accident events varies to a large degree between these different scenarios.

If sufficient cooling of the reactor core cannot be guaranteed and fuel rods are (partially) uncovered, they start to overheat and might consequently melt. During the so-called in-vessel phase, hydrogen is mainly produced by the exothermic oxidation of zirconium alloyed fuel rod cladding with steam [69]. After failure of the reactor pressure vessel, the so-called ex-vessel phase, Molten Corium Concrete Interaction (MCCI) becomes the primary mechanism for the generation of hydrogen and other (flammable) gases like carbon monoxide and carbon dioxide [255]. After assuming the release locations, LP codes are usually used to predict the *source terms* of fuel and other gases. Uncertainties in the parametric models increase with accident progression. A comparative quantitative study with respect to a Konvoi-type PWR is presented by Sonnenkalb [243]. According to Kuczera [148], several hundred kilograms of hydrogen were released in each of the affected reactor blocks in the Fukushima-Daiichi accident, eventually leading to severe explosions.

Imposing the source terms of the previous step, the outcome of this step is the spatially and temporally resolved fields of thermodynamic conditions (temperature and pressure) and mixture composition. To calculate the transport and mixing with containment atmosphere, LP codes have been increasingly replaced by CFD codes in recent years. However, reliable sub-models for phenomena like bulk/wall condensation and radiative heat transfer as well as mitigation systems like PAR and liquid water spray are still under development. Due to the sensitivity of the subsequent combustion process, a high accuracy of *distribution* simulations is required.

Deliberate and random *ignition* sources can be distinguished. Examples of the latter class are sparks by electrostatic discharge and ignition from hot surfaces or particles. It is important to note that deliberate ignition sources like spark plug oder glow plug igniters are useless in an SBO accident scenario when electric power is not available. Without further specification, both kinds of ignition are denoted as weak or thermal ignition throughout the work. Compared to other fuels, mixtures with hydrogen are characterized by relatively wide flammability and auto-ignition limits. The time of ignition cannot be predicted deterministically. Continuous checking of above mentioned limits during transient distribution simulations is therefore performed. It is not necessarily conservative to ignite the mixture as soon as possible though. Accumulation of hydrogen over a longer period will most likely result in more severe consequences.

Once the mixture is ignited, the combustion process starts as a slow (quasi-)laminar deflagration but can quickly transform into a fast turbulent deflagration through several accelerating mechanisms, e.g. flame instabilities and turbulence generation in the wake of obstacles. Via the thermal expansion of combustion products, a positive feedback promoting *Flame Acceleration* (FA) exists. The faster the flame propagates, the more pronounced gas-dynamic effects become. Based on the necessary σ-criterion (eq. 2.22), regime-optimized CFD codes for slow or fast deflagrations can be chosen for detailed analysis. The criterion and the phenomenology behind FA is elaborated in sec. 2.3.

Direct detonation initiation (strong ignition) is very unlikely in nuclear safety due to the high energy required. Assuming weak ignition, sufficiently strong flame acceleration is a prerequisite for the hazardous *Deflagration-to-Detonation Transition* (DDT). As experiments showed, the onset of detonation is an abrupt process usually occurring at flame speeds around the sound speed of the hot combustion products. Additionally, the λ-criterion (eq. 2.27), basically a comparison of length scales, must be fulfilled for possible transition to detonation. In the standard approach, strong ignition is then assumed and explosion propagation is calculated by a pure detonation solver. Since only information about mixture and geometry is needed to evaluate the FA and DDT criterion, low-order worst-case assessment can be done during distribution simulations without actually executing reactive flow simulations. Detailed explanations on the DDT phenomenon are provided in sec. 2.4.

Whereas *thermal loads* are important for low-speed combustion, *mechanical loads* prevail for high-speed combustion. Especially for fast deflagrations, the DDT phenomenon itself and detonations, substantial pressure loads on the confining structure must be expected. Pressure loads can be about two orders of magnitude higher than for slow deflagrations (overpressure usually below 1 bar). The total combustion energy released is independent of the combustion speed.

Given the loads of the previous step, evaluation of the *structural response* represents the ultimate goal of the analysis chain. Different materials, e.g. concrete, steel or elastic gaskets, respond differently. Being the final barrier against radioactive release to the environment, the containment (steel) liner is of paramount interest. Its dynamic behavior might be analyzed by simple semi-analytical methods (one-dimensional harmonic oscillator) or complex multi-dimensional Finite-Element Methods (FEM).

In principle, the methodology is not limited to nuclear safety, but can equally be applied to other potentially hazardous situations involving accidental release of hydrogen in air, e.g. in chemical and process industry. Analytical, empirical and numerical methods (at varying modeling degree) are necessary to execute the whole analysis chain. CFD approaches are well-suited for distribution and combustion analysis, marked by purple boxes in fig. 1.1.

1.2   Problem statement

In his thesis, Ettner [79] introduced two important technical innovations which are revisited in the following. The present work addresses the next logical step, namely the improvement of the explosion solver towards industry-scale applications.

Regarding the numerical modeling of reactive flows, a large variety of codes exists that are optimized for particular premixed combustion regimes depending on the underlying physics, cf. purple boxes in fig. 1.1. Whereas deflagrations are subsonic combustion waves driven by diffusive and turbulent exchange of heat and species, detonations are supersonic combustion waves mainly driven by gas-dynamic effects and auto-ignition. Since all different regimes are relevant to explosive combustion, a robust and efficient model with a wide range of validity is required. The fundamentally different mechanisms behind deflagrations and detonations complicate the development of consistent approaches. As mentioned in the nuclear safety analysis chain (sec. 1.1), the state-of-the-art in *large-scale* explosion modeling (sec. 3.2) is to evaluate empirical transition criteria providing information about the worst-case combustion regime that must be expected. Optimized solvers are then used for consequence analysis. Criticism about this approach, primarily related to mixture inhomogeneity and geometrical confinement, is discussed in chap. 2. A group of combustion and nuclear experts [40] stated that it would be a significant improvement to simulate flame acceleration, DDT and detonation propagation within one framework, not being reliant on empirical transition criteria and different CFD codes. Ettner [79] developed such a solver and successfully conducted two-dimensional simulations of a laboratory-scale DDT experiment. Unified modeling of hydrogen distribution and hydrogen explosion within the same CFD solver is not constructive since time scales of both processes are largely diverging. Scale separation should be obeyed which brings fundamentally different requirements to the solver architecture. From a mathematical point of view, fast explosions (time frame: seconds) represent hyperbolically dominated problems whereas fuel dispersion (time frame: hours) is a parabolically dominated problem to a large extent.

Homogeneous mixtures have intensely been studied in the past, experimentally as well as numerically. However, mixtures with concentration gradients represent more realistic scenarios of hydrogen distribution within large facilities like a reactor containment [9, 201, 265]. Due to gravity and the different densities of hydrogen and air (approximately one order of magnitude), hydrogen tends to accumulate below the roof of facilities. Following the scaling law of diffusion, the homogenizing effect of molecular diffusion is comparably weak in large volumes. Mentioned empirical transition criteria are mainly deduced from homogeneous experiments on laboratory scale and do not account for all of the underlying initial and boundary conditions. In contrast, CFD simulations are able to consider the complex three-dimensional geometry and the local fuel-oxidator ratio of the particular system. Ettner [79] therefore incorporated the effect of mixture inhomogeneity for all relevant physical and chemical parameters. To validate this solver extension, he studied the explosion of inhomogeneous mixtures in the GraVent channel [266]. The main direction of flame propagation is perpendicular to the vertically oriented concentration gradients in this facility.

Retaining these approved concepts, the main goal of this work is to reduce grid sensitivity of the methodology and to prepare it for the usage on massively under-resolved meshes. As described by Daudey and Champasith [59], the key point is that the method should be a balance between accuracy, robustness, sensitivity, conservatism and time of realization, depending on project-specific needs. The resolution problem is illustrated by a simple thought experiment: Consider a spherical volume V of radius $R = 26$ m which is inspired
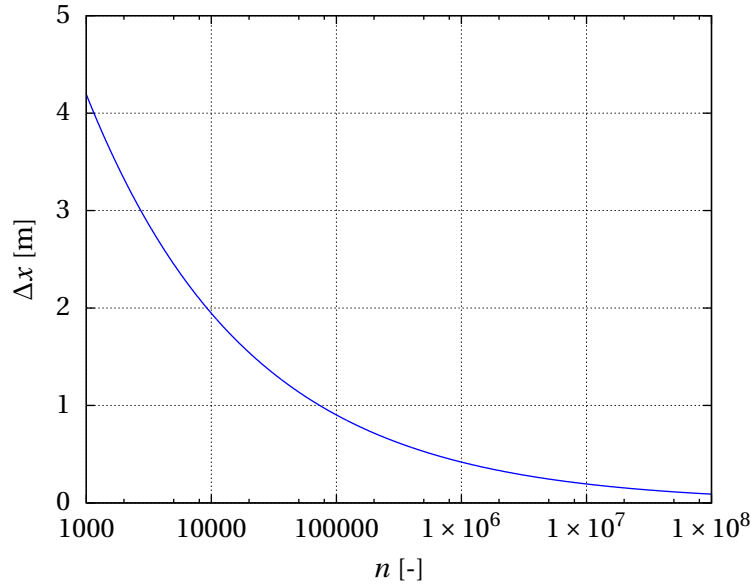
Figure 1.2: Dependency of the characteristic cell size Δx on the number of cells n for a spherical volume of radius $R = 26$ m

by the characteristic containment shape of a Konvoi-type PWR, cf. chap. 5. Assuming uniform discretization, the characteristic cell size Δx is then given by

$$\Delta x\,(n) = \sqrt[3]{\frac{V}{n}} = \sqrt[3]{\frac{\frac{4}{3}\pi R^3}{n}} \propto n^{-\frac{1}{3}} \tag{1.1}$$

as a function of the cell count n. The inverse cube root proportionality stated in eq. 1.1 leads to an increasingly slow decrease of Δx with increasing n, as can be seen in fig. 1.2 (semi-logarithmic scale). Provided that access to high performance computing facilities is granted, desired turnaround times of few days can be achieved for cell counts around 10^7 as experience showed. In this context, the necessary high temporal resolution is another important factor.

Table 1.1: Modeling approaches and corresponding resolution requirements according to [40]

Model class	Smallest scale	Resolved processes
Lumped parameter codes	> 1 m	Large-scale averaged (quasi-) thermodynamic balances
Statistical turbulence models	0.1 – 1 m	Averaged flow quantities, *including* momentum balances, *excluding* localized rare events
Large eddy simulation	0.01 – 0.1 m	Non-linear unsteady motions, *including* large-scale turbulence, *excluding* dissipation scales, chemical scales and localized rare events
Direct numerical simulation	$10^{-5} - 10^{-2}$ m	All processes and full range of scales of the underlying continuum model

A classification of popular simulation approaches is included in tab. 1.1. *Lumped Parameter* (LP) codes are widely-used in nuclear safety to calculate the thermal-hydraulic behavior in the reactor containment. Such codes are basically a system of interconnected control volumes. Whereas mass and energy conservation are guaranteed, there is usually just a rudimentary (one-dimensional) formulation of momentum conservation. The most prominent feature of LP codes is the low to negligible computational effort. However, the author is not aware of any successful attempts to reliably reproduce high-speed combustion in such a manner. Particularly, there is no realistic chance to formulate a LP model for fast deflagrations and detonations due to the complexity of the underlying processes, including gas-dynamic effects. Heavily parametrized LP models are available for slow deflagrations though [44].

The second category covers *statistical turbulence models*, also known as Unsteady Reynolds-Averaged Navier-Stokes (URANS) models. Grid size is in the order of integral turbulence scales. Computational costs are clearly higher but still at an acceptable level. Such methods define the current standard in engineering. Globally unsteady but statistically averaged flow fields, including gas-dynamic effects, can generally be described. Likewise, the important interaction between energy and momentum, i.e. the conversion of chemically bounded energy to kinetic energy is included. Especially due to the non-linear dependency on temperature, mean reaction rate closures are necessary in the Reynolds-averaged context. Often based on a comparison of turbulence and chemistry time scales, the transition between different regimes of premixed combustion can be accounted for. Regarding DDT, the triggering event itself is a highly stochastic, localized and rare event but URANS is able to predict its statistic probability.

Large Eddy Simulation (LES) represents the next level of detail. It is a reasonable compromise between URANS and DNS but can only be afforded for selected engineering applications. Most LES sub-grid models require grid sizes in the inertial range, i.e. a large share of the turbulence spectrum must be resolved. Non-linear turbulent fluctuations are therefore included whereas dissipation scales, combustion scales and localized rare events are missing.

Most expensive *Direct Numerical Simulation* (DNS) is only feasible for academic applications. The mathematical model is strictly based on first principles without any sub-grid closure. Relating to the non-linearity of the governing equations, the full interaction of processes acting on different scales is included. The complete range of flow and chemistry length and time scales, from the energy-containing range down to the dissipation range, must be resolved. As a first approximation on resolution requirements (and therefore an estimation on computational costs), the grid Reynolds number

$$\mathrm{Re_{gr}} = \frac{u_{\mathrm{ref}}\,\Delta x}{\nu},$$
(1.2)

based on a not further specified characteristic velocity u_{ref} should be less or equal to unity [40].

Following the presented classification, it is clear that three-dimensional industry-scale LES or DNS is out of reach for decades to come. A high degree of sub-grid modeling is inevitable which leaves URANS as the method of choice. For safety analysis, it is primarily interesting to know key characteristics such as flame speeds and pressure loads on the containing structure. The focus of this study is thus placed on the global propagation

behavior rather than the micro-structure of DDT. As demonstrated in this work, small-scale mechanisms must not necessarily be resolved for that purpose. Demands on the numerical model are consequently unusual compared to detailed combustion investigations in which in-flame phenomena are important. Solely a correct (integral) reactants-to-products conversion rate must be assured to reproduce global safety characteristics.

Unfortunately, due to the nature of turbulence (which plays an essential role in flame acceleration and high-speed combustion, cf. chap. 2), it is not simply possible to scale the results of small-scale investigations to large-scale applications. Depending on the size or frequency of turbulent eddies, the turbulence cascade is subdivided into an energy-containing range (depending on boundary conditions), inertial range (universal) and dissipation range [48, 212]. The effect of scale in the explosion field of study, especially on DDT, is shown by Dorofeev et al. [66]. In their study, the lower detonation limit of large-scale experiments was found to be several percent of hydrogen lower than in geometrically similar laboratory-scale experiments. This observation has a strong impact on safety analysis for industry-scale accidents. The solver is therefore validated by large-scale DDT experiments in the RUT facility (chap. 4) such that the mesh density and the range of resolved processes is comparable to the final application (chap. 5).

1.3 Thesis outline

After specifying the problem and goal of this work in the context of nuclear safety, chap. 2 introduces fundamental explosion knowledge, i.e. the theoretical and phenomenological background that is necessary to understand the proposed method. A complete literature review on explosion phenomena would certainly be beyond the scope of the present work. Chapter 3 concerns large-scale explosion modeling. A list of particular simulation challenges is followed by a review on state-of-the-art methods. Physical models and numerical techniques are described in detail. Rather than computing numerous cases (parametric studies), the focus of this work is on improving the general methodology which reflects in the fact that its description covers the largest part of this thesis. Some aspects that are elaborated in the work of Ettner [79] are only briefly summarized although they might have a strong influence, e.g. the approximate Riemann solver. Besides explanation of the modeling approach itself, much effort is devoted to generic test cases. If validation by means of global parameters like flame-tip speed is based on full-complexity experiments (including the interaction of different sub-models for flame propagation, gas-dynamics, turbulence, chemical reaction etc.), errors inherent to different solver modules can annihilate each other. For example, if gas-dynamic effects are underestimated (e.g. due to the dissipative nature of standard finite-volume schemes) and chemical reaction is overestimated (e.g. due to deficiencies of the turbulence-chemistry interaction model), the global propagation behavior can coincidentally be correct despite errors induced by both sub-models. In contrast, reduced cases allow to isolate different effects. Separate validation by means of analytical solutions is often possible. Nevertheless, full-complexity experiments are mandatory to assess the overall performance of the solver. Validation by large-scale explosion experiments in the RUT facility is discussed in chap. 4. Additionally, chap. 5 demonstrates the method's application to hypothetical accident scenarios in a full-scale Konvoi-type PWR. A summary and some ideas for further development of the solver are finally presented in chap. 6 and chap. 7, respectively.

2 Explosion fundamentals

Basic elements of globally unsteady high-speed combustion, i.e. explosions, have been understood for many years, yet without a comprehensive mathematical description. Our partly empirical and theoretical knowledge of FA and DDT is reviewed in the following.

2.1 Gas-dynamic relations

Based on the explanations of Bartlmä [17], fundamental gas-dynamic equations are derived first. A one-dimensional, steady, adiabatic (with respect to wall heat transfer), inviscid, compressible flow is considered in which the flame is treated as a reactive discontinuity. On the products side, the gas is assumed to be in thermal and chemical equilibrium. Ideal gas behavior and constant fluid properties (specific isobaric heat capacity c_p and isentropic exponent κ) are further assumed. The frame of reference is moving with the flame such that the calculated velocities are to be interpreted as relative to the reaction front, cf. fig. 2.1. Index 1 denotes the reactants side and index 2 denotes the products side. Despite several simplifications, the theory facilitates reasonable inexpensive approximations in many practical situations. For example, detonation propagation in smooth tubes features a pronounced one-dimensional character from a global point of view.

Conservation of mass, momentum and energy write

$$\rho_1 u_1 = \rho_2 u_2, \tag{2.1}$$

$$p_1 + \rho_1 u_1^2 = p_2 + \rho_2 u_2^2, \tag{2.2}$$

$$h_1^s + \frac{u_1^2}{2} + q_{12} = h_2^s + \frac{u_2^2}{2}. \tag{2.3}$$

Specific enthalpy $h = h^f + h^s$ is composed of a formation part h^f and a sensible part $h^s = c_p(T - T_{\text{ref}})$. Note that $h = h^f$ if $T = T_{\text{ref}}$. Specific heat is given by $q_{12} = c_p(T_2 - T_1) =$
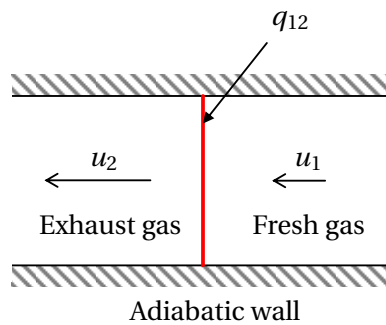
Figure 2.1: Schematic of the one-dimensional reaction front model: Reactive discontinuity colored red; Adapted from [17]

$h_1^f - h_2^f$, which strictly only holds if $h_1 = h_2$ (i.e. if changes in kinetic energy are negligible). Substituting the Mach number $\mathrm{Ma} = u/a$, the dimensionless heat $Q = q_{12}/(c_p T_1)$ and

$$\gamma = \left(\mathrm{Ma}_1^2 - 1\right) \pm \sqrt{\left(\mathrm{Ma}_1^2 - 1\right)^2 - 2(\kappa + 1)\mathrm{Ma}_1^2 Q}, \tag{2.4}$$

a compact set of useful relations is deduced:

$$\frac{p_2}{p_1} = 1 + \frac{\kappa}{\kappa + 1}\gamma, \tag{2.5}$$

$$\frac{\rho_1}{\rho_2} = \frac{u_2}{u_1} = 1 - \frac{1}{\kappa + 1}\frac{1}{\mathrm{Ma}_1^2}\gamma, \tag{2.6}$$

$$\frac{u_2}{a_1} = \mathrm{Ma}_1 - \frac{1}{\kappa + 1}\frac{1}{\mathrm{Ma}_1}\gamma, \tag{2.7}$$

$$\frac{T_2}{T_1} = \frac{p_2}{p_1}\frac{\rho_1}{\rho_2} = \left(\frac{a_2}{a_1}\right)^2. \tag{2.8}$$

The positive and negative sign of the square root expression in eq. 2.4 correspond to supersonic and subsonic flow, respectively. In the special case $Q = 0$, i.e. without chemical reaction, the set of equations resembles the normal shock relations.

Through elimination of the velocities from the governing equations, one obtains the so-called Rankine-Hugoniot relation [279]

$$\frac{p_2}{p_1} = \frac{\frac{\kappa+1}{\kappa-1} - \frac{\rho_1}{\rho_2} + \frac{2\kappa}{\kappa-1}Q}{\frac{\kappa+1}{\kappa-1}\frac{\rho_1}{\rho_2} - 1} \tag{2.9}$$

for the pressure jump as a function of the density jump and the heat release. Combination of the continuity equation 2.1 and momentum equation 2.2 yields the so-called Rayleigh line [279]

$$\frac{p_2}{p_1} = 1 + \kappa \mathrm{Ma}_1^2\left(1 - \frac{\rho_1}{\rho_2}\right). \tag{2.10}$$
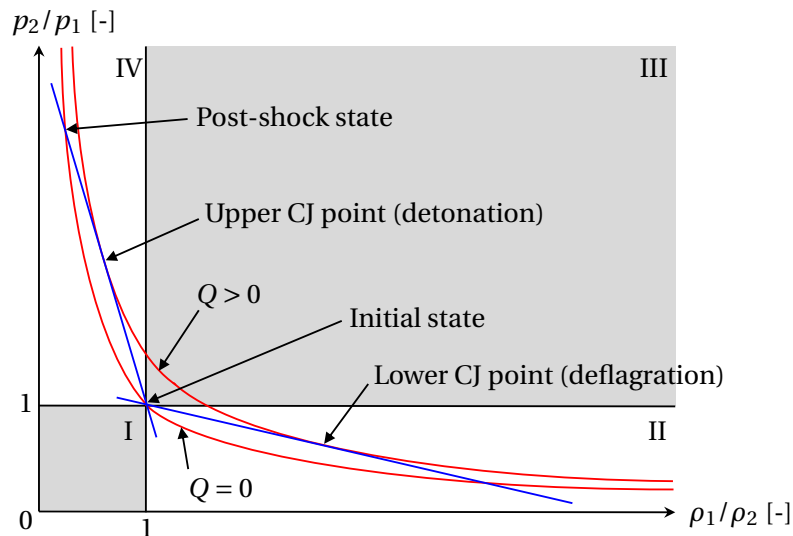
Figure 2.2: Rankine-Hugoniot diagram: Hugoniot curves colored red, Rayleigh lines colored blue; Adapted from [157]

Starting from the initial state (p_1, ρ_1) in fig. 2.2, the slope of each Rayleigh line is given by $-\kappa \mathrm{Ma}_1^2$. Due to the squared inflow Mach number, the slope is always negative which renders the gray-shaded regions I and III inaccessible. Besides, Q is always positive in exothermic reactions. Since both eqs. 2.9 and 2.10 must be satisfied, intersection points of Rankine-Hugoniot curves and Rayleigh lines in white regions II and IV represent theoretically possible solutions. Region II and region IV are known as the subsonic deflagration regime and the supersonic detonation regime, respectively. As is apparent from the Rankine-Hugoniot diagram (fig. 2.2), deflagrations are associated with a moderate pressure drop whereas detonations are associated with a strong pressure rise.

At a given inflow Mach number, the maximum amount of heat that can be transferred to the flow in a steady manner is limited (thermal choking). Supercritical heat transfer results in unsteady phenomena not covered by the theory. Vice versa, a critical inflow Mach number can be determined at a given heat release. Representing the flame propagation velocity in the fixed frame of reference, two unique solutions are found which are named after Chapman [51] and Jouguet [120]:

$$\mathrm{Ma}_{1,\mathrm{CJ}} = \sqrt{1 + \frac{\kappa + 1}{2} Q} \pm \sqrt{\frac{\kappa + 1}{2} Q}. \tag{2.11}$$

In the Rankine-Hugoniot diagram, CJ solutions are identified by the tangential contact point of Rayleigh line and Rankine-Hugoniot curve. Depending on the sign of the second square root expression, eq. 2.11 either describes the deflagration or the detonation solution. However, the deflagration solution (negative sign) is not of high practical relevance since naturally unsteady deflagrations induce flow ahead of the flame and are significantly influenced by multi-dimensional phenomena like turbulence. The detonation solution (positive sign) is separately discussed in sec. 2.5.1.

2.2 Laminar and turbulent burning characteristics

Being one of the fundamental combustion characteristics, the laminar burning velocity S_L can be determined experimentally as well as theoretically, e.g. by CANTERA [95] simulations incorporating a detailed chemical reaction scheme and molecular transport. It denotes the velocity at which an unstretched laminar flame propagates with respect to the incoming flow of unburned reactants [157, 259]. Based on experimental data, a polynomial expression of S_L (eq. 3.91) is used in this work. An approximation of the laminar flame thickness l_L, spanning both preheat and heat release zone, can then be deduced from the thermal theory of Mallard and Le Chatelier [93], cf. eq. 3.114. Combination of these two quantities yields the time scale

$$\tau_L = \frac{l_L}{S_L} \tag{2.12}$$

characterizing laminar flame propagation. Subsequently, laminar scales are synonymous to chemical scales.

By means of the flow velocity u, the kinematic viscosity ν and a characteristic, not further specified, geometrical length scale l (e.g. tube diameter), the Reynolds number

$$\mathrm{Re} = \frac{u \, l}{\nu} \tag{2.13}$$

is defined – essentially a comparison of inertia and friction forces. If Re exceeds problem-specific critical values, laminar-to-turbulent flow transition must be expected. Turbulent flows feature a naturally chaotic, irregular, anisotropic, unsteady, rotational and dissipative behavior. According to the Reynolds decomposition introduced in eq. 3.16, u' indicates the root mean square (r.m.s.) turbulent velocity fluctuation. The integral turbulent length scale l_T represents the size of the large energy-containing eddies which are imposed by the boundary condition, e.g. the height of obstacles. Modeling of u' and l_T in the solver follows eq. 3.112 and eq. 3.113, respectively. Along the lines of eq. 2.12, the turbulent time scale then writes

$$\tau_T = \frac{l_T}{u'}, \tag{2.14}$$

which can be interpreted as the circulation period of the large eddies. Depending on the size or frequency of turbulent eddies, the turbulence cascade is subdivided into an energy-containing range (depending on boundary conditions), inertial range (universal) and dissipation range [48, 212]. On average, through the non-linear interaction of eddies on all scales, turbulent kinetic energy $k = 3/2 \left(u'\right)^2$ is continuously transported from larger to smaller eddies at a rate that is equal to the viscous dissipation rate ε. Kolmogorov's seminal equilibrium theory [142, 143] provides a quantitative estimation of dissipation-level scales employing dimensional arguments. Both length scale

$$l_\eta = \left(\frac{\nu^3}{\varepsilon}\right)^{1/4} \tag{2.15}$$

and time scale

$$\tau_\eta = \sqrt{\frac{\nu}{\varepsilon}} \tag{2.16}$$

are based on ν and ε, the only quantities of relevance in this regime. The kinetic energy of the smallest turbulent eddies is not enough to overcome the viscous forces. As a consequence, flow energy is ultimately converted to heat below this scale. The interested reader is referred to the books of Pope [212] or Cant and Mastorakos [48] for a more profound description of turbulent flows.

Premixed combustion is heavily affected by turbulence. Using above definitions of chemical and flow scales, a couple of non-dimensional numbers is introduced, separating the different regimes of turbulence-chemistry interaction in the Borghi diagram, fig. 2.3. Similar to the normal Reynolds number (eq. 2.13), the turbulent Reynolds number is given by

$$\text{Re}_T = \frac{u' l_T}{\nu}. \tag{2.17}$$

The higher Re_T, the less important is the molecular exchange of heat and species in relation to turbulent exchange processes. Consequences on numerical modeling are discussed later. The Karlovitz number

$$\text{Ka} = \frac{\tau_L}{\tau_\eta} = \left(\frac{l_L}{l_\eta}\right)^2 \tag{2.18}$$

compares chemical scales with the smallest turbulent scales. A second Karlovitz number

$$\text{Ka}_\delta = \frac{\tau_\delta}{\tau_\eta} = \left(\frac{l_\delta}{l_\eta}\right)^2 \approx 0.01\,\text{Ka} \tag{2.19}$$

refers to solely the heat release zone l_δ, instead of the full laminar flame thickness l_L including the preheat zone. The widespread approximation $l_\delta \approx 0.1 l_L$ holds for hydrocarbon as well as hydrogen mixtures [93]. Furthermore, the turbulent Damköhler number

$$\mathrm{Da}_T = \frac{\tau_T}{\tau_L} \tag{2.20}$$

compares chemical scales with the largest turbulent scales. It can be shown that these quantities are linked by

$$\frac{u'}{S_L} \frac{l_T}{l_L} = \mathrm{Re}_T = \mathrm{Da}_T^2 \, \mathrm{Ka}^2. \tag{2.21}$$

In the logarithmic plot of the Borghi diagram, constant levels of the mentioned non-dimensional numbers lie on straight lines.

Description of the regime diagram mainly follows Peters [206]. Representing its historic development, flame classification by Borghi [32, 33] is additionally included. Besides, Da_T (unused by Peters) is still useful in matters of quenching effects, cf. e.g. [261].

Laminar flame propagation prevails at $\mathrm{Re}_T < 1$. The flamelet assumption (one-dimensional inner flame structure identical to laminar flames) is well justified for turbulent flames if $\mathrm{Re}_T > 1$ and $\mathrm{Ka} < 1$. In the flamelet regime, turbulent eddies are not able to penetrate the inner flame structure since the size of the smallest eddies still exceeds the laminar flame thickness. Only the global shape of the laminar flame complex is altered. Wrinkled flamelets ($u'/S_L < 1$) and corrugated flamelets ($u'/S_L > 1$) are further
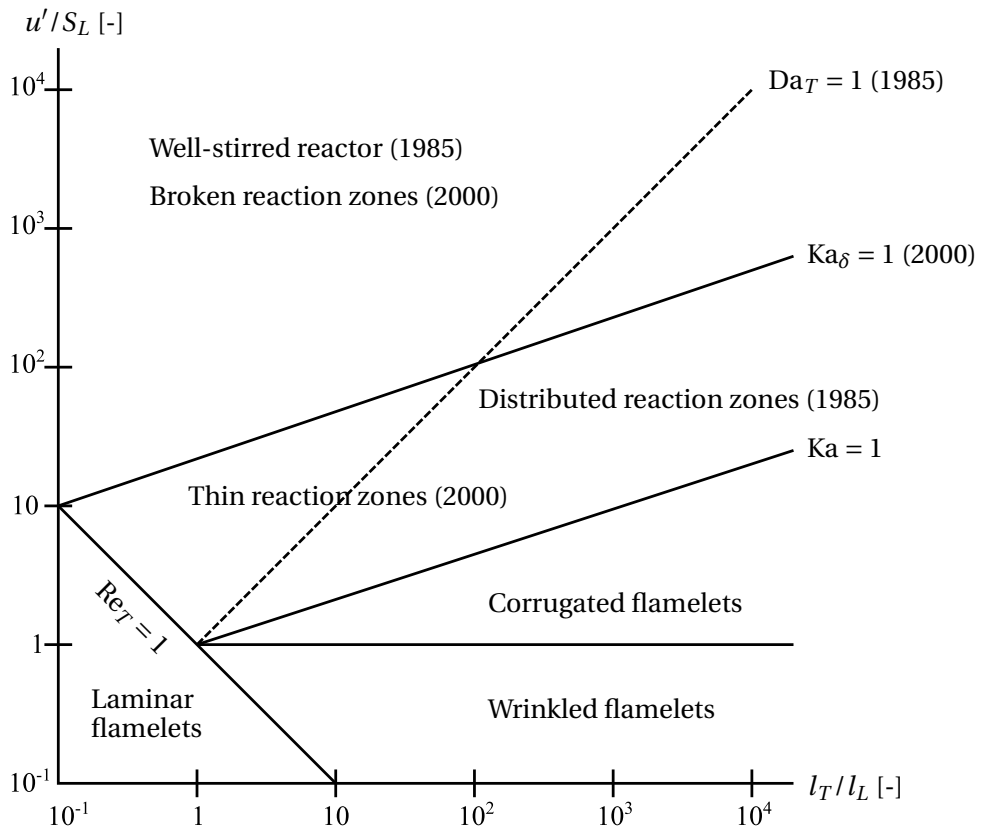
Figure 2.3: Regime diagram of turbulent premixed combustion: Versions of Borghi (1985) [32, 33] and Peters (2000) [206] combined

distinguished. Strong constrictions of the flame are prevented if the laminar flame speed outweighs the velocity of even the large energy-containing eddies. With increasing turbulence intensity, this ratio changes and turbulent eddies may lead to the spatial separation of flame kernels. The turbulent burning velocity increases approximately at the same rate as the effective flame surface increases. Thus, the reaction rate is rather controlled by turbulent 'mixing' than by chemical kinetics.

Regime classification above the Ka = 1 line is less unambiguous. According to Borghi (1985), distributed reaction zones are predicted for $\mathrm{Da}_T < 1$ and well-stirred conditions are predicted for $\mathrm{Da}_T > 1$. In the latter case, the reaction rate is primarily controlled by chemical kinetics. According to Peters (2000), the $\mathrm{Ka}_\delta = 1$ line subdivides the upper part of the regime diagram. For Ka > 1 and $\mathrm{Ka}_\delta < 1$, thin reaction zones are expected since the smallest eddies are able to penetrate the preheat zone but not the far smaller heat release zone. As a consequence, mixing in the preheat zone intensifies whereas the heat release zone remains intact. The turbulent burning velocity is further increasing compared to corrugated flamelets. For $\mathrm{Ka}_\delta > 1$, the smallest eddies are even able to manipulate the heat release zone. Reacting fluid parcels can be mixed with cold reactants prior to reaction completion ($\tau_\eta < \tau_\delta$). Instead of a compact flame structure, a multitude of partially burned pockets occurs, leading to the indication as broken reaction zones. Due to incomplete reaction, the turbulent burning velocity now decreases after reaching its maximum – the well-known bending behavior at high turbulence intensities. Extreme conditions may lead to quenching, i.e. the complete termination of chemical reaction [208, 270]. Performing two-dimensional DNS, Poinsot et al. [209] demonstrated that quenching effects do not only depend on turbulence but also on heat losses and dynamic effects. Even for Ka = 25 (non-adiabatic conditions) and Ka = 180 (adiabatic conditions), flame quenching has not been observed. The authors stated that the flamelet assumption can often be extended to Karlovitz numbers above unity.

In case of explosion accidents, a general upwards trend in the Borghi diagram is expected [41]. According to the scaling analysis of He [103], a minimum of both u' and l_T is necessary for DDT (following weak, not strong ignition). The DDT-critical regime is thus located in the upper right region. However, classification in the Borghi diagram does not fully characterize explosive combustion since neither auto-ignition effects, nor flame instabilities (intrinsic or provoked by gas-dynamic effects, cf. sec. 2.3.2) are incorporated. Both phenomena are essential in the explosion context. Detonative combustion (sec. 2.5) particularly eludes classification in the Borghi diagram. Nevertheless, it can be concluded that the flamelet assumption is the most appropriate deflagration model basis if turbulence-chemistry interaction is expected in multiple regions of the regime diagram. Only in the upper region, the flamelet assumption is clearly violated. The applied combustion model accounts for the upwards shift in the Borghi diagram (increasing turbulence intensity with increasing flame speed) as well as additional effects, cf. sec. 3.5.

2.3   Flame acceleration

Arranged around the well-known explosion symbol, the triangle displays the main influencing factors of explosive combustion in fig. 2.4: ignition, mixture and geometry. Evidently, ignition is a prerequisite for premixed combustion. As mentioned in sec. 1.1, weak spark ignition is the likeliest scenario in nuclear safety. Compared to hydrocarbons, much

lower ignition energy is required for hydrogen. In terms of the mixture, both fuel-oxidator ratio and thermodynamic state are of importance. Hydrogen-air flammability limits are discussed in sec. 3.5.3. Furthermore, mixture inhomogeneity has a strong effect on explosion progression. To accelerate the flame, geometrical confinement and congestion play a crucial role.

FA is a key element of globally unsteady explosive combustion. Particularly, it creates the critical conditions possibly leading to DDT. The phenomenology behind the process is elaborated in the next subsection. The most widely-used approach to correlate the FA potential is the so-called σ-criterion of Dorofeev et al. [67]:

$$\sigma = \frac{\rho_u}{\rho_b} > \sigma_{\text{cr}}. \tag{2.22}$$

For the transition between slow and fast deflagrations, a sufficiently high expansion ratio σ (ratio of densities of reactants ρ_u and products ρ_b) of the mixture is a necessary requirement. Contrary to slow deflagrations, the propagation velocity of the flame front with respect to an external observer v surpasses the speed of sound of the reactants for fast deflagrations. In this context,

$$v = \sigma S_L \tag{2.23}$$

gives the propagation velocity of both a spherically expanding laminar flame and a one-dimensional laminar flame departing from a fixed wall. Specific to hydrogen-air mixtures at ambient conditions, the empirically determined critical expansion ratio lies at $\sigma_{\text{cr}} \approx 3.75$, corresponding to a volumetric hydrogen concentration of about 10.5 %. Criticism about this approach is related to the influences of mixture inhomogeneity and partial confinement which are neglected in eq. 2.22.

For semi-confined stratified layers, a modified critical expansion ratio

$$\sigma_{\text{cr}}^* = \sigma_{\text{cr}} \left(1 + K \frac{s}{h} \right) \tag{2.24}$$

has been proposed to replace σ_{cr} in eq. 2.22 [86, 152]. Hence, σ_{cr}^* is a function of the facility-specific empirical constant K, obstacle spacing s and layer thickness h. σ_{cr} represents the reference value for complete confinement (equivalent to $h \to \infty$) and therefore a worst-case. The ratio s/h incorporates the opposing effects of turbulence generation by

Figure 2.4: Explosion triangle

obstacles and transverse losses on the unconfined side of the combustible layer. Increasing s reduces turbulence production and flame wrinkling whereas decreasing h increases the relative portion of transverse losses. Both effects diminish FA and higher critical expansion ratios σ_{cr}^* are consequently necessary to reach sonic flame velocities. The general tendency is confirmed by independent investigations of Vollmer et al. [80]. Transverse venting consistently extenuates FA and ultimately DDT in TUM's GraVent facility. Interestingly, flame speeds and overpressures were slightly higher for small degrees of venting in the FLAME facility of Sandia National Laboratories [237].

Relating to mixture inhomogeneity, one idea is to correlate the FA and DDT propensity with the most reactive mixture layer (usually at the top of the channel). Reasonable agreement with experiments was found for KIT's large-scale semi-confined A1 facility [98, 153]. Boeck [28] later discovered that this concept is not necessarily valid for entirely closed obstructed channels. Computing mixture-averaged combustion properties, it is possible to quantify the relative FA difference in terms of run-up distances, depending on the level of mixture inhomogeneity [26].

2.3.1 Phenomenology

Thorough reviews on the topic are available from Ciccarelli and Dorofeev [53], Ciccarelli et al. [54] and Dorofeev [64]. Characteristic stages of flame acceleration in obstructed facilities are illustrated in fig. 2.5.

Initially, the mixture is normally at rest or moving slowly (e.g. due to buoyancy) in accidental explosions. After ignition, the flame spreads more or less spherically around the ignition source until it interacts with the confining geometry. If the initial turbulence level is low, (quasi-) laminar flame propagation prevails (stage A). A promoting effect results from (intrinsic) flame instabilities, cf. sec. 2.3.2. Whereas the hydrodynamic Landau-Darrieus instability requires a certain flame speed or curvature radius, the thermal-diffusive instability develops right after ignition in sufficiently lean hydrogen-air mixtures. Given the mentioned mechanisms alone, the slow deflagration regime (flame speed below the reactants' speed of sound, transient overpressure up to approximately 1 bar) is usually not exceeded. Via turbulence production at the walls and global flame elongation, FA is basically possible in smooth channels. Both effects increase the integral reaction rate in the system. Mixture inhomogeneity is one possible reason for flame elongation. In general, the flame speed is depending on the distance traveled by the flame. The longer the channel or facility, the more serious consequences must be expected.
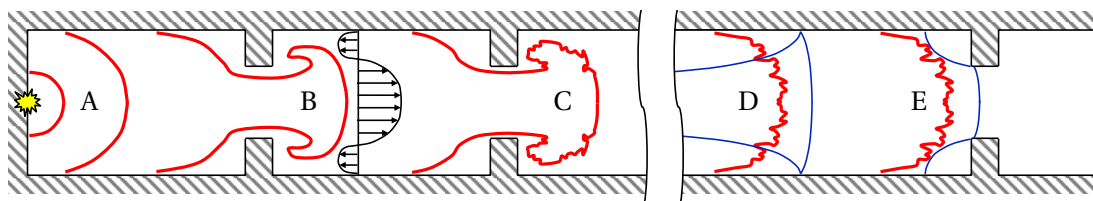
Figure 2.5: Phenomenology of FA in obstructed facilities: Flame colored red and shocks colored blue

Regardless, a strong supporting effect is attributed to obstacles partially blocking the flame path. It has to be recalled that the flame propagation velocity v (in the fixed frame of reference) is the superposition of the unburned flow velocity u and the burning velocity S:

$$v = u + S. \tag{2.25}$$

Via acoustic pressure waves permanently emanating from the flame zone, thermal expansion of the combustion products induces flow ahead of the flame. During the early stage, FA is mainly due to surface area augmentation caused by the non-uniform velocity profile of the unburned gas in the recirculation zones behind obstacles (stage B). Later, when the turbulence production in the shear layers behind obstacles becomes dominant, turbulent wrinkling of the flame has a major influence (stage C). A 'positive' non-linear feedback between fluid motion and flame propagation comes into play: Starting from an increased fluid velocity, the turbulence level is rising alike. As a consequence, local and thus global reaction rate is increasing. Stronger thermal expansion in turn leads to an elevation of the fluid velocity. Gas-dynamic (relating to pressure waves) and fluid-dynamic phenomena (relating to turbulence) of the feedback mechanism may be distinguished [160].

Due to the powerful feedback, fast turbulent deflagrations (flame speed between the reactants' and products' speed of sound, transient overpressure between approximately 1 bar and 10 bar) can develop under appropriate conditions. u outweighs S by far in this case. Acoustic pressure waves, which are permanently emitted by the flame, cause only a small pressure rise at a time but continuously precompress and preheat the unburned gas. Accordingly, the sound speed and thus the velocity of weak pressure waves increases gradually. This process leads to the coalescence of pressure waves, and eventually to the formation of shock waves which are characterized by an abrupt pressure rise (stage D). Note that the development of shock waves is only possible in the supersonic regime. The faster the flame propagates, the more pronounced those gas-dynamic effects become.

Mentioned intrinsic and provoked flame instabilities are no less important in high-speed and highly turbulent flames [54, 63, 207]. Final stages of FA, yet before DDT, are largely driven by shock-flame interaction (stage E). Approximately at the sound speed of the products, the propagation velocity is either maintained (choking regime in obstructed tubes) or experiences a sudden jump to detonation velocities. The onset of detonation is examined in sec. 2.4.

2.3.2 Flow and flame instabilities

Several instabilities, either of general hydrodynamic nature or flame-specific, considerably promote the process of FA (cf. e.g. [53]):

- The Rayleigh-Taylor instability occurs for fluids of different density in the presence of acceleration, such as gravity or by moving interfaces.

- The Kelvin-Helmholtz instability is induced by shear between two fluids which are convected at unequal velocity.

- The Richtmyer-Meshkov instability is provoked by shock waves that are running across an interface separating fluids of different density.

- The thermal-diffusive instability is an intrinsic flame instability caused by an imbalance of species and heat fluxes.

- The Landau-Darrieus instability denotes the hydrodynamic amplification of distortions due to thermal expansion across the flame front.

- The acoustic flame instability is based on the coherence between reflected acoustic waves and heat release in the flame.

In almost all cases, small initial perturbations of the interface, i.e. the flame, are amplified over time by theses mechanisms. Increased flame surface area and interconnected flame stretch effects can yield significantly higher reaction rates. The strength of these instabilities and their relative influence on FA changes during the explosion process. The list does not rise any claim to be exhaustive. Since they play a crucial role in numerical modeling and discussion of the simulation results, more extensive background is here provided about the thermal-diffusive and Richtmyer-Meshkov instability.

Characterization of the thermal-diffusive flame instability as *intrinsic* reflects the fact that it develops independent of external driving forces like buoyancy, turbulence or pressure waves. The origin of this kind of instability is an imbalance of heat and species fluxes which can be expressed by the Lewis number

$$\text{Le} = \frac{a}{D} \tag{2.26}$$

with respect to the unburned mixture. In the familiar definition, the thermal diffusivity a is divided by the diffusion coefficient D of the deficient, i.e. reaction-limiting, reactant. An issue arising from this formulation is examined in sec. 3.5.5.2. Hydrogen flames are particularly prone to this phenomenon because of the high diffusivity of hydrogen compared to all other species. Local accumulation and depletion of the limiting species according to flame topology is also known as preferential diffusion [163].

As experimental evidence (shadowgraphy images in fig. 2.6) suggests, the occurrence of thermal-diffusive instability is heavily dependent on the fuel-oxidator ratio in hydrogen flames. Whereas unstable flame propagation is observed in the lean mixture (11.5 % of
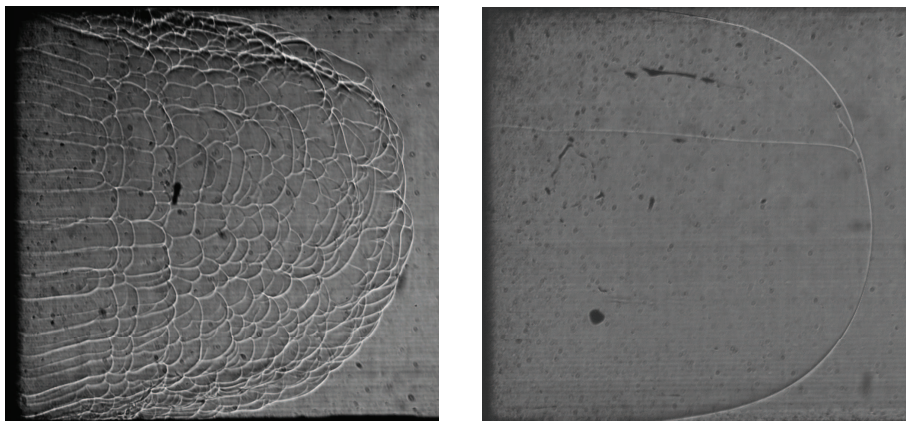
Figure 2.6: Shadowgraphy images of unstable (11.5 % of hydrogen in air, Le < 1) and stable (29.4 % of hydrogen in air, Le ≈ 1) early flame propagation in the GraVent facility; Reproduced from [123]
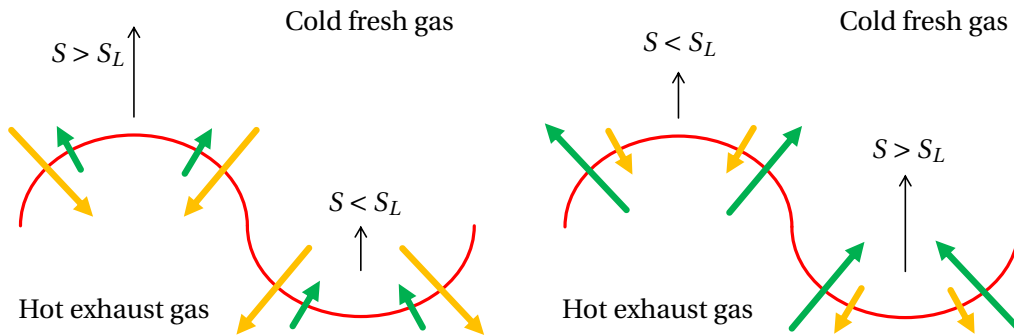
Figure 2.7: Schematic of thermal-diffusive instability: Unstable situation on the left (Le < 1), stable situation (Le > 1) on the right; Flame colored red, heat flux colored green and species flux colored orange; Adapted from [207]

hydrogen in air, Le < 1), stable laminar flame propagation is observed in the nearly stoichiometric mixture (29.4 % of hydrogen in air, Le ≈ 1). Featuring Le ≈ 1 irrespective of the equivalence ratio, most hydrocarbon flames are less sensitive to this phenomenon and show predominantly smooth flame fronts (in the absence of turbulence etc.). This Le-related behavior can indeed be explained by the underlying mechanism [207], cf. fig. 2.7.

If Le < 1, the molecular diffusion of reactants from the cold fresh gas to the hot exhaust gas outweighs the conversely oriented diffusion of heat. The behavior is consequently dominated by the concentration distribution of the deficient species (hydrogen in case of lean hydrogen-air mixtures) on the hot side where a high temperature is maintained. Due to the topological situation, hydrogen accumulates in convexly curved sections and depletes in concavely curved sections (towards the fresh gas side). As a consequence, compared to the burning velocity of a laminar planar flame S_L (cf. eq. 3.91), the local burning velocity S increases and decreases correspondingly. In addition to flame curvature effects, tangential flame strain effects are superimposed. Initial perturbations of the flame are amplified, eventually leading to the formation of a cellular flame structure. In case of extremely small curvature radius, i.e. flame constrictions, complete local extinction occurs in concave sections. The leaner the mixture, the smaller Le and the more pronounced the flame wrinkling effect becomes.

For Le > 1, heat diffusion from the hot exhaust gas to the cold fresh gas outweighs the conversely oriented molecular diffusion of reactants. The behavior is here dominated by the temperature distribution on the cold side where a high concentration of the deficient species (oxygen in case of rich hydrogen-air mixtures) is maintained. Thus, local burning velocity S shows the opposite tendency compared to Le < 1. Initial perturbations of the flame are dampened, preventing the formation of a cellular flame structure. The richer the mixture, the larger Le and the stronger the stabilizing effect becomes.

It should finally be noted that the thermal-diffusive instability is always accompanied by the hydrodynamic mechanism named after Landau and Darrieus [155]. For example in the left picture of fig. 2.6, it is not possible to determine the relative influence of both effects. However, the Landau-Darrieus instability can exist by itself if the thermal-diffusive mechanism is neither damping nor amplifying flame perturbations, i.e. Le ≈ 1. Further information on (intrinsic) flame instabilities can be found in [55, 279].

Probably the most important mechanism of shock-flame interaction is the Richtmyer-Meshkov instability [188, 219]. It can be interpreted as the impulsive acceleration limit of the Rayleigh–Taylor instability. The only difference is the driving force: shock waves in the first case and, for instance, buoyancy in the latter case. If pressure gradients (e.g. due to a shock wave) and density gradients (e.g. due to a flame) are not aligned with each other, baroclinic vorticity is generated that leads to further distortion of an initially curved light-heavy interface. Thus, the mechanism is self-supporting – the nature of an instability. The situation is idealized in fig. 2.8. A planar shock wave is propagating towards a curved flame (left picture). Vorticity is consequently deposited at the flame. Depending on the level of misalignment, the magnitude Γ and orientation of vortical motion varies alongside the surface (center picture). Deformation of the flame is finally increasing (right picture).

In both experimental [54] and computational studies [89], the importance of shock-flame interaction during later stages of FA is emphasized. From a global point of view, the Richtmyer-Meshkov instability creates characteristic funnels of unburned material extending into the burned region. Through continuous interaction on a wide range of scales, the flame surface area increases significantly on macroscopic as well as microscopic level. As a first approximation, the overall reaction rate is enhanced at the same rate. Besides, continuous shock-flame interaction maintains a highly turbulent flame brush and therefore the medium for DDT-critical phenomena. Just as much, the sudden elevation of heat release is assumed to be a key factor in triggering DDT in the vicinity of the turbulent flame brush [136].
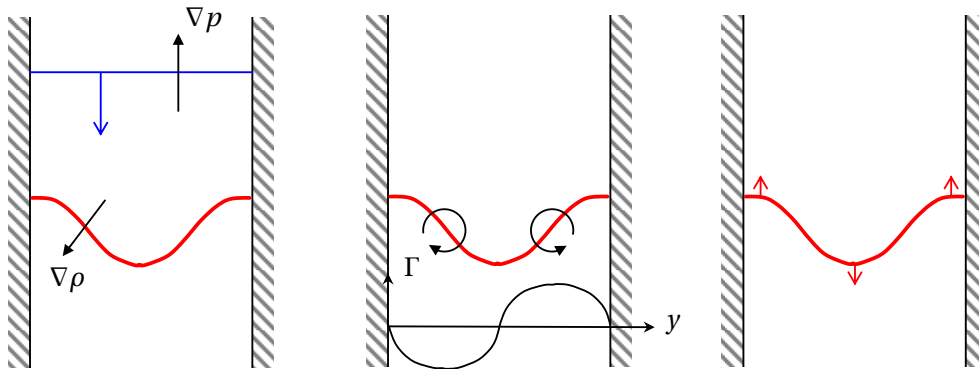
Figure 2.8: Schematic of the Richtmyer-Meshkov instability: Flame colored red and incident shock colored blue; Adapted from [45]

2.4 Deflagration-to-detonation transition

Throughout this work, Deflagration-to-Detonation Transition (DDT) denotes the onset of detonation, i.e. the transition itself, according to the etymology of the term. Other researchers like Thomas [251] include the process of FA in the term DDT. Direct detonation initiation, e.g. by high explosives, is explicitly excluded. DDT is thus a consequence of weak ignition and sufficiently strong FA to critical conditions.

On a macroscopic level, two categories of DDT are distinguished by Klein et al. [140]: The first one is based on (oblique) shock reflection at planar walls or shock focusing near edges
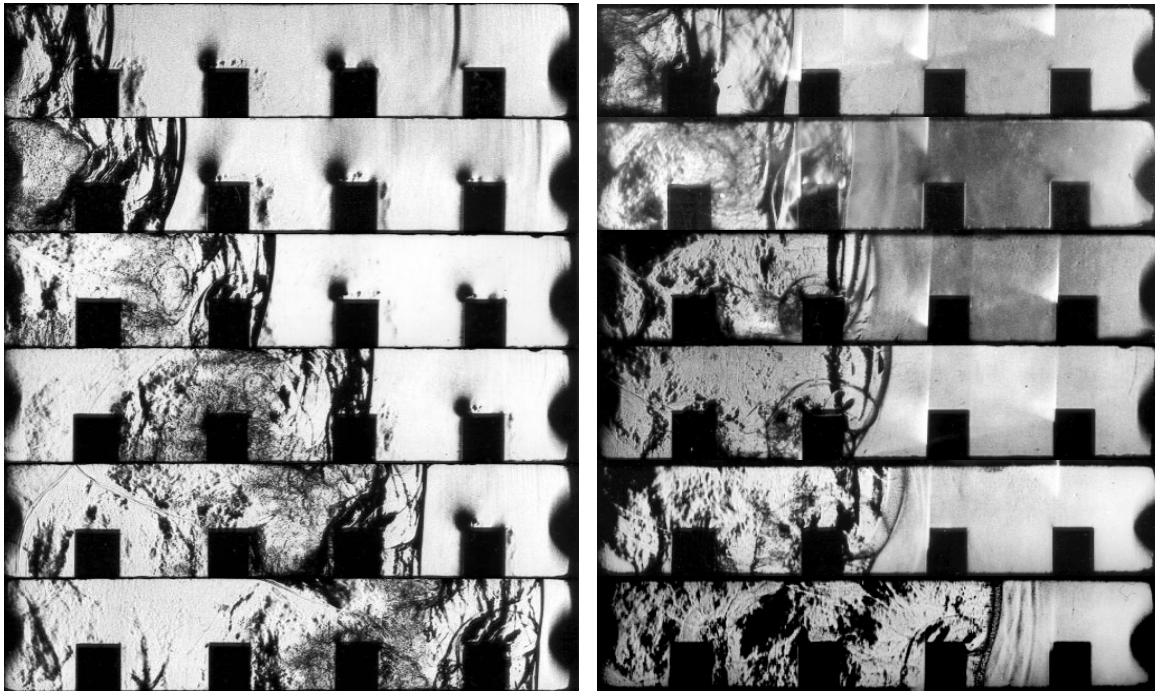
Figure 2.9: Shadowgraphy images of the miniRUT facility: Explosion propagation in the obstructed channel without (24 % of hydrogen in air) and with (29.6 % of hydrogen in air) obstacle-induced DDT; Reproduced from [66]

and corners. Via auto-ignition of the preconditioned fresh gas, the DDT-triggering phenomenon can be located ahead of the main flame brush. Critical conditions are preferably reached at the obstacle front side, at the channel wall shortly behind the obstacle or even at the centerline in symmetric configurations [54]. Formation of a strong Mach stem is often involved in the process. Such DDT mechanisms are identified as *strong solution* or *mode A* in the following.

The second category comprises all instabilities- and mixing-related mechanisms, mostly originating from the vicinity of the turbulent flame brush. Shock-flame interaction (sec. 2.3.2), the localized explosion of unburned pockets enclosed in the burned mixture [65] and shock-boundary layer interaction constitute particularly relevant phenomena. Due to the absence of behavior-dominating obstacles, shock-boundary layer interaction is especially critical for smooth tubes. As demonstrated in a computational study [73], the wall boundary layer between precursor shock and flame brush is preconditioned by a series of weaker shock waves before auto-ignition occurs. From the initiated kernel, the flame may or may not propagate in the turbulent boundary layer towards the leading shock. In either case, a strong local explosion in the boundary layer is the final cause for DDT. The respective DDT terminology is *weak solution* or *mode B*.

Independent of the initiating mechanism, it depends on the geometry and flow situation whether a local explosion is followed by self-sustained detonation propagation. For example in [128, 252], the propagation of a blast wave around an obstacle is studied. The interaction with expansion fans diminishes the strength of the blast wave and can prevent the transition to stable detonation propagation. On the downstream side of an obstacle, this corresponds to the classical diffraction problem.

Since the observed scenarios are diverse, a universally valid schematic of the DDT phenomenology, similar to fig. 2.5, cannot be provided. Nevertheless, an example of obstacle-induced DDT in the miniRUT facility [66] is shown in fig. 2.9. Designed to investigate the effect of scale, the miniRUT facility is a geometrically similar but down-scaled (by a factor of 50) version of the industry-scale RUT facility examined in chap. 4. It was found that the lower detonation limit was higher by an absolute value of more than 10 % of hydrogen in the laboratory-scale experiment. Local phenomena underlying DDT are assumed to be the similar though. Other than in the industry-scale experiment, optical access allows to analyze flame and shock behavior by means of shadowgraphy images. Explosion propagation in the obstructed part of the miniRUT facility for a very reactive, nearly stoichiometric, mixture (29.6 % of hydrogen in air, right side of fig. 2.9) is first considered. Emanating from the second obstacle, a circular blast wave structure is observed in frames 3 to 5. Latest in frame 5, the blast wave interacts with the curved leading shock. Onset of detonation is eventually triggered by this phenomenon. In the last frame, the flame brush is already coupled to the leading shock, indicating a detonation. DDT did not directly result from shock reflection at the obstacle. A less reactive mixture (24 % of hydrogen in air, left side of fig. 2.9) is presented for comparison. Apart from a larger distance between the turbulent flame brush and the leading shock complex (about one obstacle spacing, cf. frame 2), the behavior is similar. Additionally, a weak precursor shock is observed in the first frame on the far right. The characteristic circular blast wave structure is clearly visible in the last frame. However, DDT does not occur in this case.

On a microscopic level, the origin of DDT is assumed to be associated to so-called hot spots as a result of equivalence ratio, pressure or temperature fluctuations. One intrinsic property of hot spots and consequently DDT is their stochastic nature, similar to turbulence-related phenomena. Other than in simulations, perfectly identical initial and boundary conditions can never be assured in experiments of the same kind. Shedding light on the various origins of DDT in gas-phase combustion, the comprehensive review article of Oran and Gamezo [203] is an interesting reading. Earlier insightful summaries on the subject have been compiled by Kuo [151], Lee and Moen [160], Lewis and von Elbe [163], Shepherd and Lee [236].

Starting from a microscopic hot spot, a macroscopically observable blast wave or local explosion ('explosion within the explosion' according to the seminal work of Urtiew and Oppenheim [260]) can spontaneously develop under appropriate conditions. Whereas the necessary medium can be created in many ways, there seems to be general agreement (without direct experimental evidence) that spontaneous wave formation is governed by a universal mechanism involving spatial reactivity gradients. Actually, the spontaneous wave velocity is inversely proportional to the spatial gradient of the ignition delay or induction time. It is a well known fact that ignition delay times are a highly non-linear function of mixture composition, pressure and above all, temperature. This circumstance is directly employed in the combustion modeling strategy, cf. sec. 3.5.6. The gradient concept originally dates back to Zeldovich et al. [292] and has been generalized to the Shock Wave Amplification by Coherent Energy Release (SWACER) mechanism by Lee [159]. Given such a spatial reactivity gradient, the reaction is most easily initiated in those mixture portions with the lowest induction time, i.e. at hot spots. Once the reaction sets in, local thermal expansion either creates a shock wave or amplifies an existing shock. Under appropriate conditions, the strengthened shock wave can even ignite neighboring mixture portions with a higher induction time when it is propagating along the reactivity gradient. If heat

release and shock wave motion are in coherence, the self-supporting mechanism manifests in spontaneous wave formation, i.e. a local explosion which may finally undergo the transition to detonation.

In practical safety analysis, the DDT propensity is correlated by additional empirical criteria. DDT is mostly triggered at flame speeds close to the sound speed of the combustion products. The onset of detonation then manifests in a characteristic sudden jump of propagation velocity. Continuous acceleration to detonation velocities contradicts experimental observations. Hence, sufficiently strong FA to the (choked) fast deflagration regime is a first requirement for DDT. The second necessary condition,

$$L > 7\lambda, \tag{2.27}$$

is defined by means of the detonation cell width λ. According to Dorofeev et al. [66], the underlying data base includes experiments on various scale. As a measure of mixture reactivity, λ is only depending on mixture composition and thermodynamic initial conditions (in a sufficiently large volume). However, its experimental determination introduces a level of uncertainty as explained in sec. 2.5. At least for periodically obstructed channels, different rules (not shown here) are available to calculate the characteristic geometric length scale L as a function of obstacle spacing, blockage ratio etc. In even more complex geometries, L can conservatively be estimated from the flammable cloud volume V_c [41]:

$$L = \sqrt[3]{V_c}. \tag{2.28}$$

General criticism concerns the fact that detonation cells are a characteristic phenomenon of stable detonation propagation, not the onset of detonation which is of prior interest here. It is known from obstructed tube experiments that DDT and detonation propagation limits are more or less identical whereas the detonation transmission limit (from obstructed to smooth sections) is usually several percent of hydrogen above the DDT limit [58]. Further disadvantages are strongly related to the deficiencies of the standard σ-criterion in sec. 2.3: Neither mixture inhomogeneity, nor venting is explicitly included. Despite some drawbacks, it would be unfair not to pronounce one striking advantage, namely the simplicity of these empirical criteria. In possible accident scenarios, they can be evaluated in a local as well as global sense [180].

In case of semi-confined stratified hydrogen-air layers,

$$h > 13\lambda \tag{2.29}$$

has lately been proposed to replace eq. 2.27 [86, 97, 152, 154]. h indicates the layer thickness just like in eq. 2.24. Compared to complete confinement, a more reactive mixture is needed to compensate for losses on the unconfined side of the mixture layer – which agrees with intuition.

It is generally assumed that detonation propagation is prohibited in orifice-laden tubes if

$$d < \lambda, \tag{2.30}$$

where d represents the inner orifice diameter. Only in smooth pipes, sustained detonation propagation is already possible if

$$D > \frac{\lambda}{\pi}, \tag{2.31}$$

where D is the pipe diameter. A so-called spin detonation emerges in this case [141]. These widely accepted limits apply for stable detonations, generating a regular cell pattern as introduced in sec. 2.5. Limits may deviate for alternative propagation forms. For instance, Boeck et al. [30] investigated single-headed detonation propagation in inhomogeneous hydrogen-air mixtures.

2.5 Detonation

In reality, the detonation front complex is characterized by a highly three-dimensional, intrinsically unstable micro-structure, cf. e.g. [159, 196]. As is apparent from the reduced two-dimensional schematic in fig. 2.10, a rhombus-like pattern evolves for a fixed observer. A Mach stem M develops due to the interaction of a longitudinally running main shock LS with a transversally running shock TS. According to shock superposition, fresh gas pressure and temperature behind the Mach stem is higher than behind the longitudinally running main shock. Due to strongly non-linear temperature dependency of the induction time, the heat release zone (flame front F) follows more closely behind the Mach stem than behind the main shock. The collision point of Mach stem, longitudinal shock and transverse shock is referred to as the triple point T. Eventually, the triple point trajectory (dashed line) forms the characteristic rhombus-like shape of the so-called detonation cells. Their dimension perpendicular to the main propagation direction is denoted as the detonation cell size λ.
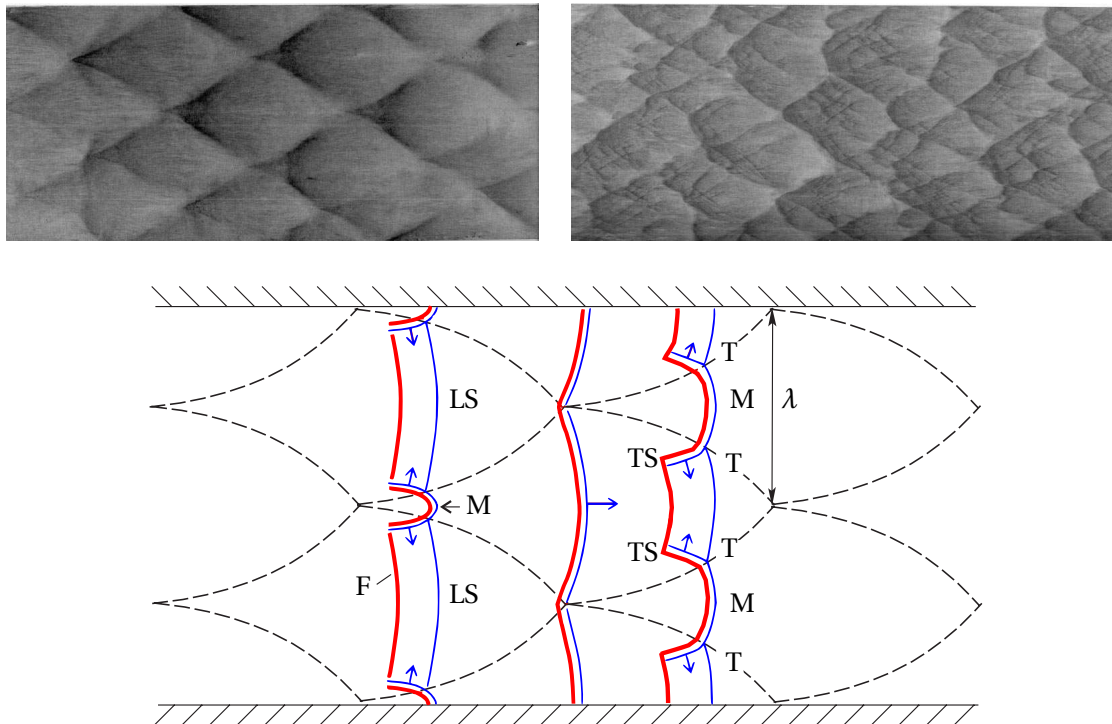
Figure 2.10: Multi-dimensional cellular detonation structure: Regular (top left) and irregular (top right) experimental soot print reproduced from [11]; Schematic (bottom) adapted from [74]; Flame colored red and shocks colored blue

The soot foil technique is used to visualize the cellular structure in experiments. Quantitative evaluation is difficult though, since fairly irregular patterns (top right in fig. 2.10) occur in highly reactive mixtures like hydrogen-air or hydrogen-oxygen. The activation energy is known to be one parameter affecting the regularity of cell patterns [90] but a thorough analytical understanding is still missing. Further non-ideal behavior relates to the fact that λ often grows during the course of detonation propagation, especially in sufficiently large volumes [96]. At ambient conditions, hydrogen-air cell sizes do not fall below 1 cm [40]. Deviating from the stoichiometric ratio, λ is rapidly increasing. Despite the experimental uncertainty, typically a factor of two, λ emerged to be the most prominent parameter to correlate the DDT propensity of reactive mixtures. Although λ is only depending on the mixture (species composition and thermodynamic state), it cannot directly be calculated from first principles.

It has been demonstrated in numerous studies (e.g. [81, 90, 133]) that regular and irregular detonation cells can be reproduced in numerical simulations. To do so, grid size must be clearly below the induction length [60] (introduced in sec. 2.5.2) which would be prohibitively expensive for industry-scale applications. The presented simulations do not intend to capture the intrinsically unstable micro-structure of the detonation front complex. The focus of this work is rather on global safety characteristics like propagation speed and associated pressure loads. Nevertheless, the introduction of λ is necessary to understand the empirical DDT criteria mentioned in sec. 2.4.

2.5.1 CJ theory

Without examining the internal structure of a detonation, the theory named after Chapman [51] and Jouguet [120] provides surprisingly accurate predictions of stable detonations (from a global point of view), particularly related to propagation velocity. The CJ state is characterized by the CJ condition

$$\mathrm{Ma}_{2,\mathrm{CJ}} = 1, \tag{2.32}$$

meaning that the burned-side flow velocity is identical to the local speed of sound. As a consequence of this sonic plane, the detonation front is not influenced by post-flame perturbations or the burned-side boundary condition. The CJ state formally relates to thermal choking mentioned in sec. 2.1. Occurring shortly after DDT for instance, overdriven detonation waves are generally possible. In such an unsteady scenario, the flow is subsonic behind the detonation front complex. Expansion waves will consequently reach the detonation front and relax it to the minimum steady wave speed, the CJ solution. Self-sustained propagation of an overdriven detonation wave is impossible.

The corresponding CJ detonation propagation velocity is given by

$$D_{\mathrm{CJ}} = \mathrm{a}_1\,\mathrm{Ma}_{1,\mathrm{CJ}} = \mathrm{a}_1 \left(\sqrt{1 + \frac{\kappa+1}{2}Q} + \sqrt{\frac{\kappa+1}{2}Q} \right), \tag{2.33}$$

utilizing the CJ inflow Mach number $\mathrm{Ma}_{1,\mathrm{CJ}}$ as stated in sec. 2.1 (positive sign of the second square root expression in eq. 2.11). Obviously, the detonation velocity is a function of the mixture composition (mainly via heat release Q) and its thermodynamic state (mainly via initial temperature T_1 and consequently a_1). It should be noted that D_{CJ} represents the

global propagation velocity of the overall detonation front complex. Due to the multi-dimensional inner structure as depicted in fig. 2.10, local velocities within the detonation front complex considerably deviate from this value.

Projection of a CJ and overdriven detonation state in the Rankine-Hugoniot diagram is included in fig. 2.11. CJ solutions are generally identified by the tangential contact point of Rayleigh line and Rankine-Hugoniot curve. The post-shock state (von Neumann spike) is further discussed in sec. 2.5.2. The pressure jump caused by the leading shock is approximately twice as large as for the overall detonation front complex.

2.5.2 ZND theory

Independently, Zeldovich [291], von Neumann [197] and Döring [68] extended the CJ theory in terms of the internal detonation structure. As can be seen in fig. 2.12, the theory distinguishes between an infinitely thin leading shock and a succeeding reaction zone of finite thickness. The shock wave compresses and preheats the unburned gas. Depending on the propagation velocity, the post-shock state (von Neumann spike) can be calculated from the normal shock relations in sec. 2.1. The reaction zone is again divided into two parts: First, the ignition delay or induction zone in which the radical pool builds up without significantly altering the flow. And second, the heat release zone, beginning when a critical radical concentration is reached. Overcoming heat and friction losses of the detonation complex, thermal expansion in the heat release zone maintains a constant shock strength. Pressure waves can catch up with the leading shock because the flow is subsonic until the end of the reaction zone. A self-sustained mechanism evolves in this way. Heat release in subsonic flow accelerates the flow (contrary to heat release in supersonic flow) up to the sonic point. In case of a CJ detonation, the sonic plane coincides with the end of the heat release zone. If the detonation front propagates more slowly, the so-called Taylor wave will weaken the strength of the detonation wave and eventually lead to a decoupling of leading shock and heat release zone. The Taylor wave is the expansion fan that follows
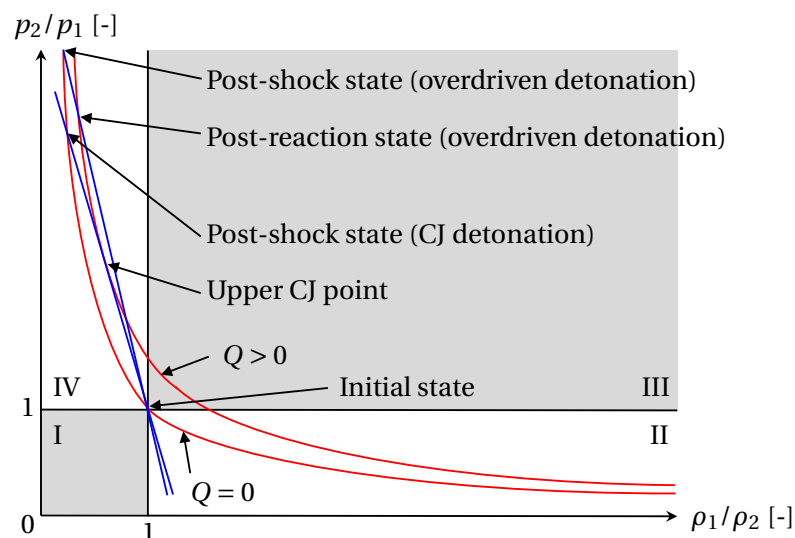
Figure 2.11: CJ and overdriven detonation in the Rankine-Hugoniot diagram: Hugoniot curves colored red, Rayleigh lines colored blue
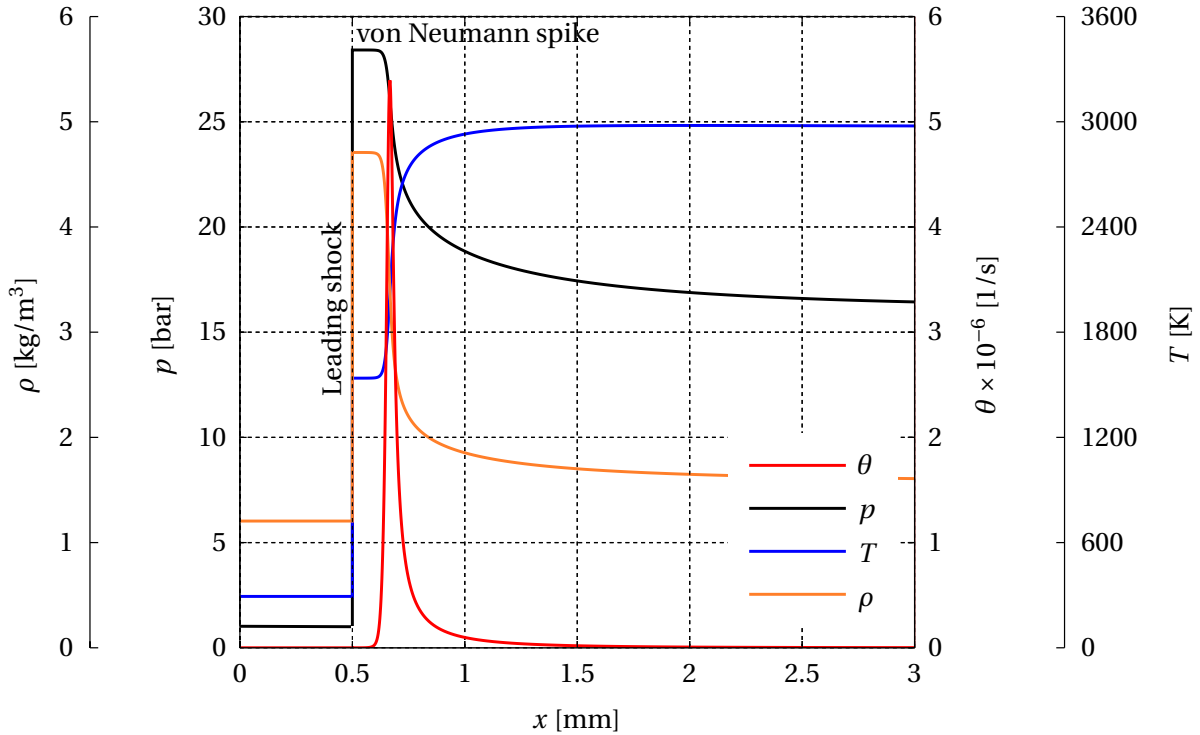
Figure 2.12: Internal structure of a CJ detonation according to one-dimensional ZND theory: Spatial profiles of thermicity θ (a measure of heat release), pressure p, temperature T and density ρ for a stoichiometric hydrogen-air mixture at ambient initial conditions; Adapted from [122]

the detonation front and gradually decreases the fluid velocity to satisfy the burned-side boundary condition. It is usually not seen as part of the detonation complex. For direct detonation initiation at the closed end of an initially quiescent tube, the expansion wave increases in width proportionally as the detonation wave propagates through the tube. Other than the CJ model, the ZND model is not restricted to ideal gases and constant specific heat. It can be extended to real gases including detailed chemical kinetics and realistic transport processes. Although the ZND theory aims at the inner detonation structure, it neglects inherent multi-dimensional effects (transverse waves, cellular structure), cf. fig. 2.10. The theory significantly improves our understanding of detonations though.

From an accident consequence point of view, the von Neumann spike is rather irrelevant due to its short existence. If the load duration is clearly shorter than the response time of the wall, structural response is dominated by the impulse (temporal integration of the overpressure profile) rather than peak pressure. Impulse contribution of short-lived pressure transients is understandably small. p_{vN} can be calculated from eq. 2.5, inserting $Q = 0$. Assuming thermal and chemical equilibrium, p_{CJ} results from a simple thermodynamic balance. Another characteristic pressure level arises at the end of the Taylor expansion wave which is following the detonation front complex [46, 249]:

$$p_{\mathrm{T}} = \left(\frac{a_{\mathrm{T}}}{a_{\mathrm{CJ}}}\right)^{\frac{2\kappa}{\kappa-1}} p_{\mathrm{CJ}} \approx 0.375\, p_{\mathrm{CJ}} \tag{2.34}$$

with the corresponding sound speed

$$a_\mathrm{T} = \frac{\kappa+1}{2} a_\mathrm{CJ} - \frac{\kappa-1}{2} D_\mathrm{CJ}. \tag{2.35}$$

Those characteristic pressure levels are particularly important for solver validation with respect to gas-dynamic phenomena and volumetric reaction modeling (sec. 3.5.6.4). Additionally, these values serve as a reference in multi-dimensional large-scale detonation simulations (sec. 4.2.1).

3 Large-scale explosion modeling

3.1 Simulation challenges

The demands to the numerical approach arise from chap. 2. It has to be ensured that the applied sub-models provide a sufficiently accurate description of the underlying phenomena. A not exhaustive list of particularly challenging aspects (from the author's point of view) is presented:

- *Disparity of Mach numbers:* Whilst the parabolic character of the governing equations is predominant shortly after weak ignition in a quiescent medium (Ma → 0, incompressible), the hyperbolic character of the governing equations prevails during the subsequent phase of flame acceleration and especially in the detonation regime (Ma ≲ 5, highly compressible).

- *Discontinuous changes of state:* Characteristic of explosive combustion, flow discontinuities (due to the flame and gas-dynamic effects like shocks) have to be advanced in space and time. The construction of adequate low-dissipation discretization schemes is an outstanding problem in computational fluid dynamics.

- *Disparity of length and time scales:* The spectrum of relevant length scales ranges from the size of the smallest Kolmogorov eddies to the dimension of the geometrical confinement. The situation is similar in time space, where the spectrum ranges from the smallest chemical time scales of hydrogen oxidation to the total time of the overall combustion process. In both cases, scales vary by several orders of magnitude.

- *Global and local unsteadiness:* Unsteady phenomena are omnipresent not only on microscopic level, i.e. turbulent fluctuations, but also on macroscopic level. Aside from time-invariant boundary conditions, all relevant flow quantities are subject to strong temporal variations in general.

- *Feedback mechanism:* The interaction between the expansion of combustion products, turbulence generation (e.g. in the wake of flow obstacles) and enhancement of the reaction rate by turbulence is essential in the process of flame acceleration. Errors in the description of this mechanism may accumulate over time.

- *Turbulence-chemistry interaction:* According to the Borghi diagram 2.3, turbulence heavily influences the structure of the flame and consequently the (integral) reaction rate. Since computational cost is usually too high to resolve this interaction, sub-grid modeling is required. The state of knowledge in this field is less advanced as for the prediction of the turbulence level or hydrogen oxidation alone.

Due to diverse underlying phenomena, the demands are diametrically opposed to some extent. The numerical approach, including simplifying assumptions, is described in the

next few sections: sec. 3.3 on the general solver framework including the governing equations, sec. 3.4 on a special technique for flame propagation, sec. 3.5 on the reaction rate model and sec. 3.6 on dynamic mesh adaptivity.

3.2 State-of-the-art

First of all, it has to be emphasized that the presented overview focuses on *large-scale* explosion modeling by means of CFD. According to their high relevance in explosion safety, hydrogen or methane fuel is investigated in most studies. In many regards, hydrogen can be considered a worst case due to its high reactivity. As mentioned earlier in sec. 1.1, the state-of-the-art particularly in nuclear safety is to employ optimized solvers based on the worst-case combustion regime that must be expected. Empirical transition criteria, most prominently eqs. 2.22 and 2.27, are required in this context. Several techniques for direct computation (not to be confounded with DNS) of regime transition evolved in recent years. Neither highly resolved simulations based on first principles (of generic cases), nor laboratory-scale explosion simulations are reviewed here. The number of such computational studies is compelling. At this point, the classical grouping (FA, DDT, detonation propagation) is abandoned because it would involve massive redundancy. Many of the mentioned techniques are applicable to multiple regimes. The structure of this section rather reflects the main issues of large-scale explosion modeling and thus the content of the next sections. Particularly interesting approaches shall be brought to the reader's attention. Since the adopted approach is subsequently presented in detail, it is largely omitted in this section. Completeness of the overview cannot be guaranteed. A separate overview of specific applications to nuclear reactors is provided in chap. 5. In the following, several categories of combustion models are briefly addressed. A proper classification is elaborated in sec. 3.5.2.

Governing equations

In accordance with the dominance of convective terms, the simulation of fast deflagrations and detonations is often based on Euler instead of Navier-Stokes equations. As an example, in the EUROPLEXUS code [263], the absence of a turbulence model is said to be compensated by numerical viscosity in some sense. Flame propagation is realized by the reactive discrete equation method of Le Métayer et al. [158], Tang et al. [247]. In doing so, the combustion wave is treated as an integral part of a reactive Riemann problem [19]. Computation of the turbulent burning velocity is based on the correlation of Bradley et al. [34]. Due to the absence of a turbulence model, the calculation of typical turbulence input parameters is quite unusual in this code framework. The r.m.s. velocity fluctuation and the integral turbulent length scale are reconstructed from the strain-rate tensor and the surface gradient of the gas velocity, respectively. Aiming at the conservative prediction of explosions on various scale, validation simulations comprise obstacle-laden channels, interconnected reactor-type compartments and vented enclosures [263]. Despite coarse cell sizes in the decimeter range, reasonable reproduction of several large-scale experiments is achieved.

A porosity-based modification of the general conservation equations can be applied to account for effects like drag, turbulence production and flame wrinkling which are caused by unresolved small-scale obstacles on sub-grid level. Known as distributed porosity concept or porosity distributed resistance, the methodology originally dates back to Patankar and Spalding [204] and has been transferred to explosion context e.g. by Arntzen [6]. The general idea is to assign volume as well as area porosities to computational cells, depending on the type of mathematical expression. For instance, an entirely blocked cell corresponds to zero porosity and an entirely unblocked cell corresponds to unity porosity. Using this concept, the commercial explosion solver FLACS was specifically designed for large-scale scenarios in oil and gas industry. Further applications concern the hydrogen risk analysis in nuclear safety [59, 110]. Required sub-grid models for drag, turbulence production and flame wrinkling involve a certain level of tuning. The combustion model is based on experimentally determined correlations for laminar and turbulent burning velocity. Artificial thickening of the flame is also employed. First attempts to incorporate DDT in such a framework appeared lately [190, 222]. The likelihood of DDT is evaluated in terms of a parameter proportional to the spatial pressure gradient across the flame brush. The parameter's critical value is empirical and therefore lacks of general validity.

Regarding the description of turbulence, LES formulations of the governing equations became increasingly popular in recent years. However, application of LES sub-grid models on industry scale (e.g. [126, 127]) must be seen with skepticism. Spatial resolution in the inertial range of the turbulence spectrum is mandatory for most LES closures. In combination with dissipative second-order discretization schemes, the numerical viscosity can easily outweigh the pseudo-viscosity of turbulent eddies [234]. The effect of the turbulence model is consequently limited in such cases. In future large-scale studies, corresponding proof in terms of the resolved turbulence spectrum would be highly valued. Considerably less expensive two-dimensional instead of three-dimensional LES or DNS of turbulent flows is questionable from a theoretical point of view, even if reasonable solutions can be achieved in practice. Three-dimensional URANS is seen as the appropriate compromise for industry-scale simulations.

Reaction rate modeling

In principle, it is possible to simulate FA, DDT and detonation propagation using one-step Arrhenius kinetics. Due to its simplicity and inexpensive computational evaluation compared to a detailed reaction scheme involving stiff source terms, the approach is employed by numerous researchers, e.g. [105, 106, 132, 165, 203]. Despite these advantages, several issues are inherent. As pointed out by Azatyan [12], one-step Arrhenius kinetics is unable to represent the characteristic thermal explosion behavior associated to chain branching. Spurious continuous heat release and thermal expansion permanently amplifies overrunning shock waves until the chemical equilibrium is reached. The tendency for self-supporting mechanisms like SWACER (sec. 2.4) is thus artificially increased using a one-step approach [166]. This fundamental problem can already be overcome by a two-step mechanism: isothermal ignition delay followed by exothermic heat release [79]. Second, a conflict arises for Arrhenius parameter calibration. Apart from a strong dependency on mesh density, it is unclear which goal variable must be used for tuning: laminar flame thickness, laminar burning velocity, ignition delay time, detonation speed, detonation cell width etc. Assuring excellent agreement for more than one variable is a chal-

lenging task. The choice depends on the considered regime and is especially challenging for regime-switching simulations. Another issue concerns the inadequate reproduction of turbulence-chemistry interaction on under-resolved meshes. Hence, one idea is to modify the one-step Arrhenius reaction rate with the partially stirred reactor concept, essentially a comparison of chemistry and turbulence scales. Kim and Hong [137] demonstrated such strategy for large-scale deflagration simulations. In case of pure detonation simulations, i.e. imposing strong ignition, the situation is less critical. If anything, kinetically controlled detonations can be described by one-step chemistry in under-resolved [104] as well as highly resolved [134] context. Yáñez et al. [283] compiled a code comparison by means of detonation propagation in the large-scale confined RUT facility, cf. chap. 4. Besides one-step chemistry, KIT's Heaviside detonation model and a so-called gradient approach [289, 290] (in which the detonation velocity is directly prescribed, similar to the turbulent flame speed closure) are checked against each other. On comparably coarse meshes, all approaches produce satisfying results in terms of propagation speed and pressure loads. Applied e.g. in [177], KIT's DET3D is another example of a detonation-optimized solver based on one-step Arrhenius kinetics.

Regarding the transition between different combustion regimes, one may think of a blending of complementary reaction rate closures. Especially the transition between fast chemistry and high turbulence intensity is relevant to a typical flame acceleration process. These extreme conditions correspond to the turbulence-limited eddy-break-up regime and the kinetically limited well-stirred reactor regime, respectively [40]. On the basis of a comparison of characteristic time scales, the standard eddy-break-up model [244] can be extended accordingly. In practice, promising agreement was found for medium and large-scale test cases [38, 147]. Using such a heuristic model, specific fine tuning of the formulation seems to be inevitable though.

Under-resolved meshes inevitably lead to inaccurate reproduction of turbulence-chemistry interaction. Therefore, a popular method is to artificially increase the flame thickness by diffusive flux scaling of the reactive scalar equation. Its source term has to be decreased proportionately. An efficiency function is additionally necessary to correct for the falsified interaction with resolved eddies. LES computations of FA and DDT with artificial flame thickening are presented in [78, 287]. Even on extremely large astrophysical scales, namely for the propagation of a thermonuclear deflagration sheet, the method is adopted: Ma et al. [172] use a kind of thickened flame model in which the flame width and velocity have to be prescribed. However, the authors state that they prefer a level-set method (cf. discussion below) for future studies. Despite the efficiency function, the artificial zone of intermediate cells heavily influences the probability of DDT. For instance the temperature field is smeared in a similar manner as for one-step Arrhenius kinetics – with corresponding consequences as discussed above. Another issue is the fact that simple division of the source term by the thickening factor does only compensate artificial flame thickening if the source term is linearly depending on the distribution of influencing parameters within the flame brush. This is generally not the case for Arrhenius-type as well as other non-linear closure. In a new development of Yu and Navarro-Martinez [287], an alternative formulation is proposed. Instead of applying thickening only to the reactive scalar equation, it is applied to all governing equations. According to the authors, the latter approach improves flame-flow interaction and an efficiency function might not be needed.

Over the last few years, some research effort has been devoted to the sub-grid modeling of unresolved cellular flame structures caused by intrinsic and driven flame instabilities, cf. sec. 2.3.2. Predominantly hydrogen mixtures are examined, but less frequently also hydrocarbon mixtures. Whereas turbulence-induced flame wrinkling is included in practically all explosion solvers, Keenan et al. [126, 127] demonstrate the implementation of the Rayleigh-Taylor instability into their multi-phenomena deflagration model. This mechanism and also the hydrodynamic instability are investigated by Bauwens et al. [18]. The mathematical formulation of corresponding models is often based on fractal theory [129, 191]. Yáñez et al. [284] place their focus on the acoustic-parametric instability for containment-typical conditions in nuclear safety. Most recently, Katzy et al. [123] presented their modeling efforts on the thermal-diffusive instability.

Flame propagation

As demonstrated in sec. 3.4, flame tracking techniques are particularly attractive for globally unsteady combustion. The innovative tracking scheme of Moser [193], Smiljanovski [241], Smiljanovski et al. [242] represents a deflagration as a reactive discontinuity embedded in a surrounding compressible flow. Flame propagation is described by the widespread *G*-equation, i.e. a dynamically evolving scalar function [206]. In this context, the flame is assumed to be the zero level-set of the *G* field. The costly iterative solution of Rankine-Hugoniot jump conditions is required to couple burned and unburned states within front cells that are intersected by the front. The reaction rate was originally derived from algebraic burning laws. Later, the scheme has been generalized [231] by replacing the net consumption rate calculation from explicit burning laws. Depending on the regime of turbulence-chemistry interaction, different internal flame structure modules incorporate the effect of dynamical events within the turbulent flame brush. Another key modification was the extension to non-homogeneous Rankine-Hugoniot jump conditions. According to its architecture, the solver is limited to regular Cartesian grids. Early validation work involves two-dimensional deflagration simulations in the RUT facility, yet without considering DDT. In some cases, flame wrinkling (approximately the ratio of turbulent to laminar burning velocity) is artificially prescribed as function of time to reach DDT-critical conditions. Such an approach is surely only eligible for demonstration purposes. By means of a generic case, DDT has successfully been reproduced in a qualitative manner. A closely related scheme is applied to astrophysical problems by Reinecke et al. [217]. Again, the level-set technique and the *G*-equation are employed to propagate a thermonuclear deflagration front in stars undergoing a supernova explosion.

Another interesting approach is the CREBCOM model of Efimenko and Dorofeev [75] to ensure approximately grid-independent flame propagation. Originally developed by Bak et al. [13], the underlying forest-fire algorithm makes sure that the flame propagates from cell to cell like fire propagates from tree to tree in a forest. Due to the algorithm's nature, it is restricted to cubic structured grids. Furthermore, calibration runs are necessary for each solver-specific implementation. A burning velocity correlation is additionally needed to close the reactive scalar equation. Satisfying simulations were achieved for slow and fast deflagrations in the RUT facility. Performance of the KYLCOM model (a variant of the CREBCOM model) and a modified gradient closure (adding negative diffusion, i.e. artificial compression, to the reactive scalar equation to avoid unnatural broadening of the flame brush) is compared in [282] with similar results. Room for improvement has

been identified related to the modeling of turbulent quenching and intrinsic flame instabilities. Both models are available in KIT's COM3D code which is primarily developed for industry-scale explosion analysis as e.g. in [61].

Additional remarks

A number of overviews and code comparisons on large-scale explosion modeling is available in literature: Sathiah et al. [224, 225] on the role of CFD combustion modeling in hydrogen safety management, Makarov et al. [176] about CFD models to predict lean and non-uniform hydrogen mixture explosions, Baraldi et al. [15] on CFD model capabilities to simulate hydrogen deflagrations in a tunnel, García et al. [91] about the capabilities of CFD models to reproduce a large-scale hydrogen deflagration in open atmosphere, and finally the International Standard Problem (ISP) 49 on hydrogen combustion [202]. Essentially all of the discussed approaches can be attributed to one of the modeling families mentioned above.

In the end, the usage of under-resolved meshes leads to the violation of well-established CFD best practice guidelines (e.g. by Menter [182]) in some aspects. For example, accurate wall treatment is out of reach (even when using wall functions), but not necessarily with significant consequences on the overall simulation result. Due to a generally higher level of modeling on large scales, expectations on solution accuracy must be below laboratory-scale simulations.

Well-defined explosion experiments in the large-scale RUT facility emerged as adequate validation cases in several earlier studies. Successful separate simulations of deflagrations (e.g. [41, 42, 193]) and detonations (e.g. [104, 283, 290]) have already been achieved. To the best of the author's knowledge, quantitative reproduction of DDT experiments (in their entirety) in the RUT facility has not been published yet.

3.3 Solver framework

The methodology described in the following is implemented using the open-source CFD package Open Field Operation And Manipulation (OpenFOAM) [273] as a basis. Two of the code's main advantages are the support of topologically complex unstructured meshes and the flexible object-oriented software architecture (written in C++).

Throughout this thesis, governing equations are stated in their strong form with respect to a fixed Cartesian coordinate system (Eulerian frame of reference). If not mentioned otherwise, Einstein's summation convention [77] is applied. A compelling advantage of this notation is its compactness. However, it should be pointed out that an integral version of the governing equations (weak form) is eventually discretized and solved in the framework of the finite volume method, cf. sec. 3.3.3.

3.3.1 Governing equations

3.3.1.1 Conservation equations

The following partial differential equations describe the well-known principles of mass, momentum, energy and species conservation. Due to the mixed parabolic-hyperbolic nature of explosion problems (assuming weak ignition), the numerical methodology is built on the unsteady and compressible formulation of the corresponding transport equations, each expressed in terms of the volume-specific form of the conserved quantity: density ρ representing mass, ρu_i representing momentum etc. The presented set of equations includes all relevant subsonic, transsonic and supersonic flow phenomena. Despite the difficulties in solving these equations numerically (discussed later), even turbulence as well as gas-dynamic effects like shocks or expansion fans are accurately described. Compared to the most general version of the conservation equations, some simplifications (especially concerning the energy equation) are introduced. A comprehensive derivation of the conservation equations with a focus on reactive flows was published by Thije-Boonkkamp [250].

The global conservation of mass is formulated as

$$\frac{\partial \rho}{\partial t} + \frac{\partial}{\partial x_j}\left(\rho u_j\right) = 0, \tag{3.1}$$

also known as the continuity equation. It encompasses the contribution of all chemical species and is characterized by the absence of a diffusive term.

Conservation of momentum in each Cartesian direction i is guaranteed by solving

$$\frac{\partial}{\partial t}\left(\rho u_i\right) + \frac{\partial}{\partial x_j}\left(\rho u_i u_j\right) = \frac{\partial \tau_{ij}}{\partial x_j} - \frac{\partial p}{\partial x_i} + \rho g_i, \tag{3.2}$$

where g_i denotes the body force, in our case due to gravitational acceleration. On the basis of Stokes' hypothesis [125], which is basically a generalization of Newton's law for multi-dimensional flows, the viscous stress tensor τ_{ij} can be calculated from

$$\tau_{ij} = \mu\left(\frac{\partial u_i}{\partial x_j} + \frac{\partial u_j}{\partial x_i} - \frac{2}{3}\delta_{ij}\frac{\partial u_m}{\partial x_m}\right). \tag{3.3}$$

δ_{ij} denotes the Kronecker delta. The relation is composed of a non-isotropic part and an isotropic part vanishing for incompressible flows. A fluid element may obviously experience a strain rate due to velocity gradients in different directions. The dynamic viscosity μ plays the role of a proportionality constant that links the velocity gradients to the resulting shear stress. It is obtained from Sutherland's formula [277]

$$\mu = A_S \frac{T^{3/2}}{T + T_S} \tag{3.4}$$

with the constants A_S and T_S, and other molecular transport properties like heat conductivity λ and species diffusivity D are derived therefrom.

The momentum equation stands out by the non-linear convective term, allowing the build-up of discontinuous solutions. The pressure term on the right-hand side of eq. 3.2

can be interpreted as a source or driving force on the velocity field. Pressure gradients can apparently accelerate or decelerate the flow. In combination, eqs. 3.1 and 3.2 are commonly referred to as the Navier-Stokes equations.

The principle of energy conservation can be written in various forms [207]. Depending on the problem, an appropriate formulation in terms of temperature, enthalpy or internal energy should to be chosen. Chemical, sensible and kinetic energy contributions can additionally be distinguished.

Assuming that the mass fraction Y_k of each of N_{sp} gas species is known, the mixture's specific total internal energy is given by

$$e_t = e + \frac{u_i u_i}{2} = \sum_{k=1}^{N_{sp}} Y_k \left(e_k^f + \int_{T_{ref}}^{T} c_{v,k}(T) \, dT \right) + \frac{u_i u_i}{2}. \tag{3.5}$$

The mass fraction weighted sum e is consequently called the specific static internal energy and e_k^f indicates the specific internal energy of species k at reference temperature T_{ref}. Following the CHEMKIN [124] thermodynamic database, implementation of temperature-dependent specific isochoric heat capacities

$$c_v = \frac{\partial e}{\partial T} \tag{3.6}$$

is realized via NASA polynomials based on NIST-JANAF thermochemical tables. Further dependencies like pressure are not taken into account, meaning that the gas is expected to behave thermally perfect. Accordingly, when a transport equation is solved for e_t, determination of the mixture's temperature T via eq. 3.5 must be done iteratively. A bounded Newton algorithm is applied for this purpose. As can be seen, all mentioned energy contributions (chemical or also termed formation, sensible and kinetic) are contained within the total internal energy.

Expressed in terms of e_t, energy conservation writes

$$\frac{\partial}{\partial t} \left(\rho e_t \right) + \frac{\partial}{\partial x_j} \left(\left(\rho e_t + p \right) u_j \right) = -\frac{\partial q_j}{\partial x_j} + \frac{\partial}{\partial x_j} (\tau_{ij} u_i). \tag{3.7}$$

In doing so, the diffusive flux q_j includes the heat flux via heat conduction whereas the enthalpy flux via species diffusion is here neglected. Utilizing Fourier's law as well as the definitions of thermal diffusivity

$$a = \frac{\lambda}{\rho c_p} \tag{3.8}$$

and specific isobaric heat capacity

$$c_p = \frac{\partial h}{\partial T}, \tag{3.9}$$

one obtains

$$q_j = -\lambda \frac{\partial T}{\partial x_j} = -\rho a \frac{\partial h}{\partial x_j}. \tag{3.10}$$

Reduction to already introduced quantities is achieved by means of the thermodynamic identity

$$h = e + \frac{p}{\rho}. \tag{3.11}$$

It should be noted that further simplifications with respect to energy conservation are incorporated: Body forces, radiation, volumetric energy sources and sinks, potential energy, Dufour effect, Soret effect etc. are assumed to be of minor importance in the context of this work and thus neglected.

Only when expressed in terms of the total internal energy, neither a temporal pressure derivative (unlike enthalpy formulations), nor a chemical source term (unlike sensible formulations) appears in the energy equation, cf. Poinsot and Veynante [207]. Chemical reaction solely shifts the portions of chemically bounded energy and sensible energy while the static internal energy remains constant. Changes in the sensible part manifest itself in temperature variation. Also, the formulation is eligible for high Mach number flows. Especially at supersonic speed, specific kinetic energy

$$\frac{u_i u_i}{2} \tag{3.12}$$

makes a substantial contribution to e_t. The exchange between kinetic energy and static internal energy is consequently included.

Pressure p appears in both momentum and energy equation but is not available from a separate conservation principle. The system of equations is rather closed by the ideal gas law

$$p = \rho R T \tag{3.13}$$

as an equation of state. R represents the specific gas constant of the mixture. Under extreme high pressure conditions, which infrequently occur in explosions, the validity of eq. 3.13 may be questioned. If the mean free path of gas molecules is in the range where intermolecular forces play a non-negligible role, real gas effects lead to deviations from eq. 3.13.

To obtain the unsteady local composition of a multi-component mixture, $N_{sp}-1$ transport equations can be solved to get the mass fractions Y_k of N_{sp} species. $Y_{N_{sp}}$ finally results from the fact that all mass fractions must sum up to unity. However, a computationally more efficient approach is employed to speed up the simulations. The reactants mixture is assumed to consist solely of hydrogen and air (relative volumetric concentrations: 21 % oxygen and 79 % nitrogen). Minor air species like Argon are not considered as part of the reactants mixtures.

In case of inhomogeneous mixtures, an additional transport equation

$$\frac{\partial}{\partial t}\left(\rho f_H\right) + \frac{\partial}{\partial x_j}\left(\rho f_H u_j\right) - \frac{\partial}{\partial x_j}\left(\rho D \frac{\partial f_H}{\partial x_j}\right) = 0 \tag{3.14}$$

with no source term is solved for the hydrogen mixture fraction f_H [210]. It is defined by

$$f_H = \sum_{k=1}^{N_{sp}} Y_{H,k} Y_k, \tag{3.15}$$

where $Y_{H,k}$ denotes the H-atoms mass fraction with respect to a molecule of species k and Y_k is the mass fraction of species k with respect to the overall mixture. Hence, $f_H = Y_{H_2}$ only holds in the unburned part of the domain. f_H can be interpreted as the mass fraction of hydrogen that would be present if no chemical reaction occurred. In partly burned cells, f_H is important for the correct evaluation of mixture-dependent quantities

like the laminar burning velocity, the Lewis number etc. Modeling of the additional effect of combustion on species composition is explained in sec. 3.5.

Although the diffusive flux of species in eq. 3.14 follows Fick's law [125], individual species diffusivities D are not considered by this approach. Accurate treatment of multi-component diffusion is outside the scope of this work. It would involve a costly iterative procedure since the sought-for diffusivities are only implicitly given by the set of Maxwell-Stefan equations [25]. A reasonable alternative would be to use a mixture-averaged approach. Anyway, such additional effort is hardly justifiable as the behavior in turbulent flows is quickly dominated by turbulent pseudo-diffusivities, see eqs. 3.36 to 3.38.

Following the nuclear safety analysis chain mentioned in sec. 1.1, realistic multi-dimensional mixture fields (e.g. gained from CFD dispersion simulations) can be imported as initial conditions for subsequent combustion simulations.

3.3.1.2 Ensemble-averaged equations

As already demonstrated in the introduction (sec. 1.2), the problem is characterized by large domains and high Reynolds numbers at the same time which renders DNS and LES methods unfeasible. Appropriate spatial and temporal resolution cannot nearly be assured given the currently available computing power. In terms of the three established categories, only the URANS framework remains to describe at least the statistical effects of turbulence.

The fundamental idea is to decompose each turbulence-affected flow quantity ϕ into a mean part $\overline{\phi}$ and a fluctuating part ϕ':

$$\phi = \overline{\phi} + \phi'. \tag{3.16}$$

In the classical RANS context, the operator $\overline{()}$ is understood as the arithmetic average with respect to a prescribed time interval Δt, the so-called Reynolds-average [218]. For locally as well as globally unsteady flows, not only unsteady turbulent fluctuations but also the unsteadiness of the mean flow has to be taken into account. In this URANS context, the operator's interpretation as a temporal average can be replaced by an ensemble-average [212]

$$\overline{\phi} = \frac{1}{N} \sum_{n=1}^{N} \phi_n, \tag{3.17}$$

which constitutes an average with respect to N instances ϕ_n of the considered quantity ϕ. It has been argued that the separate description of unsteady phenomena is readily possible as long as the averaging time step Δt is larger than the characteristic time scale of turbulent fluctuations. Pursuant to Noll et al. [199], reasonable results can even be achieved for high-frequency variations of the mean flow, featuring time scales clearly within the turbulent spectrum. As a prerequisite, variations of the mean flow must be deterministic – unlike turbulent fluctuations which occur randomly [112]. It gives the URANS framework a theoretical justification for the highly unsteady problem considered.

Definition of the averaging operator implies

$$\overline{\phi'} = 0, \tag{3.18}$$

contrary to the product of turbulent fluctuations. In general,

$$\overline{\phi'\psi'} \neq 0 \tag{3.19}$$

holds.

For reasons shown later, a density-weighted average according to Favre [84] is additionally introduced:

$$\widetilde{\phi} = \frac{\overline{\rho\phi}}{\overline{\rho}}. \tag{3.20}$$

Along the lines of eq. 3.16, the corresponding decomposition reads

$$\phi = \widetilde{\phi} + \phi''. \tag{3.21}$$

It is important to note that

$$\widetilde{\phi''} = 0 \tag{3.22}$$

following the definition of ensemble-averaging but generally

$$\overline{\phi''} \neq 0. \tag{3.23}$$

Combining above definitions, it is straightforward to derive

$$\overline{\rho}\widetilde{\phi} = \overline{\rho}\,\overline{\phi} + \overline{\rho'\phi'}, \tag{3.24}$$

i.e. a direct analytical conversion of Reynolds- and Favre-averaged quantities is not possible.

Applying the ensemble-averaging procedure to the conservation equations introduced in sec. 3.3.1.1, and eliminating unimportant terms, yields

$$\frac{\partial}{\partial t}\overline{\rho} + \frac{\partial}{\partial x_j}\left(\overline{\rho}\widetilde{u}_j\right) = 0, \tag{3.25}$$

$$\frac{\partial}{\partial t}\left(\overline{\rho}\widetilde{u}_i\right) + \frac{\partial}{\partial x_j}\left(\overline{\rho}\widetilde{u}_i\widetilde{u}_j\right) + \frac{\partial}{\partial x_j}\left(\overline{\rho\widetilde{u_i''u_j''}}\right) = \frac{\partial\overline{\tau}_{ij}}{\partial x_j} - \frac{\partial\overline{p}}{\partial x_i} + \overline{\rho}g_i, \tag{3.26}$$

$$\frac{\partial}{\partial t}\left(\overline{\rho}\widetilde{e}_t\right) + \frac{\partial}{\partial x_j}\left((\overline{\rho}\widetilde{e}_t + \overline{p})\widetilde{u}_j\right) + \frac{\partial}{\partial x_j}\left(\overline{\rho\widetilde{h''u_j''}}\right) = \frac{\partial}{\partial x_j}\left(\overline{\rho}a\frac{\partial\widetilde{h}}{\partial x_j} + \overline{\tau}_{ij}\widetilde{u}_i\right), \tag{3.27}$$

$$\frac{\partial}{\partial t}\left(\overline{\rho}\widetilde{f}_H\right) + \frac{\partial}{\partial x_j}\left(\overline{\rho}\widetilde{f}_H\widetilde{u}_j\right) + \frac{\partial}{\partial x_j}\left(\overline{\rho\widetilde{f_H''u_j''}}\right) = \frac{\partial}{\partial x_j}\left(\overline{\rho}D\frac{\partial\widetilde{f}_H}{\partial x_j}\right). \tag{3.28}$$

From eq. 3.25, the motivation of Favre-averaging in a compressible flow framework becomes clear: Unlike for exclusive Reynolds-averaging, no unclosed term appears for the continuity equation. Likewise, less unclosed terms appear for the remaining equations 3.26 to 3.28. The less naturally imperfect closure approaches are required, the less uncertainty is introduced.

The concept behind the adopted turbulence modeling approach is founded on the eddy viscosity hypothesis of Boussinesq [207]. Analogous to the calculation of viscous stresses τ_{ij} (eq. 3.3), Reynolds stresses $\tau_{ij,T}$ (eq. 3.29) are determined from the velocity gradients of the mean flow. In doing so, the effect of unresolved turbulent fluctuations on the resolved mean flow is incorporated via an artificial eddy viscosity μ_T. The closure problem

is therefore shifted to the calculation of μ_T. Complying with the same principle, all other unclosed terms are modeled by a standard gradient ansatz:

$$\tau_{ij,T} = -\overline{\rho}\widetilde{u_i''u_j''} = \mu_T\left(\frac{\partial\widetilde{u}_i}{\partial x_j} + \frac{\partial\widetilde{u}_j}{\partial x_i} - \frac{2}{3}\delta_{ij}\frac{\partial\widetilde{u}_m}{\partial x_m}\right) - \frac{2}{3}\delta_{ij}\overline{\rho}k, \tag{3.29}$$

$$-\overline{\rho}\widetilde{h''u_j''} = \overline{\rho}a_T\frac{\partial\widetilde{h}}{\partial x_j}, \tag{3.30}$$

$$-\overline{\rho}\widetilde{f_H''u_j''} = \overline{\rho}D_T\frac{\partial\widetilde{f}_H}{\partial x_j}. \tag{3.31}$$

The term containing the turbulent kinetic energy k (eq. 3.41) is usually neglected. These mathematical closure approaches are yet independent of the actual turbulence model providing the isotropic eddy viscosity. Although the Reynolds stresses derive from turbulence-related convective fluxes, they are modeled like diffusive fluxes – paradox to some extent but cleary superior first moment closure approaches have not emerged so far. More sophisticated Reynolds stress models (second moment closure) [212] are not reliant on that concept and are able to account for the anisotropic character of turbulent fluctuations.

Inserting the closure models and reorganizing some terms leads to the implemented set of equations

$$\frac{\partial\overline{\rho}}{\partial t} + \frac{\partial}{\partial x_j}\left(\overline{\rho}\widetilde{u}_j\right) = 0, \tag{3.32}$$

$$\frac{\partial}{\partial t}\left(\overline{\rho}\widetilde{u}_i\right) + \frac{\partial}{\partial x_j}\left(\overline{\rho}\widetilde{u}_i\widetilde{u}_j + \frac{2}{3}\delta_{ij}\overline{\rho}k\right) =$$
$$\frac{\partial}{\partial x_j}\left(\mu_{\text{eff}}\left(\frac{\partial\widetilde{u}_i}{\partial x_j} + \frac{\partial\widetilde{u}_j}{\partial x_i} - \frac{2}{3}\delta_{ij}\frac{\partial\widetilde{u}_m}{\partial x_m}\right)\right) - \frac{\partial\overline{p}}{\partial x_i} + \overline{\rho}g_i, \tag{3.33}$$

$$\frac{\partial}{\partial t}\left(\overline{\rho}\widetilde{e}_t\right) + \frac{\partial}{\partial x_j}\left(\left(\overline{\rho}\widetilde{e}_t + \overline{p}\right)\widetilde{u}_j\right) =$$
$$\frac{\partial}{\partial x_j}\left(\overline{\rho}a_{\text{eff}}\frac{\partial\left(\widetilde{e} + \overline{p}/\overline{\rho}\right)}{\partial x_j} + \mu\left(\frac{\partial\widetilde{u}_i}{\partial x_j} + \frac{\partial\widetilde{u}_j}{\partial x_i} - \frac{2}{3}\delta_{ij}\frac{\partial\widetilde{u}_m}{\partial x_m}\right)\widetilde{u}_i\right), \tag{3.34}$$

$$\frac{\partial}{\partial t}\left(\overline{\rho}\widetilde{f}_H\right) + \frac{\partial}{\partial x_j}\left(\overline{\rho}\widetilde{f}_H\widetilde{u}_j\right) - \frac{\partial}{\partial x_j}\left(\overline{\rho}D_{\text{eff}}\frac{\partial\widetilde{f}_H}{\partial x_j}\right) = 0. \tag{3.35}$$

Compact notation is realized by merging the corresponding laminar part and turbulent part to effective transport properties

$$\mu_{\text{eff}} = \mu + \mu_T, \tag{3.36}$$

$$a_{\text{eff}} = a + a_T = a + \frac{1}{\text{Pr}_T}\frac{\mu_T}{\overline{\rho}}, \tag{3.37}$$

$$D_{\text{eff}} = D + D_T = D + \frac{1}{\text{Sc}_T}\frac{\mu_T}{\overline{\rho}}. \tag{3.38}$$

In highly turbulent flows, the laminar part plays only a minor role. The turbulent part is equal to the eddy viscosity scaled by the turbulent equivalent of the relevant dimensionless number. Both the turbulent Prandtl number Pr_T and the turbulent Schmidt number Sc_T are set to 1.0. Especially regarding the turbulent Schmidt number, smaller values

around 0.7 are commonly recommended [92]. But this does not necessarily have to be a good choice for highly compressible reactive flows with gas-dynamic effects. Due to their lack of a direct physical interpretation, Pr_T and Sc_T are often looked upon tuning parameters to achieve optimal agreement with experiments. This questionable practice was not employed here. The scaling also means that turbulent scalar mixing on sub-grid level is only partly computed within the URANS framework. The relative distribution of turbulent mixing is indeed determined by the turbulence model whereas absolute mixing intensity is rather imposed.

Unless indispensable for understanding, averaging operators are dropped again outside of this section for improved readability.

3.3.2   SST turbulence model

Due to its importance in capturing the feedback mechanism behind flame acceleration (sec. 2.3), the adopted turbulence model is reviewed in detail. Turbulence prediction is essential not only for the closure of the Favre-averaged governing equations, but also for the calculation of averaged reaction rates. Turbulence-characterizing quantities k, ω and ε influence the combustion model in various forms, cf. sec. 3.5. Even the best turbulence-chemistry interaction model is rendered useless if turbulence is predicted at low quality.

In this work, Menter's model known as the Shear Stress Transport (SST) model is applied. Despite this name, generally anisotropic components of the Reynolds stress tensor are not directly transported. Using the Boussinesq approximation as introduced in eq. 3.29, isotropic turbulent fluctuations are implicitly assumed. Rather than Menter's frequently cited pioneering paper [184], implementation in OpenFOAM is based on a newer publication of Menter and Esch [183].

The idea underlying the SST model is to combine the advantages of the $k-\varepsilon$ and $k-\omega$ model. A blending function F_1 activates the Wilcox $k-\omega$ formulation [278] in near-wall regions and the $k-\varepsilon$ model [119] in the remaining part of the domain. Using the robust behavior of the $k-\varepsilon$ model in the bulk flow, the poor free-stream performance of the Wilcox $k-\omega$ formulation is avoided while retaining its attractive near-wall performance. As an industrial-perspective review (after more than ten years of experience with the model) shows, the SST model reliably predicts the statistical effects of turbulence for many complex flow situations [185, 186].

In order to calculate the eddy viscosity from

$$\mu_T = \frac{a_1 \overline{\rho} k}{\max\left(a_1 \omega; F_2 S\right)}, \tag{3.39}$$

and consequently the turbulent thermal and mass diffusivity (a_T from eq. 3.37 and D_T from eq. 3.38), two evolution equations are solved. In this context,

$$S = \sqrt{2} \left| \frac{1}{2}\left(\frac{\partial \widetilde{u}_i}{\partial x_j} + \frac{\partial \widetilde{u}_j}{\partial x_i}\right) \right| \tag{3.40}$$

denotes an invariant measure of the strain rate. The first transport equation for the specific turbulent kinetic energy

$$k = \frac{\widetilde{u_i'' u_i''}}{2} \tag{3.41}$$

reads

$$\frac{\partial}{\partial t}\left(\overline{\rho}k\right) + \frac{\partial}{\partial x_j}\left(\overline{\rho}k\widetilde{u}_j\right) - \frac{\partial}{\partial x_j}\left(\Gamma_{\text{k,eff}}\frac{\partial k}{\partial x_j}\right) = P_k^* - \overline{\rho}\underbrace{\beta^*\omega k}_{\varepsilon}. \tag{3.42}$$

Equation 3.42 also reveals the imposed relationship between the dissipation rate of turbulent kinetic energy ε, and the eddy frequency ω which is transported by

$$\frac{\partial}{\partial t}\left(\overline{\rho}\omega\right) + \frac{\partial}{\partial x_j}\left(\overline{\rho}\omega\widetilde{u}_j\right) - \frac{\partial}{\partial x_j}\left(\Gamma_{\omega,\text{eff}}\frac{\partial \omega}{\partial x_j}\right) =$$
$$\frac{\overline{\rho}\gamma(F_1)}{\mu_T}P_k - \overline{\rho}\beta(F_1)\omega^2 + 2(1-F_1)\overline{\rho}\alpha_{\omega2}\frac{1}{\omega}\frac{\partial k}{\partial x_j}\frac{\partial \omega}{\partial x_j}. \tag{3.43}$$

The production of turbulent kinetic energy

$$P_k^* = \min\left(P_k; c_1\overline{\rho}\varepsilon\right) = \min\left(\tau_{ij,T}\frac{\partial \widetilde{u}_i}{\partial x_j}; c_1\overline{\rho}\varepsilon\right) \tag{3.44}$$

is limited by the minimum formulation to anticipate the spurious build-up of turbulence in stagnation regions – a deficiency that is inherent to many two-equation models.

Corresponding effective diffusivities are calculated from

$$\Gamma_{\text{k,eff}} = \mu + \mu_T \alpha_k(F_1), \tag{3.45}$$
$$\Gamma_{\omega,\text{eff}} = \mu + \mu_T \alpha_\omega(F_1), \tag{3.46}$$

in which

$$\psi(F_1) = \psi_1 F_1 + \psi_2(1 - F_1) \tag{3.47}$$

for all $\psi \in \{\alpha_k, \alpha_\omega, \beta, \gamma\}$ determines the F_1-blended coefficients of the $k-\omega$ and $k-\varepsilon$ model, respectively. F_1 approaches one near walls and converges to zero for the rest of the flow.

The blending functions F_1 and F_2 (needed for eq. 3.39), depending on the wall normal y, are finally given by

$$F_1(y) = \tanh\left\{\left[\min\left(\min\left(\max\left(\frac{\sqrt{k}}{\beta^*\omega y}; \frac{500\mu}{\overline{\rho}\omega y^2}\right); \frac{4\alpha_{\omega2}k}{\text{CD}_{k\omega}y^2}\right); 10\right)\right]^4\right\} \tag{3.48}$$

with

$$\text{CD}_{k\omega} = \max\left(2\alpha_{\omega2}\frac{1}{\omega}\frac{\partial k}{\partial x_j}\frac{\partial \omega}{\partial x_j}; 10^{-10}\right) \tag{3.49}$$

and

$$F_2(y) = \tanh\left\{\left[\min\left(\max\left(2\frac{\sqrt{k}}{\beta^*\omega y}; \frac{500\mu}{\overline{\rho}\omega y^2}\right); 100\right)\right]^2\right\}. \tag{3.50}$$

Coefficients of the SST model are summarized in tab. 3.1. It should be mentioned that the constants of turbulence models are usually tuned with respect to inert canonical flows. Applying such models to highly unsteady reactive flows introduces a level of uncertainty which can hardly be estimated. For wall-bounded flows, higher-order turbulence models (e.g. second moment closure) are believed to produce only marginally better results than well-calibrated eddy viscosity models [183]. Undoubtedly, computational costs differ drastically between first and second moment closure approaches.

The no-slip condition generally holds at wall boundaries. Whereas a homogeneous Neumann condition is imposed on the k field, ω is calculated from a quadratic superposition of a viscous and a logarithmic part. If the normalized wall distance $y+$ falls below the threshold value of 11.53 (i.e. nearly linear normalized velocity profile $u+$), the eddy viscosity μ_T and the turbulent production term P_k are set to zero. A standard logarithmic wall function for $u+$ is invoked above the threshold value. For further details on wall treatment, the interested reader is referred to [183] and invited to have a look at the source code.

3.3.3   Solver architecture and discretization

The flow conservation equations (sec. 3.3.1) in conjunction with those equations of the turbulence model (sec. 3.3.2) and the combustion model (sec. 3.5) represent a system of coupled, non-linear partial differential equations. One of the main challenges arises from the fact that discontinuous solutions are possible due to the non-linearity of the convection terms. Here, the equations are solved in a segregated manner which turned out to be a robust approach for mixed parabolic-hyperbolic explosion problems. It means that the equations are solved consecutively instead of inverting the complete system matrix at once. Latter strategy is usually pursued for fully explicit solvers that are optimized for purely hyperbolic problems. However, such solvers tend to become unstable at low Mach numbers since infinite speed of sound (incompressible limit) implies decoupling between density and pressure [114].

To improve efficiency of the solver, a global burnout indicator is introduced and continuously updated. As soon as 100 % burnout is reached, the transport equations of the combustion model (including costly iterations in the framework of the flame tracking method) are not solved anymore. Also the adaptive mesh refinement algorithm (sec. 3.6) is stopped in this case. At the same time, the conservation equations for mass, momentum, energy and species are continued to be solved. This is important to predict the dynamics of pressure waves propagating in the burned mixture after complete burnout. An example can be seen in fig. 5.9, where the recurring reflection of blast waves in the containment of a pressurized water reactor is studied.

3.3.3.1   Density-based formulation

Regarding the solver architecture, two classical strategies exist. Most up-to-date CFD codes (commercial as well as open-source) are pressure-based, e.g. employing the Pressure Implicit with Splitting of Operators (PISO) or Semi-Implicit Method for Pressure Linked Equations (SIMPLE) algorithm [85]. As the name suggests, a pressure (correction) equation is solved and the density can finally be evaluated from the equation of state. Combined with implicit time-stepping, the formulation provides a robust and efficient simulation framework due to usage of large time steps. However, the pressure equation

Table 3.1: Coefficients of the SST turbulence model

α_{k1}	α_{k2}	$\alpha_{\omega1}$	$\alpha_{\omega2}$	Pr_T	γ_1	γ_2	β_1	β_2	β^*	a_1	c_1
0.85034	1.0	0.5	0.85616	1.0	0.5532	0.4403	0.075	0.0828	0.09	0.31	10.0

involves a second spatial derivate of the pressure field and is therefore highly dissipative. Discontinuous solutions are quickly degraded. Especially in the transsonic or supersonic regime, such formulation clearly reveals its drawbacks.

Contrary to pressure-based solvers, density-based solvers incorporate the continuity equation in its conservative form which does not have a diffusive term by nature, cf. eq. 3.1. The pressure field can finally be obtained from the equation of state. Explicit time-stepping is usually applied to ensure accurate resolution of compressible flow phenomena, such as shock waves and expansion fans. Since the CFL condition (eg. 3.51) strictly restricts the time step size, advanced supersonic capabilities have to be paid by higher computational costs.

In the end, a compromise between accuracy, stability and computational cost always has to be accepted. Following the reasoning of Ettner [79], a density-based formulation is preferred for DDT simulations. Accurate reproduction of gas-dynamic effects, especially shocks, is essential since auto-ignition phenomena and shock-flame interaction have to be considered.

3.3.3.2 Approximate Riemann solver

To make the non-linear continuum problem accessible to computer processing, the system of equations is discretized via the finite volume method. One of its main advantages is the flux-conservative formulation – contrary to the finite difference method for instance. The finite volume method is considered a standard in CFD and therefore not repeated in detail. The interested reader is referred to the book of Ferziger and Peric [85].

For the calculation of convective fluxes of conserved flow quantities (analogous to $\alpha_f F_f$ in eq. 3.76 with α being replaced by $\phi = \rho, \rho u_i, \rho e_t$ etc.), face-based values ϕ_f have to be determined from cell-centered values ϕ. Deviating from standard finite volume discretization which uses interpolation laws of varying complexity for this purpose, another approach is used here.

First of all, a linear reconstruction of ϕ from both sides of each considered face is performed. Left ϕ_L and right ϕ_R states are then transferred to an approximate Riemann solver for the calculation of ϕ_f and finally the face flux $\phi_f F_f$. The category of schemes is commonly known as of the Godunov-type in literature [156]. In combination with the Gaussian divergence theorem (cf. eq. 3.75), this approach assures a second-order accurate spatial discretization. Simply assigning cell mean values of both sides to ϕ_L and ϕ_R (i.e. without linear reconstruction) would yield a first-order accurate discretization. The accuracy is in fact locally reduced to first order if a multi-dimensional slope limiter is locally activated. It prevents the generation of spurious new extreme values for high-order reconstruction approaches.

ϕ_L and ϕ_R are generally not identical, meaning that a discontinuity is present at cell faces. From a mathematical point of view, the situation represents a Riemann problem [156]. Based on the one-dimensional Euler equations (neglecting diffusive terms in eqs. 3.2 and 3.7), an iterative procedure allows to calculate the exact solution of the Riemann problem. Since this strategy is computationally expensive, an *approximate* Riemann solver employing the Harten-Lax-van Leer with Contact (HLLC) scheme [254] is incorporated. Each cell pair is basically interpreted as a shock tube problem. Three characteristic waves (contact

discontinuity, shock and expansion fan) are assumed to originate from the interface at different constant speeds. Two simplifications are introduced: Instead of iterative determination, characteristic wave velocities are estimated from the initial state within each time step. Furthermore, the inner structure of an expansion fan is not resolved. Within each cell, an expansion fan is treated like a discontinuity. Implementation in the code follows the ansatz of Einfeldt [76] which was gained by an eigenvalue analysis of the linearized Euler equations. In-depth information about the approximate Riemann solver is provided by Toro [253] or Ettner [79].

Successful validation of the solver by means of a shock tube problem is shown in sec. 3.6.2. Ettner [79] further compared the solution with a pressure-based solver and attested vastly superior performance of the density-based HLLC solver. Under unfavorable circumstances, the HLLC scheme predicts non-physical values, e.g. unrealistically low temperatures. In these rare cases, the out-of-bounds value is replaced by the mean of its surrounding cells to stabilize the simulation. Also note that the Godunov-type flux calculation is eventually coupled with a flame tracking approach as described in sec. 3.4.

3.3.3.3 Time-stepping

A hybrid explicit-implicit Euler scheme is implemented for temporal discretization. While explicit time-stepping of convective terms is vital to achieve good shock-capturing capabilities, implicit time-stepping is the more appropriate choice for diffusive terms owing to their dissipative nature. Because of increasing computational costs and memory requirements, higher-order temporal discretization schemes, e.g. of the Runge-Kutta type, do not seem to be justified as long as uncertainties on the turbulence and combustion modeling side are comparably large.

The explicit part strictly restricts the time step size according to the Courant-Friedrichs-Lewy (CFL) condition

$$\text{CFL} = \max_{\Omega}\left(\frac{(|u_i| + a)\,\Delta t}{\Delta x}\right) < \text{CFL}_{\text{lim}}. \tag{3.51}$$

In this case, the CFL number is determined by the maximum characteristic wave velocity (magnitude of convective flow velocity u_i plus speed of sound of an ideal gas $a = \sqrt{\kappa R T}$) in the domain Ω. The applied definition is essential for accurate reproduction of weak pressure waves, i.e. acoustic waves, which are permanently emanating from the flame zone. In the unburned mixture, those pressure waves coalesce and can eventually form shocks if the supersonic regime is reached. Calculating the CFL number with the convective flow velocity alone would clearly be insufficient shortly after weak ignition when the medium is still at rest. As shown in sec. 3.5, chemistry is not computed during the runtime of the solver and therefore not a limiting factor on the time step size Δt. Δx denotes the characteristic cell size.

Dynamic adjustment of the time step according to eq. 3.51 results in considerable computational savings. As can be seen from above formula, the speed of sound is a function of mixture composition and temperature. Hence, the speed of sound of the hot combustion products is roughly twice the speed of sound of the cold reactants. Via the increasing convective flow velocity, the time step decreases by a multiple in the course of the explosion process. For example, a stable detonation propagates at a velocity approximately twice

the products' sound speed. Using fixed time-stepping, the time step size would have to be estimated quite conservatively, involving a large computational overhead.

The CFL criterion can be interpreted in a way that it specifies how far information is allowed to propagate within one time step. A threshold value of $CFL_{lim} = 0.3$ usually guaranteed a stable solution. By this means, it is ensured that each cell is only influenced by characteristic waves originating from direct neighbor cells. In contrast, purely implicit schemes aim to minimize the residual of transported variables iteratively. Such approaches are predominantly used in subsonic CFD but generally fail to reproduce the correct propagation velocity of characteristic waves.

3.4 Geometrical Volume-of-Fluid method

3.4.1 Motivation

The conservative propagation of discontinuous fields is one of the most challenging problems in computational fluid mechanics. Not only the widely used Finite Volume Method (FVM), but popular alternatives like the Finite Element Method (FEM) and Finite Difference Method (FDM) equally suffer from insufficient reproduction of discontinuous solutions. A decision problem arises: On the one hand, upwind-type schemes are easy to implement and stable but very dissipative. On the other hand, higher-order (central) schemes are potentially more accurate but tend to oscillate, hence necessitate undesired flux limiting. Besides, higher-order discretization is often based on an extended stencil which requires a laborious procedure on geometrically flexible unstructured meshes. Some of the most advanced high-order schemes for hyperbolically dominated equations originate from the Weighted Essentially Non-Oscillatory (WENO) family [239]. Even those sophisticated schemes are not without problems though, for example in terms of positivity preservation (i.e. prevention of negative pressure, density, etc.) [293].

Dissipation-free evolution of discontinuous fields can be achieved by so-called front-tracking techniques. Such methods have been applied to two-phase problems with remarkable success, e.g. in [87] (jet atomization), [213] (surface-tension-driven interfacial flows), [226] (free surface flows) etc. In this work, the passive discontinuity separating gas and liquid phase is replaced by a reactive discontinuity separating burned and unburned gas states. With the exception of the combustion source term, the mathematical problem is similar. The motivation is to minimize artificial dissipation and ensure a physically consistent motion of the flame. While front-tracking is mostly used in conjunction with direct numerical simulations, the technique is here used in an ensemble-averaged context. In this case, the transported interface represents the mean position of the generally turbulent flame brush, cf. sec. 3.5.4.

Other than unsteady flame propagation, gas-dynamic phenomena are treated by capturing methods. Particularly shock waves are not tracked although this has successfully been demonstrated in the past [5, 7]. Since pre- and post-shock states are unknown by default, costly iterative solution of Rankine-Hugoniot jump conditions (sec. 2.1) would be required. In the context of DDT simulations, shock-tracking can hardly be realized due to the extremely complex system of shock and weaker pressure waves including multi-dimensional intersection and wall reflections. The situation is different for pure deton-

ation propagation since a pronounced precursor shock exists. The idea of treating detonation waves strictly as gas-dynamic discontinuities is explored in Detonation Shock Dynamics (DSD) theory [8]. As Tryggvason et al. [258] state, artificial interface thickening can be fast compared to the timescales of interest and can quickly degrade the quality of the solution. Contrary to the flame, shock waves tend to sustain their discontinuous character by nature. Accurate shock capturing is in fact delegated to the approximate Riemann solver (sec. 3.3.3.2). The overall method can thus be termed a *hybrid flame-tracking shock-capturing* scheme.

3.4.2   Method classification

Independent of the physical background, various numerical techniques for explicit *tracking of interfaces* (not capturing) became accepted over the last decades. Terms and definitions are sometimes ambiguous. Following e.g. Hyman [111], Scardovelli and Zaleski [226], Tryggvason et al. [258], some of the most widely used approaches are briefly reviewed:

- *Arbitrary-Lagrangian-Eulerian* (ALE): Such techniques (partially) eliminate the grid or are based on moving meshes. Using the ALE approach, mesh vertices may be moved with the fluid (Lagrangian point of view), be held fixed (Eulerian point of view), or be moved in any other prescribed manner [108]. For example, it is possible to dynamically adapt the mesh to the motion of the interface in a way that the interface coincides with mesh lines at all times. Basically, the procedure has to be executed every time step which can be computationally expensive. Full re-meshing is required in case of large deformations and topological changes. This idea is consequently limited to special applications involving only weakly deformed interfaces.

- *Marker* methods: Tracers or marker particles are utilized to locate the phases. Interfacial or surface-marker methods employ marker particles only at the interface, whereas volume-marker methods employ marker particles in the whole domain. The technique basically facilitates to capture details of interface motion on scales much smaller than the grid spacing. In the popular Marker-and-Cell (MaC) method [109, 272], the interface is marked by massless particles that are convectively transported and used to reconstruct the interface on a fixed mesh. As a weak point, the strong dependency on the number and distribution of particles has to be mentioned. For example, accumulation of marker particles at stagnation points of the flow can result in locally poor representation of the interface.

- *Surface-Tracking*: Often, this category is also called front-tracking. The interface is described by a height function or by a polygonal representation, for instance. High accuracy can be achieved at moderate computational effort since the underlying grid can be relatively coarse while the free surface is represented exactly. The interface is directly propagated by displacing the front vertices. Disadvantages concern topological changes and strong deformations which are difficult to handle, especially on multi-dimensional unstructured meshes. Surface-tracking approaches are not necessarily volume-conserving [139]. Popular formulations are available from Popinet and Zaleski [214] and Tryggvason et al. [257].

- *Level-Set* (LS): Such methods solve an advection equation for a scalar quantity without direct physical meaning, i.e. the LS field. A *continuous* iso-line in 2D or iso-surface in 3D of the LS field is then interpreted as the propagated interface. Information related to interface topology, e.g. local normal or curvature, can accurately be calculated on that basis. LS methods naturally adopt topological changes and are comparably simple in terms of the advection algorithm. Although numerical diffusion of the LS field does not degrade the sharpness of the interface, it does deteriorate the accuracy of interface propagation, especially in highly curved regions. As a consequence, LS methods sometimes massively violate volume-conservation. In some applications, e.g. two-phase flows, this deficiency is crucial. Moreover, special measures like re-initialization of the LS field are necessary due to numerical reasons – eventually providing the physical meaning as a signed distance function to the LS field. Sethian and Smereka [235] provide an overview on LS methods for fluid interfaces. An interesting application to large-scale astrophysics problems is presented by Reinecke et al. [217]. Their approach utilizes the LS technique to describe a turbulent thermonuclear deflagration front (i.e. the propagated discontinuity) in white dwarfs undergoing a Type Ia supernova explosion.

- *Volume-of-Fluid* (VoF): VoF methods, also known as volume-tracking, are based on an advection equation for the volume fraction which is a strictly defined quantity. Other than *algebraic* VoF methods using (dissipative) interpolation laws of varying complexity, *geometrical* VoF methods calculate convective fluxes by means of geometric operations, cf. sec. 3.4.3.2. Since information about interface topology is not directly available from the volume fraction field, a reconstruction approach is necessary, resulting in additional algorithmic effort. Two of the method's main advantages are its robustness against topological changes and strong interface deformations as well as volume conservation. The performance of VoF methods heavily depends on the interface orientation scheme. Several improvements are addressing this fact. Historically, the development started with Simple Line Interface Calculation (SLIC) which is now commonly replaced by Piecewise Linear Interface Calculation (PLIC). Recent advancements are the Moment-of-Fluid (MoF) method and Patterned Interface Reconstruction (PIR). The mentioned interface reconstruction methods are elaborated in sec. 3.4.3. A review on VoF for the dynamics of free boundaries is given by Hirt and Nichols [109]. Examples of SLIC- and PLIC-VoF in reactive flow context were published by Barr and Ashurst [16], Chorin [52] and Bielert et al. [23], respectively.

Recently, attempts have been made to combine the advantages of different approaches, e.g. leading to the Coupled Level-Set Volume-of-Fluid (CLSVoF) method [246], the Coupled Level-Set Moment-of-Fluid (CLSMoF) method [117] or a hybrid level-set surface-tracking method [179].

Probably because they offer the best compromise between accuracy, computational speed, storage requirements, algorithmic complexity and topological flexibility, LS and VoF emerged as the best established methods over the years. The geometrical VoF method was favored in the end since it assures conservative local reconstruction of the front to a prescribed tolerance. This feature is neither inherent to LS methods, nor guaranteed by the contour-based reconstruction approach of Kunkelmann [150] which cannot be employed for flux calculation. In chap. 4, the latter is solely used as a runtime post-processing

tool for flame surface area calculation, without affecting the computation. Global volume conservation is irrelevant to this work because of the combustion source term permanently increasing the burned gas volume. Additionally, it is unclear how to incorporate the volumetric source term (sec. 3.5.6) in a LS framework since it cannot directly be recast as an additional dilatational component of flame propagation. The VoF formulation is compatible with both combustion source terms introduced in sec. 3.5.

The implemented approach can be characterized more precisely as an unsplit multi-dimensional geometrical VoF method based on conservative PLIC with full unstructured mesh support. The meaning of this classification will be explained thoroughly in the following sections. Especially the mesh flexibility comes at the prize of high algorithmic complexity.

3.4.3 Reconstruction step

The VoF method consists of two elementary steps: reconstruction step (this section) and advection step (sec. 3.4.4). To begin, some important definitions have to be introduced. One fundamental quantity is the volume fraction α. It describes the volume ratio of fluid A to the total in each computational cell:

$$\alpha = \frac{V_A}{V} = \frac{V_A}{V_A + V_B}. \tag{3.52}$$

Continuity requires the volume sum of both fluids (or phases) A and B to be equal to the cell volume V. In turn, the volume of fluid A

$$V_A = \int_V \vartheta(x_i)\, dx_i \tag{3.53}$$

is defined by integration of the discontinuous phase indicator function

$$\vartheta(x_i) = \begin{cases} 1 & \text{where fluid A is present,} \\ 0 & \text{where fluid B is present (otherwise).} \end{cases} \tag{3.54}$$

The volume fraction α can thus be interpreted as a discretized version of the indicator function ϑ that can be represented by the computational grid. In this work, fluid A indicates burned gas and fluid B indicates unburned gas, respectively. Interface-containing cells are called *front cells* in the following. An identification tolerance of $\epsilon_{id} = 10^{-4}$ is introduced to constrain execution of the costly reconstruction algorithm to the vicinity of the flame, i.e. $\alpha \in [0 + \epsilon_{id}; 1 - \epsilon_{id}]$. Below $\epsilon_{id} = 10^{-3}$, a low sensitivity of the results on the choice of ϵ_{id} was found.

Reconsidering its integral definition in eq. 3.52, it is clear that α does not provide direct information about interface topology within front cells. However, the interface can be reconstructed from the α field in an indirect way, which is the main purpose of the reconstruction step. Several techniques exist to approximate the a-priori unknown exact interface. The general procedure is visualized in fig. 3.1. Since the interface geometry is later used to determine the volume fluxes during the advection step, its reconstruction has a significant influence on the accuracy of the overall VoF method. Different types of reconstruction and advection errors are summarized in sec. 3.4.5.
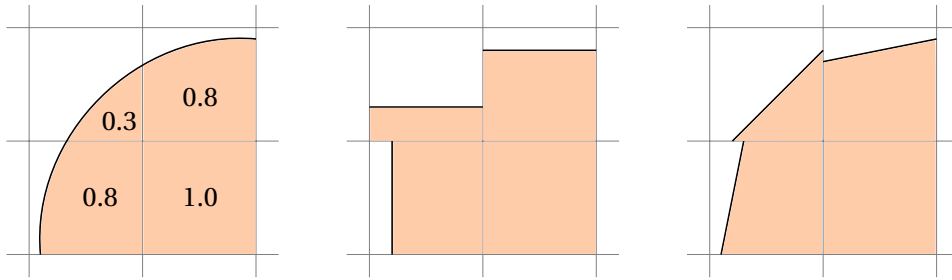
Figure 3.1: Exact interface position including discrete volume fraction values α (left), SLIC-reconstructed interface (center), PLIC-reconstructed interface (right); Two-dimensional example adapted from [220]

From a historical perspective, the development started with Simple Line Interface Calculation (SLIC) by Hirt and Nichols [109], Noh and Woodward [198] which denotes a piecewise constant approximation of the interface. The two-dimensional example shows the interface being parallel to one of the mesh lines or coordinate axes. Spurious behavior of SLIC reconstruction can especially be observed in highly vortical flows.

Newer *Piecewise Linear Interface Calculation* (PLIC) dating back to Youngs [285, 286] and Rider and Kothe [220] describes a piecewise linear approximation of the interface. Orientation of the interface is another degree of freedom. The two-dimensional example reveals its superior performance compared to SLIC. Nearly all up-to-date geometrical VoF methods, and also the one realized here, are based on the PLIC technique. A planar interface is generally characterized by its orientation and location. The first property is obtained from the gradient of the volume fraction field, cf. sec. 3.4.3.1. The second property results from the enforcement of local volume conservation. In each front cell, the interface is iteratively positioned (sec. 3.4.3.3) such that the truncated volume (sec. 3.4.3.2) assures the correct discrete volume fraction value.

Whereas orientation calculation takes into account information from neighboring cells, this is not the case for the positioning of the interface. As is evident from fig. 3.1, such procedure generally leads to a disconnected reconstruction at the faces of adjacent front cells. The smaller the curvature radius of the interface in relation to the cell size, the stronger the problem gets. Besides increasing the mesh resolution, the problem can be extenuated by higher order interface orientation methods. Using Patterned Interface Reconstruction (PIR) which was recently published by Mosso et al. [194], standard PLIC reconstruction is followed by linear or spherical smoothing operations to facilitate better connected interfaces at cell faces. Computational costs rise accordingly since interface smoothing operations require information from neighboring cells. Dyadechko and Shashkov [72] proposed a generalization of VoF, the so-called Moment-of-Fluid (MoF) method. It is superior in terms of accuracy and improves the representation of sharp corners, especially on highly irregular grids. The method does not require any information from adjacent cells but involves clearly higher algorithmic complexity. In the end, it is assumed that the benefit of these recent developments is not worth the additional computational or algorithmic effort. The improvement due to these advanced techniques is not comparable to the improvement from SLIC to PLIC.

3.4.3.1 Gradient calculation

For each front cell, the orientation of the interface plane is given by the normalized volume fraction gradient

$$n_j = \frac{\dfrac{\partial \alpha}{\partial x_j}}{\left| \dfrac{\partial \alpha}{\partial x_m} \right|}. \tag{3.55}$$

Hence, it is clear that the gradient scheme is crucial for the performance of PLIC methods [50]. Numerous approaches have been developed in the past to improve gradient computation. Most schemes apply Gauss' divergence theorem to transform cell-centered gradient calculation to face-centered quantities. Accordingly, relation

$$\frac{\partial \psi}{\partial x_j} = \frac{1}{V} \sum_f \psi_f A_{j,f} \tag{3.56}$$

is the common basis. ψ denotes any quantity of which the gradient is sought, ψ_f represents its face-centered value and $A_{j,f}$ is the surface area vector of the corresponding face f. Since ψ_f is unknown by default, interpolation with adjacent cells is usually performed.

In the simplest scheme, ψ_f is calculated by linear interpolation between cell-centered values of direct neighbor cells. A fourth-order scheme, investigated in [135], involves an extended stencil including further neighbor layers. Interpolation accuracy is supposed to be increased by this means. Another frequent choice in literature is the least squares approach [220, 286]. It is based on an error minimization and does not rely on the Gaussian divergence theorem. All three variants are available in OpenFOAM and work well (almost equally) for smooth fields, but clearly reveal their drawbacks for discontinuous fields. In the context of interface tracking, the volume fraction changes between bulk values within a single cell layer. As a consequence of low accuracy gradient calculation, interface propagation via the geometrical VoF method can become unstable. In some codes, the robustness is improved by smoothing or filtering a copy of the volume fraction field before using it for gradient computation. The actual volume fraction field is not manipulated. The main reason for the poor performance is that all of the mentioned schemes exclusively rely on direct face neighbors F which share a common face with the cell in question C. The influence of point neighbors P, also called skew cells, which are connected only through a point or an edge, are neglected. The situation is illustrated in fig. 3.2. Due to a lower number of direct face neighbors and a higher number of point neighbors at the same time, the issue can be even more pronounced for unstructured meshes. From the discretization scheme's point of view, the limited neighborhood connectivity of triangular or tetrahedral meshes is generally problematic [114].

To overcome the deficiencies of the standard gradient schemes, the recently developed *Node-Averaged Gauss* (NAG) scheme of Marić et al. [178] is implemented. It is based on Gauss' divergence theorem but differs in the calculation of ψ_f. Volume fraction values of direct face neighbors as well as point neighbors are taken into account indirectly, without the need of constructing an extended connectivity stencil. As stated by the authors and confirmed by own investigations, the NAG scheme results in very accurate and convergent interface reconstruction. Coupling with a flow solver was not yet demonstrated by Marić et al. [178]. First of all, cell-centered volume fraction values are extrapolated to
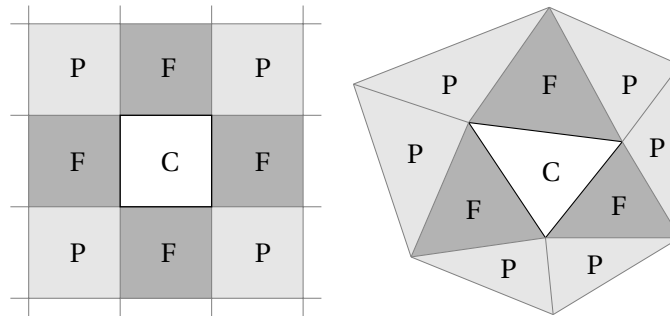
Figure 3.2: Two-dimensional stencil of a cell C with face neighbors F and point neighbors P: Structured orthogonal mesh (left) and unstructured triangular mesh (right); Adapted from [135]

cell points by the inverse distance weighting method. The face-centered values are then obtained from area-weighted averaging of the mesh point values. In doing so, the shape of arbitrary cell faces is taken into account by a triangulation procedure. Being one of the big advantages, execution of the NAG scheme does not involve costly loops over neighbor cells. Moreover, it works well on arbitrary unstructured meshes and does not require preceding smoothing of the volume fraction field.

Offering similar benefits as the NAG scheme, a generalized version of the least squares approach [181] comes into consideration. Because of the necessary construction of an extended connectivity stencil, it was not applied in this work though. Such an approach is further disadvantageous in terms of parallelization since information exchange with neighbor cells at processor boundaries requires special treatment.

3.4.3.2 Volume truncation

Only in section 3.4.3.2 and 3.4.3.3, Einstein's summation convention is suspended to avoid confusion with excessive variable indexes. Instead, tensors of first (vectors) and second order (matrices) are identified by bold characters.

Another key building element of the geometrical VoF method is the volume truncation procedure. It determines the volume of a truncated polyhedron V_T resulting from the splitting of the original polyhedron of volume V by a planar interface. This information is required for the next step, namely the positioning of the interface via the principle of local volume enforcement (sec. 3.4.3.3). The applied procedure is based on [170] and works for general convex polyhedrons, hence structured as well as unstructured meshes.

Separating both discrete states $\vartheta = 0$ and $\vartheta = 1$, the mathematical representation of the cutting plane is introduced first. In Hesse normal form, any plane can be described by

$$\boldsymbol{n} \cdot \boldsymbol{x} + C = 0 \tag{3.57}$$

in which the normal vector $\boldsymbol{n}$ (eq. 3.55) defines the orientation of the plane. The offset C denotes the distance from the origin of the coordinate system to the plane. The sum of all points $\boldsymbol{x}$ satisfying eq. 3.57 eventually constitutes a complete description of the plane.

The original polyhedron consists of J faces (index j), each comprising I_j vertices (index i). Consistent with formula 3.57, the signed distance $\phi_{j,i}$ of every polyhedron vertex $\boldsymbol{x}_{j,i}$ to the cutting plane is given by

$$\phi_{j,i} = \boldsymbol{n} \cdot \boldsymbol{x}_{j,i} + C. \tag{3.58}$$

Based on a comparison of the signs of $\phi_{j,i}$ and $\phi_{j,i+1}$, corresponding to two adjacent vertices, it is decided whether the connecting polyhedron edge is cut by the interface or not. The position vector of newly arising intersection points $\boldsymbol{x}_{j,\text{new}}$ along the connecting edge of adjacent points $\boldsymbol{x}_{j,i}$ and $\boldsymbol{x}_{j,i+1}$, is determined from

$$\boldsymbol{x}_{j,\text{new}} = \boldsymbol{x}_{j,i} - \frac{\phi_{j,i}}{\phi_{j,i+1} - \phi_{j,i}} (\boldsymbol{x}_{j,i+1} - \boldsymbol{x}_{j,i}). \tag{3.59}$$

Figure 3.3 illustrates the procedure. The truncated polyhedron (colored orange and bounded by thick lines), can now be constructed from those vertices with positive signed distance (filled dots) and the new intersection points (crosses).

To compute the volume of the truncated polyhedron V_T, an elegant way is to use

$$V_T = \frac{1}{3} \sum_{j=1}^{J} (\boldsymbol{n}_{\Gamma j} \cdot \boldsymbol{x}_{j,1}) \, A_{\Gamma j} \tag{3.60}$$

which essentially is a discrete version of the cone volume formula ($1/3 \cdot$ height $\cdot$ base area) applied to each face Γ_j of the truncated polyhedron [232]. $\boldsymbol{n}_{\Gamma j}$ denotes the normal vector of face Γ_j which always points outwards from the truncated polyhedron. Accordingly, $\boldsymbol{n}_\Gamma = -\boldsymbol{n}$ holds for the cutting plane. Computing the truncated face area as

$$A_{\Gamma j} = \frac{1}{2} \boldsymbol{n}_{\Gamma j} \cdot \sum_{i=1}^{I_j} (\boldsymbol{x}_{j,i} \times \boldsymbol{x}_{j,i+1}) \tag{3.61}$$

finally yields

$$V_T = \frac{1}{6} \sum_{j=1}^{J} \left[(\boldsymbol{n}_{\Gamma j} \cdot \boldsymbol{x}_{j,1}) \boldsymbol{n}_{\Gamma j} \cdot \sum_{i=1}^{I_j} (\boldsymbol{x}_{j,i} \times \boldsymbol{x}_{j,i+1}) \right]. \tag{3.62}$$

To ensure the closed-loop condition, subscript $i+1$ must be replaced by 1 for $i = I_j$. Equation 3.62 is valid for arbitrary polygonal or polyhedral bodies. The only restriction on this formula is that the polyhedron must not be self-intersecting [281]. Bounding faces are planar by definition. Alternative efficient volume calculation approaches were published by Schneider and Eberly [232].

A strict requirement to calculate the truncated volume by eq. 3.62 is the counterclockwise ordering (viewed from outside of the polyhedron) of the bounding vertices $\boldsymbol{x}_{j,i}$. Special attention has to be paid to the correct ordering of intersection points $\boldsymbol{x}_{j,\text{new}}$ spanning one face of the truncated polyhedron. The cutting algorithm therefore visits the original polyhedron faces by a specific sequence. Instead of processing the faces consecutively according to their index, they are visited along the cutting line of the interface. The next face has to contain the same edge with the same intersection point. Since the number of vertices of the interface and of truncated faces is not known a priori, dynamic lists are employed to store the corresponding coordinates. To avoid spurious multiple registration, it is checked whether points are already contained before appending them to the list. Having assured consistent point lists, the (truncated) face area $A_{\Gamma j}$ and its contribution to the truncated volume V_T can be determined from formulas 3.61 and 3.60, respectively.
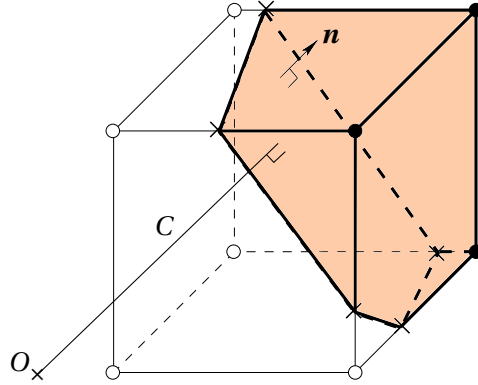
Figure 3.3: Truncation of a general polyhedron (vertices • and ○) by an interface of orientation $\boldsymbol{n}$; Points of positive signed distance (•) and intersection points (×) form the truncated polyhedron (thick lines); C denotes the interface offset to the origin O; Adapted from [170]

3.4.3.3   Conservative interface positioning

After introducing the geometrical volume truncation tool, the next step is to find the correct interface location under the constraint of local volume conservation. The offset C is the only remaining degree of freedom in the Hesse normal form 3.57 specification of the cutting plane. It describes the distance from the plane to the origin. Orientation of the interface $\boldsymbol{n}$ is already fixed according to eq. 3.55. The task is to determine the value of C for which the truncated volume V_T results in a truncated volume fraction α_T equal to the a priori given volume fraction α. Mathematically spoken, the non-linear interface position function $f(C)$ is required to be zero:

$$f(C) = \alpha_T(C) - \alpha = \frac{V_T(C)}{V} - \alpha = 0, \tag{3.63}$$

i.e. interface positioning constitutes a one-dimensional root finding problem in terms of the offset C. Equation 3.63 can be solved directly or iteratively. Most direct methods are restricted to specific cell types or limited in dimensionality. Scardovelli and Zaleski [227] derived analytical relations for rectangular grids to eliminate the need to iterate. Extended analytical relations for triangular and tetrahedral grids were published by Yang and James [281]. Lately, López and Hernández [170] provided a compilation of analytical and geometrical tools for general grids. Computational speed is generally higher employing direct methods. Depending on the geometrical flexibility, the price to pay is an increased algorithmic complexity. To the best of the author's knowledge, no direct method for arbitrary cell types exists to date that is fully compatible with the unstructured mesh-handling paradigm of OpenFOAM. Straight-forward but more costly iterative interface positioning is therefore pursued.

The sought-after root has to be bracketed, meaning that the root lies in the interval spanned by two bounds a and b. The corresponding function values $f(a)$ and $f(b)$ have opposite signs. In the context of interface positioning, the interval is bracketed by the plane-normal distance to the origin C_p of cell vertices $\boldsymbol{x}_p$:

$$C_p = \boldsymbol{n} \cdot \boldsymbol{x}_p. \tag{3.64}$$

Representing the boundary of interface-containing cells, the root of function $f(C)$ lies between the minimum $C_{\min}$ and maximum vertex distance $C_{\max}$. Since the plane normal $\boldsymbol{n}$ always points in the direction of the volume fraction gradient, the offset $C_{\min}$ corresponds to a phase indicator of $\vartheta = 0$ and conversely for $C_{\max}$ and $\vartheta = 1$.

All iterative root-finding methods require an approximate starting solution. Depending on the algorithm, the initial guess C_0 can have a strong influence on the overall performance. Compared to using the cell center or a simple average of $C_{\max}$ and $C_{\min}$, two to three iterations are saved by

$$C_0 = C_{\min} + (1 - \alpha)(C_{\max} - C_{\min}) \tag{3.65}$$

which serves as a reasonable initial approximation. Figure 3.4 provides a graphical representation of the iterative interface positioning process. Starting from the initial solution, the tolerance-satisfying end solution is obtained after three iterations. The volume fraction value is approximately 0.7 in this generic example.

Iterations are continued until a predefined convergence criterion, i.e. desired solution accuracy, is reached. Here, the iterative tolerance is specified as $\epsilon_{\mathrm{it}} = 10^{-6}$, which is smaller than the identification tolerance ϵ_{id} by two orders of magnitude. For combustion simulations, application of the geometrical VoF method is motivated by the preservation of a physically consistent motion rather than exact volume conservation. ϵ_{it} is the first and foremost parameter to control computational costs and thus kept as loose as possible. In other applications, e.g. two-phase flow simulations where local and global volume conservation is vital, much finer tolerances are established. The maximum number of iterations is limited to 30. This value proved to be sufficiently high in this work.

Since geometrical volume truncation operations have to be repeated at each iteration, it is of highest importance to ensure a stable and fast-converging root-finding method. Overall computational cost heavily depends on the efficiency of the interface positioning process. Following this motivation, Ketterl [135] evaluated the performance of five algorithms that might be appropriate:

- Bisection
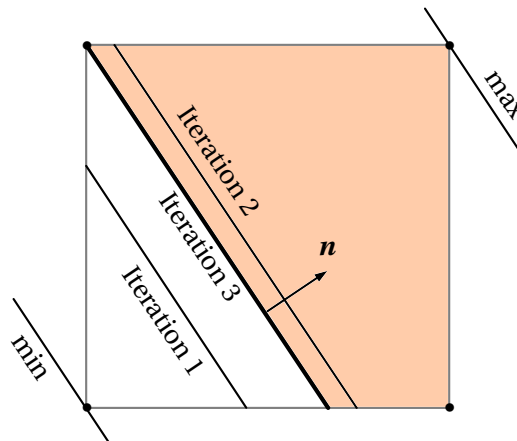
Figure 3.4: Principle of iterative interface positioning to fulfill local volume conservation: Two-dimensional example adapted from [220]

- False position

- Combination of secant and bisection

- Modified Newton-Raphson

- Brent

Implementation in the solver is based on [216] to a large extent.

Bisection (also called method of nested intervals) is the simplest method, guarantees to find a root but is only of linear convergence. The required number of iterations can a priori be determined from

$$\log_2 \frac{\epsilon_0}{\epsilon_{it}}, \tag{3.66}$$

where ϵ_0 is the size of the initial bracketing interval and ϵ_{it} is the desired ending tolerance. The secant (not individually assessed in [135]) and *false position* method behave similarly and converge faster than bisection for functions that are smooth near a root. Comparing both methods, the secant method converges more rapidly but the root does not necessarily remain bracketed. Thus, convergence cannot be guaranteed. A *combination of secant with bisection* was therefore proposed by Ahn and Shashkov [2] in the context of interface reconstruction. The idea is to use the efficient secant method whenever possible and switch to bisection if divergence is identified. Another possibility is the popular *Newton-Raphson* method which impresses by its quadratic convergence order on the one hand. On the other hand, it suffers from a strong dependency on the initial guess for the root. Unlike the previous methods, it does not only require the function $f(C)$ itself but also its derivative $f'(C)$. Since the derivative is not directly available, it is here approximated by a finite difference ansatz. The theoretical quadratic convergence order is abandoned by this means. Additionally, a scaling of the derivative is introduced such that the new solution remains in the bracketed interval. This modification further deteriorates the convergence rate but guarantees to find a root. Finally, *Brent*'s method is supposed to combine super-linear convergence with the sureness of bisection. If only the function's value and not its derivative is directly available, Brent is said to be the method of choice for one-dimensional root finding problems [216, 220].

In his systematic study, Ketterl [135] evaluated the algorithms' performance mainly by analyzing the average and maximum iteration count as well as the overall computation time. Since the algorithmic effort is not identical for the different root-finding methods, it is not enough to compare only the iteration count. A strong scaling between both quantities does indeed exist. Results were not unique and depended on grid structure (structured versus unstructured mesh) as well as dimensionality (two- versus three-dimensional test cases). Meaningful tendencies were observed nevertheless. According to the high number of iterations and consequently the high computation time, pure bisection and the false position method showed the weakest performance. Brent's algorithm and the modified Newton-Raphson algorithm emerged to be the best compromise between convergence rate and stability. The combination of the secant method with bisection can be ranked in the middle of both groups. Eventually, Brent's method was applied here because it can be used in its original form without modifications like for the Newton-Raphson method (derivative approximation and scaling, see above).

The basic idea behind Brent's algorithm [43] is to keep track of the convergence behavior of a super-linear method and to intersperse bisection steps if necessary. Contrary to false position and secant methods which assume approximately linear behavior between two prior root estimates, three prior solutions are used here to fit an inverse quadratic function. The assumed shape is an appropriate choice since $V_T(C)$ often varies quadratically with C [220]. Given the three point pairs $[C_{k-1}; f(C_{k-1})]$, $[C_k; f(C_k)]$ and $[C_{k+1}; f(C_{k+1})]$, the next root estimate is calculated by

$$C = C_k + \frac{P}{Q} \tag{3.67}$$

with

$$\begin{aligned} P &= S\,[T(R-T)(C_{k+1} - C_k) - (1-R)(C_k - C_{k-1})] \\ Q &= (T-1)(R-1)(S-1) \end{aligned} \tag{3.68}$$

and

$$R = \frac{f(C_k)}{f(C_{k+1})}, \quad S = \frac{f(C_k)}{f(C_{k-1})}, \quad T = \frac{f(C_{k-1})}{f(C_{k+1})}. \tag{3.69}$$

C_k represents the current best estimate of the root and P/Q can be interpreted as a 'small' correction. Quadratic methods can run into problems when the function is not sufficiently smooth. Division by a very small number in eq. 3.67, i.e. $Q \to 0$, has to be prevented. As a countermeasure, the algorithm keeps the solution bracketed and checks the result of the inverse quadratic interpolation before evaluating eq. 3.67. Whenever the solution lands out of bounds or the bounds are not collapsing rapidly enough, Brent intersperses bisection steps to guarantee at least linear convergence.

3.4.4 Advection and reaction step

Having completed the interface reconstruction step (sec. 3.4.3), the second step of the geometrical VoF method is to advance the interface in time according to the underlying velocity field u_j. This is done indirectly by solving an advection equation in non-conservative form (substantial or material derivative)

$$\frac{\mathrm{D}\alpha}{\mathrm{D}t} = \frac{\partial \alpha}{\partial t} + u_j \frac{\partial \alpha}{\partial x_j} = 0 \tag{3.70}$$

for the volume fraction α [220, 258]. Equation 3.70 distinguishes itself from a standard transport equation by the absence of a diffusive term. Diffusive transport perpendicular to the interface contradicts its discontinuous character. Parallel to the interface, no gradient of the discontinuous field (ϑ and consequently α), being the driving force of diffusive transport, exists. Although explosions come along with high flow compressibility, the VoF concept relies on the non-conservative form of the advection equation. The conservative form would require $\rho\alpha$ (instead of α) to be transported which is unknown by default in the bulk on both sides of the interface. This quantity, $\rho\alpha$, cannot be interpreted as a volume fraction anymore.

To extend the methodology for reactive discontinuities, an additional dilatational component specifying the relative propagation velocity normal to the interface (effective burning velocity S_{eff}) can be included. Replacing u_j with $u_j - n_j S_{\text{eff}}$ yields

$$\frac{\partial \alpha}{\partial t} + (u_j - n_j S_{\text{eff}})\frac{\partial \alpha}{\partial x_j} = 0, \tag{3.71}$$

which can be reformulated to

$$\frac{\partial \alpha}{\partial t} + u_j \frac{\partial \alpha}{\partial x_j} = S_{\text{eff}} \left| \frac{\partial \alpha}{\partial x_j} \right| \tag{3.72}$$

after inserting the definition of the front normal vector 3.55. As a consequence, the well-known gradient formulation of the combustion source term appears. Integration of the combustion source term will be thoroughly explained in sec. 3.5.

The convection term in eq. 3.72 cannot directly be recast in conservative form since the velocity field is not divergence-free. This would only be the case for incompressible flows. Thus, a so-called 'divergence correction' proposed by Rider and Kothe [220] is applied by adding

$$\alpha \frac{\partial u_j}{\partial x_j} \tag{3.73}$$

on both sides of eq. 3.72:

$$\frac{\partial \alpha}{\partial t} + \frac{\partial}{\partial x_j} \left(\alpha u_j \right) = \alpha \frac{\partial u_j}{\partial x_j} + S_{\text{eff}} \left| \frac{\partial \alpha}{\partial x_j} \right|. \tag{3.74}$$

Equations 3.74 and 3.72 are mathematically equivalent, but not in the discrete sense. The convection term on the left-hand side is now in conservative form (αu_j appears under the divergence operator) which is beneficial in terms of the discretization procedure. The divergence correction term on the right-hand side can be interpreted as an additional source term of the conservative advection equation.

The special treatment of the conservative convection term is explicitly demonstrated (unlike standard algebraic discretization of all other terms of eq. 3.74). Following the finite volume discretization procedure, integration over the cell volume V and application of Gauss' divergence theorem leads to

$$\int_V \frac{\partial}{\partial x_j} \left(\alpha u_j \right) dV = \oint_A \alpha u_j m_j dA. \tag{3.75}$$

Here, A denotes the cell's boundary and m_j the corresponding normal vector. Approximation of the surface integral by

$$\oint_A \alpha u_j m_j dA \approx \sum_f \alpha_f u_{j,f} A_{j,f} = \sum_f \beta F_f = \sum_f F_{f,T} \tag{3.76}$$

finally allows to assemble the matrix representing the discrete system. In the finite volume framework which ultimately solves for cell mean values, face-based quantities (subscript f) are not directly available, apart from mesh inputs like the cell surface vector $A_{j,f}$. From this point, the key difference between *algebraic* and *geometrical* VoF methods originates. Algebraic approaches adopt (dissipative) interpolation laws of any kind to reconstruct α_f values from the α field. To emphasize this fundamental difference to geometrical approaches where α_f is calculated by geometrical operations, α_f is identified by β in the latter case. Face fluxes $F_f = u_{j,f} A_{j,f}$ are provided by the Riemann solver discussed in sec. 3.3.3. In those generic test cases without flow solver coupling, face fluxes are directly calculated from the prescribed velocity field. The strong effect on interface propagation problems is shown in sec. 3.4.6.
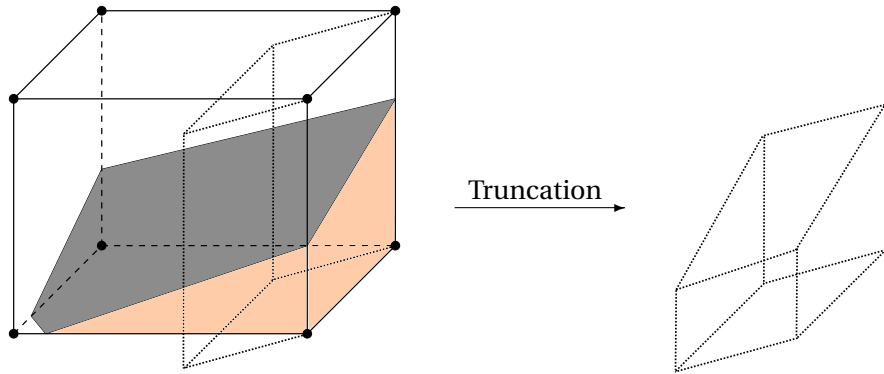
Figure 3.5: Principle of unsplit multi-dimensional geometric advection: Reconstructed interface (gray), flux polyhedron (dotted on the left) and advected volume (dotted on the right); Adapted from [135]

Considering temporal integration over one time step Δt, the face-based quantity β is generally interpreted as the ratio of the truncated flux volume $V_{f,T}$ to the total volume of the flux polyhedron V_f:

$$\beta = \frac{F_{f,T}\Delta t}{F_f \Delta t} = \frac{V_{f,T}}{V_f}. \tag{3.77}$$

The procedure to determine β is illustrated in fig. 3.5. At first, the so-called flux polyhedron (dotted on the left) has to be constructed which is discussed in sec. 3.4.4.1. It represents the maximum possible flux volume within one time step. The actually fluxed volume $V_{f,T}$ (dotted on the right), and finally β, is then obtained by truncating the flux polyhedron with the reconstructed interface (gray plane on the left). Whereas the cutting algorithm is the same as for interface reconstruction (cf. sec. 3.4.3.2), there is no need to iterate here. To consider only outflow faces is a convention resulting from the disconnected interface reconstruction across adjacent front cells. Outflow and corresponding inflow fluxes of neighboring cells are normally not identical, cf. fig. 3.1. Considering only inflow fluxes or an average of both would be feasible alike but is not the standard in literature [223, 285, 286].

To guarantee robustness of the geometrical VoF method, β is initially approximated as the surface ratio

$$\beta \approx \frac{A_{\Gamma,f}}{A_f} \tag{3.78}$$

instead of the volume ratio specified in eq. 3.77. Without additional operations, all necessary information (truncated face area $A_{\Gamma,f}$ and original face area A_f) is already available from the reconstruction step, cf. sec. 3.4.3.2. Should the subsequent more complex calculation of β as a volume ratio fail due to unexpected reasons, the volume fraction advection equation 3.74 can still be solved. Anyway, using this initial value is similar to neglecting the evolution of the interface within one time step. As long as the time step is sufficiently small, i.e. far below the CFL limit, there is no significant difference between the surface ratio and volume ratio interpretation of β. Closer to the CFL limit, the interface moves comparably far relative to cell size, meaning that the volume-interpretation is clearly superior in terms of accuracy.

Time stepping of the volume fraction advection equation is consistent with all other transport equations as described in sec. 3.3.3.3. Since there is no diffusive term in eq. 3.74, temporal integration resembles a purely explicit Euler scheme. Old and new solution are denoted as α^n and α^{n+1}, respectively. Regarding the advection step in multiple spatial dimensions, directional *split* and directional *unsplit* approaches are commonly distinguished [118, 168]. Using directional split advection, the solution is integrated successively in each spatial dimension, leading to a three-stage update process

$$\alpha^n \xrightarrow{x} \alpha^* \xrightarrow{y} \alpha^{**} \xrightarrow{z} \alpha^{n+1} \tag{3.79}$$

in the general case. Three different one-dimensional fluxes aligned with coordinate axes have to be calculated for that purpose. In contrast, directional unsplit advection is based on a single update

$$\alpha^n \xrightarrow{xyz} \alpha^{n+1}. \tag{3.80}$$

The multi-dimensional volume flux takes into account all components of the velocity vector at once. Latter approach involves higher algorithmic complexity but is significantly less expensive than a three-stage update. Directional unsplit advection is consequently applied in this work.

Compared to the reconstruction step, the advection step is less critical in terms of computational cost. The main reason is that geometrical operations (of any kind) do not have to be repeated in an iterative manner as for the reconstruction step.

3.4.4.1 Flux polyhedron construction

Several important aspects of flux polyhedron construction have to be emphasized. At least in two dimensions, it is popular to use face point velocities $u_{j,fp}$ which can be obtained from cell-centered values u_j by inverse distance weighting. Multiplication by the time step size Δt provides the increment between mesh vertices $x_{j,fp}$ and corresponding vertices of the swept polyhedron face $x'_{j,fp}$ along their Lagrangian trajectories [71]:

$$x'_{j,fp} = x_{j,fp} - u_{j,fp}\Delta t. \tag{3.81}$$

All vertices are thus available to construct the flux polyhedron. Figure 3.6 (right) outlines the procedure for a reduced two-dimensional example. Because of unique point velocities, flux polyhedrons of adjacent front cells do not overlap which represents the technique's main benefit. Problems arise as soon as the methodology is extended to three dimensions. In two dimensions, important features are naturally given: convexity of the flux polyhedron and planarity of the polyhedron faces. Especially for highly vortical three-dimensional flows, flux polyhedrons are not necessarily convex and bounded by planar faces. The situation is demonstrated in fig. 3.7. It has to be mentioned that the area and volume calculation formulas introduced in sec. 3.4.3.2 are invalid under such non-ideal conditions. One way to overcome this problem is via tetrahedral decomposition. Specific analytic relations are known for tetrahedral bodies. The method proposed by Ivey and Moin [113] allows to compute the volume of non-convex flux polyhedrons with non-planar faces but appears unattractive due to high computational costs. Another technique is available from Jofre et al. [118]. Its main idea is to split up the non-convex polyhedron into several convex bodies before known formulas for area and volume calculation are applied. Algorithmic complexity is increased by this means. Furthermore, adaptive mesh

refinement in the vicinity of the interface is likely to reduce the number of non-convex polyhedrons in complex flow fields. However, it does neither ensure complete absence of non-convex polyhedrons, nor does it ensure planar polyhedron faces. Quite the contrary, most polyhedron faces are non-planar if based on unique point velocities.

Problems associated to non-convex flux polyhedrons with non-planar faces are avoided by employing face velocities $u_{j,f}$ instead of face point velocities $u_{j,fp}$. Concretely, interpolated face velocities are directly assigned to all vertices of the considered face. All swept vertices belonging to one cell face follow the same Lagrangian trajectory, i.e.

$$x'_{j,fp} = x_{j,fp} - u_{j,f}\Delta t. \tag{3.82}$$

As a result, convex flux polyhedrons bounded by planar faces are guaranteed (fig. 3.7). This strategy can be seen as a generalization of the two-dimensional unsplit advection scheme by Rider and Kothe [220]. Liovic et al. [168] identify the planarity-preserving scheme as Piecewise Constant Flux Surface Calculation (PCFSC). Figure 3.6 (left) illustrates its behavior for the reduced two-dimensional example. Being the technique's main drawback, overlapping flux polyhedrons of adjacent front cells can clearly be seen. Erroneously, parts of the volume might either be fluxed twice or not at all in some regions. This type of error is classified as advection error in the following section. An advanced advection scheme improving the face velocity technique is proposed by Hernández et al. [107]. Despite small inherent advection errors, the face velocity technique is more robust and thus preferred over the point velocity technique.

It remains the question which velocity is used to create the flux polyhedron. In the ensemble-averaged framework, face velocities $u_{j,f}$ are linearly interpolated from cell-averaged values u_j. In those test cases without flow solver coupling, simply the prescribed velocity field is used.

3.4.5 Reconstruction and advection errors

Errors are inherent to both main parts of the geometrical VoF method. Errors of the reconstruction step can be attributed to the gradient scheme (determining front orientation), iterative front positioning and the general limitation of piecewise linear interfaces. Advection step errors, also called integration inaccuracies, arise in the determination of advected volumes. Mainly the face velocity based construction of flux polyhedrons is critical. Prior to the introduction of several countermeasures, different error symptoms are categorized [99, 135, 178].

3.4.5.1 Error symptoms

In the framework of the VoF method, *numerical boundedness* of the volume fraction field is not guaranteed per se. Colliding with the volume fraction's definition 3.52, overshoots ($\alpha > 1$) and undershoots ($\alpha < 0$) can occur – not only because of the deficiencies of the advection scheme but also due to generally non-divergence-free velocity fields. Additionally, being a unique feature of this work, the combustion source term tends to cause small overshoots in the vicinity of the interface.
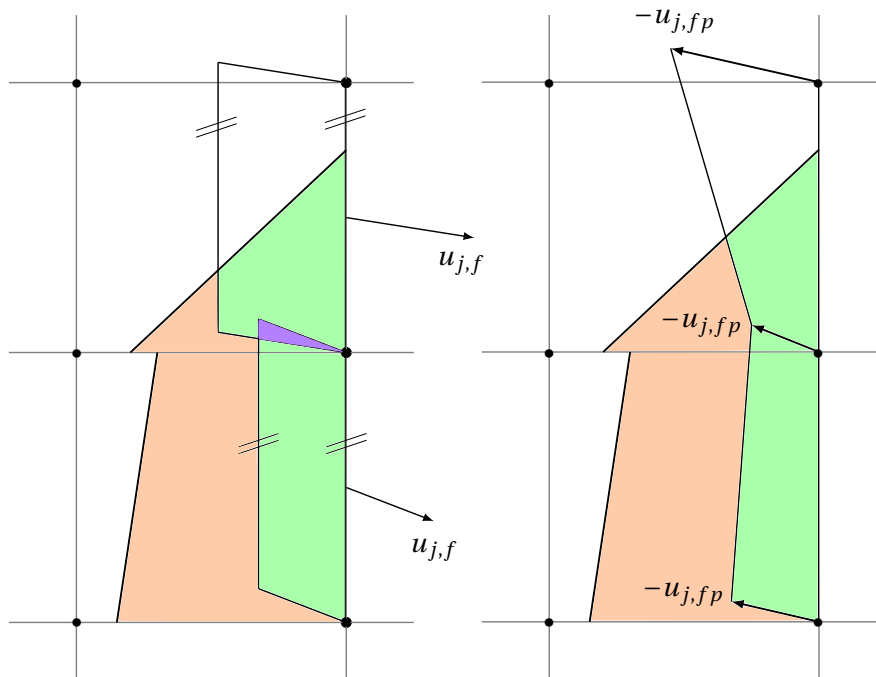
Figure 3.6: Advection step mechanism in two dimensions: Based on flux polyhedron construction by face velocities (left) and based on flux polyhedron construction by unique point velocities (right); Different color levels distinguish empty part of cell (white), occupied but not advected part of cell (orange), advected volume (green) and erroneously twice fluxed region (purple); Adapted from [171]
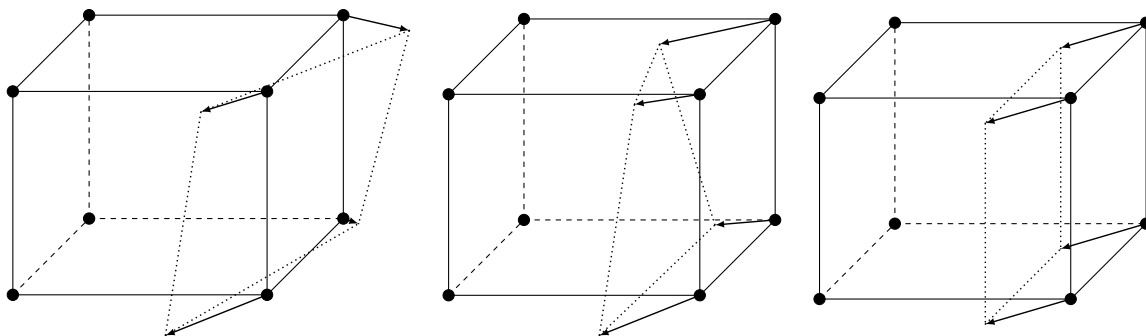
Figure 3.7: Flux polyhedron examples resulting from different construction techniques: Non-convex body created from point velocities (left), convex body with non-planar faces created from point velocities (center) and convex body with planar faces created from face velocities (right); Reproduced from [135]

Within bulk regions, volume fraction values are supposed to remain unchanged during the course of the simulation. According to its construction, also the combustion source term vanishes in this part of the domain. Nevertheless, artificial deviations from unity or zero (*wisps*) are possible due to integration inaccuracies or the non-divergence-free character of the velocity field. In the latter case, more volume can be transported into a cell than leaving it (and vice versa). Aforementioned wisps must therefore result in violation of numerical boundedness within bulk regions. The divergence correction 3.73 is introduced to counteract such phenomena from the beginning.

Flotsam or *jetsam* denote the artificial separation of volume from the bulk zone. Compared to wisps, flotsam associated volume fraction errors are large and directly visible. Such artifacts usually appear when the bulk region becomes increasingly thin or spiky.

Artificial *interface deformation* can deteriorate the preservation of a physically consistent motion. Limitations are mainly related to the basic properties of the method, e.g. piecewise linear interface reconstruction including flux polyhedron construction by face velocities. For instance, sharp edges of the interface are always rounded off. In this work, flame-to-flow coupling (discussed in sec. 3.5.4) is rather critical in terms of front stability.

Monitoring of global *volume conservation* is also popular to assess the quality of VoF methods. Accuracy strongly depends on the imposed tolerances for identification of front cells, iterative interface positioning and overshoot/undershoot redistribution. For combustion simulations, global volume conservation is less important as compared to non-reactive two-phase flows.

3.4.5.2 Countermeasures

In order to counteract the presence of overshoots and undershoots, a local redistribution algorithm (schematic in fig. 3.8) is executed after each advection step. Redistribution of the overshooting/undershooting amount to surrounding cells definitely improves global volume conservation. In contrast, stringent clipping results in the ongoing loss of overshooting/undershooting volume. Considering the mechanism of wisp generation, cells with too high and too low values usually lie right next to each other. Moreover, a stabilizing effect on reactive interface propagation has been observed in this study. The algorithm applied here is inspired by the work of Harvie and Fletcher [99] but involves modifications with respect to several key aspects.

First of all, violation of global boundedness is checked by the volume fraction's extreme values in the field. To avoid execution for a large number of cells with extremely small deviations from correct threshold values, a redistribution tolerance of $\epsilon_{re} = \epsilon_{it} \cdot 10^{-3}$ (i.e. sufficiently below the iterative tolerance ϵ_{it}) is introduced. Only if global boundedness is violated, a loop over all cells is started. As soon as a violating cell is found, a search for the minimum/maximum of the surrounding cells is initiated. Only face neighbors are taken into account. Extending the stencil for point neighbors did not improve the results decisively. After successful search, the overshooting/undershooting amount is transferred to the corresponding neighbor cell. Generation of new overshoots/undershoots is prohibited by the scheme.

Compared to the original algorithm of Harvie and Fletcher [99], inner as well as outer iteration loops (until all overshoots/undershoots are conservatively distributed) are removed.

Small boundedness and thus volume conservation errors are accepted in favor of computational efficiency. Overall results are yet similar. Second, partner cells for the exchange of volume fraction are selected by a different criterion. In the modified algorithm, the exceeding amount of overshoots is moved to the minimum neighbor cell instead of the maximum neighbor cell. The approach holds for undershoots in an analogous manner. In terms of flame front stability, this alternative criterion showed superior performance. Unlike in the original algorithm, overshoots and undershoots remaining after the redistribution procedure are finally clipped. Sometimes, when no partner cell can be found for the exchange of volume fraction, this rigorous measure is inevitable. Flame-to-flow coupling ($\alpha \rightarrow c$, cf. sec. 3.5.4) for out-of-bound values is not defined.

An issue arises when material is transferred between cells of different size. According to its nature, adaptive mesh refinement produces cells of largely varying size. Due to the combustion source term, most overshoots occur at the flame front. The problem is therefore avoided by assuring uniform refinement in the vicinity of the interface, cf. refinement criterion 3.131. Anyway, the issue can be fixed by scaling the transferred amount with the volume ratio of both cells.

Mainly to remove wisps, further measures are taken. Correct bulk values are ensured by the following expression: $\alpha = 1$ is enforced if

$$\left| \left(\frac{\partial \alpha}{\partial x_j} \right)^{\mathrm{NAG}} \right| < 0.01 \cdot \max_{\Omega} \left[\left| \left(\frac{\partial \alpha}{\partial x_j} \right)^{\mathrm{NAG}} \right| \right] \ \wedge \ \alpha > 0.5 \tag{3.83}$$

and $\alpha = 0$ is enforced if

$$\left| \left(\frac{\partial \alpha}{\partial x_j} \right)^{\mathrm{NAG}} \right| < 0.01 \cdot \max_{\Omega} \left[\left| \left(\frac{\partial \alpha}{\partial x_j} \right)^{\mathrm{NAG}} \right| \right] \ \wedge \ \alpha < 0.5 \ \wedge \ \tau < 0.99. \tag{3.84}$$

The first term of condition 3.83 generally identifies bulk regions (α-gradient less than one percent of the domain maximum). The second term ($\alpha > 0.5$) is only true in the burned part of the domain. Condition 3.84 is constructed analogously with the second term being only true in the unburned part of the domain. To preserve auto-ignition kernels ahead of the main flame, the third requirement in terms of the auto-ignition precursor τ is additionally included on this side of the interface. Since volume fraction deviations due to wisps are rather small (before being amplified over time), volume conservation is not affected significantly by this correction.

3.4.6 Fundamental test cases

Despite the many potential error sources, the overall performance of the geometrical VoF method can still be much better than for algebraic calculation of face fluxes as the subsequent generic examples demonstrate. The price has to be paid by increasing computational cost. Concerning the first two cases (sec. 3.4.6.1 and sec. 3.4.6.2) without coupling to a flow solver, the VoF simulation is significantly more expensive. However, the relative cost increase is considerably less relevant when coupled to the full set of flow equations (sec. 3.4.6.3).

In one dimension, almost perfect advection of a rectangular profile can be achieved by the VoF technique. Dissipation-free propagation with algebraic flux calculation is practically
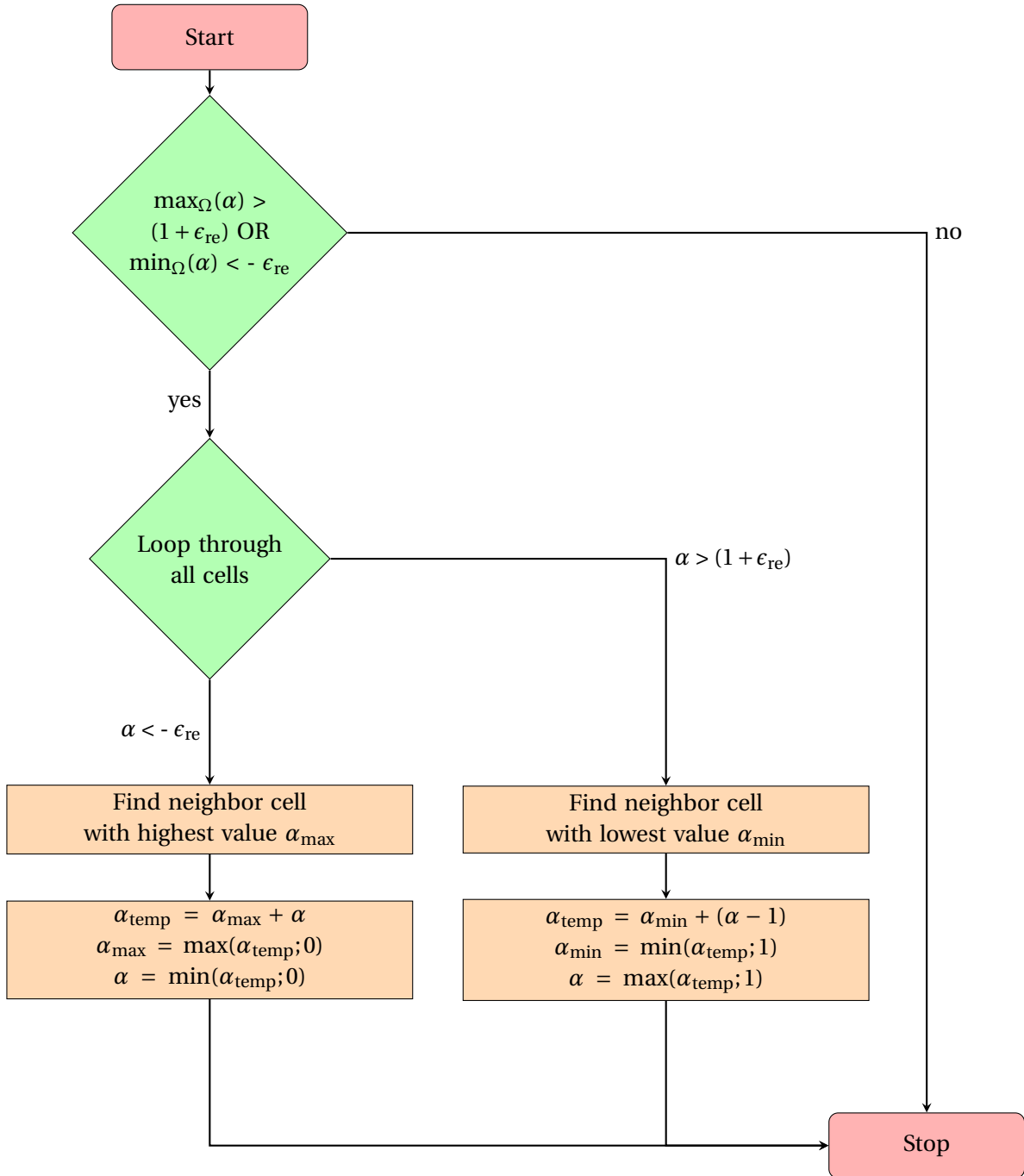
Figure 3.8: Schematic of the modified redistribution algorithm

impossible, even with the newest-generation high-order schemes. The following multi-dimensional cases are more challenging than one-dimensional problems, and designed to reveal benefits and drawbacks of the geometrical VoF method.

To assess the unaltered output of the finite volume solver, cell mean values are directly visualized in the subsequent contour plots. The common interpolation in the post-processing step to obtain smooth fields is intentionally deactivated.

3.4.6.1 Non-reactive rotating cross

The first example (fig. 3.9) comprises the two-dimensional evolution of a sharp initial profile in a constant velocity field given by the stream function

$$\Phi = -\frac{\omega}{2}\left((y - y_0)^2 + (x - x_0)^2\right).\tag{3.85}$$

The velocity components, describing divergence-free rigid body rotation in clockwise direction, can be derived:

$$u_j(x_j) = \begin{pmatrix} \frac{\partial \Phi}{\partial y} \\ -\frac{\partial \Phi}{\partial x} \end{pmatrix} = \begin{pmatrix} \omega \cdot (y - y_0) \\ -\omega \cdot (x - x_0) \end{pmatrix}\tag{3.86}$$

with $(x_0 = 0, y_0 = 0)$ being the rotation axis and $\omega = 2\pi/\text{s}$ representing the angular velocity. The analytical solution at $t = 1.0$ s, i.e. after one revolution, is equal to the initial condition. Concerning the volume fraction initial condition, the length of the red cross in one dimension is 0.3 m. The rectangular domain $\Omega = [-0.5 \text{ m}, 0.5 \text{ m}] \times [-0.5 \text{ m}, 0.5 \text{ m}]$ is uniformly discretized by 100×100 square cells. Hence, interface propagation is generally not aligned with mesh lines, making the problem more challenging than steady one-dimensional propagation. A constant time step of $\Delta t = 0.001$ s fulfills the CFL condition, even with level 1 adaptive mesh refinement. The same test case was investigated by Kirmeß [138] to evaluate his front tracking scheme.

Pictures 2 to 7 of fig. 3.9 depict the VoF solution at six points in time. The interface remains sharp, i.e. thickness of the transition region does not grow larger than one cell. The congruent cross position at the beginning and after one revolution means that no noticeable dispersive error occurs. Being a known drawback of all VoF schemes based on piecewise linear interface calculation, sharp corners are slightly rounded off. Compared to the work of Kirmeß [138], results are still superior.

In the last row of fig. 3.9, the geometrical VoF method is opposed to algebraic face flux calculation. Representing popular standard schemes in OpenFOAM, a first-order upwind and a second-order Total Variation Diminishing (TVD) central scheme are used for comparison. Significantly higher numerical dissipation can be observed in both cases. Cells containing material are spread over a wide range. Especially the upwind scheme is known for its robustness but strong dissipative behavior. The limited central scheme suffers to a lesser extent from numerical dissipation but is still clearly inferior to the geometrical VoF scheme. Other TVD schemes (e.g. applying van Leer's limiter [161]) produce similar results. Identification of the cross geometry is hardly possible for the central scheme and completely impossible for the upwind scheme. For both schemes, no correct bulk values are preserved. The last picture in fig. 3.9 reveals the dissipative error which scales with the local velocity magnitude. The solution deteriorates with increasing distance from the

(a) Velocity field   (b) $t = 0.0$ s; geom. VoF   (c) $t = 0.2$ s; geom. VoF

(d) $t = 0.4$ s; geom. VoF   (e) $t = 0.6$ s; geom. VoF   (f) $t = 0.8$ s; geom. VoF

(g) $t = 1.0$ s; geom. VoF   (h) $t = 1.0$ s; upwind scheme   (i) $t = 1.0$ s; central scheme
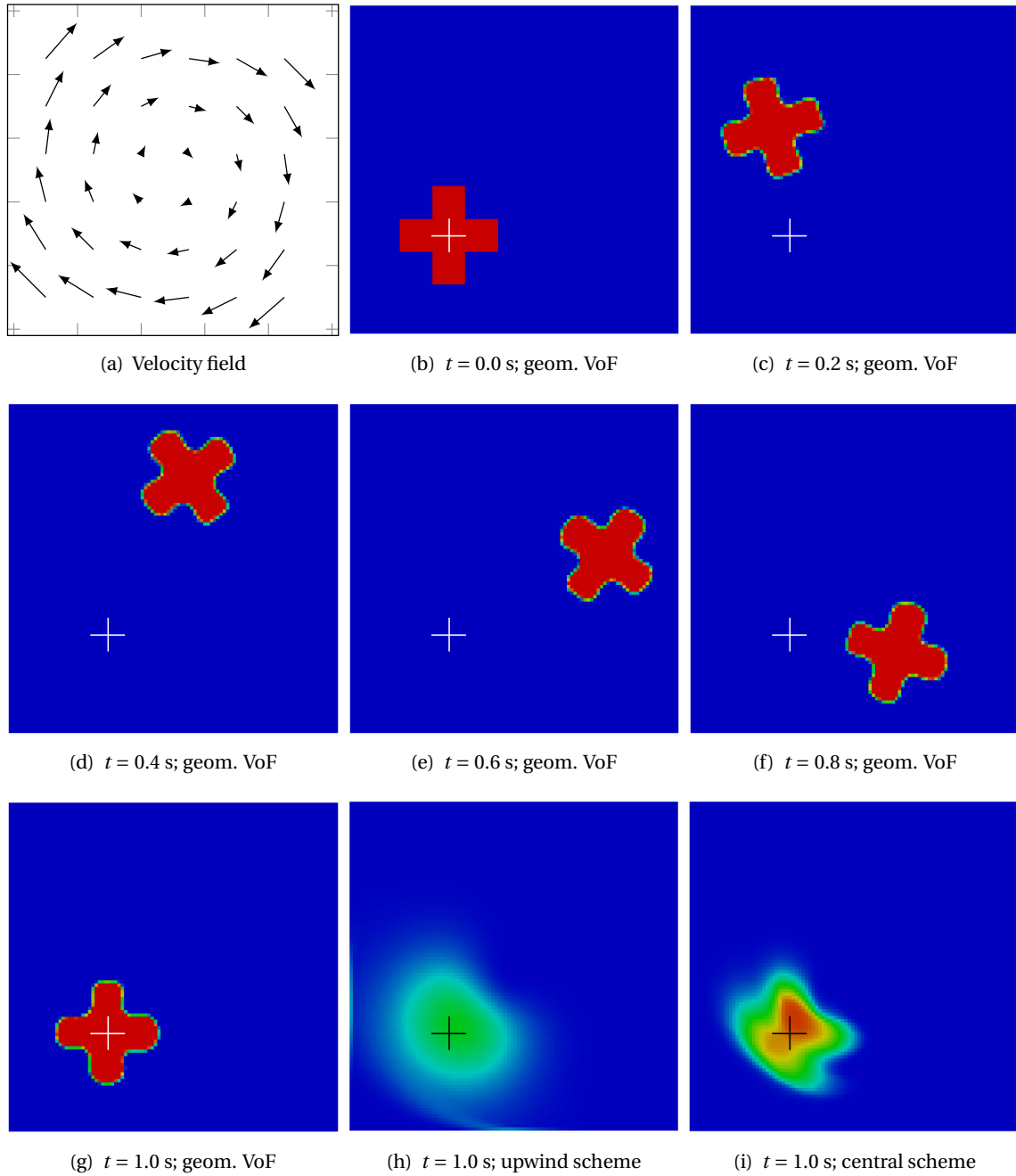
Figure 3.9: Non-reactive rotating cross example: Velocity field including magnitude-scaled arrows; Volume fraction at different points in time and by using different discretization schemes; Rainbow color scale (appendix A) from $\alpha = 0$ to $\alpha = 1$

rotation axis. Algebraic face flux calculation is eventually not an adequate approach to advect discontinuous solutions.

It should be mentioned that OpenFOAM two-phase flow solvers offer the possibility to artificially compress the interface in an algebraic VoF context [269]. Basically by adding negative diffusion, smearing of the interface can indeed be minimized. Since artificial numerical dissipation is antagonized by artificial negative diffusion, a justification problem does not arise. However, results cannot compete with the geometrical VoF method in terms of a physically consistent motion, especially in multi-dimensional simulations when the propagation direction is not aligned with mesh lines. The cross geometry was not preserved in the corresponding simulations (not shown here). Additionally, depending on the choice of the compression weighting factor which has to be specified a priori, over- and undershoots can occur. Necessary clipping violates global volume conservation. One of the main advantages of algebraic methods is therefore lost.

Further improvement can be achieved by combining front tracking with adaptive mesh refinement (sec. 3.6). In this case, mesh refinement in the vicinity of the interface is controlled by the volume fraction gradient field, i.e. the first part of inequality 3.131. Within the general limitations, fig. 3.10 proves excellent preservation of the cross shape after one revolution. Obviously, the combination of both techniques works as intended.

The computational effort of the VoF technique primarily scales with the number of iterations required to meet the iterative tolerance ϵ_{it} within the reconstruction step (sec. 3.4.3). Necessary geometrical operations have to be repeated for each iteration. On its right-hand side, fig. 3.10 shows the iteration counter in the so-called front cells satisfying the identification tolerance ϵ_{id}. Besides ϵ_{it}, the number of iterations also depends on the volume fraction in the considered cell. The highest number of iterations is required if α is close to zero or unity in front cells. In the presented simulation, the maximum of 13 is considerably greater than the average iteration count of 5.4.
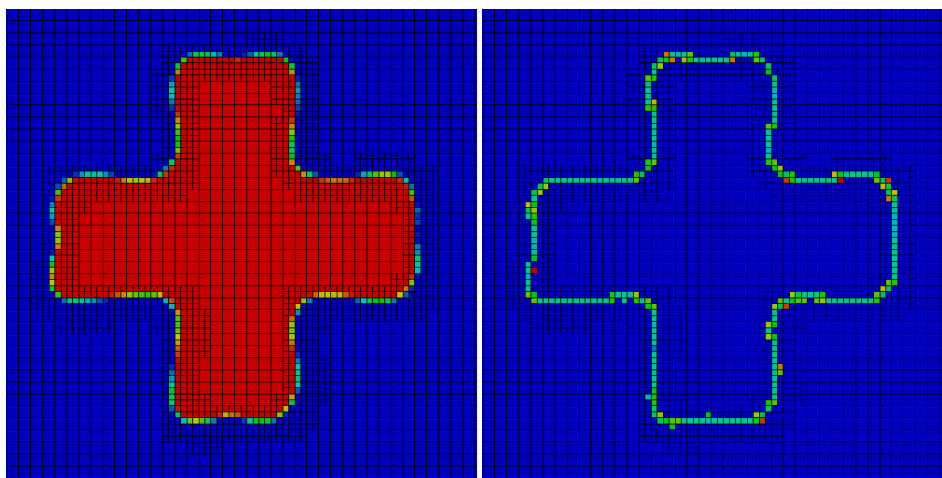
(a) Volume fraction; Scale from 0 to 1 (b) Iteration counter; Scale from 0 to 13

Figure 3.10: Non-reactive rotating cross example: Front tracking combined with level 1 adaptive mesh refinement; Magnified solution and mesh lines at $t = 1.0$ s; Rainbow color scale according to appendix A

Further well-established VoF test cases (Zalesak's slotted disk [288], three-dimensional deformation test [162], vortex in a box in two and three dimensions [21]) were investigated by Ketterl [135]. He concluded that the implemented VoF algorithm is capable of competing with recent approaches in literature in terms of volume conservation and preservation of a physically consistent motion.

3.4.6.2 Reactive rotating circle

To validate the proper integration of the combustion source term in the volume fraction evolution equation, another test is performed. Both advection and simultaneous reaction is taken into account. The setup (mesh, solver settings, velocity field etc.) is the same as before with the exception of the volume fraction initial condition. Here, the cross is replaced by a circle of diameter $d_0 = 0.1$ m. Its center is initially placed at ($x = -0.15$ m, $y = -0.15$ m).

According to the constant burning velocity of $S_{\text{eff}} = 0.1$ m/s, the diameter of the circle should grow by $\Delta d = 2\,\Delta r = 2\,S_{\text{eff}}\,\Delta t = 2 \cdot 0.1$ m/s $\cdot 1.0$ s $= 0.2$ m until the simulation ends at $t = 1.0$ s. Figure 3.11 shows the expected behavior with an end diameter of $d_0 + \Delta d = 0.3$ m. Second, the circle's center correctly arrives at the initial position after one revolution in clockwise direction. Spurious preferred propagation orthogonal to mesh lines does not appear. Both influences, advection and reaction, are well reflected.

Quantitative analysis of the volume (actually area in this two-dimensional example) conservation properties is provided in fig. 3.12.

$$A(t) = \left(\frac{d_0}{2} + S_{\text{eff}}\,t\right)^2 \pi \tag{3.87}$$

states the time-dependent analytical solution in terms of circle area $A(t)$. The corresponding relative error is given by

$$E(t) = \frac{A_{\text{analytical}} - A_{\text{simulation}}}{A_{\text{analytical}}} = \frac{A(t) - \sum_i V_i \alpha_i(t)}{A(t)} \tag{3.88}$$

with the cell volume V_i, and index i running over all cells in the whole domain Ω. In general, the quadratic dependence of A is well reproduced by the simulation. However, E reveals overestimation of A at the beginning which is due to the inaccurate discrete representation of the initial condition, cf. fig. 3.11 (a). Later, the simulation tends to underestimate A and the relative error seems to saturate around $+1\%$ – an acceptable level. Results are even better in cases without source term. Error levels on unstructured meshes are generally higher [118, 135].

3.4.6.3 Merging detonation kernels

In this last example, integration of the geometrical VoF method for flame propagation into the full set of flow equations is tested. Coupling is achieved via the reaction progress variable c, being directly related to the solved-for volume fraction α (cf. sec. 3.5.4). In a first approximation, c and α can be assumed to be identical. Contrary to the first two examples, the velocity field now is self-induced and not divergence-free. Thus, the divergence correction of the α evolution equation 3.74 comes into effect.

(a) $t = 0.0$ s   (b) $t = 0.2$ s   (c) $t = 0.4$ s

(d) $t = 0.6$ s   (e) $t = 0.8$ s   (f) $t = 1.0$ s
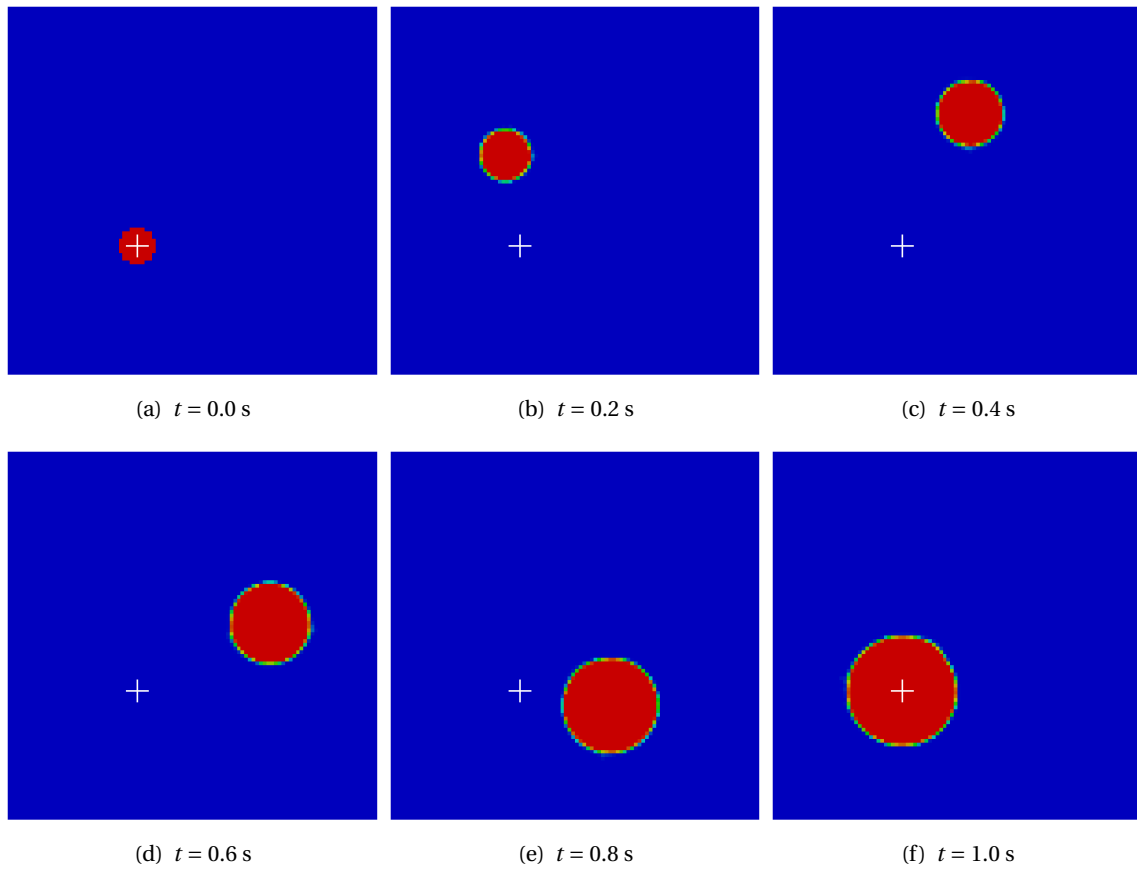
Figure 3.11: Reactive rotating circle example: Volume fraction at different points in time; Rainbow color scale (appendix A) from $\alpha = 0$ to $\alpha = 1$
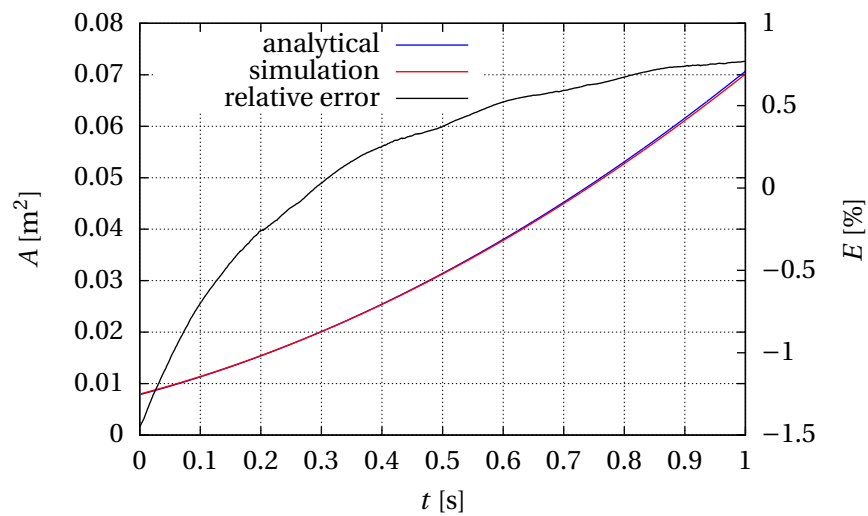
Figure 3.12: Rotating reactive circle example: Temporal evolution of circle area A and relative error E

Being one of the main differences to most geometrical VoF methods reported in literature, the implemented algorithm is able to handle arbitrary unstructured meshes. To demonstrate this capability, an irregular mesh consisting of 9,768 triangular cells is used here (fig. 3.13). The resolution is similar to 10,000 cells of the aforementioned structured meshes. Superior mesh flexibility has to be paid by a more complex and costly algorithm. The fastest geometrical VoF methods require no inner iterations, but are often limited to orthogonal structured meshes and therefore not fully compatible with the mesh handling paradigm of OpenFOAM.

The initially quiescent mixture consists of 20 % of hydrogen in air. The centers of two separated circular ignition kernels (initial radius $r_0 = 0.1$ m; $\alpha = 1$) are specified as ($x = -r_0, y = -r_0$) and ($x = r_0, y = r_0$), respectively. Pressure and temperature in the ignition regions are set to the corresponding Chapman-Jouguet values of the mixture. In the rest of the domain, $T = 293$ K, $p = 1.013$ bar and $\alpha = 0$ is prescribed.

This setup has been chosen because front tracking schemes are susceptible to front merging failures. Detailed reproduction of detonation properties is not the purpose of this under-resolved test case. Similar cases were investigated by Schneider [233] and Smiljanovski et al. [242]. For example in [233], inability of their scheme to reproduce reactive front merging is reported. Figure 3.13 visualizes the sequence over six points in time. Shortly after $t = 40$ μs, the originally separated detonation kernels start to merge. Apparently, the coalescence of the detonation fronts works well with the proposed VoF scheme. No artificial constriction in the merging zone (bisecting line) occurs.

In the last row of fig. 3.13, the corresponding volume fraction (i.e. reaction progress), temperature and pressure fields are shown at $t = 100$ μs. The comparison is supposed to highlight the strong flame-flow coupling. Other thermodynamic quantities like temperature and pressure directly follow the front shape that is governed by the VoF evolution equation. Hence, it makes sense to assign a higher computational effort to the accurate solution of the behavior-dominating equation. Besides, even for a numerically suboptimal triangular mesh, the behavior is robust.

(a) Triangular mesh (b) $t = 0$ μs; Scale from $\alpha = 0$ to $\alpha = 1$ (c) $t = 20$ μs

(d) $t = 40$ μs (e) $t = 60$ μs (f) $t = 80$ μs

(g) $t = 100$ μs (h) $t = 100$ μs; Temperature scale from 293 K to 3000 K (i) $t = 100$ μs; Pressure scale from 1 bar to 25 bar
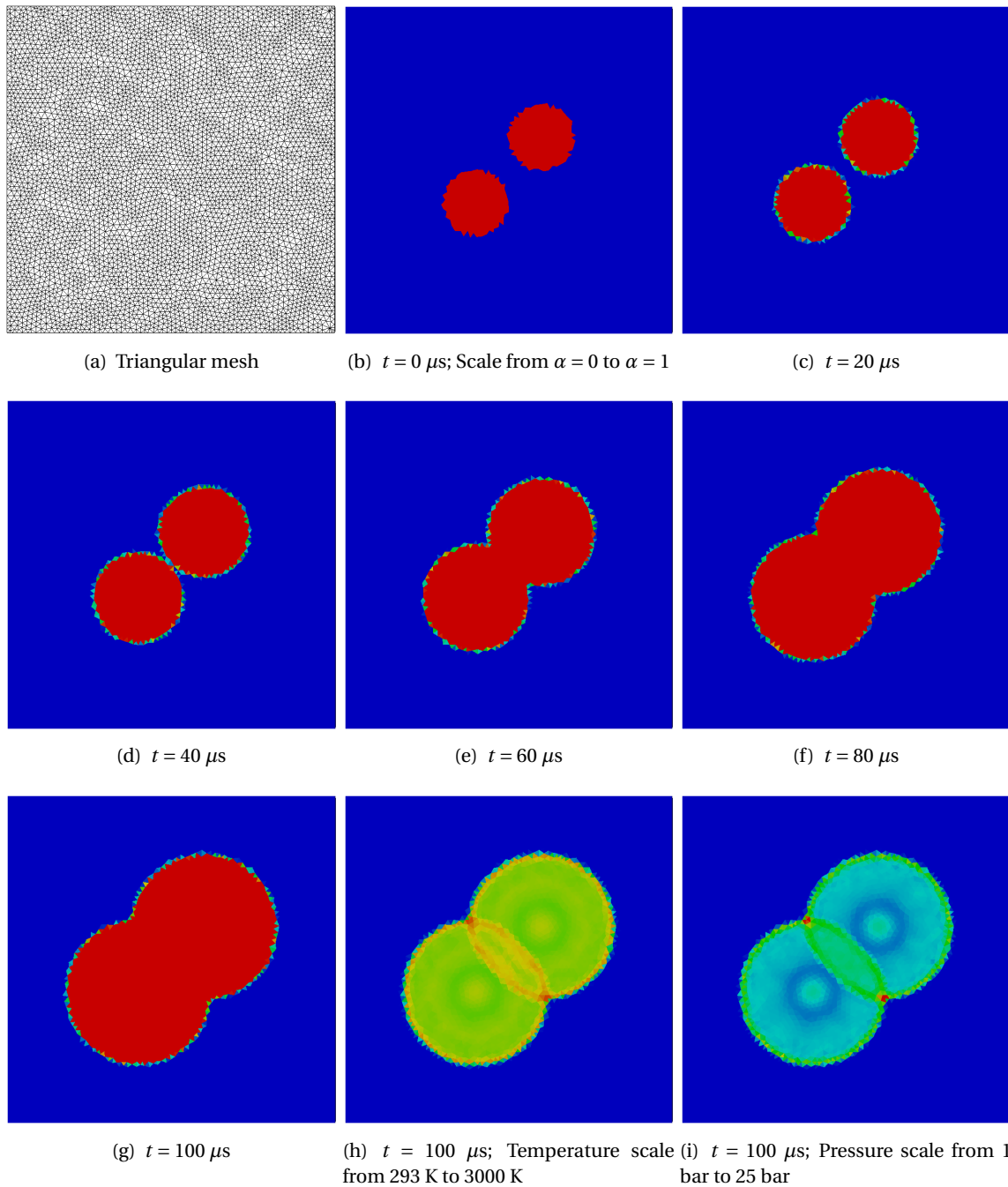
Figure 3.13: Merging detonation kernels example: Unstructured mesh, volume fraction, temperature and pressure at different points in time; Rainbow color scale according to appendix A

3.5   Combustion model

3.5.1   Motivation

Following the *hybrid flame-tracking shock-capturing* concept as introduced in sec. 3.4, the flame (or reactive discontinuity) is explicitly tracked by a geometrical Volume-of-Fluid method. In accordance with the URANS framework, the term *flame* is here used to describe the mean position of the generally turbulent flame brush. A more precise definition in terms of the ensemble-averaged reaction progress variable $\overline{c}$ is given in sec. 3.5.4.

Justification of this hybrid approach is based on two observations: First, the equation describing the kinematics of unsteady flame propagation shows the strongest grid dependency of all the transport equations. As can be seen for example in one of the generic cases (merging of two initially separated detonation fronts in fig. 3.13), strong coupling exists between the flame and other flow properties, especially temperature and density. Hence, it makes sense to devote additional computational resources to accurate flame propagation (sec. 3.5.3). Quasi complete removal (to the prescribed tolerance) of numerical dissipation and therefore a massive reduction of grid sensitivity is demonstrated by the test cases in sec. 3.4.6.

Second, the tracking scheme prevents artificial thickening of the turbulent flame brush. The gradient closure of the flamelet source term (eq. 3.90) does indeed make the reaction rate integral independent of the flame brush width [62, 79], but it does not avoid unnatural thickening of the flame brush. Whereas this problem does not excessively occur for globally steady combustion (like in stationary burners), it leads to delayed energy release, extenuated thermal expansion and ultimately weaker flame acceleration for globally unsteady combustion (like explosions). Consider the following situation: Reaction progress decreases and consequently density increases linearly within the flame brush. To fulfill the principle of mass conservation and the zero velocity boundary condition behind the flame, flow velocity in the fixed Eulerian frame has to increase linearly, see one-dimensional gas dynamics theory in sec. 2.1. Accordingly, the tip of the flame brush is advected at a higher velocity than the tail which is at rest. If not counteracted e.g. by special discretization of the source term, the effect amplifies over time. In contrast to this problem adherent to flame-capturing, flame-tracking strictly preserves the discontinuous character of the flame independent of mesh resolution.

3.5.2   Model classification

The problem of turbulent combustion modeling is two-fold: One challenge is the complexity of chemical kinetics. But at least for hydrogen-oxygen chemistry, this issue may be overcome by the application of one of the numerous simplified reaction schemes. And even more serious is the fact that ensemble-averaged reaction rates cannot simply be calculated from averaged flow quantities. Neglecting turbulent fluctuations, particularly of temperature, has a significant impact on the evaluation of generally non-linear reaction rate expressions, e.g. of the Arrhenius type. This has led to the development of a large variety of modeling approaches which shall briefly be summarized.

The following classification is essentially an extension of the categories in [215]. On the highest level, so-called flame-capturing and flame-tracking models are distinguished. The first kind is based on conservation equations valid in the whole domain. Distributed over several cells, the propagated interface is implicitly represented in a diffuse manner. The second kind explicitly calculates interface topology and its propagation, resulting in a sharp interface representation (transition between bulk states within one cell layer) over the whole simulation. *Flame-capturing* models can be based on a description of

- *mixing intensity*: For the classical Eddy-Break-Up (EBU) [244] and Eddy-Dissipation Model (EDM) [174], the authors assume that chemistry is fast and the burning rate is controlled by small-scale turbulent mixing with a characteristic time scale related to the turbulent dissipation scale. In the context of premixed combustion, turbulent mixing refers to cold reactants and hot products, not fuel and oxidizer. It is generally known that combustion models utilizing the EBU proportionality fail to reproduce even the qualitative behavior of flames near walls, in complex flow fields and in large geometries [274]. Approaching a wall, the expression ε/k leads to increasing reaction rates towards infinity which contradicts physical reality. Furthermore, quenching effects (at high turbulence intensities) are not included by nature and quantitative agreement with experiments can usually not be achieved without tuning of the model coefficients. Considering also chemical limitation, the newer Eddy-Dissipation Concept (EDC) [175] is an extension aiming at a wider applicability. Similar assumptions and limitations underly the popular models of Schmid et al. [230] and Bray-Moss-Libby (BML) [37]. The Partially-Stirred-Reactor (PaSR) model [94] is another example in which turbulent and chemical scales are compared. As soon as chemical scales are calculated by a detailed reaction scheme, computational costs rise drastically.

- *turbulent burning velocity*: Such approaches are called Turbulent Flame-speed Closure (TFC) or sometimes Burning Velocity Model (BVM), shifting the modeling effort from the averaged source term to the turbulent burning velocity. Corresponding models are partly based on theoretical considerations and partly on empirical data. One advantage is the gradient formulation of the source term which makes the integral burning rate independent of the reaction zone width [62]. Comparably low grid dependency (in terms of unsteady flame propagation) is due to the fact that the burning velocity is rather imposed than intrinsically calculated. Representatives of this category are, for instance, the models of Zimont and Lipatnikov [295], Peters [206] and Dinkelacker et al. [63].

- *flame surface density*: This kind of models share the thin flame assumption, meaning that mainly the altered flame surface area is responsible for changes of consumption rate. Besides algebraic closure, an additional evolution equation might be solved for the Flame Surface Density (FSD) [49, 256] to allow for the fact that the area is influenced not only by the local turbulence field but also by the flame itself and by non-local effects. By transporting a closely related quantity, namely the flame wrinkling factor, the model of Weller et al. [276] features similar properties.

- *statistical effects of turbulence*: A mathematically elegant way to describe the statistical effect of turbulent fluctuations is via Probability Density Functions (PDF). Early work demonstrating their application to turbulent combustion is available e.g. from Pope [211]. The PDF represents the probability that a fluctuating quantity takes a

certain value. Averaged reaction rates can consequently be obtained by integration over the PDFs of relevant quantities like temperature. In principle, all regimes of turbulence-chemistry interaction can be characterized by a different shape of the PDF. Determination of PDFs from transport equations is possible but uncommon in computational practice due to enormous costs. Instead, the shape of PDFs is presumed and the result of PDF integration is provided to the solver in the form of look-up tables. Efficiency can further be improved by state-space reduction methods known as Intrinsic Low-Dimensional Manifolds (ILDM) [173]. Besides comparably high computational costs, another drawback is the inability of established PDF approaches to represent discontinuous changes of state as for non-isobaric explosive combustion [79].

In addition to the family of flame-capturing models, *flame-tracking* methods coexist. Besides being applied to combustion waves (reactive discontinuities), explicit tracking of shock waves (gas-dynamic discontinuities) has successfully been realized according to literature [4]. Treating the flame as a reactive discontinuity does not necessarily imply combustion in the thin flame regime. It is the mean position of a generally turbulent flame brush that is advected by the tracking algorithm. The structure of the flame is rather reflected by the source term. Smiljanovski et al. [242] and Schmidt and Klein [231] use a level-set technique (cf. sec. 3.4.2) to describe the unsteady propagation of deflagration discontinuities. Flame-to-flow coupling is enforced by invoking the Rankine-Hugoniot equations which connect the burned and unburned state in computational cells intersected by the front. Note that the Volume-of-Fluid (sec. 3.4) based algorithm in this work avoids the costly iterative solution of jump conditions at the front.

None of the models is ideally suited for all kinds of combustion regimes that are relevant to explosive combustion. To combine their advantages, the hybrid method proposed in this thesis resembles elements from different categories. Offering the best chance of grid-independency, the flame is explicitly tracked. The evaluation of numerically stiff (Arrhenius) source terms is avoided by using a TFC-like closure of the flamelet source term. Similar to flame surface density models, dynamic and non-local effects of turbulence-chemistry interaction are included by solving an additional flame wrinkling evolution equation. To summarize, the proposed method is fairly efficient and shows robust behavior in terms of scale invariance which is important for engineering-type simulations. Since chemical reaction is not directly solved, the effects of pressure, temperature, composition, turbulence etc. need to be modeled explicitly as shown in the next few sections. There are indeed combustion models that are more advanced from a theoretical point of view (e.g. ILDM with PDF integration), but might perform worse in practice when a large share of the underlying physics is not resolved. Implementation of new sub-models must be done with great care and step-by-step validation.

3.5.3 Flame propagation

The combustion model consists of two parts which are coupled on the basis of the flame-describing quantity α. On the one hand, a flame wrinkling model accounts for flamelet-like reaction (subscript fl) and on the other hand, a two-step model accounts for volumetric reaction (subscript vol) including auto-ignition.

Unlike the standard procedure to solve a compressible transport equation for $\rho\alpha$, the flame is explicitly tracked in this work. The reasons are explained in sec. 3.4 (general advantages in terms of interface propagation) and sec. 3.5.1 (specific motivation in the context of unsteady combustion). Flame propagation is consequently governed by the inhomogeneous advection equation

$$\frac{\partial \alpha}{\partial t} + u_j \frac{\partial \alpha}{\partial x_j} = \max\left(\omega_{\mathrm{fl}}; \omega_{\mathrm{vol}}\right), \tag{3.89}$$

which is equally used in the ensemble-averaged sense, i.e. $\overline{\alpha} = \alpha$. Application of the averaging operator to eq. 3.89 basically introduces an additional unclosed term originating from the convective term. Modeling of this fluctuation term by an eddy viscosity scaled gradient ansatz, similar to eq. 3.31, had a negligible influence on the results and is therefore neglected. It is known that the standard gradient closure does not reproduce well the observed effect of counter-gradient transport in turbulent premixed flames [92]. Anyway, such closure introduces a diffusive term which contradicts the discontinuous character of the interface to some extent. More sophisticated turbulence closure models in the Volume-of-Fluid context are still a matter of ongoing research [238, 264]. Discretization of eq. 3.89, especially including the VoF tracking technique, is shown in sec. 3.4.4.

The coupling of both source terms ω_{fl} and ω_{vol} by the maximum function is inspired by another DDT simulation method in [88]. During the initial stage of flame propagation, from low to moderate turbulence intensities, the flamelet assumption is well justified. Compared to the time scales of turbulence, chemical kinetics is clearly faster and thus not the limiting factor. In the course of the explosion process, the interaction of the flame with turbulent eddies intensifies, causing a vertical shift in the Borghi diagram 2.3 towards higher turbulence intensities and turbulent Karlovitz numbers above unity. Though not reflected by the Borghi diagram, also flame instabilities (sec. 2.3.2) and auto-ignition effects play an important role during the later stage of flame acceleration [53, 236]. Beyond the flamelet regime, the concept of a flame surface is not valid anymore. The character of the reaction zone becomes more distributed with local conditions similar to a (perfectly) stirred reactor. Latter is the only regime in which it is justified to calculate non-linear (Arrhenius) reaction rates by cell mean values. Under such well-mixed conditions, the reaction rate is limited by chemical kinetics and it is more appropriate to speak of volumetric reaction.

The first source term

$$\omega_{\mathrm{fl}} = \underbrace{\frac{\rho_u}{\rho} G \Xi S_L}_{S_{\mathrm{eff}}} \left| \frac{\partial \alpha}{\partial x_j} \right| \tag{3.90}$$

incorporates flamelet-like combustion. As demonstrated by eqs. 3.71 and 3.72, S_{eff} is equivalent to an additional propagation velocity normal to the flame's surface. In contrast, volumetric reaction cannot easily be formulated as an additional dilatational component of flame propagation. Integration of the second source term ω_{vol} is separately discussed in sec. 3.5.6. The quenching factor G and flame wrinkling factor Ξ are introduced in sec. 3.5.5.3 and sec. 3.5.5.1, respectively.

Calculation of the stoichiometry, temperature- and pressure-dependent unstretched laminar burning velocity with respect to the unburned gas [259]

$$S_L = S_{L,\mathrm{ref}} \left(\frac{T_u}{T_{\mathrm{ref}}}\right)^{1.75} \left(\frac{p}{p_{\mathrm{ref}}}\right)^{-0.2} \tag{3.91}$$

is based on a solely stoichiometry-dependent expression of the unstretched laminar burning velocity at standard conditions ($T_{\text{ref}} = 298$ K, $p_{\text{ref}} = 1.013$ bar):

$$S_{L,\text{ref}} = \begin{cases} \left(A_1\, X_{H_2}^4 + A_2\, X_{H_2}^3 + A_3\, X_{H_2}^2 + A_4\, X_{H_2} + A_5 \right) \text{m/s if } X_{H_2} \leq 0.35 \\ \left(B_1\, X_{H_2}^4 + B_2\, X_{H_2}^3 + B_3\, X_{H_2}^2 + B_4\, X_{H_2} + B_5 \right) \text{m/s if } X_{H_2} > 0.35 \end{cases} \tag{3.92}$$

Ettner [79] derived eq. 3.92 through a sectioned polynomial fit of experimental data compiled by Konnov [144]. The corresponding coefficients A_i and B_i are summarized in tab. 3.2. Flame stretch effects [10, 157] were corrected for in the experimental data.

Table 3.2: Coefficients of Ettner's correlation 3.92

i	A_i	B_i
1	-488.9	-160.2
2	285.0	377.7
3	-21.92	-348.7
4	1.351	140.0
5	-0.040	-17.45

According to the exponents in eq. 3.91, the influence of temperature and pressure are antipodal. Figure 3.14 shows the profile of S_L as a function of the hydrogen mole fraction X_{H_2} at three different combinations of unburned gas temperature and pressure. Those elevated levels, compared to T_{ref} and p_{ref}, are identical to the initial conditions of the final full-scale reactor simulations (chap. 5). As can be seen, the temperature effect is stronger than the pressure effect for this particular choice. Maximum values of S_L are reached slightly on the fuel-rich side ($X_{H_2} \approx 42$ %) rather than at the stoichiometric point ($X_{H_2} \approx 29.5$ %).

Although it is not the purpose of burning velocity correlations, a robustness check in terms of flammability limits can be performed. Predicted limits on the rich and lean side agree well with empirically measured values in literature: Lower limit of 4.1 % for upward, 6.0 % for horizontal, 9.0 % for downward propagation and upper limit of 74 % [57]. Expression 3.92 does apparently not distinguish between different flame propagation directions but the correlation seems to be sufficiently conservative close to the lean limit. The decline of the curve towards the rich limit is more abruptly in experiments than predicted by the polynomial. In general, the correlation should not be used beyond the underlying experimental data base.

The density correction ρ_u/ρ in eq. 3.90 accounts for the variation of burning velocity normal to the flame surface because of thermal expansion. Fundamental combustion properties like S_L are usually referring to the precompressed but unreacted gas, i.e. $S_L = S_{L,u}$. Thanks to a mass balance over the flame, the corrected burning velocity in flame-containing cells can be written as

$$S_L^* = S_{L,u} \frac{\rho_u}{\rho}. \tag{3.93}$$
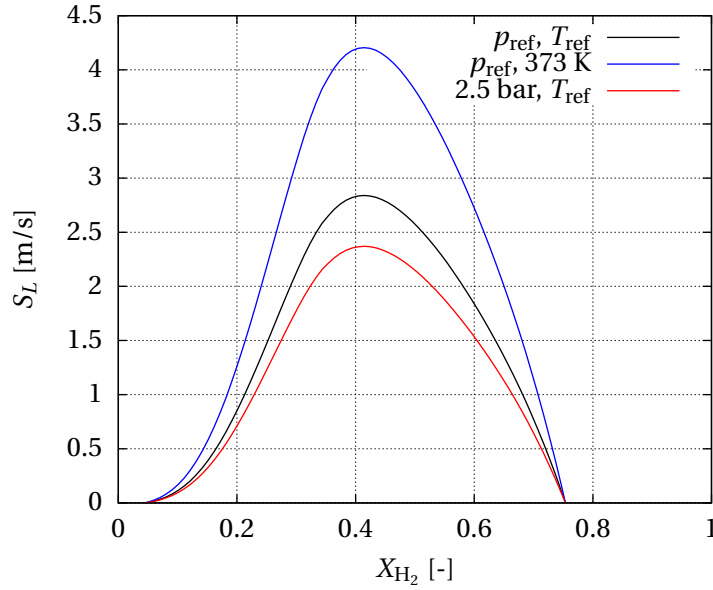
Figure 3.14: Laminar burning velocity S_L depending on mixture composition, temperature and pressure of the unburned gas

For that, the unburned density ρ_u is obtained from the isentropic relation

$$\rho_u = \rho_u^0 \left(\frac{p}{p^0} \right)^{\frac{1}{\kappa}} . \tag{3.94}$$

Superscript 0 denotes an arbitrary reference state (the initial condition in this case) and κ the isentropic coefficient, i.e. the ratio of specific heats. ρ_u^0 is prescribed as a fuel concentration dependent polynomial. Implicitly assumed isobaric combustion ($p_u = p$) is well justified in the deflagration but not in the detonation regime. However, no problem arises since latter regime is governed by the volumetric source term ω_{vol} which does not rely on unburned properties. Of course, the computation of intrinsic flow quantities (ρ, p, T etc.) is not affected by these simplifications. Accurate reproduction of gas-dynamic phenomena, especially non-isentropic shocks, is ensured by the Godunov-type flux calculation, cf. sec. 3.3.3.2.

In the same manner, the unburned temperature is given by

$$T_u = T_u^0 \left(\frac{p}{p^0} \right)^{\frac{\kappa - 1}{\kappa}} . \tag{3.95}$$

It is required in partly burned cells (ensemble-averaged context), e.g. for the temperature correction of the laminar burning velocity, eq. 3.91. In a macroscopic view of flamelet-like combustion without heat losses, only the unreacted gas state determines the net consumption rate over the flame. The unburned temperature at the reference state T_u^0 is assumed to be independent of mixture composition.

Apart from initial and boundary conditions, the model requires no case-specific tuning (particularly of the reaction rate) and is therefore valid for a wide range of different configurations. As shown later, it is also unnecessary to incorporate empirical combustion

regime transition criteria as e.g. in [190] where the likelihood of DDT is evaluated in terms of a parameter proportional to the spatial pressure gradient across the flame. Both is essential regarding the model's predictive capabilities for general large-scale accident scenarios. However, a number of modifications is obviously necessary for fuel-oxidizer mixtures other than hydrogen-air.

3.5.4 Flame-to-flow coupling

In terms of the reaction progress variable, or normalized product concentration, $c = 0$ identifies the pure reactant mixture and $c = 1$ the corresponding chemical equilibrium. Its averaged equivalent $\overline{c}$ is calculated from the transported field α by a weighted arithmetic average including the surrounding cells:

$$\overline{c} = \frac{1}{N_{\text{fn}}\, w + 1} \left(w \sum_{k=1}^{N_{\text{fn}}} \alpha_k + \alpha \right) \tag{3.96}$$

with N_{fn} being the number of direct face neighbors k and w the weighting coefficient. For this work, values up to $w = 0.25$ proved to be a good compromise between front stability and sharpness, i.e. the value of neighbor cells α_k is weighted only a fourth of the cell's own value α. Note that the transported field α is not directly affected by this operation. Decoupling of both quantities allows to control the flame structure without manipulating the actual transported field in a dissipative manner. In that sense, the method resembles elements from level-set techniques since the kinematics-determining field α is not directly describing flame-to-flow coupling.

In the ensemble-averaged framework, the non-bulk part of $\overline{c}$ can be interpreted as the turbulent flame brush. $\overline{c}$ then represents the probability of finding burned material within a computational cell at a specific point in time and space. The transported reactive discontinuity can thus be understood similar to the $\overline{c} = 0.5$ contour line. Depending on the value of w, thickness of the flame brush is distributed over more than one cell. The larger the cells get, the smaller w should be since the entire turbulent flame brush is eventually contained within one computational cell. $\overline{c} = \alpha$ appears as a special case when $w = 0$. However, slightly larger values than zero are generally recommended to prevent numerical instability of the advected front. The reason is connected to the effect of thermal expansion on the velocity field which itself is used to propagate the flame. If $w > 0$, the velocity field changes more gradually over the flame which improves front stability.

Equation 3.96 maintains a practically constant flame brush width throughout the simulation without progressive artificial thickening. Contrary to popular artificially thickened flame models in LES context (e.g. [78, 287]), an efficiency function [207] to correct for the falsified interaction with resolved turbulent eddies is not required since the entire turbulence spectrum remains unresolved in URANS context. Turbulence-chemistry interaction is modeled to its full extent, see sec. 3.5.5.

The averaging procedure is similar to some explicit LES filters [212] using a prescribed filter width larger than the cell size. A smooth representation of the transported interface is achieved by this means. A numerically robust blending between both extreme states ($\overline{c} = 0$ and $\overline{c} = 1$) might also be realized by means of a signed distance function. Testing of alternative flame-to-flow coupling methods could be an interesting future task.

As mentioned earlier, the composition of the unburned mixture (mass fraction $Y_{k,u}$ of all species k) can be determined from the hydrogen mixture fraction f_H (eq. 3.15) alone. Hence, the following relations are executed consecutively:

$$Y_{\mathrm{H_2},u} = f_H, \tag{3.97}$$

$$Y_{\mathrm{O_2},u} = 0.23295 \left(1 - f_H\right), \tag{3.98}$$

$$Y_{\mathrm{N_2},u} = 1 - Y_{\mathrm{H_2},u} - Y_{\mathrm{O_2},u}. \tag{3.99}$$

The mass-specific factor 0.23295 corresponds to a relative volumetric concentration of 21 % of oxygen in air. All other considered species $(\mathrm{H, OH, O, H_2O, HO_2, H_2O_2})$ are assumed to be zero in the entirely unburned part of the domain.

Once chemical reaction sets in, $Y_{\mathrm{H_2}} = f_H$ is not valid anymore and an additional dimension, namely the reaction progress c, is needed to describe the species composition in (partly) burned cells:

$$Y_k = (1 - c)\, Y_{k,u} + c\, Y_{k,b}. \tag{3.100}$$

A multi-dimensional look-up table provides the mass fraction $Y_{k,b}(f_H, p, T_u)$ of each of the pre-elected nine species at chemical equilibrium conditions. One has to be aware that the linear blending 3.100 is designed with respect to the ensemble-averaged framework. It does not reflect species distribution *within* the flame. If latter information is of interest (in highly resolved simulations), it would be necessary to extend the species look-up table by c as a fourth input dimension. Unlike for other combustion simulations, e.g. aiming at the prediction of pollutant emissions, the inner structure of the flame is of inferior importance. In the examined explosion context, only the correct rate of reactants to products conversion is essential. Inducing flow ahead of the flame, thermal expansion of the combustion products substantially contributes to the velocity of flame propagation. Computation of the chemical source term is also independent of species distribution within the flame, cf. sec. 3.5.3.

After evaluating eq. 3.100, resulting Y_k are finally inserted into the definition of the total internal energy 3.5 for iterative determination of the temperature and finally density.

3.5.5 Dynamic flame interaction

To account for the effect of turbulence-chemistry interaction, the flamelet source term 3.90 is usually closed by empirically tuned algebraic relations for the effective or turbulent burning velocity S_T (cf. TFC/BVM model category in sec. 3.5.2) – at least for large-scale applications. The approach in this work is unusual in the sense that an additional evolution equation is solved to close the source term. Nevertheless, a burning velocity correlation is still necessary to weight the equation's source and sink term.

As shown subsequently, the reaction rate is not only influenced by turbulence, but also by flame instabilities. From a macroscopic point of view, both effects alter the effective flame surface area.
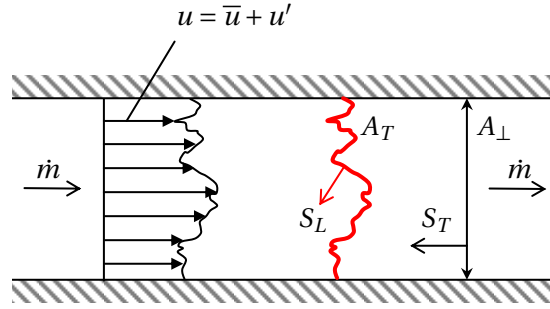
Figure 3.15: Topological interpretation of the turbulent burning velocity; Turbulent flame colored red; Adapted from [206]

3.5.5.1 Flame wrinkling

The topological interpretation of S_T is depicted in fig. 3.15. Continuity over the flame requires

$$\dot{m} = \rho_u S_L A_T = \rho_u S_T A_\perp = \text{const.} \tag{3.101}$$

where A_T is the instantaneous turbulent flame surface area and $A_\perp$ is the cross-sectional area. The density ρ_u cancels out because burning velocities S_L and S_T are both referring to the unburned mixture. The ratio of corresponding quantities,

$$\Xi = \frac{A_T}{A_\perp} = \frac{S_T}{S_L}, \tag{3.102}$$

is identified as the flame wrinkling factor and facilitates closure of the flamelet source term 3.90. Especially for large-scale and low to moderate intensity turbulence, the assumption of purely kinematic interaction between the wrinkled flame front and the turbulent flow is justified, cf. Borghi diagram 2.3.

In the context of ensemble-averaging, A_T denotes the average flame area per unit volume in the control volume and $A_\perp$ denotes the average flame area projected onto the mean propagation direction

$$n_j^c = -\frac{\dfrac{\partial \overline{c}}{\partial x_j}}{\left| \dfrac{\partial \overline{c}}{\partial x_m} \right|} \tag{3.103}$$

per unit volume in the control volume. In other words: The global topological interpretation is applied to each computational cell. Apart from pointing in the opposite direction, the definition of n_j^c is slightly different to the VoF normal n_j specified by eq. 3.55. Also, it has to be mentioned that identity 3.102 strictly only holds for unity Lewis number. An issue arising from non-unity Lewis numbers is discussed in the next section. Ξ is formally related to the better-known flame area density Σ by $\Sigma = \Xi |\nabla \overline{c}|$. Hence, one recognizes that the following model is conceptually similar to the widespread dynamic flame surface density models, with only a different quantity being transported.

Taking definition 3.102 as a basis, Weller [274] derived through conditional averaging the simplified evolution equation

$$\frac{\partial}{\partial t}\left(\overline{\rho}\Xi\right) + \frac{\partial}{\partial x_j}\left(\overline{\rho}\Xi\widetilde{u}_j\right) + \Psi_\Xi\frac{\partial\Xi}{\partial x_j} = \overline{\rho}\Xi G_\Xi - \overline{\rho}(\Xi-1)R_\Xi + \overline{\rho}\Xi\max(0;\sigma_s-\sigma_r) \qquad (3.104)$$

including a flame related Ξ flux

$$\Psi_\Xi = \left(\overline{\rho}_u S_L\Xi + \frac{\dfrac{\partial}{\partial x_j}\left(\overline{\rho}\,a_{\text{eff}}\dfrac{\partial\overline{c}}{\partial x_j}\right)}{\left|\dfrac{\partial\overline{c}}{\partial x_j}\right|} + \overline{\rho}S_L\left(\frac{1}{\Xi}-\Xi\right)\right)n_j^c. \qquad (3.105)$$

The transport equation is apparently not in standard form: Regarding the convection part, as well as diffusion which is absent.

To calculate the sub-grid turbulent generation and removal rates $G_\Xi\Xi$ and $R_\Xi(\Xi-1)$, the corresponding rate coefficients are modeled as

$$G_\Xi = R_\Xi\frac{\Xi_{\text{eq}}-1}{\Xi_{\text{eq}}} \qquad (3.106)$$

and

$$R_\Xi = \frac{0.28}{\tau_\eta}\frac{\Xi_{\text{eq}}^*}{\Xi_{\text{eq}}^*-1}. \qquad (3.107)$$

In order to avoid the production of flame wrinkling ahead of the flame, the linear correction function

$$\Xi_{\text{eq}} = 1 + 2\overline{c}(\Xi_{\text{eq}}^*-1) \qquad (3.108)$$

is introduced. Only the equilibrium flame wrinkling Ξ_{eq} and thus the source term is manipulated, not the flame wrinkling Ξ itself. Note that the generation rate coefficient G_Ξ reduces to $0.28/\tau_\eta$ if $\Xi_{\text{eq}} = \Xi_{\text{eq}}^*$, i.e. at the center of the turbulent flame brush ($\overline{c} = 0.5$). From direct numerical simulation and spectral analysis [275] (in terms of the turbulence spectrum), Weller [274] found that the rate of generation of area per unit area of a passive surface in homogeneous turbulence is approximately 0.28 in relation to the Kolmogorov time scale of turbulence τ_η which is estimated through dimensional analysis in eq. 2.16. The equilibrium flame wrinkling Ξ_{eq} characterizes the state in which the sub-grid generation and removal rates (the first and second term on the right-hand side of eq. 3.104) cancel out. If Ξ approaches its lower bound 1.0, only the production term is active whereas the reduction term vanishes. Differing from Weller's original formulation, the calculation of equilibrium wrinkling Ξ_{eq}^* is replaced by the recently published correlation 3.115 of Dinkelacker et al. [63] for reasons discussed later.

The third term on the right-hand side of eq. 3.104 includes the effect of flame stretch resolved by the grid. Fundamental considerations on the nature of flame stretch [47] suggest a model of the following form. The resolved strain rate σ_r and the surface-averaged strain rate σ_s are eventually obtained by removing the dilatational component from the strain rate in the direction of propagation n_j^c:

$$\sigma_r = \frac{\partial}{\partial x_j}\left(\widetilde{u}_j + S_L\Xi n_j^c\right) - n_j^c\left(\frac{\partial}{\partial x_i}\left(\widetilde{u}_j + S_L\Xi n_j^c\right)\right)n_j^c \qquad (3.109)$$

and

$$\sigma_s = \frac{\dfrac{\partial \widetilde{u}_j}{\partial x_j} - n_j^c \left(\dfrac{\partial \widetilde{u}_j}{\partial x_i} \right) n_j^c}{\Xi} + \frac{(\Xi + 1) \left(\dfrac{\partial}{\partial x_j} \left(S_L n_j^c \right) - n_j^c \left(\dfrac{\partial}{\partial x_i} \left(S_L n_j^c \right) \right) n_j^c \right)}{2\Xi}. \tag{3.110}$$

This dynamic turbulence-chemistry interaction approach allows for the fact that the flame area is influenced not only by the turbulence field, but also by the flame itself and by non-local effects. It incorporates non-equilibrium effects (in terms of flame wrinkling) which typically arise for rapid changes of state as in accelerated flames. The faster the flame, the more Ξ lags behind its equilibrium value as is evident from the flame surface area analysis of validation simulations in sec. 4.3.

3.5.5.2 Flame instabilities

Earlier simulations of Hasslberger et al. [101] showed that the original model of Weller [274] clearly underestimates the flame acceleration for lean mixtures in RUT experiments (chap. 4). Insufficient modeling of flame instabilities is assumed to be one of the main deficits as only turbulence-induced flame wrinkling is accounted for in the original model. As explained in sec. 2.3.2, intrinsic flame instabilities can considerably influence the effective burning velocity for lean hydrogen-air mixtures. Particularly the thermal-diffusive instability with subsequent secondary hydrodynamic instabilities require special treatment since they are not naturally included in under-resolved simulations.

In combustion regimes subject to cellular instabilities, the assumption of purely kinematic interaction between the wrinkled flame front and the turbulent flow no longer holds. The flamelet concept (following Damköhler's classical understanding) and accordingly identity 3.102 is not strictly correct anymore. Nevertheless, such instabilities alter the effective flame surface area, suggesting a consistent modeling approach combining the effects of turbulence-related and instabilities-related flame interaction in the form of the equilibrium value Ξ_{eq}. Ξ shall therefore be interpreted in a more general manner as the ratio between effective and laminar burning velocity.

The general trend towards stable or unstable behavior can be described by the Lewis number as introduced in sec. 2.3. The range of eligible burning velocity laws is therefore narrowed down to models including Le as an additional parameter. A potentially suitable correlation has been proposed by Bradley et al. [34]:

$$\Xi_{eq}^* = \max \left(1.0; 1.53 \left(\frac{u'}{S_L} \right)^{0.55} \left(\frac{l_T}{l_L} \right)^{0.15} \text{Le}^{-n} \right). \tag{3.111}$$

Due to its inappropriate asymptotic behavior at vanishing turbulence intensity ($\Xi_{eq}^* \to 0$ if $u' \to 0$), the formulation is bounded by the maximum function such that the effective burning velocity does not fall below the laminar burning velocity. According to the implicit isotropy assumption of the SST turbulence model (sec. 3.3.2), the turbulent velocity fluctuation is computed from

$$u' = \sqrt{\frac{2}{3} k}. \tag{3.112}$$

The integral turbulent length scale

$$l_T = C \frac{k^{3/2}}{\varepsilon} \tag{3.113}$$

estimates the size of the large energy-containing eddies and should obviously not be larger than the dimension of the problem. A wide range of different prefactors C can be found in literature. Due to the lack of general validity, $C = 1.0$ is used here without any fine-tuning of the results. Employing the thermal theory of Mallard and Le Chatelier [93], the laminar flame thickness is approximated by

$$l_L = \frac{a_u}{S_L} \tag{3.114}$$

using the laminar flame speed S_L and the thermal diffusivity of the unburned mixture a_u. Bradley specifies the exponent of the Lewis number as $n = 0.3$, whereas Driscoll [70] determines the value to be $n = 1.0$ in a more recent study.

An alternative is available from the paper of Dinkelacker et al. [63] published lately. Besides Le and standard input parameters characterizing turbulence (u' and l_T), their model

$$\Xi_{\text{eq}}^* = 1 + \frac{0.46}{\text{Le}} \text{Re}_T^{0.25} \left(\frac{u'}{S_L} \right)^{0.3} \left(\frac{p}{p_{\text{ref}}} \right)^{0.2} \tag{3.115}$$

is written in terms of the turbulent Reynolds number Re_T (specified in eq. 2.17) and additionally contains a dependency on pressure p. The authors found that the Lewis number effect is especially important for increased pressure. In the context of explosion problems which are massively accompanied by pressure increase, this seems to be an important finding. Strong evidence on the influence of pressure is also provided by Vukadinovic et al. [268]. Moreover, even at high turbulence intensities, a significant influence of the Lewis number has been observed for lean premixed combustion [63]. Although not explicitly developed for pure hydrogen-air mixtures (but for hydrogen-enriched hydrocarbon-air mixtures), Dinkelacker's model is preferred over Bradley's model because of its additional pressure influence and its robust asymptotic behavior at vanishing turbulence intensity ($\Xi_{\text{eq}}^* \to 1$ if $u' \to 0$). Thus, Dinkelacker's correlation has eventually been applied for all the simulations discussed later.

In terms of instability modeling, there is one minor but systematic error of both models including the Lewis number influence. At vanishing turbulence intensity (e.g. shortly after weak ignition of a quiescent mixture and before an interaction with turbulence-inducing obstacles takes place), the laminar burning velocity is applied instead of an instabilities-enhanced quasi-laminar burning velocity. However, in the framework of DDT simulations, the initial stage of flame acceleration is of inferior importance. During the main stage of flame acceleration (interaction with confining geometry etc.), enough turbulence is present which implicitly activates the Le influence.

It should be mentioned that the development of turbulent burning laws is usually not targeted to explosion problems covering a wide range of different combustion regimes. Most of the established burning laws were developed for quasi-steady combustion, e.g. in gas turbines. The empirical calibration involved inevitably leads to a limited range of validity. Using such models is therefore considered best practice in engineering applications, yet without a sound derivation from first principles.

It remains the question, how the Lewis number Le can generally be determined for hydrogen-air mixtures of varying mixture composition. Following the standard defini-

tion in eq. 2.26 (thermal diffusivity of the mixture a divided by the diffusion coefficient of the deficient reactant D) results in a problem at the stoichiometric point where the deficient reactant switches. Since nitrogen is assumed inert, Le related to the fuel H_2 shall be used for under-stoichiometric conditions whereas Le related to the oxidizer O_2 shall be used for over-stoichiometric conditions. Because of the direct influence in eq. 3.115, a sudden jump in Lewis number leads to a sudden jump in reaction rate likewise. Considering mixtures with strong spatial concentration gradients which are crossing the stoichiometric point, such an approach is apparently unnatural. The dependency of both Lewis numbers on mixture composition was calculated by the chemical package CANTERA [95] using a mixture-based approach and is visualized in fig. 3.16.

To remedy the problem inherent to the standard definition, an effective Lewis number ansatz is applied. In literature, it is sometimes referred to as reduced Lewis number. First of all, the normalized equivalence ratio

$$\Phi = \frac{\phi}{1 + \phi} \tag{3.116}$$

is introduced which is bounded above by 1.0 in contrast to the equivalence ratio ϕ. Additionally, compared to the hydrogen mass or mole fraction, the stoichiometric point lies in the middle of the parameter space, thus at $\Phi = 0.5$. Thanks to these properties, a simple blending between the asymptotic values Le_{H_2} and Le_{O_2} can be constructed:

$$\text{Le} = \text{Le}_{H_2}(1 - \Phi) + \text{Le}_{O_2}\Phi = \text{Le}_{H_2} + \Phi\left(\text{Le}_{O_2} - \text{Le}_{H_2}\right). \tag{3.117}$$

Despite the linear blending, a non-linear dependency $\text{Le}(\Phi)$ is eventually obtained due to the non-linear dependency of the asymptotic values on Φ. Coinciding with theory, fuel and oxidizer related Lewis numbers are weighted evenly at the stoichiometric point.

As can be seen from fig. 3.16, effective Lewis numbers fall clearly below unity on the lean side. Inserting such values in eq. 3.115 leads to increased reaction rates. It is well-
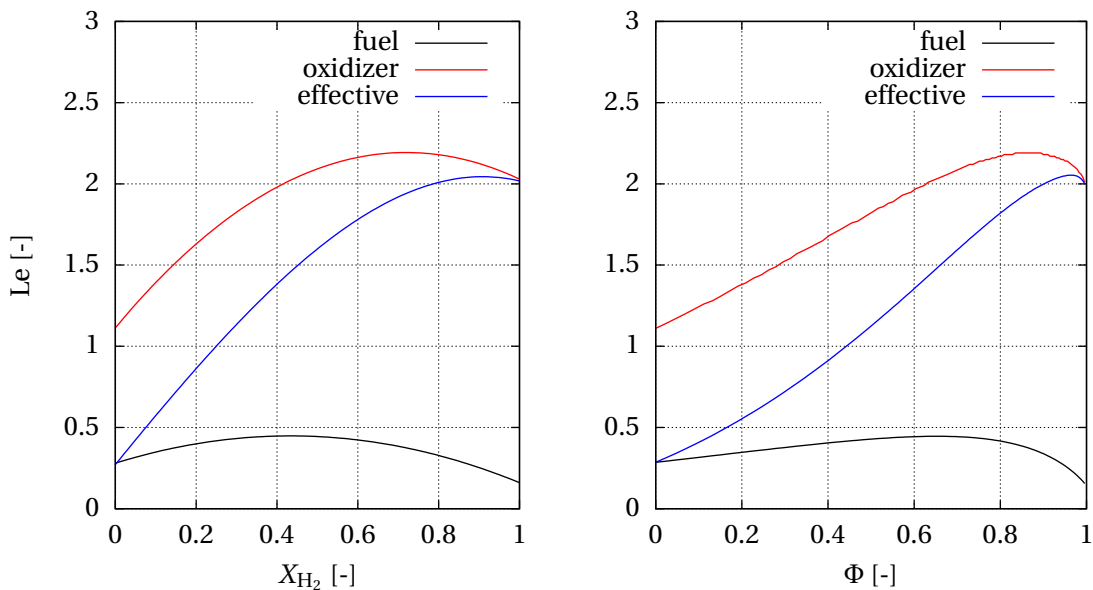

Figure 3.16: Lewis number Le depending on hydrogen mole fraction X_{H_2} and normalized equivalence ratio Φ

known from experiments that cellular flame instabilities promote flame acceleration in this regime, cf. 2.3.2. On the rich side, effective Lewis numbers rise clearly beyond unity, meaning that there is a stabilizing effect. Named flame instabilities do not occur. The effective Lewis number is prescribed in the CFD code as a fuel concentration dependent third-order polynomial:

$$\text{Le} = -1.0248\, X_{\text{H}_2}^3 - 0.2822\, X_{\text{H}_2}^2 + 3.0531\, X_{\text{H}_2} + 0.2717. \tag{3.118}$$

More complex approaches to compute an effective Lewis number are presented by Joulin and Mitani [121] or Bechtold and Matalon [20], but are difficult to implement for the wide range of thermodynamic conditions required for explosion simulations. Curve fitting of experimentally determined effective Lewis numbers was discarded since data from different sources involves excessive scatter. Other ways of instability modeling, e.g. via Markstein number based correlations, might be a reasonable alternative [205]. The trend towards stable or unstable behavior can equally be described by this characteristic quantity.

3.5.5.3 Flame quenching

The factor G of the flamelet source term 3.90 corrects the turbulent burning velocity by incorporating quenching effects. Without this modification, the well-known 'bending' behavior (decrease of the reaction rate) at high turbulence intensities is not captured. Since the effect is believed to be due to small-scale flame stretching unresolved in the ensemble-averaged context, modeling is required. The applied formulation was introduced by Zimont and Lipatnikov [295] and was originally inspired by ideas of Bray [35]. Practical implementation is demonstrated in [210, 294].

The probability of unquenched flamelets G is given by

$$G = \frac{1}{2}\text{erfc}\left[-\frac{1}{\sqrt{2\sigma}}\left(\ln\left(\frac{\varepsilon_{\text{cr}}}{\varepsilon}\right) + \frac{\sigma}{2}\right)\right] \tag{3.119}$$

with erfc indicating the complementary error function [187] and σ representing the standard deviation of the log-normal distribution of the turbulent dissipation rate ε. Modeling by

$$\sigma = 0.26\ln\left(\frac{l_T}{l_\eta}\right) \tag{3.120}$$

uses the integral turbulent length scale l_T (eq. 3.113) and the Kolmogorov length scale l_η (eq. 2.15). The critical dissipation rate

$$\varepsilon_{\text{cr}} = 15\nu g_{\text{cr}}^2 \tag{3.121}$$

depends on the critical flamelet quench rate g_{cr} which can be obtained from laminar flame computations or, as in this case, can be estimated by dimensional considerations from

$$g_{\text{cr}} = \frac{S_L^2}{a_u}. \tag{3.122}$$

Regarding its asymptotic behavior, the model predicts no flame quenching for very low dissipation rates ($\varepsilon \ll \varepsilon_{\text{cr}}$), i.e. $G \to 1$. If very high dissipation rates ($\varepsilon \gg \varepsilon_{\text{cr}}$) occur, the flame locally quenches, i.e. $G \to 0$ and the flame wrinkling source term locally vanishes.

It has to be accentuated that the approach involves empiricism in several points. In particular, estimates of g_{cr} are connected with relatively large uncertainties. The authors [210, 294] recommend to look upon g_{cr} as a tuning parameter to assure optimal agreement with experiments.

3.5.6 Volumetric reaction

The flamelet model works well for low to moderate turbulence intensities. Characterized by a vertical shift in the Borghi diagram, the interaction of the flame with turbulent eddies intensifies with increasing flame acceleration. As is evident from the flame surface analysis of a DDT simulation in fig. 4.15, flame wrinkling drops at elevated flame speeds due to its limited production rate (eq. 3.106). The flamelet model alone can obviously not reproduce the behavior of near-sonic deflagrations and especially detonations. Additional shock-flame interaction and auto-ignition effects play an increasingly important role during the course of explosion progression. Hence, the character of the reaction zone becomes more distributed without a distinct flame surface (i.e. volumetric reaction). The reaction rate is rather kinetically controlled in this regime.

Similar to approaches by Colin et al. [56] and Michel et al. [189], a two-step formulation is pursued to account for this mechanism. The first step representing the isothermal ignition delay is followed by the second step representing the exothermic heat release. Two properties of the approach are compelling: First, it is not necessary to solve independent transport equations (including Arrhenius-type source terms) for all the reactive species. Second, and as a consequence, stiff hydrogen-oxygen chemistry (meaning that the chemical scales are clearly smaller than the characteristic flow scales) is not a limiting factor regarding spatial and temporal discretization in CFD.

Another transport equation

$$\frac{\partial}{\partial t}\left(\overline{\rho}\widetilde{\tau}\right) + \frac{\partial}{\partial x_j}\left(\overline{\rho}\widetilde{\tau}\widetilde{u}_j\right) - \frac{\partial}{\partial x_j}\left(\overline{\rho}D_{\text{eff}}\frac{\partial\widetilde{\tau}}{\partial x_j}\right) = \frac{\overline{\rho}}{t_{\text{ign}}} \tag{3.123}$$

is introduced, in which the normalized quantity

$$\tau = \frac{t}{t_{\text{ign}}(T, p, f_H)} = \frac{Y}{Y_{\text{cr}}} \tag{3.124}$$

compares the current simulation time t with the local auto-ignition delay time $t_{\text{ign}}(T, p, f_H)$. Latter is a highly non-linear function of temperature T, pressure p and hydrogen mixture fraction f_H. Alternatively, τ can be interpreted as the ratio between the mass fraction of a fictitious intermediate species Y and its critical mass fraction Y_{cr} at which auto-ignition occurs. The source term of eq. 3.123 results from the definition of τ:

$$\frac{\partial}{\partial t}\left(\overline{\rho}\widetilde{\tau}\right) = \frac{\partial}{\partial t}\left(\frac{\overline{\rho}}{t_{\text{ign}}}t\right) = \frac{\overline{\rho}}{t_{\text{ign}}} \tag{3.125}$$

assuming that $\overline{\rho}$ and t_{ign} are fixed within each time step (explicit treatment). The formulation can thus be seen as a linearization.

The Min-Max model (separately balancing shocked and unshocked parts of computational cells with respect to τ) proposed by Ettner et al. [82] is not applied here due to its additional cost but small impact in practice.

Ignition delay times t_{ign} are provided via multi-dimensional look-up tables obtained from zero-dimensional isochoric explosion calculations with CANTERA [95]. For that purpose, the detailed reaction scheme of O'Conaire et al. [200] consisting of 9 species and 19 reversible elementary reactions is employed. Because of its wide validation range (pressure from 0.05 to 87 atm, temperature from 298 to 2700 K and equivalence ratio from 0.2 to 6), O'Conaire's mechanism seems to be an adequate choice for this kind of simulations. The ignition delay time is defined as the time interval until the inflection point of the temperature curve is reached. In terms of accuracy, the tabulation of ignition delay times is assumed superior to algebraic correlations which are commonly used.

Independent of the data source, general criticism about such an approach is raised by Taylor et al. [248]. Arrhenius parameters of chemical reaction schemes are practically never calibrated for simultaneous high pressure and temperature conditions as in gas-phase detonations. Ignition delay times computed in this way must be assessed as an extrapolation. Besides, the assumption of thermodynamic equilibrium used in the development of these mechanisms can be questioned. Non-equilibrium vibrational modes seem to play a non-negligible role under such extreme conditions. More sophisticated but equally simple alternatives are unavailable though.

Two different possibilities to incorporate the second step in the flame evolution equation 3.89 are examined. The Heaviside function $\text{H}(\tau - 1)$ included in each formulation locally activates the source term when the auto-ignition delay time has expired, i.e. $\tau = 1$. Validation of the model variants is mostly done for steady detonation propagation, since powerful one-dimensional theories (sec. 2.5.1 and sec. 2.5.2) are available and flame propagation is mainly driven by successive auto-ignition in this regime.

To study the fundamental behavior of both formulations, the compressibility of the fluid as well as transport processes are initially neglected in fig. 3.17. Inspecting the source term profiles in the reaction progress space, model identification as *linear* or *parabolic* becomes clear. Since volumetric reaction cannot directly be formulated as an additional dilatational component of flame propagation, the standard gradient closure of the flamelet source term cannot be reused. To make the reaction rate integral independent of the averaging procedure 3.96, it is essential to calculate the source term with α, not $\bar{c}$ representing the distributed flame brush. The discontinuous character of the α-field is preserved by the VoF technique.

3.5.6.1 Linear model

The *linear* volumetric reaction model

$$\omega_{\text{vol}} = \dot{\alpha}\,\text{H}(\tau - 1) = \frac{1 - \alpha}{t_{\text{exo}}}\text{H}(\tau - 1) \tag{3.126}$$

is based on the relation

$$\dot{\alpha}(t) = \frac{\partial}{\partial t}\underbrace{\left(1 - e^{-\frac{t}{t_{\text{exo}}}}\right)}_{\text{assumed } \alpha(t)} = \frac{1 - \alpha(t)}{t_{\text{exo}}}. \tag{3.127}$$

The only free parameter t_{exo} somehow scales the thickness of the reaction zone, but lacks of a straight-forward mathematical definition. At least, $1/t_{\text{exo}}$ can be interpreted as an initial reaction rate. Without any loss of generality, $t_{\text{exo}} = 1$ s is set in fig. 3.17.
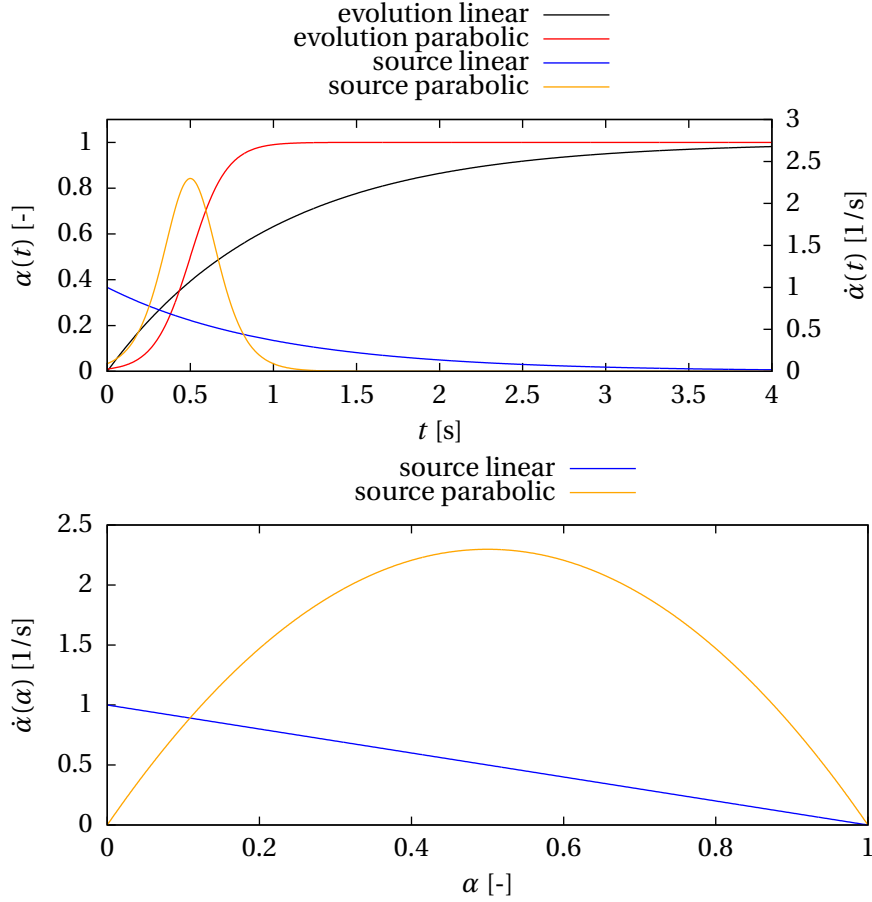
Figure 3.17: Evolution of α and corresponding source term profiles $\dot{\alpha}$ for both volumetric reaction models in time space t (top) and reaction progress space α (bottom)

The model of Ettner et al. [82] can be recognized as a special case of this generalized formulation. The authors use $t_{\text{exo}} = \Delta t$ owing to the fact that reaction is usually very fast compared to the numerical time step Δt. However, this special formulation behaves like a Dirac delta pulse and has to be assessed stiff in the numerical sense. Not only reaction, but also transport processes are present in each time step. In this context, stiffness means that spurious overshoots of α are likely to appear which require undesired artificial bounding.

Moreover, starting with the highest value and slowly decreasing, the source term profile is rather unnatural – especially compared to the parabolic model discussed next.

3.5.6.2 Parabolic model

To counteract the drawbacks of the linear model, the *parabolic* volumetric reaction model

$$\alpha^* = \alpha + 0.001 \cdot \mathrm{H}(10^{-15} - \alpha) \cdot \mathrm{H}(\tau - 1)$$

$$\omega_{\text{vol}} = \dot{\alpha}^* \, \mathrm{H}(\tau - 1) = \frac{2B}{t_{\text{exo}}} \alpha^* (1 - \alpha^*) \, \mathrm{H}(\tau - 1)$$

(3.128)

based on relation

$$\dot{\alpha}(t) = \frac{\partial}{\partial t} \underbrace{\left(0.5 + 0.5 \tanh\left(B \frac{t}{t_{\text{exo}}}\right)\right)}_{\text{assumed } \alpha(t)} = \frac{2B}{t_{\text{exo}}} \alpha(t)(1 - \alpha(t)) \tag{3.129}$$

has been constructed in this work. If t_{exo} is defined as the time span in which α rises from 0.01 to 0.99, then $B \approx 4.5951$ can be determined from first principles. The derivation is given in appendix B. The source term's α-proportionality is apparently the same as for the widespread Schmid [229, 230] and Bray-Moss-Libby model [36]. Again, $t_{\text{exo}} = 1$ s is set in fig. 3.17 and t is shifted by 0.5 $t_{\text{exo}} = 0.5$ s since $\alpha(t = 0) = 0.5$. This shifting is only done for the time space illustration in fig. 3.17. Implementation in the code is via the reaction progress space and therefore independent of time.

Despite the definite mathematical interpretation, it is still not clear how the characteristic reaction time t_{exo} has to be chosen. In case of highly resolved simulations, t_{exo} should be on the order of the exothermic pulse width which can a priori be calculated by a chemical kinetics package like CHEMKIN [124] or CANTERA [95]. Doing under-resolved simulations however, such small scales are not resolved and other constraints prevail. It is recommended to prescribe a reaction time as small as possible but large enough to avoid disproportionate stiffness errors. Values of $t_{\text{exo}}/\Delta t$ between 15 and 30 proved to be a robust choice in the present application. If a more sophisticated model for t_{exo} is found in the future, it can easily be plugged in while keeping the framework of the parabolic formulation. It should additionally be noted that flame propagation in the detonation regime, in which the source term of eq. 3.89 is dominated by ω_{vol}, is independent of t_{exo}. According to CJ theory introduced in sec. 2.5.1, the detonation velocity is determined by the mixture's thermodynamic state and *integral* heat release. Nevertheless, it is possible to improve the pressure load prediction by t_{exo}.

Compared to the linear model, the source term profile of the parabolic model is more meaningful from the chemistry point of view. Starting from zero, it peaks at $\alpha = 0.5$ before decreasing again towards the chemical equilibrium ($\alpha = 1$). The general profile agrees well with ZND detonation theory, fed by detailed chemical kinetics, in sec. 2.5.2.

Because of the vanishing source term at $\alpha = 0$, a correction from α to α^* is necessary in eq. 3.128 for DDT simulations where auto-ignition can occur ahead of the main flame. If the ignition delay time has expired ($\tau = 1$) and the cell is still unburned ($\alpha < 10^{-15}$), α is increased by the sufficiently small value $\Delta \alpha = 0.001$, i.e. the correction locally provides an initial push to the source term. The simulation results are insensitive to the particular choice of $\Delta \alpha$.

3.5.6.3 Extended heat release criterion

In the framework of under-resolved detonation simulations (with cell sizes larger than the induction length), a pseudo-stable coupling between the leading shock and the succeeding reaction zone develops. The solver is not able to distinguish between both phenomena within computational cells, especially when using $t_{\text{exo}} = \Delta t$. As a result, the von Neumann spike is not captured correctly, cf. fig. 3.18.

To restore the von Neumann spike, a modified criterion for the second step of the auto-ignition model is proposed. It can either be formulated in terms of pressure or in terms of density:

$$\omega_{\text{vol}}^* = \omega_{\text{vol}}\Theta$$
$$\text{with}$$
$$\Theta = \max\left[\Theta; H\left(-\frac{\partial p}{\partial t}\right) \cdot H(\tau - 1)\right] \tag{3.130}$$
$$\text{or}$$
$$\Theta = \max\left[\Theta; H\left(-\frac{\partial \rho}{\partial t}\right) \cdot H(\tau - 1)\right].$$

Basically, the modification can be used in conjunction with both ω_{vol} models, linear and parabolic. It prevents the heat from being released until the pressure or density maximum (characterized by the temporal derivative of the pressure or density becoming negative) is reached. Leading shock and reaction zone are consequently not overlayed in the front cells. The maximum function makes sure that the additional restriction is removed, once the criterion is fulfilled for the first time. This is essential since reaction can take more than one time step – depending on the choice of t_{exo}. In compliance with its construction, the Θ field is of binary character (zero or unity).

3.5.6.4 One-dimensional test cases

At first, the performance of different volumetric reaction source term formulations is tested for steady one-dimensional detonation propagation. The investigated case represents a 10 m long channel (1 cm cell size) filled with 20 % of hydrogen in air. Initially, the quiescent mixture is at ambient conditions (1.013 bar, 293 K). Strong ignition at one end of the channel is realized by patching several cells with the corresponding CJ values ($p_{\text{CJ}} = 13.34$ bar, $T_{\text{CJ}} = 2441.5$ K, $u_{\text{CJ}} = D_{\text{CJ}} - a_{\text{prod,v}} = 771.9$ m/s, $\alpha_{\text{CJ}} = 1.0$).

Four source term formulations are checked against each other in fig. 3.18: linear model (using $t_{\text{exo}} = \Delta t$) with and without both versions of the second heat release criterion versus parabolic model (using $t_{\text{exo}} = 25 \, \Delta t$). Being the most significant output in terms of structural integrity, numerical pressure profiles are compared to characteristic pressure levels from one-dimensional detonation theories, cf. sec. 2.5. The von Neumann spike $p_{\text{vN}} = 24.2$ bar describes the post-shock state. After all the heat is released, the pressure drops to the Chapman-Jouguet value $p_{\text{CJ}} = 13.3$ bar. The pressure level at the end of the Taylor expansion wave is approximated by $p_{\text{T}} \approx 0.375 \, p_{\text{CJ}} \approx 5.0$ bar. These specific values for $X_{\text{H}_2} = 20$ % were calculated by the EDL Shock and Detonation Toolbox [83].

Depending on the formulation, the behavior is somewhat different. The extended heat release criterion generally improves reproduction of the von Neumann spike for the linear model. Small overshoots of the peak value might originate from the segregated solver architecture (cf. sec. 3.3.3) or the convective flux limiter (cf. sec. 3.3.3.2). Although the criterion extension works well in one dimension, it can be problematic in multi-dimensional simulations under certain circumstances. It can either lead to disintegration of the leading shock and the reaction zone. Or, it provokes instabilities of the detonation front which do not only depend on stoichiometry and thermodynamic state (as in reality, cf. sec. 2.5)
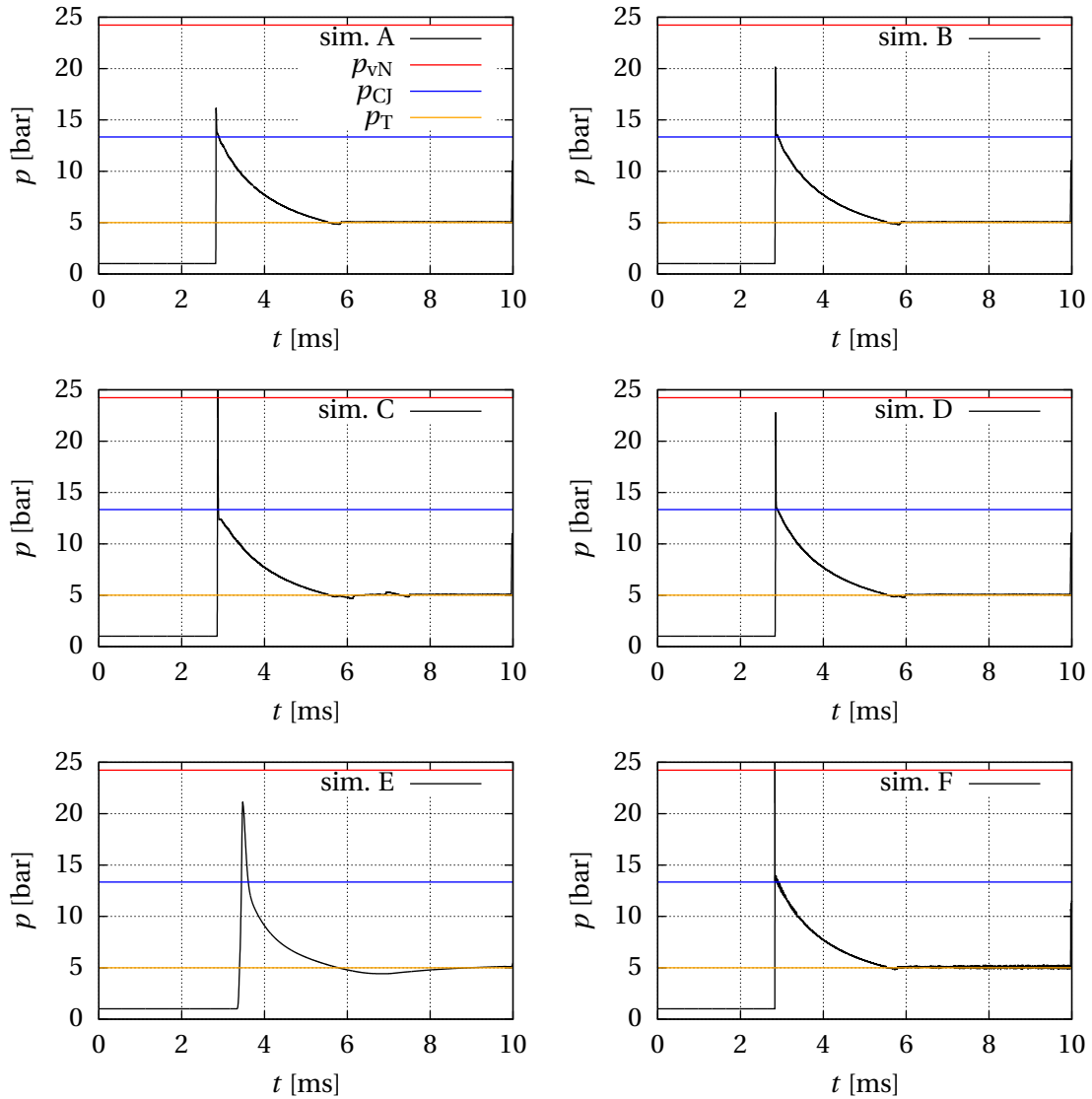
Figure 3.18: Temporal pressure profiles (fixed observer) for one-dimensional detonation propaga-
tion; Variation of volumetric reaction models and cell size:
sim. A: linear ansatz, without second criterion, 1 cm;
sim. B: linear ansatz, with density-based second criterion, 1 cm;
sim. C: linear ansatz, with pressure-based second criterion, 1 cm;
sim. D: parabolic ansatz, without second criterion, 1 cm;
sim. E: parabolic ansatz, without second criterion, 1 dm;
sim. F: parabolic ansatz, without second criterion, 1 mm

but also on mesh density. For the parabolic model, the criterion extension seems to be unnecessary if only t_{exo} is large enough. At the same time, it has to be small enough to avoid the mentioned disintegration problems.

Anyway, the pseudo-stable front coupling does not controvert the under-resolved simulation concept which aims at predicting the correct global propagation behavior. Due to its short existence, the von Neumann spike can be looked upon as an unnecessary detail for safety analysis. The detonation velocity is primarily determined by the heat release according to CJ theory, sec. 2.5.1. Accurate reproduction of the detonation velocity automatically results in accurate reproduction of the CJ pressure. Prediction of the correct DDT location as the ultimate goal is unaffected since the shock-reaction coupling does not yet occur before this event.

It can further be stated that the finally chosen parabolic model is fairly robust against variation of the spatial resolution by two orders of magnitude. Investigated cell sizes of 1 mm, 1 cm and 1 dm represent the relevant spectrum of mesh densities ranging from laboratory-scale to industry-scale facilities. Time step sizes change accordingly due to the adaptive time stepping discussed in sec. 3.3.3.3. The observed behavior is an important property regarding the geometrical scalability of the approach.

Additional validation computations for a large-scale facility are discussed in sec. 4.2.1. Since analytical reference solutions are not available for detonation propagation including diffraction, reflection and focusing in a three-dimensional complex geometry, comparison with experimental data is provided.

The parabolic model's ability to reproduce DDT by shock reflection is demonstrated in fig. 3.19. In this one-dimensional example, a shock approaches the fixed wall boundary at x = 10 m from left to right. Spatial discretization and mixture composition are the same as above. Analyzing chemical kinetics with the detailed reaction scheme of O'Conaire et al. [200], Boeck [28] found that an overpressure of the incident shock of around 10 bar is necessary to provoke strong ignition after shock reflection. These findings are insensitive to hydrogen concentration and were confirmed by experiments in the GraVent facility [27]. To guarantee an overpressure of the incident shock in the over-critical range, the sufficiently high shock Mach number of $\mathrm{Ma}_S = 3.1$ was thus imposed in this test case. The corresponding post-shock state is given by eqs. 2.5 to 2.8: pressure $p_S = 11.19$ bar, temperature $T_S = 819.99$ K and velocity $u_S = 882.29$ m/s. According to the analysis of the extended second explosion limit (i.e. chain-branching criterion), the critical Mach number would indeed be 3.1. As examined by Boeck et al. [31], other strong ignition criteria yield lower critical values in the range 2.7 to 2.9, which seems more reasonable and closer to experiments.

Cell mean values of pressure p and reaction progress α at four points in time are plotted in fig. 3.19. In the first and second picture, the shock wave propagates from left to right without igniting the mixture. Due to the absence of loss mechanisms in the one-dimensional adiabatic simulation, a constant shock strength is maintained. Yet without ignition, reflection of the shock wave at the domain end (fixed wall at $x = 10$ m) can be seen in the third picture. Another 0.2 ms later, the direct coupling of leading shock and flame indicates successful transition to detonation. Since it is an essential mechanism for DDT mode A (cf. sec. 2.4), special attention has to be paid to the model's ability to reproduce strong ignition in the unburned mixture. Other than in the temporally continuous depiction in
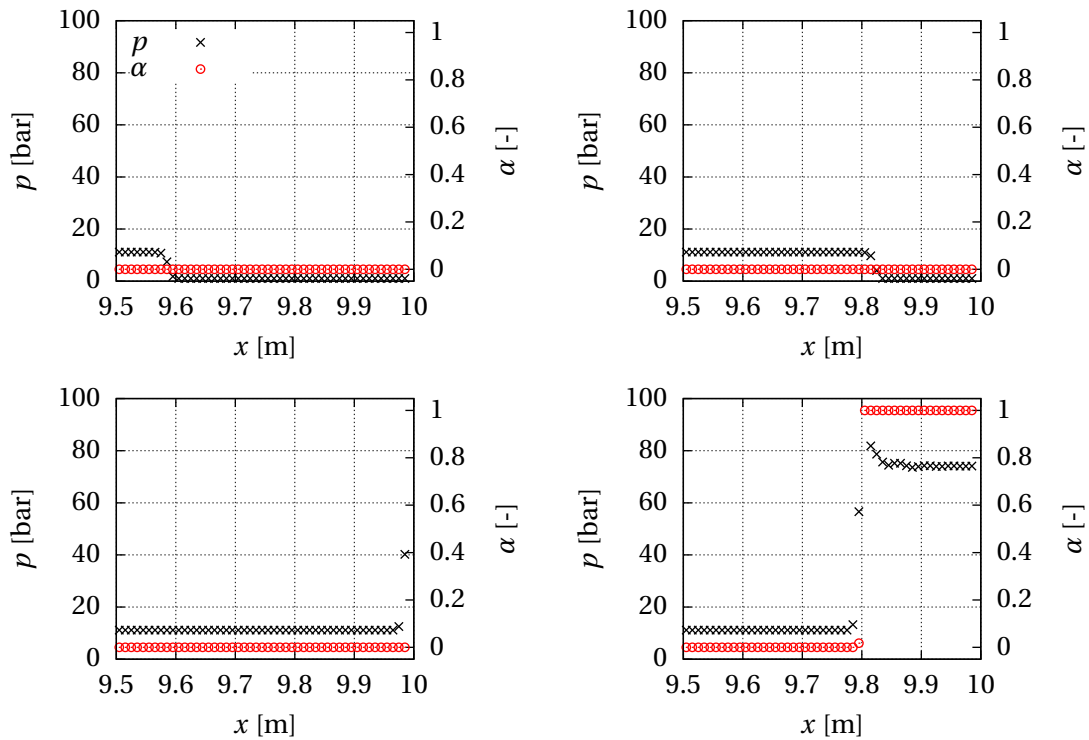
Figure 3.19: Temporal evolution of DDT by shock reflection in one dimension: Spatial profiles of pressure p and reaction progress α; Time difference between snapshots is 0.2 ms

fig. 3.18, the observation of realistic pressure peak values must not be expected here. In this discrete representation, the pressure peak value changes as the shock or detonation front propagates through one computational cell.

3.6 Adaptive mesh refinement

For the purpose of computational cost reduction, the solver is enhanced by dynamic mesh functionality. The technique is called local Adaptive Mesh Refinement (AMR), because it automatically adapts the computational grid to the current fields. Manually adjusting the mesh, at fixed points in time, is not an option due to the highly unsteady nature of explosions. While high spatial resolution is assured in regions where crucial phenomena are present, the base mesh can be chosen comparably coarse.

Simulation errors can be divided into independent modeling errors and discretization errors. AMR aims at minimizing discretization errors due to insufficient resolution while discretization errors due to poor topological mesh quality or inappropriate numerical schemes are largely unaffected [114].

3.6.1 Algorithm

The underlying principle of the algorithm is isotropic cell division. Accordingly, each parent cell fulfilling the refinement criterion 3.131 is split into eight children cells for three-

dimensional simulations. Multiple splitting operations are possible and only limited by a maximum refinement level related to the affordable computational effort. This kind of AMR is known as octree-based AMR in literature. It characterizes a tree structure in which each eligible cell has exactly eight children. Unlike many other codes, OpenFOAM can handle hanging nodes which always arise from the cell splitting process, cf. fig. 3.20 and 3.21.

In this context, the algorithm is fully compatible with the unstructured mesh handling paradigm of OpenFOAM [116]. Even for topologically identical grids, the way of mesh indexing (how the solver addresses individual cells) is fundamentally different for structured and unstructured grids: Unlike for structured meshes, cell connectivity is stored rather than calculated. As a consequence, cell connectivity has to be rebuilt each time the mesh topology changes. The number of points, faces and cells or their connectivity may vary during runtime. Simple mesh deformation, which is not applied in this work, does not necessitate such rebuilt. The flexibility in dealing with complex geometries is thus paid by a certain computational overhead for data structure adjustments including memory reallocation. Additionally, fields have to be mapped between different refinement levels and face fluxes have to be recalculated. Associated interpolation or data redistribution errors are assumed to be small. The overall procedure consists of two sub-cycles for refinement and un-refinement. It is decided by the refinement criterion whether none, one or both sub-cycles are executed within a time step. To facilitate un-refinement, it is necessary to store the refinement history, i.e. the children-parent relationship.

Good mesh quality is maintained through assuring the 2:1 rule, i.e. cell faces can have a maximum of four neighbors in three-dimensional simulations. All octrees obeying the rule are called balanced trees [245]. A generic example of level 2 AMR is shown in 3.20. For demonstration purposes, dimensionality is reduced by one. The three-dimensional octree structure is consequently replaced by a two-dimensional quadtree structure, but the basic principle remains. The interface between two generic bulk states (blue and red) is locally refined. Intermediate states (greenish) appear within the refined region. Obeying the 2:1 rule results in a level 1 buffer zone between the base mesh (level 0) and the level 2 part of the domain. Furthermore, fig. 3.21 directly opposes an ill-conditioned mesh on the left to a well-conditioned mesh on the right.

The benefits of AMR outweigh the drawback of additional algorithmic effort. Compared to the solution of the equation system, mesh operation requires only a fraction of the overall CPU time. For the present calculations, the algorithm is executed every ten time steps due to the profoundly unsteady nature of the problem. There might be potential to further reduce computational costs by suspending AMR for a larger number of time steps.

Thanks to its general architecture, the algorithm can be adapted to account for a wide range of phenomena: tracking of shocks, phase interfaces, combustion waves etc. However, limits of applicability have to be admitted. For instance, the Richtmyer-Meshkov flame instability (sec. 2.3.2) is effective on a large spectrum of length scales down to Kolmogorov level. It is usually not appropriate to increase the local resolution to this level, because of the fast rise of cell number with increasing refinement level as demonstrated by tab. 3.3. Such practice is anyway not desired when aiming at a computationally efficient under-resolved simulation framework. An issue of AMR related to parallel efficiency is discussed in sec. 3.7.

Table 3.3: AMR-induced cell augmentation reflecting the octree-structure

Refinement level	Number of cells
0	$8^0 = 1$
1	$8^1 = 8$
2	$8^2 = 64$
3	$8^3 = 512$
4	$8^4 = 4,096$
5	$8^5 = 32,768$
...	...
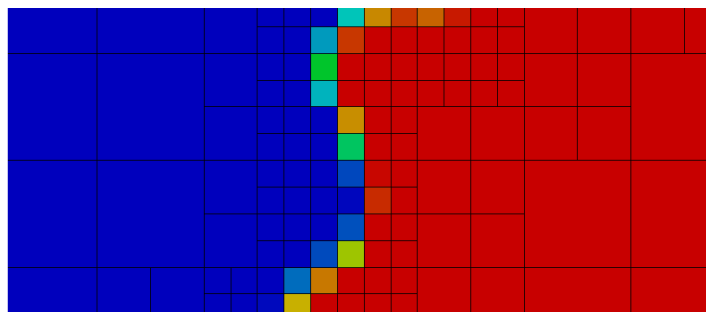
Figure 3.20: Locally refined interface between two generic bulk states (blue and red)
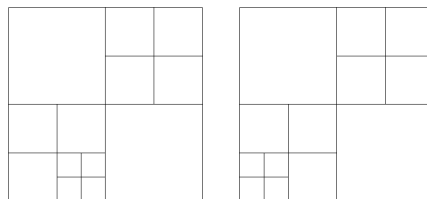
Figure 3.21: 2:1 rule violated by the left and satisfied by the right mesh

Indicator- as well as error-driven adaptivity (see e.g. [115]) are generally possible. Latter strategy is unfeasible for this work due to the lack of error estimators as well as residuals in the (partly) explicit solver framework. Following an indicator-driven strategy, mesh refinement is controlled via the refinement criterion

$$
\mathrm{H}\left(\frac{\left|\left(\frac{\partial \alpha}{\partial x_j}\right)^{\mathrm{NAG}}\right|}{\max_{\Omega}\left[\left|\left(\frac{\partial \alpha}{\partial x_j}\right)^{\mathrm{NAG}}\right|\right]} - 0.01 \right) + \frac{\left|\frac{\partial \rho_u}{\partial x_j}\right|}{\max_{\Omega_u}\left[\left|\frac{\partial \rho_u}{\partial x_j}\right|\right]} + \frac{\left|\frac{\partial \left|u_i^*\right|}{\partial x_j}\right|}{\max_{\Omega_u}\left[\left|\frac{\partial \left|u_i^*\right|}{\partial x_j}\right|\right]} > 0.1. \qquad (3.131)
$$

The construction of the refinement criterion reflects the different nature of essential explosion phenomena. Primarily the flame front requires finer resolution as it dominates the propagation behavior. One straight-forward possibility would be to specify the refined region by means of the strictly bounded reaction progress field. However, the refined region is rather specified by its gradient to include the flame's close vicinity. This quantity is already available in the framework of the geometrical Volume-of-Fluid method (sec. 3.4). The NAG gradient field provides a smooth representation of the flame's vicinity, but is not strictly bounded and thus requires a normalization procedure to set a relative threshold value. Referring to the first term of inequality 3.131, the Heaviside function makes sure that the flame's vicinity (normalized NAG gradient above 1 %) is definitely refined, independent of the threshold value for the second and third term.

Neither burned, nor unburned bulk regions (normalized NAG gradient below 1 %) are refined due to the first term. The second and third term of inequality 3.131 are designed to account for relevant physics ahead of the flame. Enhanced turbulence production in the obstacles' wake and precursor shock waves constitute two further phenomena of major importance in turbulent reactive flows with gas-dynamic effects. In this context, the second term is supposed to track shocks on the basis of density gradients. In order to include density gradients by gas-dynamic effects, but exclude density gradients produced by the flame itself, the unburned density ρ_u (eq. 3.94) is used instead of the ordinary density ρ. Pressure gradients could equally track shocks but would miss e.g. the contact wave (density jump but no pressure jump) in the shock tube problem, cf. sec. 3.6.2.

Additionally, according to the third term, the mesh is refined if the normalized velocity gradient exceeds a certain threshold value. Turbulence production is known to be high in such regions. The ansatz is thus conceptually similar to the turbulence modeling approach (sec. 3.3.2) where the production of turbulent kinetic energy scales with velocity gradients in the resolved mean field. The only difference between u_i and u_i^* concerns the boundary condition. On the latter field, a homogeneous Neumann condition is imposed instead of a no-slip condition to avoid disproportionately high velocity gradients at wall boundaries. For the same reason, wall functions are used for all turbulence-characterizing quantities (k, ω, μ_T, a_T, etc.). Owing to the unbounded nature of gradient fields, a normalization procedure is again required for both the second and third influence. Contrary to the first term, normalization is performed with respect to the maximum value in the unburned part of the domain Ω_u (reaction progress below 0.001).

A cumulative relative threshold value of 10 %, appearing on the right-hand side of inequality 3.131, evolved as a reasonable compromise. There might be potential to improve the performance of the algorithm by allowing separate relative threshold values for each term

instead of one cumulative value. Furthermore, it is conceivable to specify different maximum refinement levels for flame, gas-dynamic effects and turbulence. The effect of the refinement criterion for large-scale explosion simulations in the RUT facility can be seen in fig. 4.23.

3.6.2 Shock tube validation

To validate the implemented algorithm, the well-known shock tube problem is investigated numerically. Primarily, the case puts the gas-dynamics part of the solver to the test. Due to the presence of discontinuities in the solution, the shock tube problem is highly demanding for numerical schemes and reveals corresponding deficiencies. Turbulence modeling is irrelevant to this hyperbolically dominated, one-dimensional and inviscid problem. Likewise, the chemical reaction part of the solver is turned off.

According to the chosen initial conditions (the same as investigated in [82]), the solution consists of a left-running expansion wave, a right-running contact wave and a right-running shock. In the experimental analogy, left (800 K, 10 bar, 4.34 kg/m^3) and right state (300 K, 1 bar, 1.16 kg/m^3) are separated by a diaphragm which ruptures at $t = 0$. The initially quiescent air medium is characterized by a molecular weight of 28.85 kg/kmol and an isentropic exponent of 1.4. The one-dimensional domain, 0.2 m in length, is uniformly discretized by 50 cells. To assess the solver's performance on under-resolved (base) meshes, the grid is intentionally coarse. Gray symbols depict the discrete initial solution in fig. 3.22. From a mathematical point of view, the case represents a Riemann problem. The semi-analytical reference solution is available from Anderson [5].

Figure 3.22 compares analytical and numerical solution at $t = 0.1$ ms for level 0 (base mesh) as well as level 2 adaptive mesh refinement. Being the direct outcome of the finite-volume method, cell mean values (blue symbols) are plotted without the usual smoothing in the post-processing step. Thanks to the approximate Riemann solver (HLLC scheme including multi-dimensional gradient limiters as explained in sec. 3.3.3), satisfying results are achieved even on the coarse base mesh. Advantages of the density-based architecture, compared to pressure-based solvers, are extensively discussed by Ettner [79]. In the shock tube case, AMR is mainly controlled via the influence of density gradients on the refinement criterion 3.131. AMR clearly improves accuracy of the numerical solution, especially regarding the discontinuous nature of contact wave and shock. The propagation speed of the different characteristic waves is reproduced correctly. Obviously, AMR was successfully combined with the approximate Riemann solver for the calculation of convective fluxes. It can be concluded that the AMR-enhanced solver serves as a solid basis for the description of transonic and supersonic reactive flows.
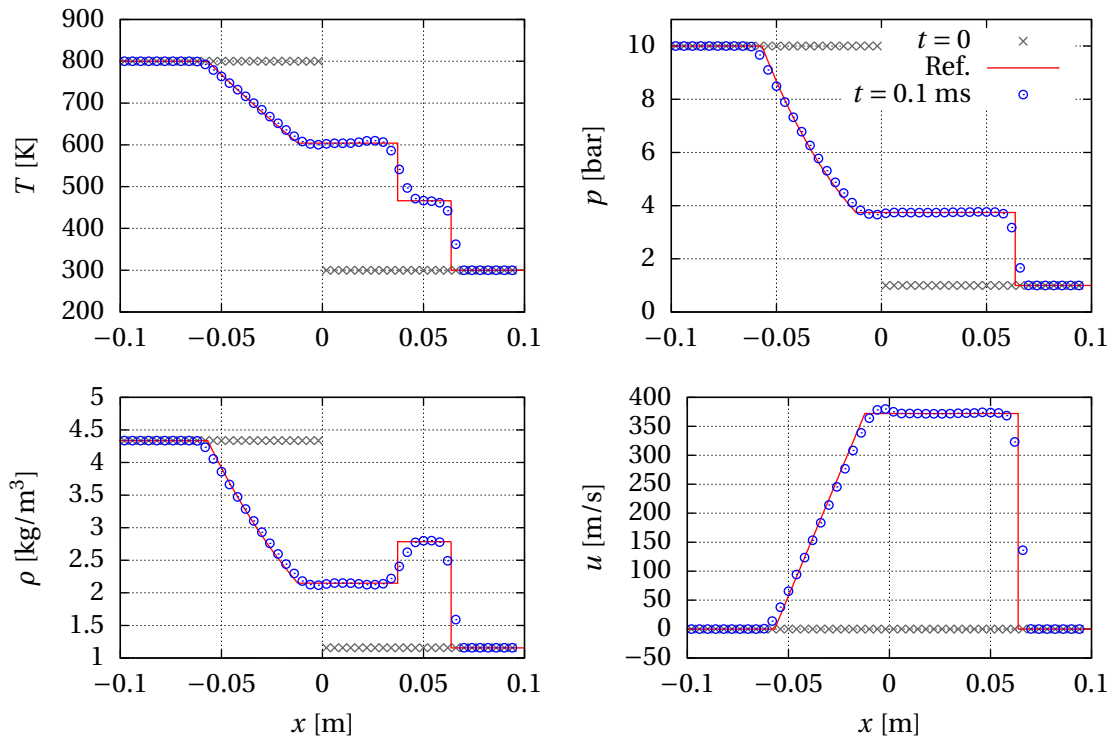
(a) Without adaptive mesh refinement (level 0)
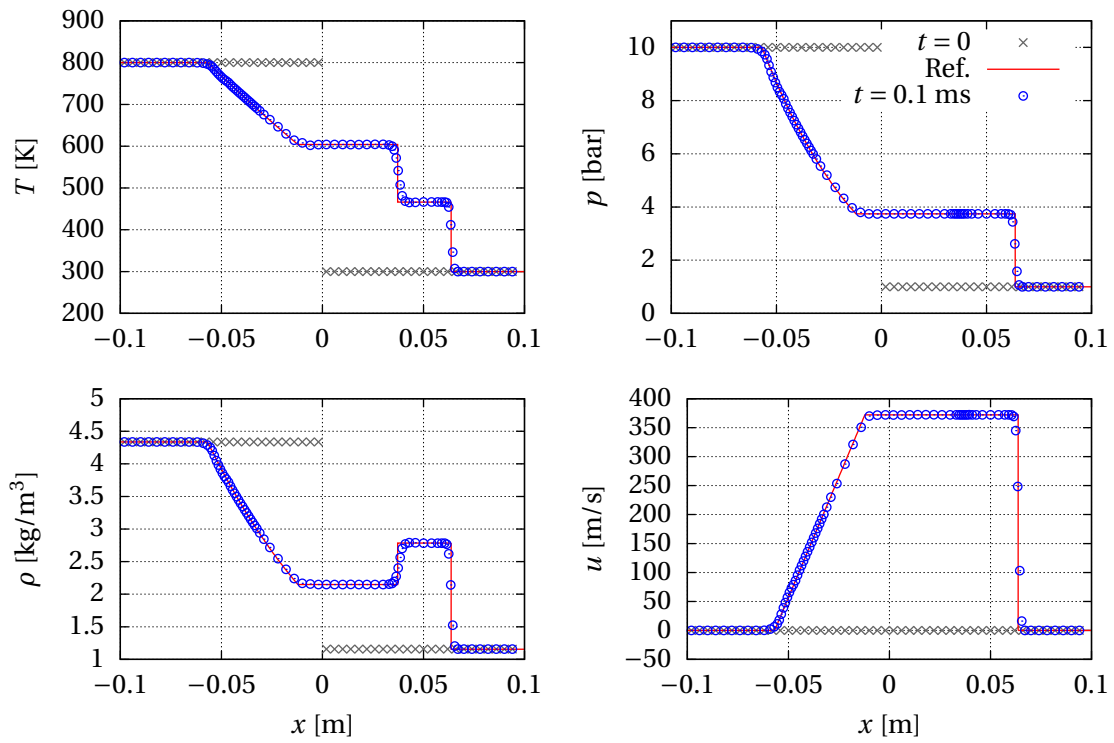
(b) Level 2 adaptive mesh refinement

Figure 3.22: Shock tube solution of temperature T, pressure p, density ρ and velocity u at $t = 0.1$ ms: Comparison of analytical (red line) and numerical solution (blue symbols); Discrete initial solution depicted by gray symbols

3.7 Parallel performance

Thanks to the modern solver architecture of OpenFOAM, almost all procedures can be executed in parallel. Parallelization in OpenFOAM is actually based on the domain decomposition technique, i.e. each processor executes operations only on a portion of the overall domain. Communication between processors is realized via the OpenMPI library. To minimize the corresponding information transfer, the commonly applied partitioning method tries to optimize the boundary-to-volume ratio of computational cells on each processor core.

Massive parallelization is seen as the paradigm of choice in dealing with industry-scale computational domains like reactor containments. Despite efficient numerical techniques, enormous computational cost results from the high number of computational cells as well as the high number of time steps. Operated by the Leibniz Supercomputing Center in Garching (Germany), the SuperMUC high performance cluster proved to be an adequate platform. The system is equipped with Intel Xeon processors and features a peak performance of more than 3 PetaFLOPS. Using up to 1024 cores, turnaround times could be kept below two days in any of the presented simulations.

To avoid the evaluation of numerically stiff source terms (of the Arrhenius type), required quantities of chemical kinetics are provided to the solver in the form of correlations or look-up tables. Chemical reaction usually takes place only in a small portion of the overall domain for explosion problems. If chemistry was calculated during runtime, most processors would be waiting for a few processors engaged with the costly evaluation of combustion source terms. Heavy load imbalances would consequently drop the overall performance. The code is already optimized for parallel execution in this regard.

However, a performance issue arises from two essential numerical techniques. Both adaptive mesh refinement and explicit flame tracking involve unbalanced processor loads in a parallel environment. The situation is implicitly illustrated by fig. 3.10 showing a non-uniform distribution of refined regions and front cells in the domain. Iterative interface positioning is only necessary in front cells that are intersected by the reactive discontinuity. According to the VoF-based algorithm, the number of iterations and therefore computational costs are naturally unequal. Relating to AMR, an example of poor processor balance is given on the left side of fig. 3.23. A simplified two-dimensional quadtree structure is shown instead of the actual three-dimensional octree structure for demonstration purposes. The highest refinement level and also the highest cell count occurs for processor 3. Assuming that no flame is present in all four sub-domains, its load is surely higher than for the remaining processors. Depending on the dynamically changing position of refined zones, the number of cells per core can vary significantly. Since domain decomposition is fixed during runtime, not more than two refinement levels were used in this work.

Specific load balancing measures are currently not implemented. One may think of a dynamic redistribution of processor sub-domains depending on their load. The first question thus concerns the measurement of load. It might be possible to use a combined criterion counting the number of normal cells as well as the number of front cells weighted by VoF iterations. The following procedure would be straightforward: Stop and save the simulation, apply a slightly modified partitioning algorithm as for initial domain decomposition, load and resume the simulation. Unfortunately, the partitioning algorithm itself
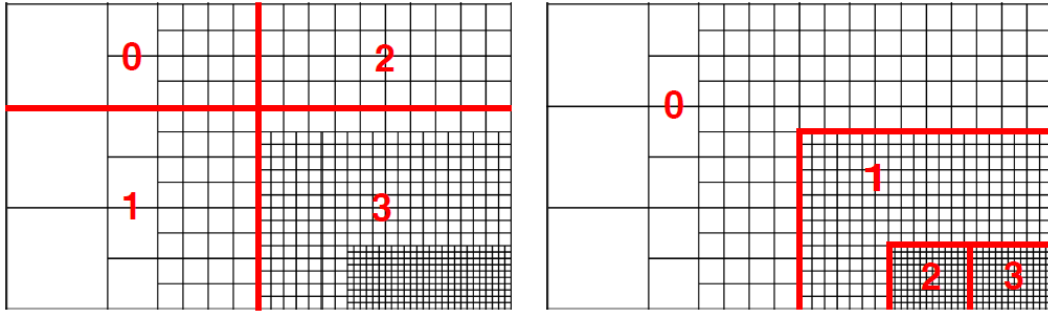
Figure 3.23: The load balancing issue in two dimensions: Poor processor balance on the left and better processor balance on the right; Processor indexes and interfaces colored red; Adapted from [192]

is usually a serial process. A truly parallel partitioning algorithm would be necessary to avoid respective overheads in a massively parallel environment. Similar to the AMR algorithm, such procedure could be executed periodically but certainly not after each time step. A possible well-balanced domain decomposition is indicated on the right side of fig. 3.23. The number of cells per core is now comparable. Load balancing of a dynamic mesh method in OpenFOAM is examined by Liefvendahl and Troëng [167]. Combined with VoF and AMR, an advanced parallel load balancing technique is available in the GERRIS two-phase flow solver which is restricted to structured meshes [1]. Comparable serial and parallel efficiency can hardly be achieved with general-purpose CFD codes based on unstructured meshes. Apart from dynamic load balancing, there is room for improvement in terms of a fully parallelized work-flow (including not only parallel execution of the CFD solver itself but also parallelized data input and output as well as pre- and post-processing) which is currently missing.

A quantitative speedup study is omitted because the behavior changes significantly in the course of one simulation run. Mainly because of VoF and AMR, parallel efficiency might be completely different at the beginning and at later stages of explosion progression. General conclusions based on particular situations could be highly misleading. Further influencing factors comprise the particular problem setup, the computing platform and the Message Passing Interface (MPI) software distribution. Anyway, the performance decreases when the communication between processors at their interface is increasing disproportionately. As a rule of thumb, the number of cells per core should not fall below $5 \cdot 10^3$ to achieve nearly linear speedup. An adequate boundary-to-volume ratio of processor domains is thus guaranteed for the most extensive simulations in chap. 5.

According to Amdahl's law [3], the speedup is also theoretically limited by the inherently serial part of the solver f. Assuming that the remaining part $1 - f$ scales perfectly (which is never the case for above mentioned reasons), the computing time T_n on n processors is given by

$$T_n = f T_1 + \frac{1-f}{n} T_1. \tag{3.132}$$

The speedup compared to serial execution S_n is consequently bounded:

$$S_n = \frac{T_1}{T_n} = \frac{1}{f + \frac{1-f}{n}} < \frac{1}{f}. \tag{3.133}$$

Further grid partitioning is counterproductive once the asymptotic limit is approached.

4 Validation on industry scale: RUT facility

Mainly for two reasons, the RUT facility located at Kurchatov Institute, Moscow region [65] has been chosen for the validation of the computational model. First, the well instrumented (photo diodes and pressure transducers) facility allows for detailed investigation of the largest ever conducted indoor DDT experiments. Second, its geometrical scales are closer to reactor dimensions than of any other large-scale explosion experiment: e.g. length of RUT facility $\approx$ 62 m compared to diameter of Konvoi reactor $\approx$ 56 m. Being the ultimate goal of the solver development, final application to a Konvoi-type pressurized water reactor is shown in sec. 5.

Three different cases are investigated regarding geometry, mixture composition and type of ignition. The selection comprises experiments of different character in terms of the underlying mechanism and hazard potential. The ascending order reflects the level of challenge posed to the numerical model:

1. RUT 09: direct detonation initiation,

2. RUT 22: DDT mode A,

3. RUT 16: DDT mode B.

Detailed specification of the cases is available in sec. 4.1. Depending on the setup (configuration 22 or 16 in tab. 4.1), the observed mechanism behind DDT differs. As reflected in sec. 2.4, Klein et al. [140] generally distinguish between DDT by shock focusing e.g. near corners (strong solution or mode A) and DDT originating from hot spots and ultimately local explosions in the vicinity of the turbulent flame brush (weak solution or mode B). Latter can be triggered by shock-flame interaction or the local explosion of unburned pockets enclosed in burned mixture for instance. The simulation results of all three cases are presented and discussed in sec. 4.2.

Further investigations include the influence of mixture inhomogeneity (sec. 4.4) as well as the evolution of flame surface area on macroscopic and microscopic level (sec. 4.3). The issue of dimensionality reduction is discussed in sec. 4.5. Grid dependency is finally studied in sec. 4.6.

4.1 Experiment and computational setup

Performing three-dimensional [100] instead of two-dimensional [82] simulations of laboratory-scale DDT experiments (undertaken by Vollmer et al. [267] in the GraVent facility) had a relevant influence on the flame acceleration process. Dorofeev et al. [65] further conclude that multi-dimensional effects are an integral part of the DDT phenomenon.

Despite significantly higher computational cost, a three-dimensional model is therefore preferred to represent the complex geometry of the RUT facility visualized in fig. 4.1.

The first channel (length ≈ 35 m, height 2.3 m, depth 2.5 m) causes effective flame acceleration via turbulence generation in the wake of obstacles etc. and is followed by a sudden jump in cross-section. A curved ramp (second channel) succeeds the canyon (length ≈ 10.5 m, height 4 m) after a sudden decrease in cross-section. It is thus possible to examine various influences on flame acceleration and DDT, such as obstructions, transverse expansion, shock focusing, shock-flame interaction etc. The three geometrical variants in fig. 4.1 result from obstacle arrangement and complete closure (RUT 09) or opening (RUT 22 and 16) of the baffle plate between the first channel and the canyon section. For better interpretation, beginning and end of the canyon are indicated by straight lines in the subsequent plots describing the flame acceleration etc.

Geometrical details (e.g. chamber bevels or obstacle slits due to constructional reasons), which are expected to be important in terms of flame acceleration, are taken from Moser [193] and Breitung et al. [42]. Measurement infrastructure and further (turbulence-inducing) channel installations like obstacle strutting had to be neglected due to their small dimensions and insufficient documentation.

The most important parameters characterizing the investigated reference configurations are summarized in tab. 4.1. Supplementary generic configurations (i.e. not investigated experimentally) vary in terms of mixture composition, geometry and discretization. Deviations to the reference configurations are explicitly mentioned in the corresponding sections.

The computational domain is discretized by (distorted) hexahedral cells such that the confining geometry is well approximated, and such that a preferably uniform mesh is assured regarding the discretization error. Creating a tetrahedral mesh of equivalent resolution would yield a significantly higher cell count. Additionally, tetrahedral meshes are inferior from the discretization schemes point of view due to their limited neighborhood connectivity [114]. There is no specific refinement towards walls. Accurate reproduction of boundary layer effects (e.g. microscopic interaction with flames or shocks) is clearly out of the scope of this work. Wall functions guarantee reasonable mean values in the wall-adjacent cell layer.

Table 4.1: Investigated RUT configurations

Configuration	09	22	16
Ignition	TNT	Spark	Spark
Detonation initiation	Direct	DDT mode A	DDT mode B
Vol. hydrogen concentration [%]	25.5	14	12.5
Obstacle count	-	6	12
Obstacle spacing [m]	-	5	2.5
Obstacle blockage ratio [%]	-	60	30
Fluid volume [m^3]	242.5	423.7	423.9
Cell count (reference mesh)	646,278	1,142,822	1,121,815
Average cell size [cm]	7.21	7.18	7.23

(a) Configuration 09


(b) Configuration 22

(c) Configuration 16
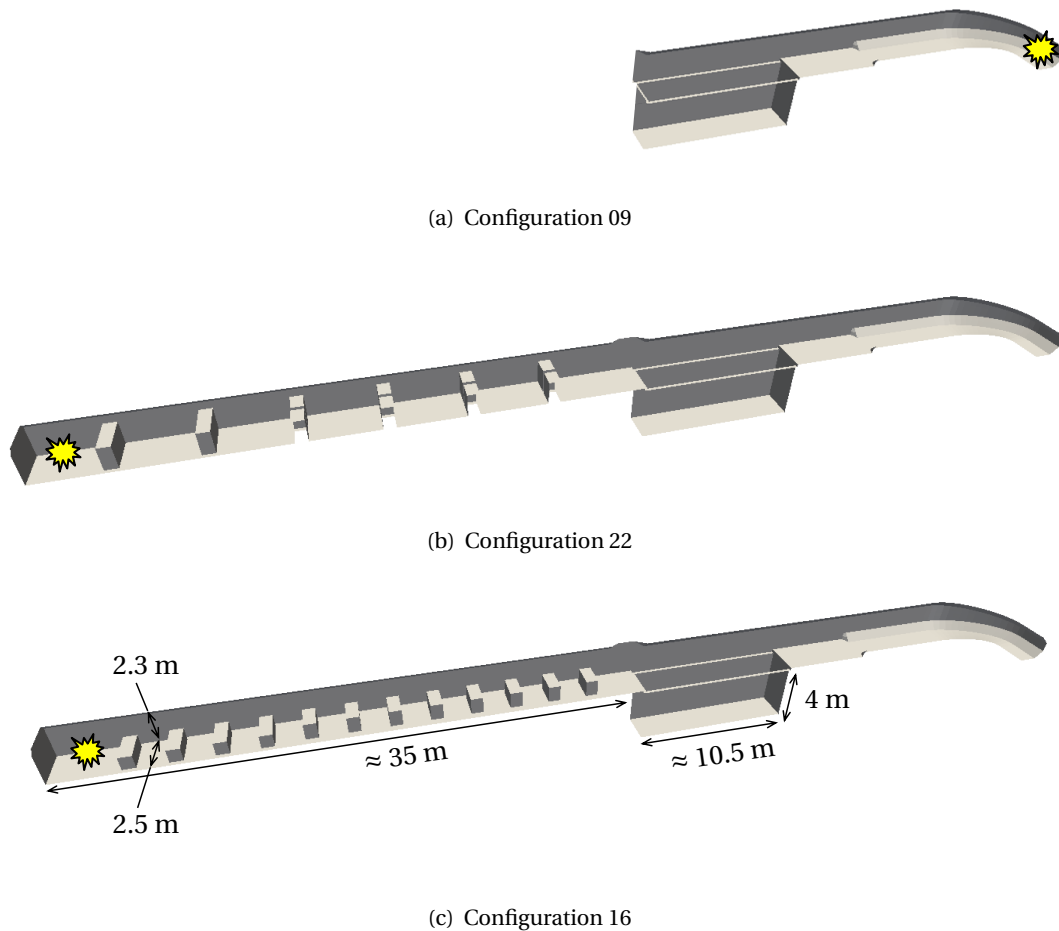
Figure 4.1: Investigated RUT geometries; From left to right: obstructed first channel, canyon, curved second channel; Ignition location indicated by the yellow explosion symbol

The average cell size of the reference meshes, ≈ 7 cm, is apparently much larger than resolution requirements for detailed DDT simulations would suggest, cf. tab. 1.1. The resolution of first principle combustion simulations is usually given relative to the laminar flame thickness or half-reaction length. It is by far not possible to resolve such characteristic scales in a full-scale model of the RUT facility. However, it may not be necessary for safety analysis to resolve the micro-structure of all underlying processes as the subsequent results demonstrate. The method has to prove its reliability for under-resolved meshes in order to be applicable to large-scale scenarios. The significance of sub-grid models (for gas-dynamics, turbulence, chemical reaction etc.) in the URANS framework becomes obvious. Another limitation on the mesh density arises from the temporal discretization. It should be kept in mind that the discrete system of equations has to be solved for each time step. The number of time steps can be substantial given the strong (global) unsteadiness of the problem. Much finer meshes are not reasonable anyway since the application to realistic scales would then demand access for supercomputers which are not broadly available to industry.

Adiabatic walls are imposed at all boundaries including the vent opening at the end of the second channel which had no effect on the transition to detonation according to Dorofeev et al. [65]. Heat losses to the walls are assumed to be negligible for the fast explosion

processes studied. The situation is different for moderate propagation speeds. Despite little effect on flame-tip trajectories, heat transfer modeling is important to accurately reproduce pressure profiles in this regime. Especially pressure decay, after reaching the peak value, is underestimated without heat losses [280]. In any case, adiabatic walls must be understood as a conservative assumption in terms of explosion severeness. Homogeneous Neumann boundary conditions are imposed for all remaining transported quantities.

Initial values of turbulence-characterizing quantities k and ω are chosen comparably low, and in any case, are not crucial as the main stage of flame acceleration is dominated by the turbulence production behind obstacles. Basically, some initial turbulence must have been present since mixing fans were used until shortly before ignition to assure a nearly homogeneous mixture. A mixing accuracy of 0.1 % in terms of the hydrogen content is reported [65]. The turbulence level was not measured however. The applied uniform initial values were identical for all simulations: specific turbulent kinetic energy of $k = 0.1 \ \mathrm{m^2/s^2}$ (equivalent to r.m.s velocity fluctuation of $u' = 0.258 \ \mathrm{m/s}$) and eddy frequency of $\omega = 10 \ \mathrm{Hz}$. The turbulent dissipation rate is implicitly specified as $\varepsilon = 0.09 \ \mathrm{m^2/s^3}$. According to eq. 3.113, these values correspond to an integral turbulent length scale of $l_T = 0.351 \ \mathrm{m}$ which is in the order of obstacle dimensions. Temperature and pressure of the initially quiescent mixture are set to 293 K and 1.013 bar, respectively. Stoichiometry-dependent initial values of flame wrinkling Ξ are determined by eqs. 3.108 and 3.115. It is assumed that flame instabilities develop immediately after ignition.

The ignition location depends on the geometrical setup, see fig. 4.1. Two types of ignition are examined. For spark plug ignition (weak ignition), sufficient flame acceleration is a prerequisite to reach critical conditions for the onset of detonation. In contrast, a detonation can directly be initiated (strong ignition) by means of a high explosive charge, 200 g TNT in case of RUT configuration 09. The delicate issue of accurate ignition modeling is avoided in both cases by starting at a predefined flame front, i.e. by patching a sphere of 0.5 m radius around the ignition spot to the completely burned state. It is important to note that inappropriate modeling of ignition conditions might shift the flame trajectory in time but it does not significantly distort the flame acceleration behavior. In case of weak ignition, adiabatic flame temperature (calculated by CANTERA [95]) is imposed. Assuming isobaric combustion, pressure remains unchanged. As it is equally challenging to accurately reproduce the overdriven state due to TNT explosion and since the focus is on the subsequent stage of steady detonation propagation, strong ignition is approximated by patching with CJ temperature and pressure of the mixture (calculated by the EDL Shock and Detonation Toolbox [83]). A similar procedure is followed by Heidari et al. [104].

An array of numerical pressure gauges is placed at the same locations as in the experiment. A lower line (sensors 2 to 5) as well as an upper line (sensors 7 to 12) is installed at the channel side walls. Two sensors are additionally placed at the beginning (sensor 1) and end of the canyon (sensor 6). Corresponding coordinates are listed in tab. 4.2. Figure 4.2 shows the location of pressure gauges in the RUT 09 geometry as an example.

Table 4.2: Coordinates of pressure gauges in the RUT facility

| Sensor	x [m]	y [m]	z [m]
Domain bounding box	[0.0;62.5]	[−4.0;2.3]	[−1.25;5.3]
01	35.35	−1.0	0.00
02	35.62	−2.5	1.05
03	38.09	−2.5	1.05
04	42.10	−2.5	1.05
05	44.09	−2.5	1.05
06	45.90	−2.5	0.00
07	35.35	1.0	−1.25
08	41.01	1.0	−1.25
09	43.59	1.0	−1.25
10	46.29	1.0	−1.25
11	52.49	1.0	−1.25
12	52.99	1.0	−1.25
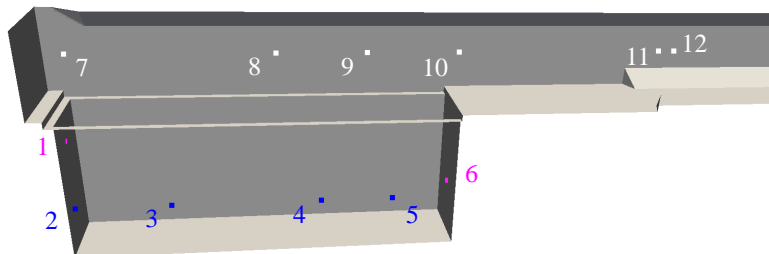
Figure 4.2: Pressure gauges in the RUT facility: Canyon start and end colored purple, lower line (installed at the front wall) colored blue, upper line (installed at the rear wall) colored white

4.2   Results and discussion

4.2.1   Configuration 09

The large-scale confined detonation experiment RUT 09 was carried out in the framework of the 'Safety of Hydrogen as an Energy Carrier (HySafe)' network. Unlike DDT configurations 22 and 16, configuration 09 has been investigated by several authors before and can be considered a standard validation problem in the field of research. In the context of this work, configuration 09 is supposed to validate the volumetric reaction part of the combustion model since self-sustaining detonation propagation is mainly driven by successive auto-ignition.

In their CFD detonation model, Heidari et al. [104] and Efimenko [283] use the classical approach based on Euler equations and single-step Arrhenius kinetics. Parameters of the chemical reaction model have to be tuned depending on the grid size to obtain correct detonation speed and pressure. In the ansatz of Zbikowski et al. [290], the reaction rate is calculated by the so-called 'gradient method' for which the detonation propagation velocity has to be specified explicitly. Yáñez et al. [283] apply the so-called 'Heaviside detonation model' to obtain nearly grid-independent propagation characteristics. The spatial resolution is similar in all cases. Cell sizes are on the order of several centimeters. None of the simulations intends to capture the intrinsically unstable micro-structure of the detonation front, cf. sec. 2.5. The focus is rather on the global propagation behavior for safety analysis. The alternative results presented here can thus be seen as part of a code intercomparison.

By means of pressure fields at the channel rear wall, fig. 4.3 visualizes the sequence of events after strong ignition ($T_{CJ} = 2807.8$ K and $p_{CJ} = 15.3$ bar for 25.5 % of hydrogen) near the right end of the channel. A detonation is directly initiated, propagates through the curved part of the channel (5 ms) and diffracts around the backward-facing step into the canyon (10 ms). After reaching the canyon floor, an upward-running reflection develops (between 10 ms and 15 ms). At 15 ms after ignition, the detonation front has already arrived at the left end of the channel, causing a strong reflection which propagates in the opposite direction (20 ms). The process continues, including forward- as well as backward-running secondary reflections in the burned mixture (25 ms and 30 ms).

Quantitative comparison with experimental data (upper line sensors 7 to 11) is provided in fig. 4.4. Experimental pressure recordings are taken from Kotchourko [146], numerical pressure recordings were obtained on the reference mesh specified in tab. 4.1. Separate pressure plots are arranged like a space-time diagram to reflect the characteristic wave propagation behavior. The lowest row (sensor 11) is closest to the ignition location, i.e. shows pressure increase first. The top row (sensor 7) is closest to the left end of the channel where the strong reflection occurs. As an example, three distinct pressure peaks can be observed in the middle row (sensor 9). In chronological order, they belong to detonation front, primary reflection from the canyon floor and primary reflection from the left end of the channel.

Good agreement between simulation and experiment is achieved, especially in terms of the detonation wave and mentioned primary reflections. The velocity of reflected waves in the burned mixture is slightly overestimated. It is noticeable that, unlike in the simulation,

(a) 5 ms

(b) 10 ms

(c) 15 ms

(d) 20 ms

(e) 25 ms

(f) 30 ms
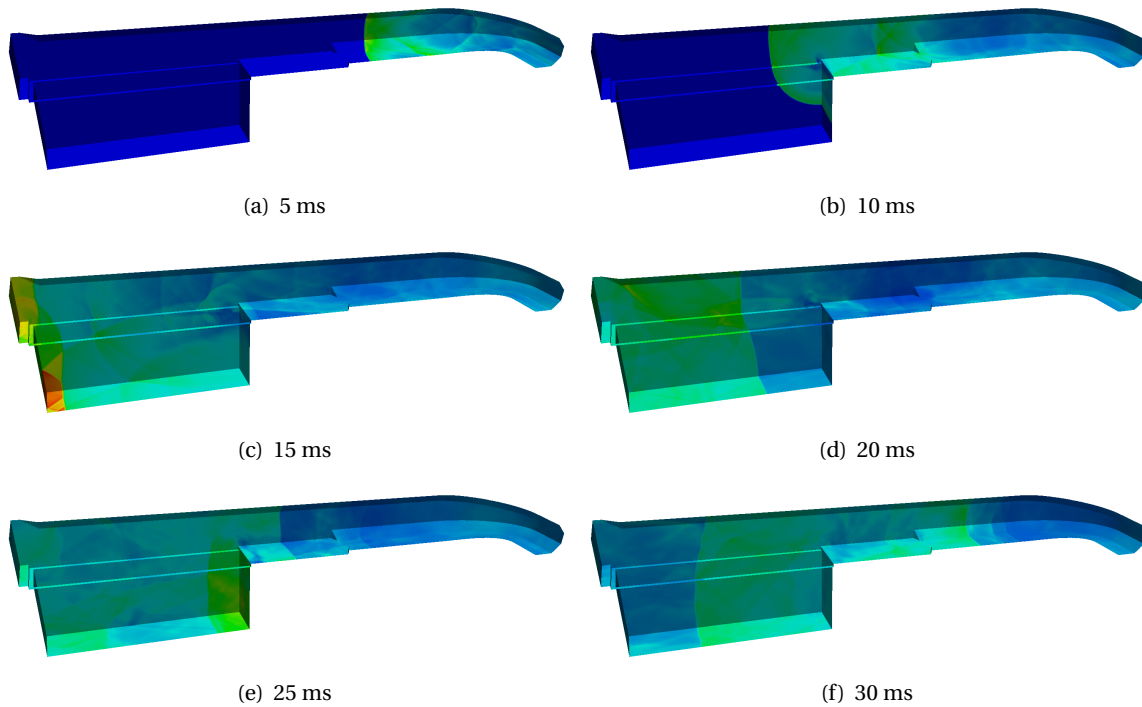
Figure 4.3: RUT 09: Pressure field at the channel rear wall at six points in time after ignition; Rainbow color scale (appendix A) from 1 bar to 30 bar

the experimental pressure level at sensor 11 (lowest row) falls far below the Taylor expansion wave pressure. The observation might be connected to a thermal shock effect of the transducer which can lead to unrealistically low pressure recordings. The phenomenon is intensely discussed by Boeck [28].

Compared to earlier simulations of configuration 09, results are partly of equal and partly of superior quality. Deviations might be explained by the geometrical model. For instance, other than in [104], the model depicted in fig. 4.1 includes geometrical details like chamber bevels. Furthermore, combustion modeling is based on different principles. Contrary to other approaches, the utilized model requires no tuning of the reaction rate, particularly depending on hydrogen content and grid size. The correct detonation speed rather evolves from the heat release that is implicitly given by the change in species composition (at constant internal energy). According to CJ theory (sec. 2.5.1), heat release primarily determines the detonation velocity.

Characteristic pressure levels of one-dimensional detonation theory (von Neumann spike pressure $p_{vN} = 27.4$ bar, Chapman-Jouguet pressure $p_{CJ} = 15.3$ bar and Taylor expansion wave pressure $p_T = 5.7$ bar) are additionally plotted to demonstrate the benefit of performing CFD simulations. In case of complex three-dimensional geometries including detonation diffraction, reflection and focusing due to edges or corners, latter is the preferred technique to determine the pressure load (or even more relevant, the impulse) on the confining structure.

Keeping the coarse reference mesh, the effect of the extended heat release criterion introduced in sec. 3.5.6.3 can be seen in fig. 4.5 (left column). Only the density-based formulation of the extended heat release criterion is applied. The pressure-based formulation
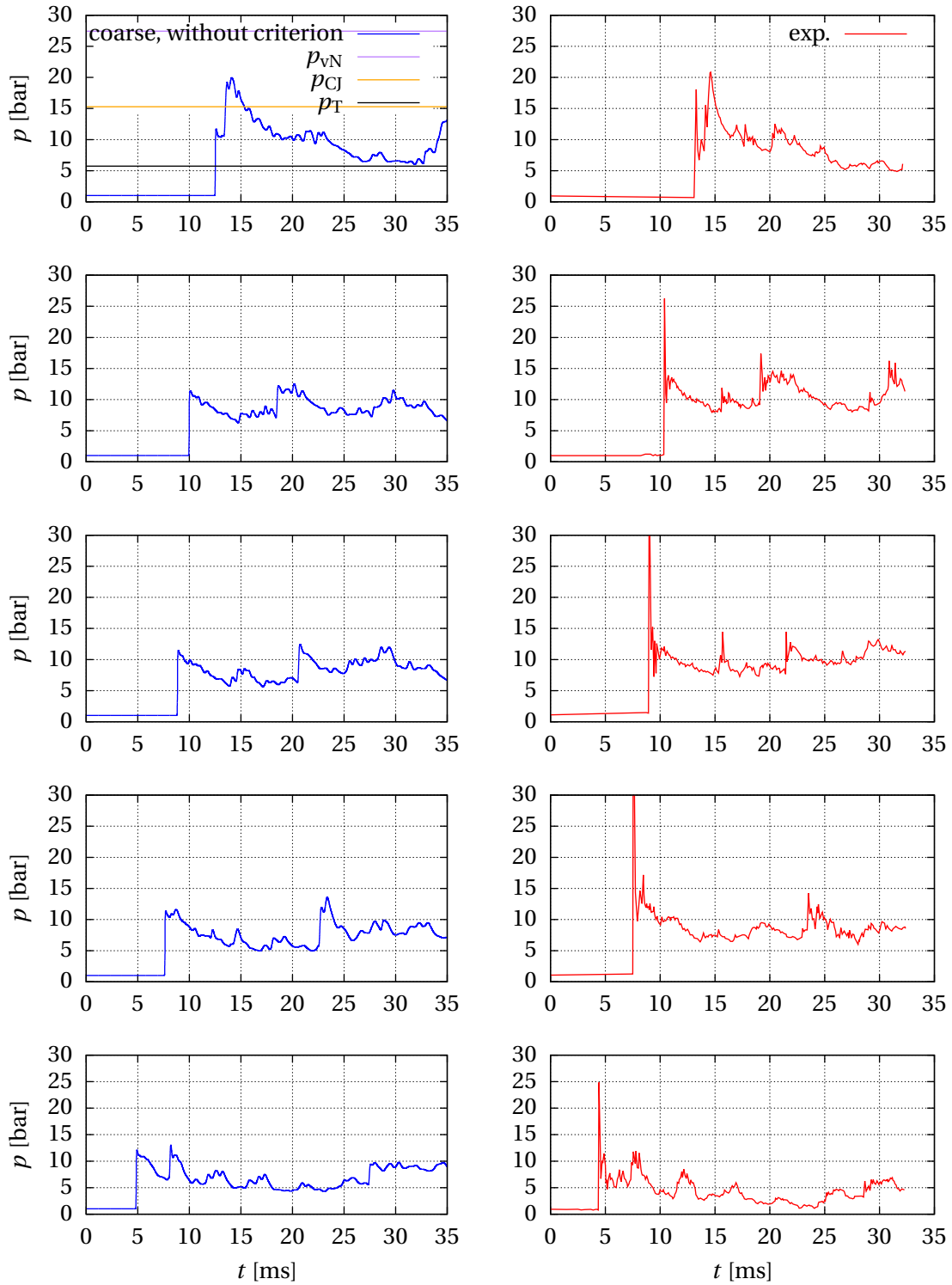
Figure 4.4: RUT 09: Numerical (blue, left column) and experimental (red, right column) pressure recordings at sensors 7 to 11 (top to bottom)

yields similar results. Figure 4.5 (right column) additionally provides simulation results on a finer mesh consisting of 5,572,213 cells. Compared to the reference mesh consisting of 646,278 cells, the average cell size is reduced from 7.21 cm to 3.52 cm. Only here, static uniform mesh refinement is preferred over local adaptive mesh refinement since the refinement criterion 3.131 is designed for DDT simulations. In the latter case, pressure waves in the burned mixture are assumed to be of minor importance and are consequently not refined.

Using approximately ten times more cells leads to a visible, but not significant improvement of pressure profile prediction. Application of the extended heat release criterion clearly improves reproduction of the von Neumann spike without increasing computational costs. However, the extended criterion tends to destabilize the detonation front as discussed in sec. 3.5.6.4 and is therefore not applied in the following DDT simulations. Non-simultaneous activation of the extended heat release criterion in neighboring front cells (not existent in one-dimensional simulations) induces small front topology perturbations which can be amplified over time. For safety analysis, the von Neumann spike can be looked upon as an unnecessary detail due to its short existence. Prediction of correct DDT location, being the ultimate goal of this work, is unaffected since the pseudo-stable shock-reaction coupling (explained in sec. 3.5.6.3) does not yet occur before this event.

The code successfully reproduces key safety characteristics such as detonation speed and associated pressure loads. Due to the encouraging results presented, it is assumed with respect to DDT simulations of configurations 22 and 16 that pressure load prediction is sufficiently accurate if corresponding flame velocity is captured correctly. Reversely thinking, it is not meaningful to compare pressure profiles if reproduction of flame acceleration is poor.

4.2.2 Configuration 22

In the following, the quantitative comparison between simulation and experiment is based on flame-tip trajectories, cf. fig. 4.6 for instance. Although the flame acceleration behavior is basically visible in the space-time diagram, the flame speed v (eq. 2.25) is additionally evaluated to draw direct conclusions about the explosion regime (slow deflagration, fast deflagration, detonation). To improve the interpretation of geometrical influences, v is plotted over the distance from the ignition point x instead of time after ignition t. Unfortunately, this can only be done for the numerical trajectory. From only a few experimental data points, it is hardly possible to derive a continuous and accurate flame speed curve. Whenever the most advanced flame tip proceeds in axial direction, the runtime tracing algorithm appends the x-coordinate of the corresponding cell, i.e. another discrete value, to the trajectory list. Due to the resulting step character of the trajectory $x(t)$, the raw signal of its temporal derivative $v = \dot{x}$ is heavily oscillating. Hence, the raw signal is first rendered monotonic and then approximated by a Bezier curve that connects the end points. The curve's degree is specified by the number of data points. As an important feature and different to most polynomial or spline fitting methods, the data points are generally not lying on the determined Bezier curve. This filtering process is executed in a post-processing step and provides a reasonable approximation of the instantaneous flame speed in axial direction. It removes unrealistic oscillations while preserving essential details. For the sake of clarity, only the computed Bezier curve is in-
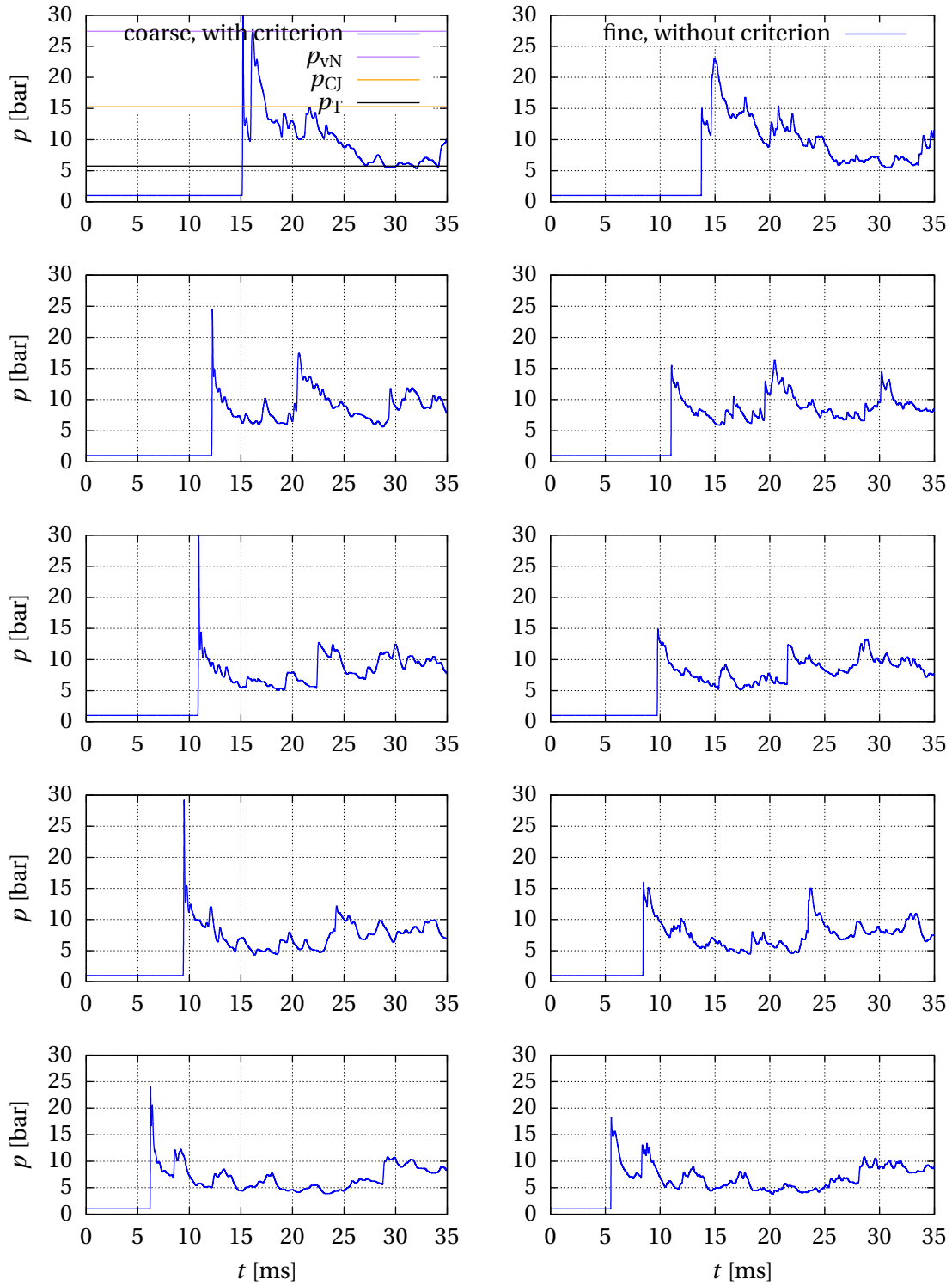
Figure 4.5: RUT 09: Numerical pressure recordings with extended heat release criterion (left column) and on finer mesh (right column) at sensors 7 to 11 (top to bottom)

cluded in subsequent diagrams. It should be mentioned that this combined runtime- and post-processing procedure requires no case-specific adjustments like to mesh resolution. An alternative would be to directly fit the trajectory by a spline and analytically calculate the derivative on that basis. Preliminary test revealed inferior performance though. Especially kinks of the trajectory, e.g. caused by obstacles or DDT, are rounded off. A smooth transition to detonation disagrees with reality.

The numerical results of RUT configuration 22 together with experimental data from Dorofeev et al. [65] are shown in fig. 4.6. The temporal shifting of experimental data facilitates better comparison and does not distort the flame acceleration behavior which is of prior interest for safety analysis. Excellent agreement can be observed between simulation and experiment. The flame gradually accelerates until DDT occurs in the vicinity of the last obstacle. DDT is recognizable by the kink of the flame-tip trajectory in the distance-time diagram as well as the sudden jump of velocity in the velocity-distance diagram. Shortly before DDT, flame velocity is on the order of the products' sound speed ($a_{\mathrm{prod,p}} = 746.0$ m/s) – an observation that agrees well with experiments, cf. sec. 2.4. The development of sufficiently fast 'sonic' or 'choked' flames is considered a necessary requirement for DDT. After the transition process is finished, the detonation front steadily propagates at speeds close to the theoretically predicted Chapman-Jouguet velocity ($D_{\mathrm{CJ}} = 1480.1$ m/s). The velocity-distance diagram provides additional insight into the effect of obstacles. Instead of continuous acceleration, the flame-tip velocity oscillates which is due to the jet behavior when the flow passes each obstacle. The effect of obstacles is further attributed to the influence on flame surface area. Its evolution, on macroscopic as well as microscopic level, is depicted in fig. 4.15.

A detailed look at DDT is presented in fig. 4.7. The three-dimensional view from the outside is preferred over a two-dimensional cutting plane to give an impression of the multi-dimensional phenomenon. In the field of view, obstacles are not blocking the entire depth of the channel but feature a slit at the channel's center line. In the first picture (187 ms), from left-to-right propagating precursor shock waves and the flame are clearly separated,
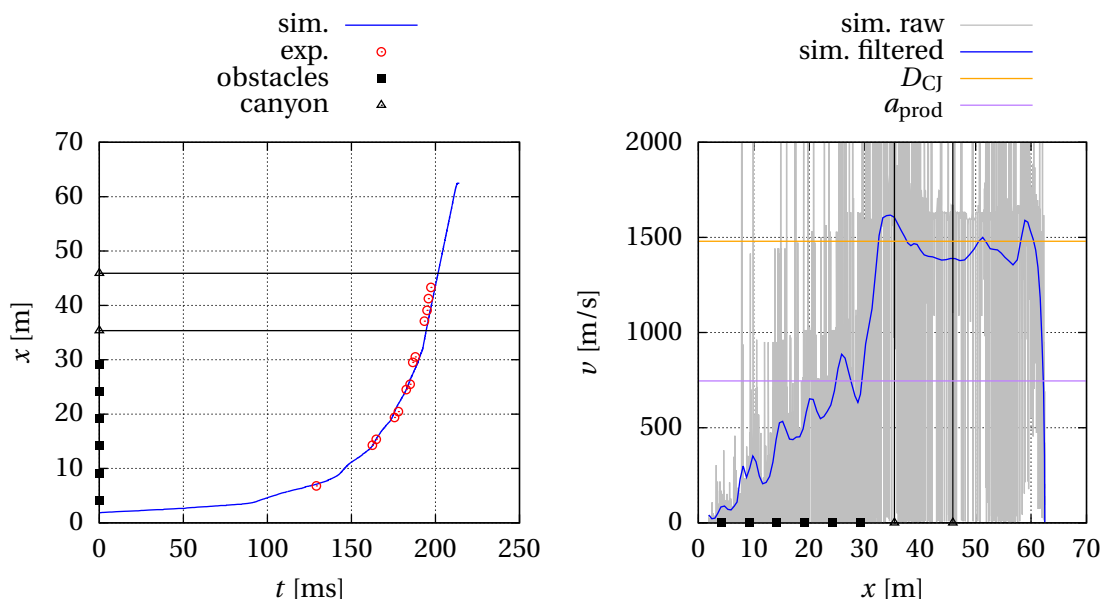

Figure 4.6: RUT 22: Flame-tip acceleration

indicating a deflagration. At 188 ms after ignition, the leading shocks are reflected off the sixth obstacle. The reflection is obviously not strong enough to cause auto-ignition directly at the obstacle (189 ms). Nevertheless, starting from 190 ms, the blast wave emanating from the obstacle corner leads to a local coupling with the flame near the bottom of the channel. The strong backward-propagating wave is known as the retonation wave. After diffracting around the obstacle, the blast wave additionally couples with the forward-propagating flame in the upper part of the channel (192 ms). The resulting overdriven wave is characterized by propagation velocities higher than CJ velocity as can be recognized by the velocity-distance diagram in fig. 4.6. Shortly after, the overdriven wave has overrun the precursor shock waves, eventually leading to a coupling over the entire cross-section of the channel (193 ms). The overdriven wave finally decays to the steady CJ solution, transition to detonation is finished. Detonation and retonation wave are stably propagating in opposite directions (194 ms). The projection of both overdriven and steady detonation solution in the Rankine-Hugoniot diagram is provided in fig. 2.11.

Categorization of the observed DDT mechanism as mode A or mode B is not straightforward. At least in the examined snapshots, no independent flame kernels develop ahead of the main flame. However, since the triggering blast wave does indeed arise from obstacle reflection, the complex multi-dimensional mechanism is rather classified mode A than mode B. Also in the experiment [65], definite conclusions on the detailed mechanism are difficult due to the absence of optical access to the facility. Measurements by conventional techniques suggest rather mode A which corresponds well with the simulation. Contrary to the large-scale RUT facility, its geometrically similar but down-scaled (by a factor of 50) version called miniRUT [66] allows optical access. Shadowgraphy images of a similar obstacle-induced DDT process in the obstructed part of the miniRUT channel (fig. 2.9) support the DDT mode conclusion drawn here. It is known that significantly higher fuel concentrations are necessary to reach critical conditions for the onset of detonation on laboratory scale (effect of scale). The detonation limit is higher by more than 10 % of hydrogen in the miniRUT apparatus. Local phenomena underlying DDT are assumed to be the same though.

Flame tracking, as introduced in sec. 3.4, comes at additional cost of course. Figure 4.8 quantifies the relative increase in computational effort which scales with the number of front cells in the domain. Only in the close vicinity of the flame, the front tracking algorithm is executed. To reflect the dynamic behavior, the current ratio of front cells N to the overall cell count n in the domain is plotted versus the flame-tip position x (analogous to the velocity-distance diagram in fig. 4.6). The curve scales well with the macroscopic flame surface area as can be identified by the flame surface analysis of RUT 22 presented in fig. 4.15. Due to the iterative algorithm, computational cost is indeed high for front cells but their relative number usually remains at an acceptable level. A maximum of $\approx 2\%$ appears in this case. Consequences on parallel efficiency are discussed in sec. 3.7.

4.2.3   Configuration 16

An overview of the results is given in fig. 4.9. Unfortunately, experimental data points for the canyon section are missing in the original publication by Dorofeev et al. [65]. The simulation somewhat underestimates flame acceleration in this case. DDT does not occur for the same hydrogen concentration as in the experiment (12.5 %, $a_{\mathrm{prod,p}} = 714.6\,\mathrm{m/s}$,

(a) 187 ms; Scale from 1 bar to 10 bar

(b) 188 ms; Scale from 1 bar to 10 bar

(c) 189 ms; Scale from 1 bar to 30 bar

(d) 190 ms; Scale from 1 bar to 30 bar

(e) 191 ms; Scale from 1 bar to 30 bar

(f) 192 ms; Scale from 1 bar to 30 bar

(g) 193 ms; Scale from 1 bar to 30 bar

(h) 194 ms; Scale from 1 bar to 30 bar
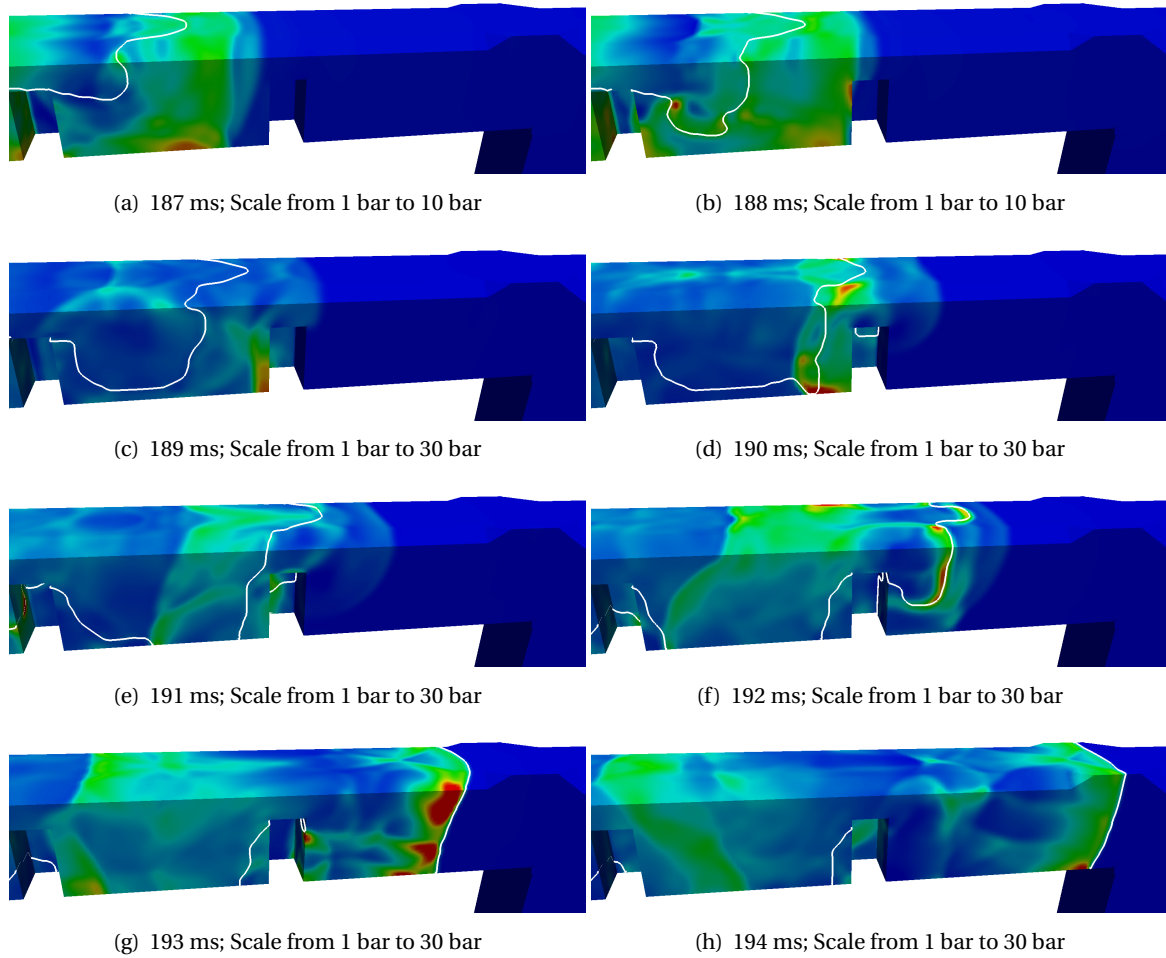
Figure 4.7: RUT 22: DDT by interaction with the sixth obstacle; Pressure field at eight points in time after ignition; White-colored contour line indicating the flame front; Rainbow color scale according to appendix A
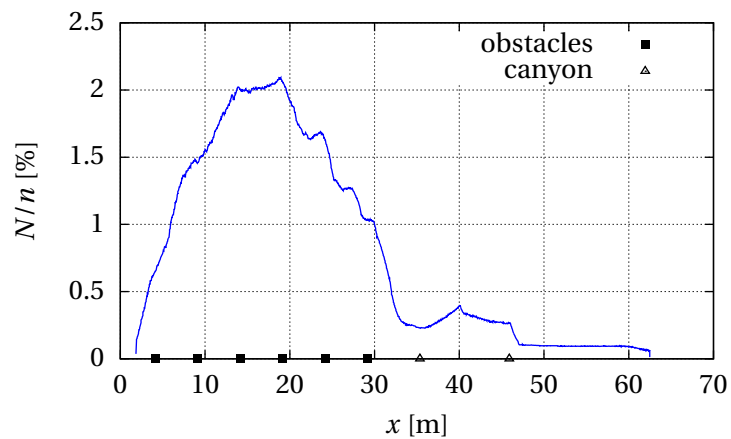

Figure 4.8: RUT 22: Evolution of the normalized front cell count (number of front cells N relative to overall cell count n in the domain)

D_{CJ} = 1411.9 m/s). Flame velocity remains below the products' sound speed at all times. Due to recurrent interaction with strong pressure waves reflected from both ends of the channel, the flame-tip trajectory shows several kinks within the second channel. This behavior is probably less pronounced in the experiment since the vent opening at the end of the second channel is neglected in the simulation. Whereas a deflagration decelerates when passing the canyon (momentum loss due to transverse expansion), a stable detonation as in fig. 4.6 continues to propagate at constant velocity independent of changes in cross-section thanks to its self-sustaining mechanism. Under certain conditions, depending on the ratio of cross-section to detonation cell width, failure of the detonation due to diffraction effects may also occur.

To enforce DDT for this geometrical configuration, insufficient reproduction of flame acceleration is compensated by an artificially increased mixture reactivity. The molar hydrogen concentration is raised by 1 % to 13.5 % ($a_{prod,p}$ = 735.6 m/s, D_{CJ} = 1457.6 m/s). Fine tuning the reaction rate model is not regarded an option due to the lack of universal validity and scientific justification. As a consequence, flame acceleration corresponds better to the RUT 16 experiment, cf. fig. 4.10. The evidently faster flame acceleration underlines the strong sensitivity on hydrogen concentration close to the lower detonation limit which is well-known from experiments. DDT now occurs in the canyon section at a flame velocity close to the products' speed of sound.

In the original publication, the mechanism behind DDT in configuration 16 is analyzed by means of pressure recordings and two-dimensional front reconstructions from a photo diode matrix installed in the canyon (fig. 4.11). The authors conclude that the onset of detonation did not directly result from the reflection of the leading shock at the canyon end wall – a mechanism that was observed in the down-scaled miniRUT apparatus and illustrated by shadowgraphy images [66]. Instead, in the large-scale facility, DDT was triggered by local explosions in the close vicinity of the flame brush, i.e. DDT mode B. This particular experiment represents the lowest ever measured detonation limit (12.5 %) of
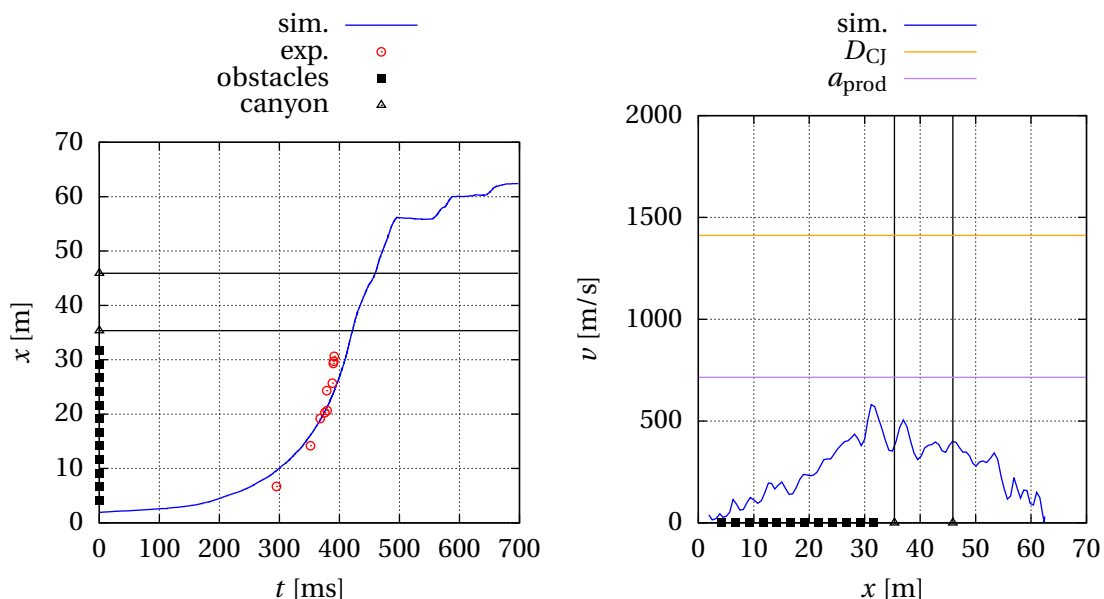
Figure 4.9: RUT 16: Flame-tip acceleration
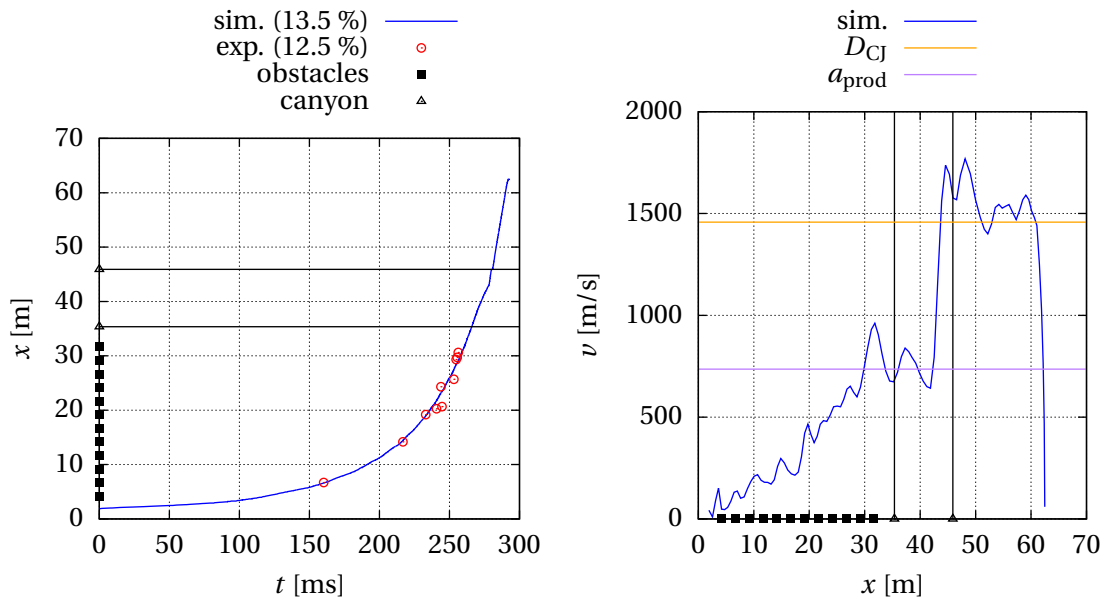
Figure 4.10: RUT 16 with increased hydrogen content of 13.5 %: Flame-tip acceleration

hydrogen-air mixtures. For laboratory-scale facilities, the lower detonation limit usually is several percent of hydrogen higher (minimum of $\approx$ 15 %) [65].

(a) Primary combustion wave

(b) Secondary blast wave; Numbers quantify local wave velocities in m/s
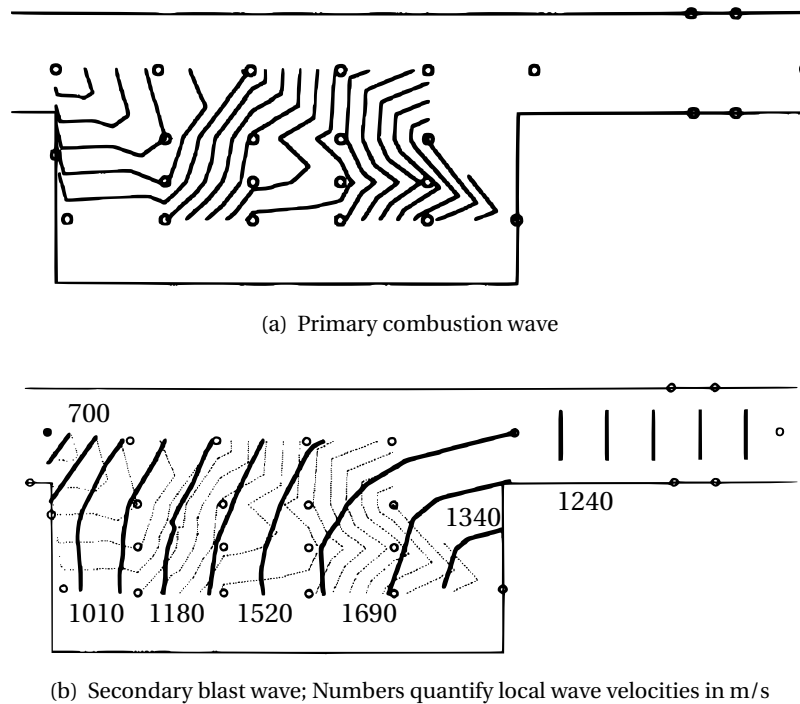
Figure 4.11: RUT 16: Two-dimensional front reconstructions from photo diode measurements (small circles) in the experiment; Time interval between lines is 0.91 ms; Reproduced from [65]

The mechanism in the simulation (fig. 4.12) is similar to, but not exactly the same as in the experiment (fig. 4.11). Following the turbulent recirculation structure behind the backward-facing step, a strong downward motion of the flame can be observed after entering the canyon section (274 ms). Although less pronounced than in the simulation, this behavior also emerges in the experiment (recognizable by comparably large distance between temporally equidistant front lines). The sharp precursor shock is already reflected off the canyon bottom, shortly before interacting with the primary combustion wave. At 276 ms after ignition, a distinct pressure peak can be identified in the close vicinity of the flame. It can further be seen that the reflected shock propagates faster in the burned mixture than in the unburned mixture. Speed of sound differs approximately by a factor of two in both regions. Two ms later, a local explosion has formed in the vicinity of the pressure peak, eventually catching up with the Mach stem of the precursor shock at the bottom of the canyon. The spreading local explosion gets reflected off the canyon end wall (280 ms) which results in a secondary blast wave propagating in backward and upward direction (282 ms) – similar to the experiment. In the last picture (284 ms), the over-driven detonation wave finally overruns the precursor shock in the second channel and relaxes to steady CJ propagation.

A spatially one-dimensional but temporally continuous visualization of the process is depicted in fig. 4.13. Transient pressure recordings are shifted in space according to the x-coordinate of the sensor position. Due to the non-uniform development in transverse direction, there is naturally a discrepancy between upper (top picture) and lower line sen-

(a) 274 ms; Scale from 1 bar to 15 bar

(b) 276 ms; Scale from 1 bar to 15 bar

(c) 278 ms; Scale from 1 bar to 30 bar

(d) 280 ms; Scale from 1 bar to 30 bar

(e) 282 ms; Scale from 1 bar to 30 bar

(f) 284 ms; Scale from 1 bar to 30 bar
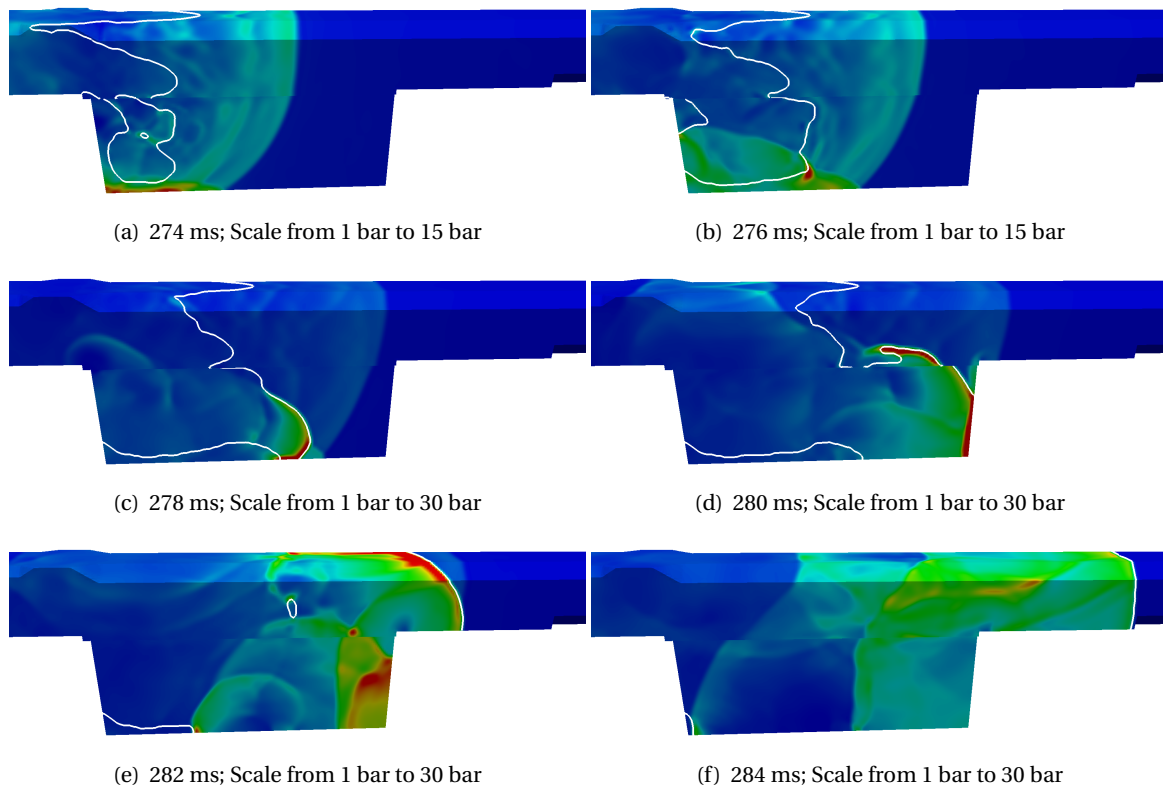
Figure 4.12: RUT 16 with increased hydrogen content of 13.5 %: DDT in the vicinity of the flame in the canyon section; Pressure field at six points in time after ignition; White-colored contour line indicating the flame front; Rainbow color scale according to appendix A

sors (bottom picture). The first kink of the superimposed flame-tip trajectory relates to DDT whereas the second kink is caused by the forward-facing step. Note that the canyon section ranges approximately from $x = 35$ m to $x = 46$ m. The dynamic explosion behavior is well reflected by the combination of both data sources. Until DDT occurs close to the canyon floor, continuous steepening of pressure waves in the unburned mixture is observed. Characterized by an abrupt pressure increase and proximate flame coupling, the detonation wave propagates in the second channel. In the burned mixture, a complex system of weak and strong pressure waves can be identified. The retonation wave and the strong reflection from the canyon end wall particularly stand out.

DDT mode B seems to be more ambitious to simulate than DDT mode A. Klein et al. [140] have drawn similar conclusions. The reason is probably connected to several flame instabilities (cf. sec. 2.3.2) that are crucial but not adequately treated (modeled or resolved).
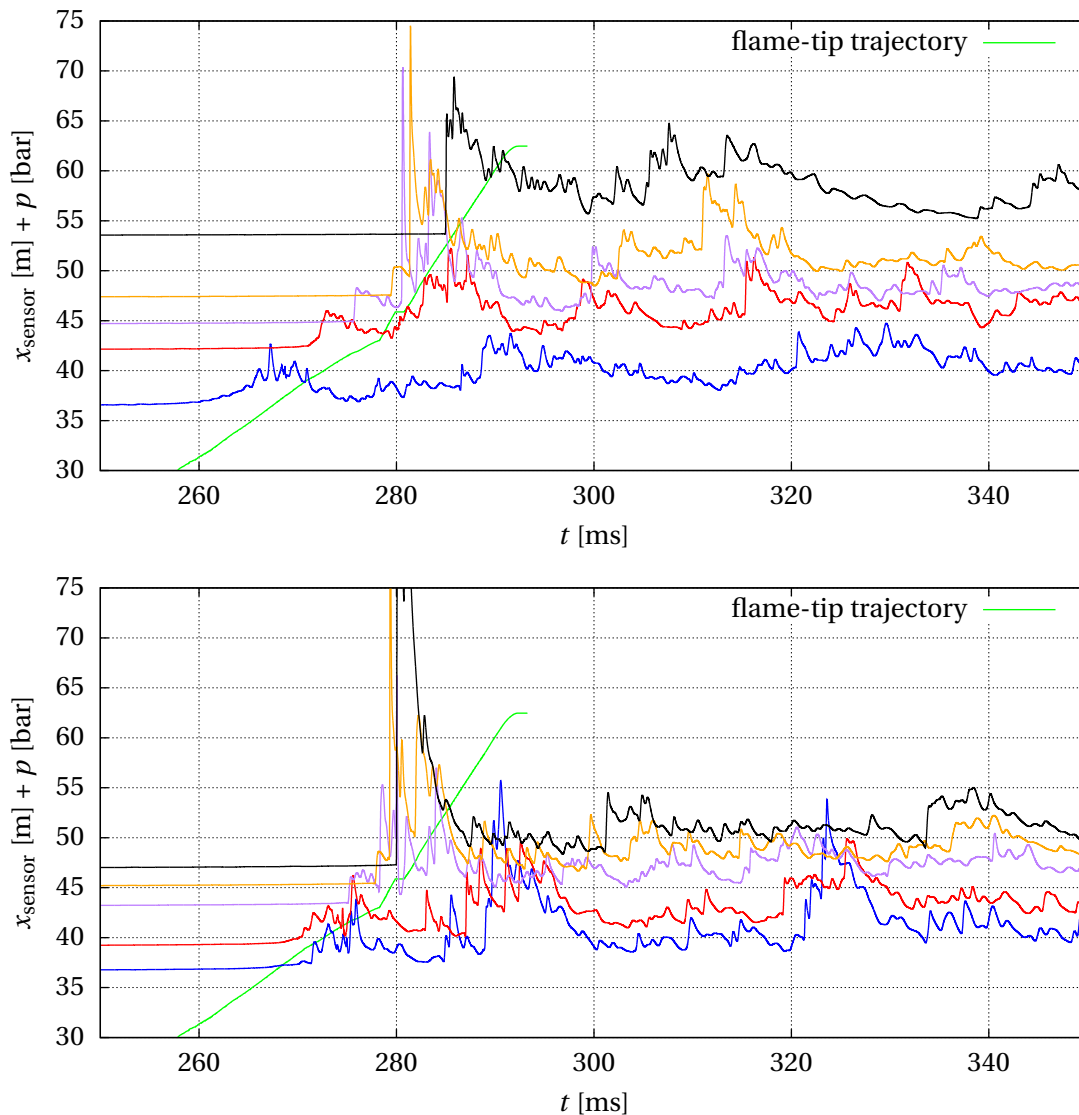

Figure 4.13: RUT 16 with increased hydrogen content of 13.5 %: Flame-tip trajectory including shifted transient pressure recordings at upper line sensors 7 to 11 (top) and lower line sensors 2 to 6 (bottom)

Particularly the Richtmyer-Meshkov instability can play a key role for DDT mode B via shock-flame interaction [136]. If pressure gradients (due to shocks) and density gradients (due to flames) are not aligned with each other, baroclinic vorticity is generated that wrinkles the flame and suddenly leads to enhanced heat release. Pressure influence of the flame wrinkling sub-grid model 3.115 might be beneficial in this context. Secondary instabilities like the Kelvin-Helmholtz instability follow [45]. Another important mechanism might be the turbulent mixing of hot products and cold reactants, eventually causing explosions of enclosed unburned pockets. Relevant instabilities are partly acting on very small scales compared to the length scales of the geometry which explains the difficulties in doing under-resolved CFD simulations. Nevertheless, the combustion model is expected to capture even DDT mode B if only the resolution is high enough. This seems especially reasonable with respect to the widespread assumption that DDT is always based on the universal SWACER mechanism (sec. 2.4) on microscopic level. Temperature, pressure and mixture dependent ignition delay times t_{ign} are provided to the solver in the form of multi-dimensional look-up tables, cf. sec. 3.5.6. Accordingly, the solver can reproduce temporal and spatial gradients of t_{ign} depending on the thermodynamic state, as well as the corresponding amplification of shock waves since coherent reduction of t_{ign} is followed by coherent energy release.

Numerical pressure recordings in fig. 4.14 impressively demonstrate the hazards associated with DDT. Sensor 6 is located at the canyon end wall, 1.5 m above the canyon bottom, i.e. directly facing the local explosion in the 13.5 % case. According to Boeck et al. [27], 10 bar roughly represents a critical overpressure level for the onset of detonation after planar shock reflection. A sufficiently intense precursor shock, to provoke a local explosion at the canyon end wall, did not develop in the 12.5 % simulation. The overall peak pressure is at about 7 bar in this case without DDT, contrary to about 65 bar in the 13.5 % simulation with DDT.

In summary, DDT simulations show a strong dependency on initial and boundary conditions. Even small deviations can lead to largely different DDT location and mechanism. This behavior can be compared to the stochastic nature of DDT in experiments for which the conditions can never be assured to be identical down to the microscopic level. The performed simulations itself are deterministic though.
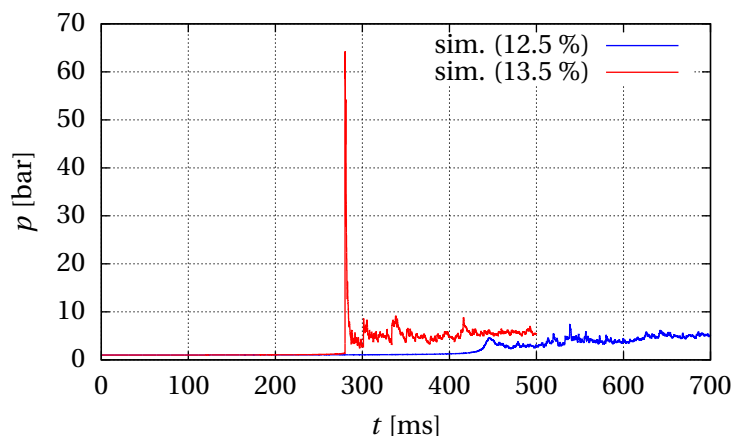

Figure 4.14: RUT 16: Transient pressure recordings at sensor 6 (canyon end wall)

4.3   Flame surface area analysis

To understand the process of flame acceleration in obstructed geometries, it is instructive to analyze the corresponding evolution of flame surface area. For instance, enlargement of flame surface area implies increasing integral heat release rate, which in turn promotes the feedback mechanism behind flame acceleration via the expansion of combustion products. Obstacles generally affect the flame on macroscopic level (e.g. adaptation of the global flame shape to changes in cross-section) as well as on microscopic level (e.g. small-scale flame wrinkling by turbulent eddies).

Three area-describing quantities are introduced: First, the macroscopic flame surface area (*macro*)

$$\sum_F A_F \tag{4.1}$$

is defined by means of A_F, the piecewise-linear reconstruction of the $c = 0.5$ contour surface on the given computational grid. Summation over all cells F intersected by the reconstructed surface yields integral values that can be plotted over the moving flame-tip position x. For that reason, the contour-based reconstruction algorithm [150] has to be evaluated during the runtime of the solver. More precisely, the algorithm is executed each time the flame surface output is saved for post-processing. Second, the microscopic flame surface area (*micro*)

$$\sum_F A_F \Xi_F \tag{4.2}$$

includes the wrinkling of the flame on sub-grid level Ξ. Third, the quenching-corrected microscopic flame surface area (*micro quenched*)

$$\sum_F A_F \Xi_F G_F \tag{4.3}$$

additionally includes the probability of unquenched flamelets G. Ξ and G are thoroughly explained in conjunction with the combustion model (sec. 3.5). Being the most complete representation, the last quantity provides a dimensionality-reduced measure of the flamelet source term 3.90 which can easily be analyzed. The definitions depend on the computational grid and naturally adapt for varying mesh density.

For both reference simulations of RUT configuration 22 (fig. 4.6) and configuration 16 (fig. 4.9), the flame surface analysis is depicted in fig. 4.15 and fig. 4.16, respectively. One commonality is the fact that the quenching-corrected microscopic area maximum is on the order of ten times the macroscopic area maximum. This value of ten agrees well with the widespread rule of thumb, usually formulated in terms of the turbulent to laminar burning velocity ratio. Equivalence of both ratios, turbulent to laminar flame surface area and turbulent to laminar burning velocity, is discussed in sec. 3.5.5.1.

Interaction with obstacles can clearly be identified for RUT configuration 22. While oscillations are moderate for the macroscopic area, strong oscillations of the microscopic area appear due to the turbulent wake behind obstacles. Especially when the flame-tip reaches the second half of the channel, the flow is highly turbulent. Mainly peak values are reduced by the quenching model. At the same time, the flame structure steepens, leading to a decline of the macroscopic area and consequently of the other quantities. Another interesting observation is the drastic collapse of microscopic area after the onset of detonation at the last obstacle. The generation of sub-grid flame wrinkling (Ξ is being produced
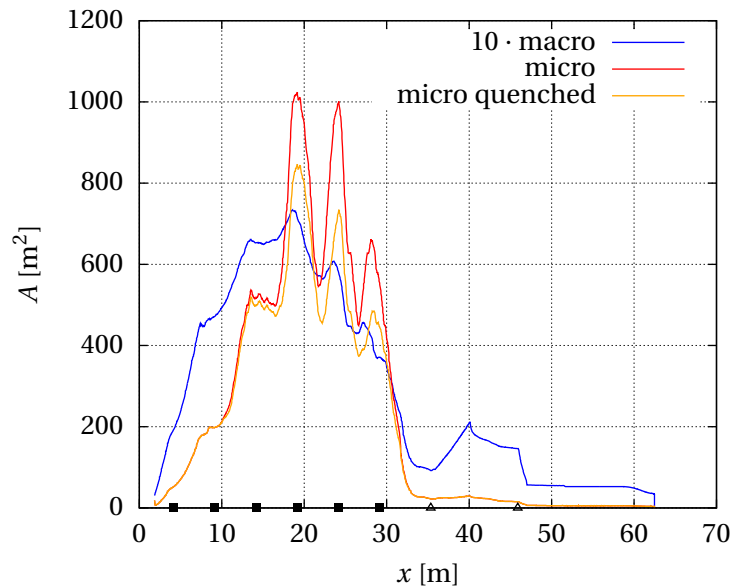
Figure 4.15: RUT 22: Macroscopic and microscopic flame surface area evolution

at a particular rate, cf. eq. 3.106) is obviously too slow to follow the detonation front. Coinciding with theory, flame propagation in this regime is rather governed by successive auto-ignition, i.e. by the volumetric reaction source term 3.128.

For the reference simulation of RUT configuration 16, without transition to detonation, the behavior is quite different. Owing to the higher obstacle count (12 instead of 6) and the lower blockage ratio (30 % instead of 60 %), interaction with single obstacles is not clearly reflected in the integral area values. Local interaction with obstacles is of course existent. After continuous growth in the obstructed channel as well as in the turbulent wake of the backward-facing step (large recirculation zone), all curves start to decline within the unobstructed canyon section. A second rise occurs in the second channel by elongation of the global flame shape and by the turbulent wake of the forward-facing step (small recirculation zone). Similarly, each obstacle in the first channel induces a small recirculation zone at the leading edge and a large recirculation zone at the trailing edge. Finally, repeated interaction of the flame with shock waves, reflected from the end of the second channel, manifests in the development of flame surface area on both levels. Compared to RUT configuration 22, all area-describing quantities are generally higher. Likewise, the influence of the quenching model is stronger. A direct conclusion on flame acceleration cannot be drawn from that since stoichiometry, and thus thermal expansion, is different in both cases.
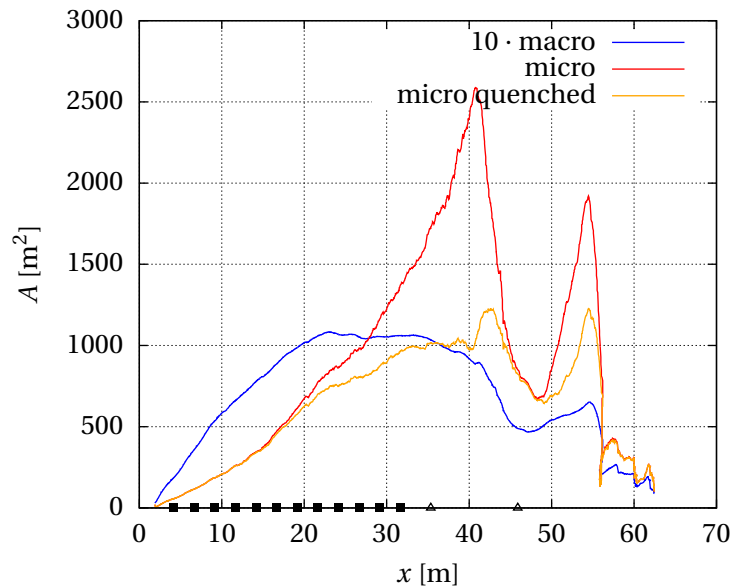
Figure 4.16: RUT 16: Macroscopic and microscopic flame surface area evolution

4.4 Mixture inhomogeneity

Mixture inhomogeneity is an issue rarely considered in explosion research. A generic study is conducted on the influence of spatial concentration gradients to make another step towards realistic accident scenarios. As explained in the introduction (chap. 1), vertical concentration gradients are likely to develop because hydrogen tends to accumulate under the roof of facilities. The geometry is the same as for RUT configuration 16. For the sake of simplicity, a one-dimensional vertical concentration gradient (i.e. perpendicular to the main direction of flame propagation as in the GraVent facility [266]) is assumed. Basically, there is no impediment in importing realistic multi-dimensional mixture fields from CFD dispersion simulations. A linear vertical distribution yields 15.5 % of hydrogen at the top and 10.5 % at the bottom of the obstructed channel. Accordingly, the gradient is given by the difference of 5 % along the channel height of 2.3 m. The average concentration in the obstructed channel is $\approx$ 13 % whereas it is $\approx$ 11.6 % in the whole domain because of the very lean region in the canyon. The ignition kernel is patched with the burned state corresponding to 13 % of hydrogen.

Snapshots of the hydrogen mixture fraction f_H (equivalent to the molar hydrogen concentration in the unburned part of the domain) can be seen in fig. 4.17. Contrary to the homogeneous reference case, the inhomogeneous mixture field does not remain at the unperturbed initial state during the explosion. Before the flame reaches the first obstacle (150 ms), the mixture ahead of the flame is largely unaltered. 100 ms later, the induced flow leads to large-scale mixing in the turbulent recirculation zones behind obstacles. The entire length of the channel is affected. At 300 ms after ignition, mixing intensifies but does not cause complete homogenization. The non-symmetric obstacles (with respect to the direction of the concentration gradient) lead to more intense mixing in the lower part than in the upper part of the obstructed channel. A vertical gradient, now of non-linear shape, is still present. The mixture fraction after almost complete burnout of the

obstructed channel is visualized in the last picture (350 ms). Extreme values at the top and bottom are finally being reduced.

Despite the same average fuel concentration of $\approx$ 13 % ($a_{\mathrm{prod,p}}$ = 725.2 m/s, D_{CJ} = 1435.1 m/s) in the first channel, the flame-tip acceleration diagram 4.18 reveals transition to detonation for the gradient case but not for the homogeneous case. In the latter simulation, flame velocity remains below the products' speed of sound. For the gradient mixture, flame acceleration in the obstructed part of the channel is stronger. Onset of detonation occurs when a pressure wave diffracting around an obstacle is reflected off the channel top. According to fig. 4.17, the mixture is richest at the top during the whole explosion process. Although there is no direct validation in the RUT facility, the result generally agrees with experimental observations of Boeck et al. [26] on laboratory scale. In both studies, it is concluded that mixture inhomogeneity can promote flame acceleration and ultimately DDT, especially in the very lean regime. Compared to the theoretical CJ velocity, a deficit of the detonation velocity appears. Boeck et al. [29] observe the same tendency in the entirely closed GraVent experiment, though less pronounced. In this context, it should be mentioned that the detonation wave disintegrates on its way to the canyon floor where the mixture is outside of the flammability limit. Mass, momentum and energy losses in transverse direction from the reacting mixture layer to the non-flammable mixture layer additionally impact the process, similar to large-scale semi-confined experiments in KIT's A1 facility [98, 153]. Stable shock-reaction coupling only sustains in the upper part of the canyon.

(a) 150 ms

(b) 250 ms

(c) 300 ms

(d) 350 ms
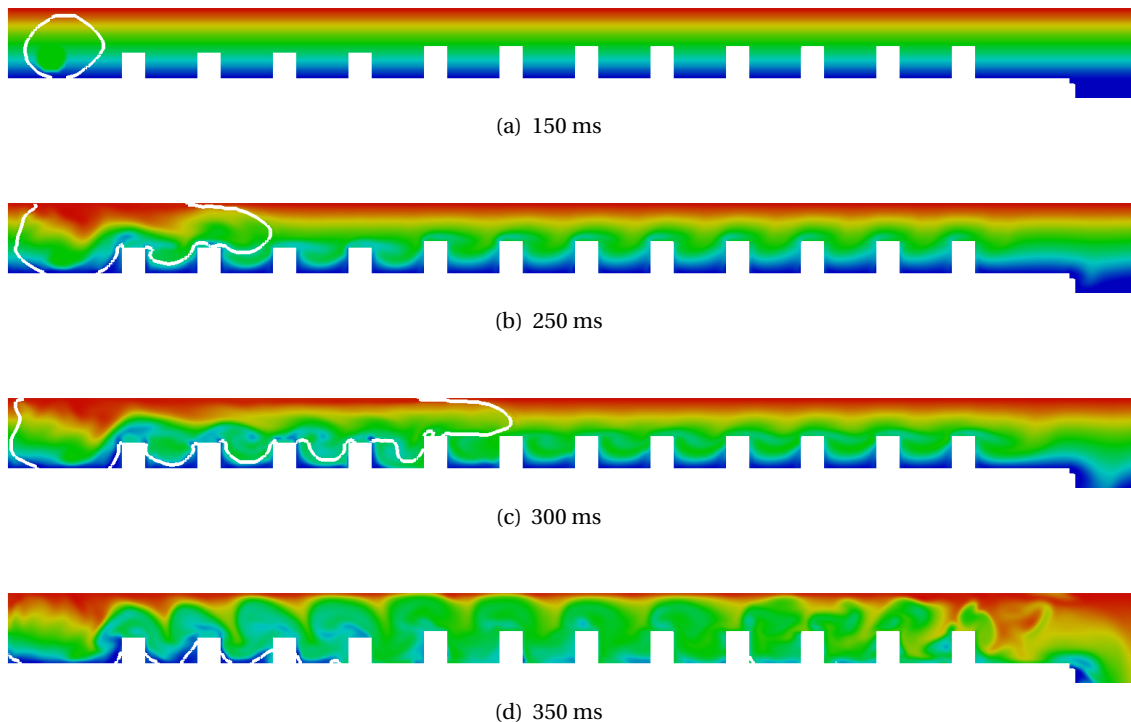
Figure 4.17: RUT 'inhomogeneous': Hydrogen mixture fraction at four points in time after ignition; Cutting plane located on the center line of the channel; Rainbow color scale (appendix A) from 10.5 % to 15.5 %
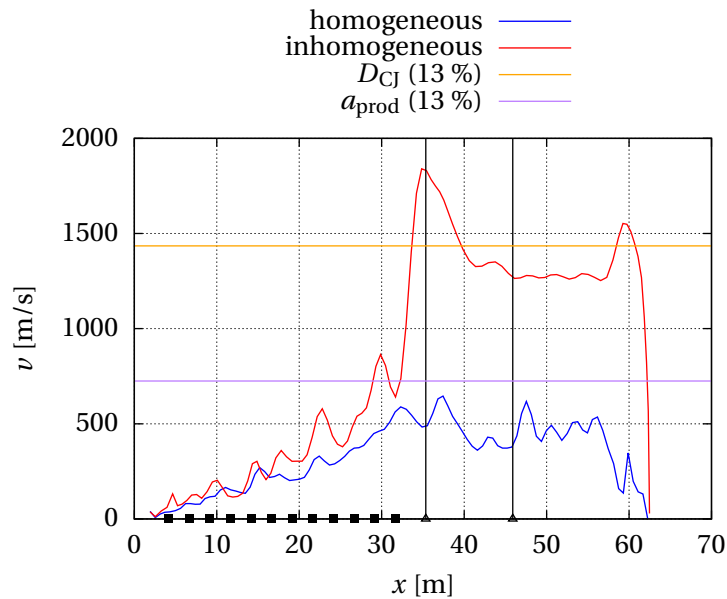
Figure 4.18: RUT 'inhomogeneous': Flame-tip acceleration

The reason for the diverging flame acceleration might be connected to a different evolution of the flame surface area. Since the (laminar) burning velocity is higher at the top than at the bottom, the flame is likely to elongate more for the gradient case, thus relatively increasing its macroscopic surface area. However, no significant differences are recognized in the corresponding analysis in fig. 4.19. Only in terms of the quenching-corrected microscopic area, the maximum value (at the end of the obstructed section) is slightly lower in the homogeneous case. Besides, the burning velocity is a non-linear function of the fuel concentration. Assuming that the presence of obstacles assimilates flame shapes and neglecting the effect of turbulence, the integral burning rate can thus be higher in gradient mixtures than in mixtures of the same average fuel concentration [26]. Comparison of the post-DDT behavior is less instructive due to the fundamentally different driving mechanisms in both cases (deflagration versus detonation).
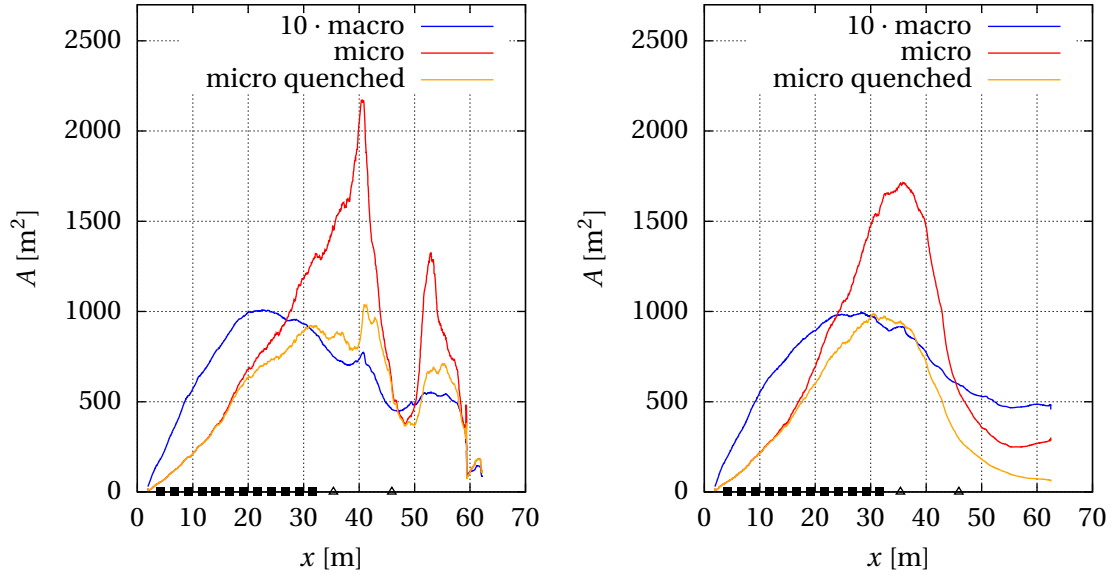
Figure 4.19: RUT 'inhomogeneous': Macroscopic and microscopic flame surface area evolution; Homogeneous without DDT (left picture), inhomogeneous with DDT (right picture)

4.5 Dimensionality reduction

Since two-dimensional (2D) simulations generally require considerably less computational resources than three-dimensional (3D) simulations, dimensionality should be reduced whenever possible. Basically, a 2D channel corresponds to a 3D channel of infinite thickness. There exists no boundary of the third dimension which would reflect waves of any kind or generate wall boundary layers. The larger the width is, relative to height and length, the better the simplification becomes.

In the simplified 2D model of the RUT facility, chamber bevels and obstacle slits have to be neglected. Obstacle height is adjusted such that the blockage ratio, being the dominant geometrical parameter in terms of flame acceleration, remains constant. Regarding obstacle arrangement, configuration 22 is adopted. The 2D channel is elongated in axial direction according to the arc length of the curved second channel. Compared to the reference simulation of RUT 22 (fig. 4.2.2), the cell count is reduced by a factor of 1,142,822 / 36,296 = 31.49, i.e. approximately the 3D model's number of cells in span-wise direction. Setting up an average cell size of ≈ 7.2 cm assures equal mesh density in both cases (within the limits of geometrical constraints).

For both setups, the result in terms of flame-tip behavior is shown in fig. 4.20. Flame acceleration in 2D is stronger at the beginning but slower at the end of the obstacle section. The reason is probably connected to a different evolution of flame surfaces, on macroscopic as well as microscopic level, as the corresponding flame surface analysis in fig. 4.21 reveals. Due to cylindrical instead of spherical ignition (at the same kernel radius), the initial value of macroscopic flame area is noticeably larger in 2D. However, the situation quickly reverses within the first channel. Maximum values of all area-describing quantities remain clearly below the 3D values. Besides, oscillations on microscopic level are weaker in 2D. Obstacle slits, which are only accounted for in the 3D model, surely en-

hance flame wrinkling on sub-grid level via induced turbulent jets. Absence of DDT in 2D might be a consequence of insufficient flame velocity towards the end of the obstacle section, or, the attenuation of shock focusing in corners (which is 3D by nature). Divergences within the canyon section and second channel shall not be compared here as they are rather governed by the different combustion regime (deflagration in 2D versus detonation in 3D).

Another 3D computation (fig. 4.22) is intended to isolate the effects of geometrical simplifications on the one hand, and, multi-dimensional flame propagation itself on the other hand. For that purpose, the simplified 3D mesh (no chamber bevels, no obstacle slits) is generated by straight extrusion of the 2D mesh in span-wise direction. Spatial resolution is equal in all directions. In this case, DDT does indeed occur – but at the beginning of the second channel, i.e. not at the correction location. Within the obstructed channel, macroscopic flame surface area is between the levels of the reference 3D mesh and the 2D mesh. Microscopic interaction is similar to the 2D case. On this basis, it can be argued that macroscopic flame propagation is essentially three-dimensional. Satisfying the no-slip condition, the flame is always bent from the bulk flow towards walls. Furthermore, the important role of turbulence-inducing obstacle slits on microscopic level is confirmed by explicitly excluding them in the additional 3D computation.

In the end, one has to be aware of making a systematic error in 2D simulations of the RUT facility. The simplification might be less problematic for facilities featuring a more favorable width to height and length ratio. In earlier simulations of the laboratory-scale GraVent facility (somewhat more favorable ratio of length scales), Hasslberger et al. [100] found the same tendency of reduced flame acceleration in 2D compared to 3D. DDT run-up distances develop accordingly. Independent evidence supporting the conclusion is available from Kessler et al. [131]. Ideas to compensate the underestimation of flame surface growth in 2D by artificially increased reaction rate would probably work. Universal validity is difficult to assure though.
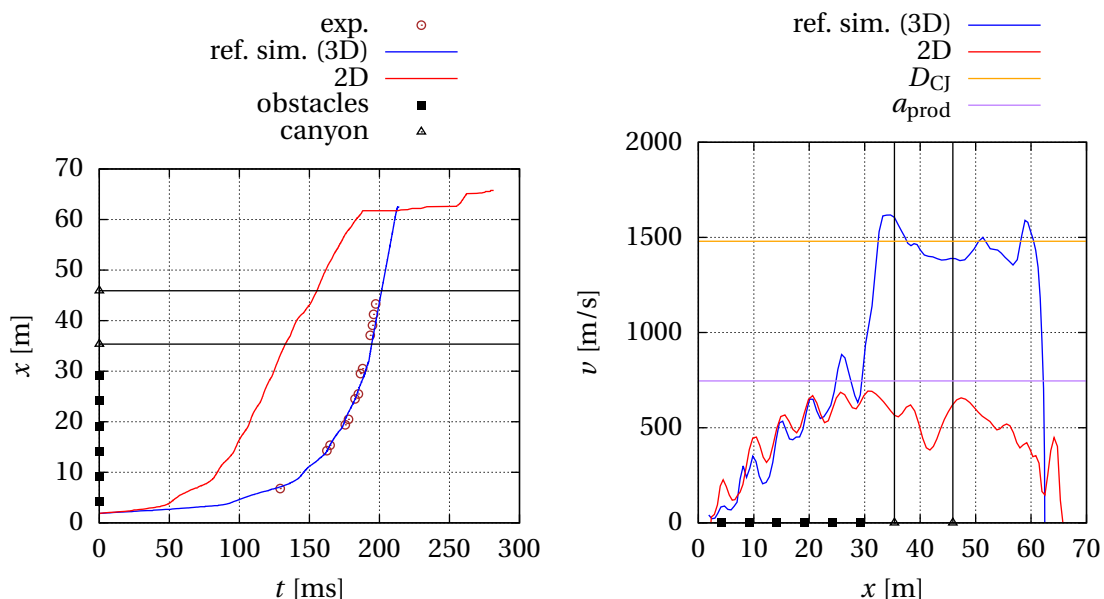

**Figure 4.20:** RUT 'two-dimensional': Flame-tip acceleration
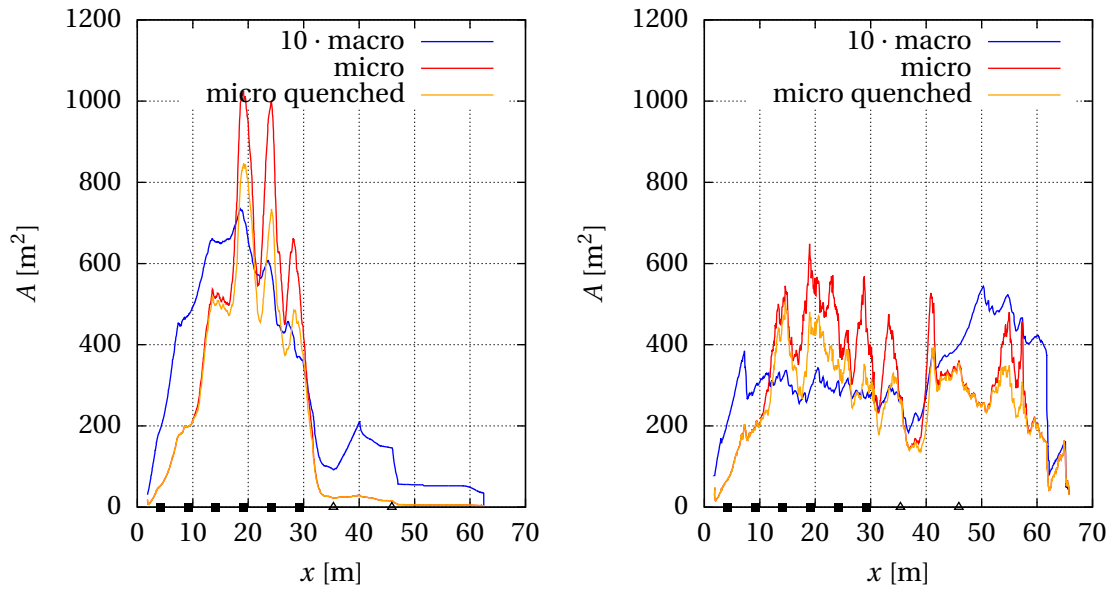
Figure 4.21: RUT 'two-dimensional': Macroscopic and microscopic flame surface area evolution; Reference 3D mesh (left picture), 2D mesh (right picture)
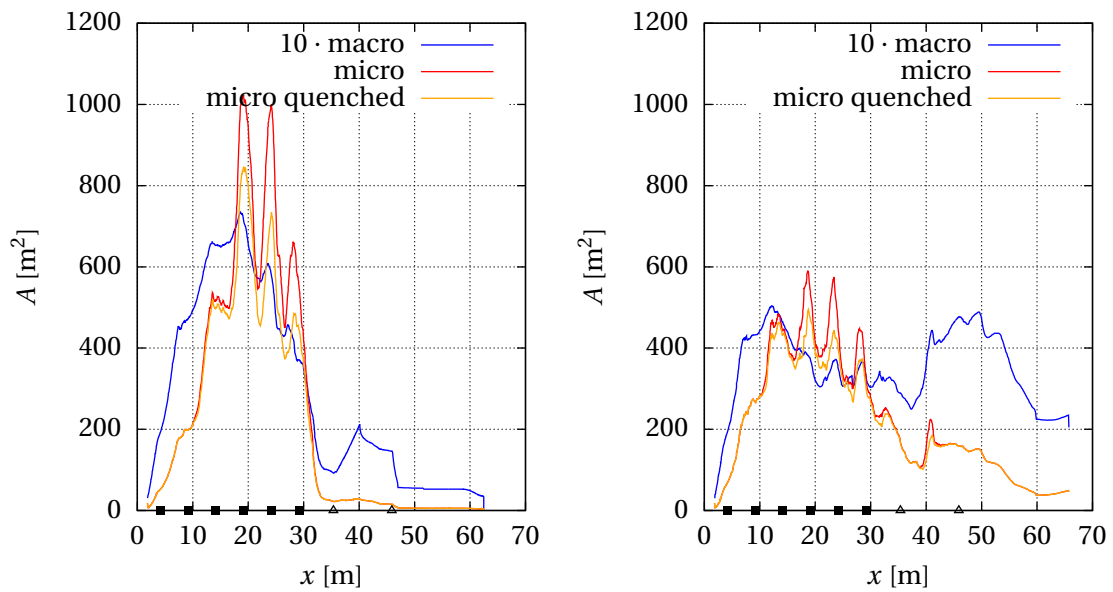

Figure 4.22: RUT 'two-dimensional': Macroscopic and microscopic flame surface area evolution; Reference 3D mesh (left picture), simplified 3D mesh (right picture)

4.6   Grid dependency

To demonstrate the benefit of AMR (adaptive mesh refinement as described in sec. 3.6), three cases with different maximum refinement levels are compared with each other. RUT configuration 22 is investigated here since the reference simulation presented in sec. 4.2.2 was able to reproduce not only flame acceleration but also the correct DDT location. The intentionally coarse base mesh, consisting of only 10517 cells, is supposed to demonstrate the method's applicability to real-world accident scenarios at reasonable computational costs. Given this low mesh density, grid lines are partly stretched or compressed to ensure accurate projection of the geometry. The average cell size of the base mesh (i.e. level 0 AMR) is approximately 34.3 cm and, according to the isotropic splitting algorithm, 17.1 cm for level 1 and 8.6 cm for level 2 AMR. Latter value is on the same order as for the reference mesh (7.2 cm, cf. tab. 4.1). On the coarse base mesh, obstacle slits are represented by a single cell layer. In this context, the sophisticated discretization basis of OpenFOAM is of great advantage. Instead of directly manipulating cell mean values, boundary conditions are rather imposed on separate boundary fields. The no-slip wall condition does consequently not prohibit flow trough single cell layer obstacle slits. Two and four cells over the slit width improve discretization for level 1 and level 2 AMR in this region, respectively.

The effect of the refinement criterion stated in sec. 3.6 is highlighted in fig. 4.23. Two different stages of explosion in the deflagration regime (yet without strong coupling between reaction zone and leading shock) are selected for that purpose. The mesh is permanently refined in the vicinity of the flame front (white-colored contour line). Refinement ahead of the flame includes regions of enhanced turbulence production, e.g. in the wake of obstacles (example with maximum refinement level 2), and precursor shock waves (example with maximum refinement level 1). The burned part of the domain is regarded as minor important and thus, in order to save computational resources, not refined. In the upper case, a level 1 buffer zone appears between level 0 and level 2 regions. Satisfying the 2:1 rule maintains good mesh quality. Conservation properties are preserved by the AMR-inherent mapping process. For instance, propagation of pressure waves between different refinement levels works without difficulty.

Apparently, the initial stage of flame propagation directly after ignition strongly depends on the local discretization (flame-tip trajectory in fig. 4.24). But this does not have a direct implication on flame acceleration in the obstacle section as is evident from the velocity-distance diagram. Flame acceleration slightly intensifies with increasing maximum refinement level and generally agrees well with the experiment. However, prediction of the correct DDT location is only successful with AMR level 2. Presumably because of insufficient reproduction of the strength of shocks, AMR is essential in this case to capture the critical conditions for the onset of detonation. In summary, grid dependency is surprisingly weak. Even on the coarse base mesh and without AMR, flame acceleration results are satisfying. Fast parametric studies seem to be feasible without complete loss of validity. The flame tracking scheme (sec. 3.4) is surely beneficial to reduce grid sensitivity.

Pressure recordings are used in fig. 4.25 to compare the AMR level 2 computation with the reference simulation of RUT 22. To avoid overlapping, the AMR level 2 signal is shifted in time. In both computations, transition to detonation is already finished at the canyon entry (sensor 7). Clearly higher values, due to detonation reflection, occur at the canyon end wall (sensor 6). Whereas peak values are higher in the reference case, the general trend
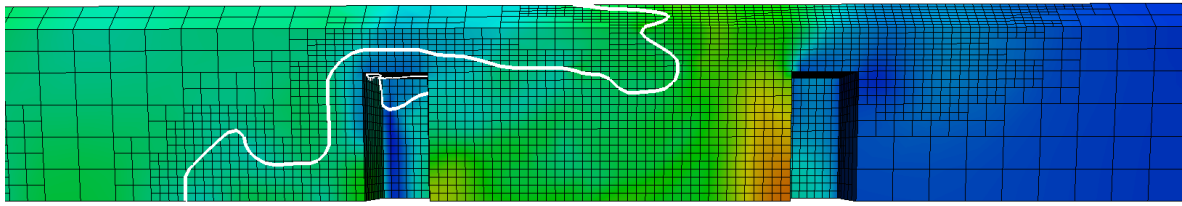
(a) Level 2 refinement including the turbulent wake behind the fourth obstacle; Pressure scale from 1 bar to 7 bar
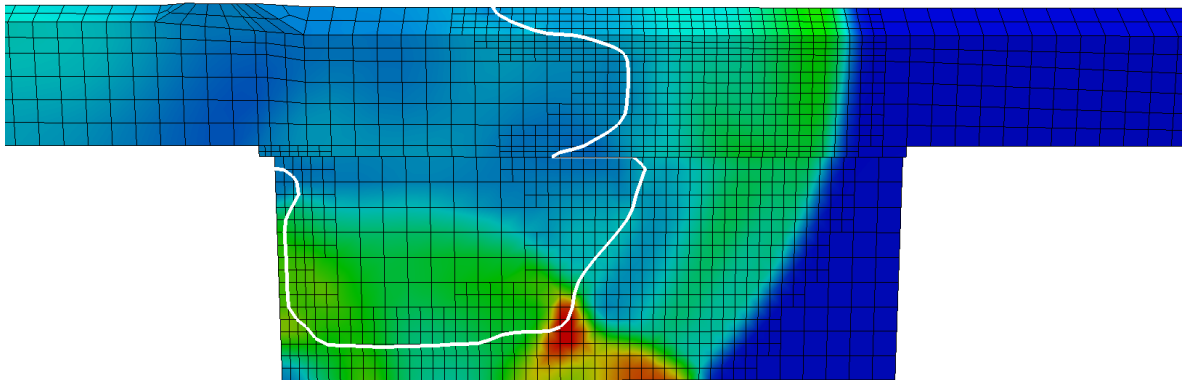
(b) Level 1 refinement including the precursor shock in the canyon; Pressure scale from 1 bar to 10 bar

Figure 4.23: RUT 22: Independent examples of local adaptive mesh refinement for different maximum refinement levels; White-colored contour line indicating the flame front; Rainbow color scale according to appendix A
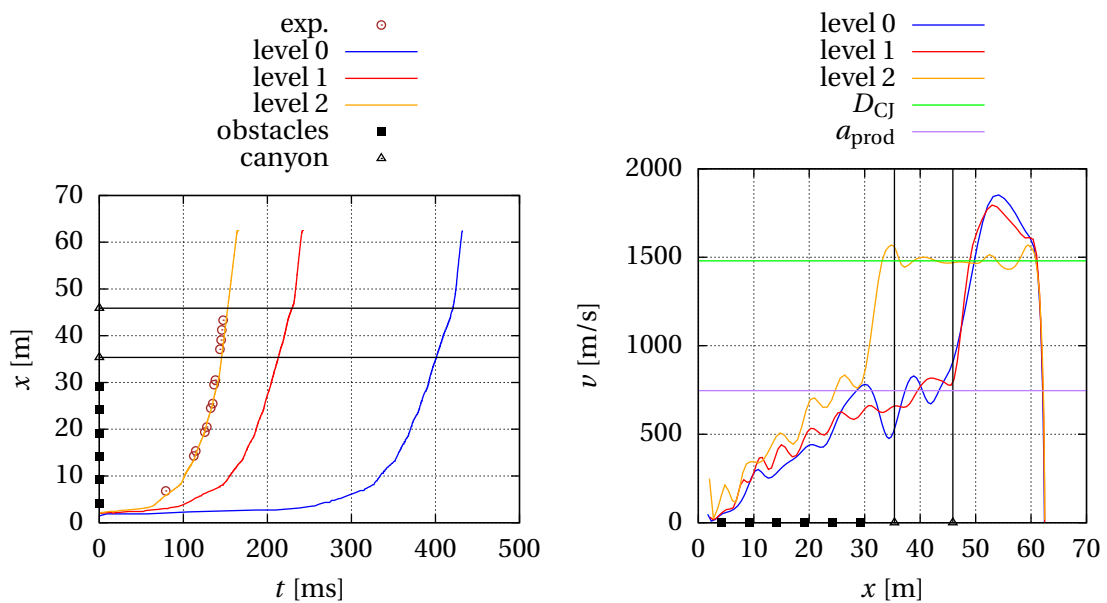
Figure 4.24: RUT 22: Flame-tip acceleration for different maximum refinement levels

matches excellently. Small pressure fluctuations are smoothed in the AMR case because of absent refinement in the burned part of the domain.
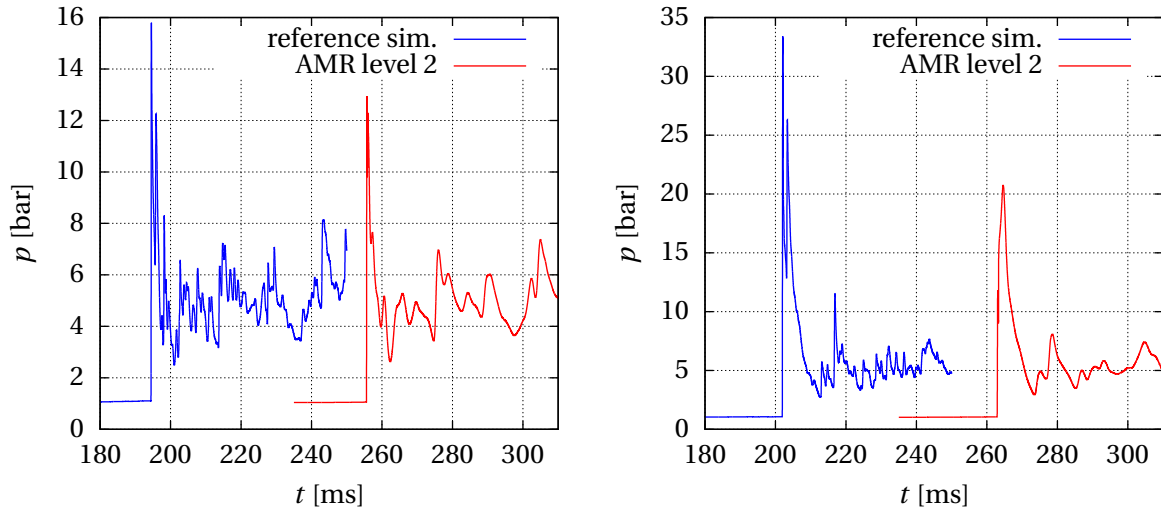
Figure 4.25: RUT 22: Transient pressure recordings at sensor 7 (canyon entry, left picture) and sensor 6 (canyon end wall, right picture)

One indicator for the increase in computational cost by AMR is the overall cell count n. Its evolution with moving flame-tip position x is plotted in fig. 4.26. The high initial level results from the applied normalization procedure in the refinement criterion 3.131. No distinct gradients of the unburned density ρ_u (other than the normal density ρ) and the velocity u_i exist at the beginning. As soon as distinct maximum values of these quantities develop, e.g. in the form of pressure waves, the curve starts to decrease. Visible oscillations can be traced back to the interaction with obstacles. After transition to detonation, the profile of n follows well the macroscopic flame surface (cf. sec. 4.15) since the mixture ahead of the flame is predominantly unaffected.

By reason of different simulation end time, time step size, cluster architecture, number of cores and parallel efficiency, it is difficult to quantify the saving of computational cost through AMR. Neglecting some of the mentioned points, an estimate is made on the basis
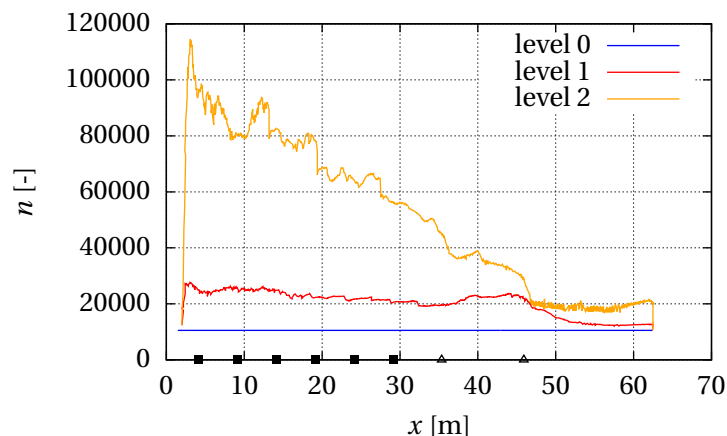
Figure 4.26: RUT 22: Overall cell count evolution for different maximum refinement levels

of core hours: number of cores multiplied by execution time on the particular system. A factor of approximately five emerges from this comparison. Opposing the number of cells alone (1,142,822 cells of the reference simulation versus $\approx$ 115,000 cells, being the maximum of the AMR level 2 simulation), would suggest an even higher saving factor around ten. Additional influencing factors, as stated above, obviously play a role. Nevertheless, it is out of doubt that an enormous reduction of cost can be achieved by means of AMR. From this point of view, the method is predestined for the application to real-world accident scenarios.

5 Application on industry scale: Konvoi-type pressurized water reactor

Following the nuclear safety motivation, the purpose of this chapter is to demonstrate the applicability of the developed solver on full reactor scale. The underlying geometry approximates a Konvoi-type pressurized light-water reactor of the 1,300 to 1,400 MW class. In addition to four units with a very similar design, of the so-called pre-Konvoi-type, three units of the Konvoi-type are still operating in Germany to date: Isar 2, Emsland and Neckarwestheim 2. These are the latest developments realized by former Siemens-KWU. Related designs are operational in Spain and the Netherlands [164]. Validation of the solver by means of the RUT facility (chap. 4) involves reactor-typical length scales. The total volume and consequently the affordable mesh resolution are different though. Besides, validation is limited to ambient initial conditions due to sparsely available experiments at elevated initial conditions, particularly on large scale. The simulations are to be regarded as an extrapolation to some extent. It is obvious that a rigorous validation of the investigated hypothetical accident cases is impossible.

Representing the evolution of reactor-scale combustion simulations over the last 15 years, several contributions are reviewed. In 2000, Breitung and Royl [39] published a procedure for the deterministic analysis of hydrogen behavior in severe accidents. The developed solver COM3D was exemplarily applied to a PWR containment. This pioneering work was followed by the analysis of a BWR reactor building outside of the inertized containment (Olkiluoto plant in Finland) by Manninen et al. [177]. The codes FLUENT and DET3D were separately employed for deflagration and detonation simulations, respectively. Approximately ten years later, application of COM3D to a modern EPR reactor (descendant of the Framatome N4 and Siemens Konvoi reactors) was demonstrated by Dimmelmeier et al. [61]. In 2014, Hsu et al. [110] as well as Daudey and Champasith [59] used the simulation tool FLACS to analyze explosion hazards in a PWR containment (Maanshan plant in Taiwan) and an operating room of the EPR reactor (currently being constructed at Flamanville in France), respectively. As a unique feature, FLACS provides the possibility to include the effect of small-scale obstacles on sub-grid level via the distributed porosity concept. In the latest publication in 2015, Kim and Hong [137] achieved promising results with OpenFOAM on South Korea's newest generation APR1400 reactor. If at all, the possibility of DDT is evaluated by means of empirical criteria (most prominently eqs. 2.22 and 2.27) in the mentioned studies. By direct computation of DDT (not to be confounded with direct numerical simulation) on full reactor scale, the presented work is supposed to advance the state-of-the-art in this field.
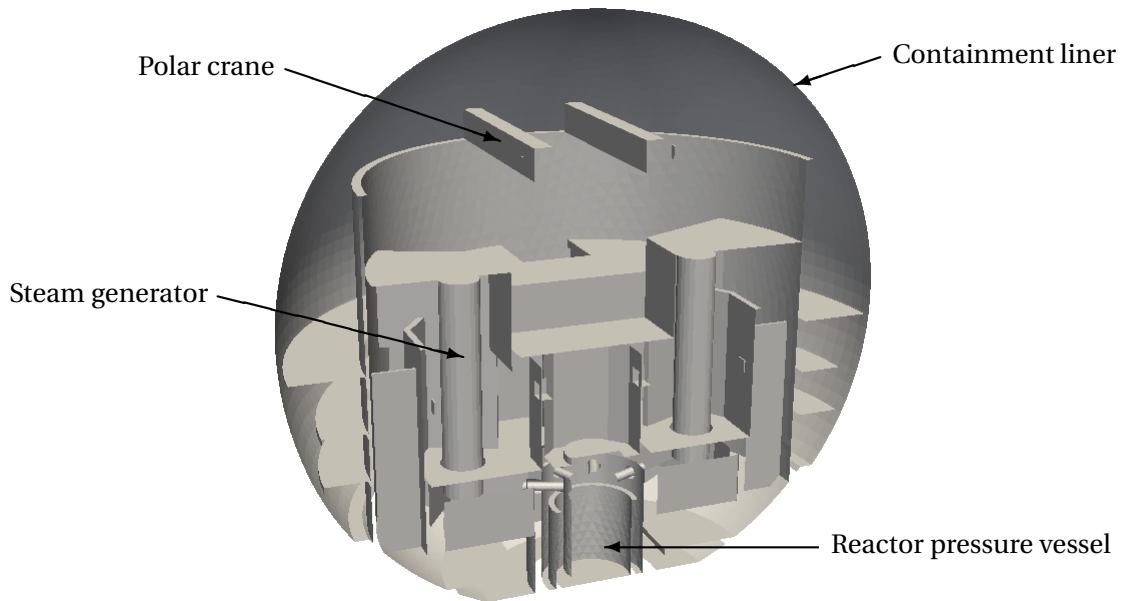
Figure 5.1: Sectional view of the Konvoi-type pressurized water reactor model

5.1   Computational setup

A spherical shape of the containment is characteristic of the Konvoi design. It contains the entire four-loop reactor coolant system which is under operating pressure. The steel-made spherical structure is self-supported and provides a barrier against the release of radioactive substances to the environment. Its diameter is 56 m and its wall thickness is typically 38 mm. According to Liang et al. [164], the containment is designed to withstand a static pressure of 6.3 bar. A filtered venting system is additionally installed. Hydrogen mitigation measures include passive auto-catalytic recombiners. The surrounding reactor building is built of reinforced concrete to shield the reactor against external events. Here, the primary question to answer is whether the integrity of the steel liner containment is jeopardized by explosions of certain severeness. The domain of interest is thus limited to the inside of the containment. Reactor building rooms outside of the containment are not taken into account.

The corresponding three-dimensional model in fig. 5.1, provided by Germany's nuclear safety agency GRS gGmbH, includes typical plant components (reactor pressure vessel, steam generators, pressurizer, polar crane etc.) as well as internal concrete structures (steam generator towers, reactor cavity, spent fuel pool, sump etc.). Small-scale installations like pipes in the low-level rooms have to be neglected given a reasonable mesh density. It remains an open question to what extent the combustion process is influenced by such simplifications. Doors and burst disks, mounted at the top of the steam generator towers, are assumed open. They either failed prior to ignition or they are destroyed by precursor pressure waves. In any case, these components do not hinder explosive flame propagation decisively. Technically, the geometry is imported in the meshing software ANSYS ICEM CFD as one of the widespread formats: Standard for the Exchange of Product model data (STEP), Initial Graphics Exchange Specification (IGES) or Stereo Lithographic surface (STL). These universal file formats can usually be created from CAD packages.

Because of the PWR's large inner volume (especially compared to (inertized) containments of boiling water reactors) of approximately 74,800 m^3, massively parallelized computations were conducted on the SuperMUC high performance cluster operated by the Leibniz Supercomputing Center in Garching (Germany). Parallel execution on 1024 cores resulted in calculation times around two days. The computational domain is discretized by (distorted) hexahedral cells. The generation of tetrahedral meshes is more straightforward but the cell count to achieve equivalent resolution is clearly higher than for hexahedra. Tetrahedral meshes also suffer from limited neighborhood connectivity [114] and are therefore suboptimal from the discretization schemes point of view. In wall-distant regions, a preferably uniform and orthogonal mesh is assured regarding the discretization error. Close to walls, hexahedral cells are distorted if necessary to guarantee a reasonable approximation of the confining geometry. Since there is no refinement towards walls and boundary layers are far from being properly resolved, wall functions are imposed at all no-slip adiabatic wall boundaries.

In terms of containment pressure load analysis, the maximum cell size for combustion simulations depends on the highest relevant natural frequency of the structure. According to Breitung et al. [42], cell sizes smaller than 1 m are acceptable. Theoretical considerations for the geometrically similar EPR reactor showed that the highest relevant natural frequency of the containment structure is lower than 150 Hz, which leads to maximum cell sizes of about 60 cm [195]. Using 7,015,188 computational cells yields a sufficiently fine average cell size of 22 cm in this work.

The varying pressure probe and ignition locations are illustrated in fig. 5.2. Ignition location 2 is not explicitly investigated here but its definition is necessary to understand one reference in sec. 5.3. Table 5.1 summarizes the corresponding coordinates in which the x-axis points from the bottom (sump) to the top (dome). To account for the asymmetry of the problem (due to the chosen ignition location), pressure sensors are placed in the dome as well as on both sides in the steam generator towers and the reactor adjacent rooms.

If all countermeasures fail in case of core meltdown emergency, several hundred kilograms of hydrogen can be produced during the so-called *in-vessel* phase by oxidation of the zircaloy fuel rod cladding. Additionally, several tons of hydrogen can be released during the so-called *ex-vessel* phase by Molten Corium Concrete Interaction (MCCI), since this process can last for many days [243]. Coexisting amounts of carbon monoxide and steam had to be neglected in a first step. Carbon monoxide is an additional flammable gas which

Table 5.1: Reactor dimensions and coordinates

	x [m]	y [m]	z [m]
Domain bounding box	[−1.9;51.0]	[−28.0;28.0]	[−28.0;28.0]
Ignition location 1	45.0	15.0	0.0
(Ignition location 2)	5.0	10.0	0.0
Pressure probe 1	45.0	0.0	0.0
Pressure probe 2	25.0	−15.0	0.0
Pressure probe 3	25.0	15.0	0.0
Pressure probe 4	5.0	−10.0	0.0
Pressure probe 5	5.0	10.0	0.0
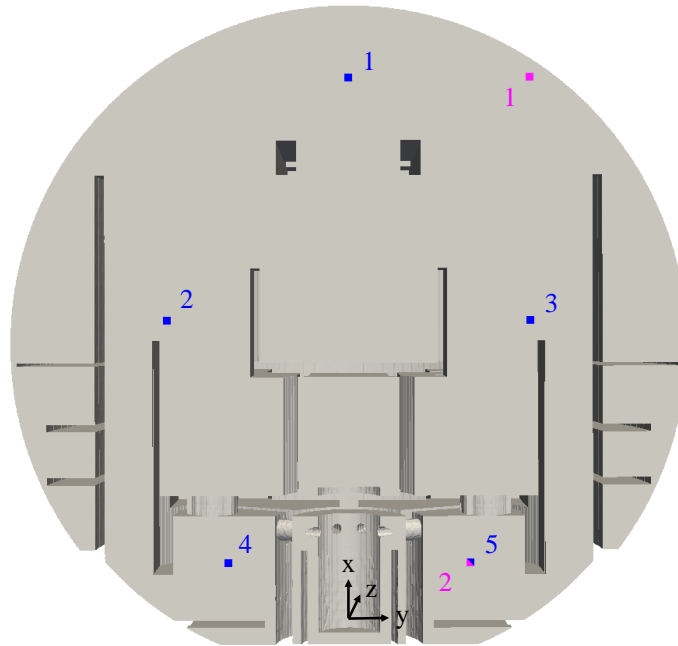
Figure 5.2: Ignition (purple) and pressure probe locations (blue)

is mainly produced through MCCI. Partial replacement of hydrogen by carbon monoxide diminishes the most important reactivity parameters [149]. The simulations performed can consequently be interpreted in a way such that the neglected carbon monoxide is compensated by a modified hydrogen concentration. To define a meaningful scaling of different fuels is out of the scope of this work however. Dilution with non-flammable steam further reduces the burning velocity [145, 169]. While the effect on chemical kinetics of hydrogen oxidation is small, the influence of steam is dominated by its thermodynamic effect [145].

Following the nuclear safety analysis chain in sec. 1.1, fuel dispersion simulations can be employed to determine the initial conditions (particularly the mixture composition) for subsequent combustion simulations. CFD methods are currently being discussed for that purpose, but are still subject to uncertainties. For example, models for bulk and wall condensation need to be improved. Also the time of ignition and therefore the amount of ignited hydrogen cannot be predicted deterministically. Generic mixture compositions are thus presumed.

Three cases with average dry hydrogen concentrations of $\widehat{X}_{H_2} = 12.5\ \%$ and $\widehat{X}_{H_2} = 15\ \%$ are examined in this work, cf. fig. 5.3. According to Breitung et al. [40], average hydrogen concentrations in this range represent realistic values for European pressurized water reactors provided that countermeasures (if available) fail. Local peak values are likely to be even higher, up to the over-stoichiometric region [40]. The lowest ever measured detonation limit in hydrogen-air mixtures (12.5 % at ambient initial conditions as reported on the large-scale RUT facility [65]) suggests that DDT might be possible with these setups. However, the reactor containment is not designed for effective flame acceleration in contrast to the entirely closed RUT channel which is equipped with periodically arranged obstacles. For both $\widehat{X}_{H_2} = 12.5\ \%$ cases, a spatial concentration gradient in vertical direction is imposed such that the maximum concentration corresponds to the homogeneous
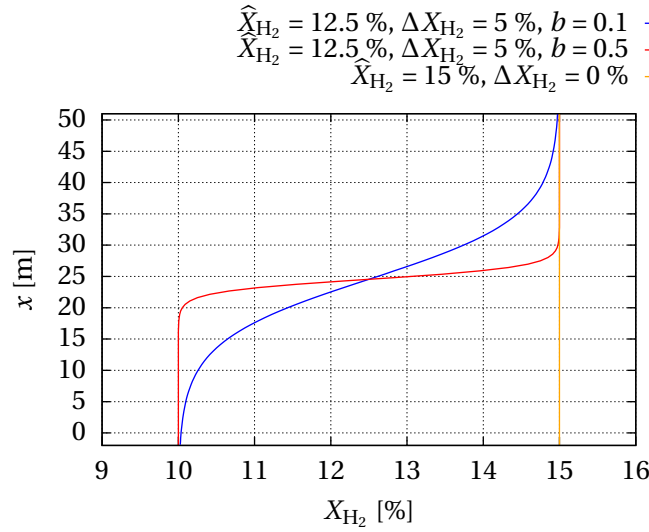
Figure 5.3: Initial mixture distribution in the containment: Molar hydrogen concentration X_{H_2} depending on vertical position x

reference mixture ($\widehat{X}_{H_2} = 15\,\%$). This comparison is motivated by large-scale explosion experiments with a semi-confined hydrogen-air layer. In this context, Kuznetsov et al. [153] and Grune et al. [98] found that the DDT propensity correlates well with the maximum fuel concentration (at the top of the channel). Boeck [28] later confirmed this observation for smooth channel experiments but also discovered a different behavior for entirely closed obstructed channels.

Hydrogen tends to accumulate below the roof of buildings (the reactor dome in this case) due to its low density compared to air. The homogenizing effect of molecular diffusion is comparably slow in large volumes. The assumption of one-dimensional vertical concentration gradients is surely a simplification. Local accumulation is likely to occur if the natural upwards-oriented flow path is blocked by internal structures. Nevertheless, the vertical direction is the predominant gradient direction from a global point of view. CFD dispersion simulations of Manninen et al. [177] demonstrated a surprisingly one-dimensional character of fuel distribution in a reactor building. Profiles of the molar hydrogen concentration are eventually given by equation

$$X_{H_2}(x) = 0.5\,\Delta X_{H_2} \tanh\left[b(x - x_{\text{center}})\right] + \widehat{X}_{H_2} \tag{5.1}$$

in which ΔX_{H_2} indicates the maximum concentration difference and $\widehat{X}_{H_2}$ the average concentration in the containment. The average hydrogen concentration is consequently reached in the center of the reactor containment at $x_{\text{center}} = 0.5\,(51.0 - 1.9)$ m $= 24.55$ m. b represents the level of stratification as is apparent from fig. 5.3. The profile characterized by $b = 0.1$ is therefore identified as a continuous concentration gradient like in the GraVent facility [26, 267]. The $b = 0.5$ curve rather describes a stratified mixture similar to experiments in the A1 facility, operated by Karlsruhe Institute of Technology and Pro-Science GmbH [98, 153]. Both gradient configurations feature a minimum concentration of 10 % (at the bottom of the containment).

Since no glow plug igniters (as part of the hydrogen mitigation system) are installed in Konvoi-type reactors, the ignition location is another parameter which cannot be ascertained deterministically for accident scenarios. All kinds of electric installations repre-

sent potential spark ignition sources. Even if the plant is disconnected from the electric grid (as in the Fukushima incident), ignition can occur anywhere in the flammable mixture by electrostatic discharge or at hot surfaces. Following the σ-criterion (eq. 2.22), the minimum hydrogen concentration of 10 % lies below the critical value for effective flame acceleration. Correspondingly, weak initial flame acceleration must be expected for hypothetical ignition in the lean region, i.e. at ignition location 2. All three investigated cases are ignited in the rich region, i.e. at ignition location 1, where transition from slow to fast deflagration is generally possible right after ignition. During the initial stage, the explosion process is thus phenomenologically similar to large-scale experiments in the A1 facility: lateral flame propagation in a stratified mixture with one-sided confinement (in the containment dome).

As known from studies by GRS gGmbH, elevated thermodynamic initial conditions, i.e. temperature and pressure, are present in realistic accident scenarios. In accordance with the conditions calculated by Sonnenkalb [243], an initial pressure of 2.5 bar and an initial temperature of 373 K were chosen for the simulations. Depending on the particular accident scenario, (local) deviations from these values are to be expected. Due to sparsely available experiments at elevated initial conditions (particularly on large scale), validation of the solver was limited to standard ambient initial conditions (1.013 bar, 293 K) in the RUT facility (chap. 4). Increasing initial temperature and pressure has an impact on the simulation model in various forms – with opposing trends to some extent. The most obvious influences on the reaction rate are the pressure and temperature correction of the laminar burning velocity (eq. 3.91) as well as the sub-grid flame wrinkling model (eq. 3.115). Tabulated ignition delay times (sec. 3.5.6) and gas properties are affected likewise. Generally, there are several influences on the explosion process, e.g. in terms of crucial parameters like the speed of sound. A probable tendency regarding the onset of detonation is obtained by analyzing the variation in detonation cell sizes, being the most prominent parameter for DDT propensity. Both, elevated initial temperature and pressure, lead to smaller detonation cell sizes [40]. The detonation limit is thus expected to be even lower than for ambient initial conditions.

Since few turbulence-inducing obstructions are present during the initial phase of flame acceleration (for ignition in the dome), the choice of the initial turbulence level is more important than in obstacle-laden channels. Because of the lack of explicit guidelines and since geometrical scales are on the same order of magnitude, the applied uniform initial values were identical to RUT simulations: specific turbulent kinetic energy of $k = 0.1 \, \mathrm{m^2/s^2}$ (equivalent to r.m.s velocity fluctuation of $u' = 0.258$ m/s) and eddy frequency of $\omega = 10$ Hz.

5.2 Results and discussion

For one of the investigated cases ($\widehat{X}_{H_2} = 12.5$ %, $\Delta X_{H_2} = 5$ %, $b = 0.5$), fig. 5.4 gives an impression of the complexity of the explosion process in a nuclear reactor. It underscores the point of doing extensive CFD simulations for this kind of analysis. At two points in time, the wall pressure and the semi-transparent flame contour are visualized for one half of the reactor. The snapshot at 450 ms after ignition (left picture) is before DDT, and 500 ms (right picture) is after DDT. With the onset of detonation comes a strong rise in wall

pressure load. A detonation wave and reflected pressure waves are propagating in the upper part of the containment.

Due to the highly three-dimensional character of flame propagation in the containment, the common acceleration diagrams (time-space trajectories based on one-dimensional tracing of the flame tip) are omitted. Instead, the burnout (percentage of burned volume) is analyzed, representing a global direction-independent measurement. In fig. 5.5, a similar general trend can be observed for all three mixture cases. The exponential rise is mainly traced back to the enlargement of the flame surface area and interconnected flame acceleration. As soon as the flame tip reaches the bottom of the reactor, a kink of the burnout curve appears. Due to algorithmic reasons, burnout values are only written if the flame proceeds in x-direction. In this kind of diagram, the kink must not be interpreted as a DDT indicator. As expected, the combustion process is finished first for the homogeneous mixture with the highest average hydrogen concentration. Despite the same average hydrogen concentration, the inhomogeneous mixtures behave differently. During the initial phase, the stratified mixture curve follows closely the homogeneous mixture curve. When the flame approaches the hydrogen concentration jump in the center of the reactor, latter curves start to diverge. The case with the continuous concentration gradient diverges from the homogeneous case right from the beginning. In summary, the burnout curves are in accordance with expectations based on initial concentration profiles. Nevertheless, it should be kept in mind that the hydrogen distribution in the unburned mixture changes in the course of the explosion process. Such behavior is demonstrated in sec. 4.4.

Pressure fields at discrete points in time are shown in figs. 5.6, 5.7 and 5.8. The cutting plane is positioned in a way that two of the four, structurally dominant, steam generators are centrically intersected. The reactor pressure vessel is not directly intersected by this eccentric plane ($z = 2$ m). Note the change of color scale between different picture rows. The white-colored $c = 0.5$ contour line indicates the flame front. Combining this data

|	
(a) 450 ms	(b) 500 ms
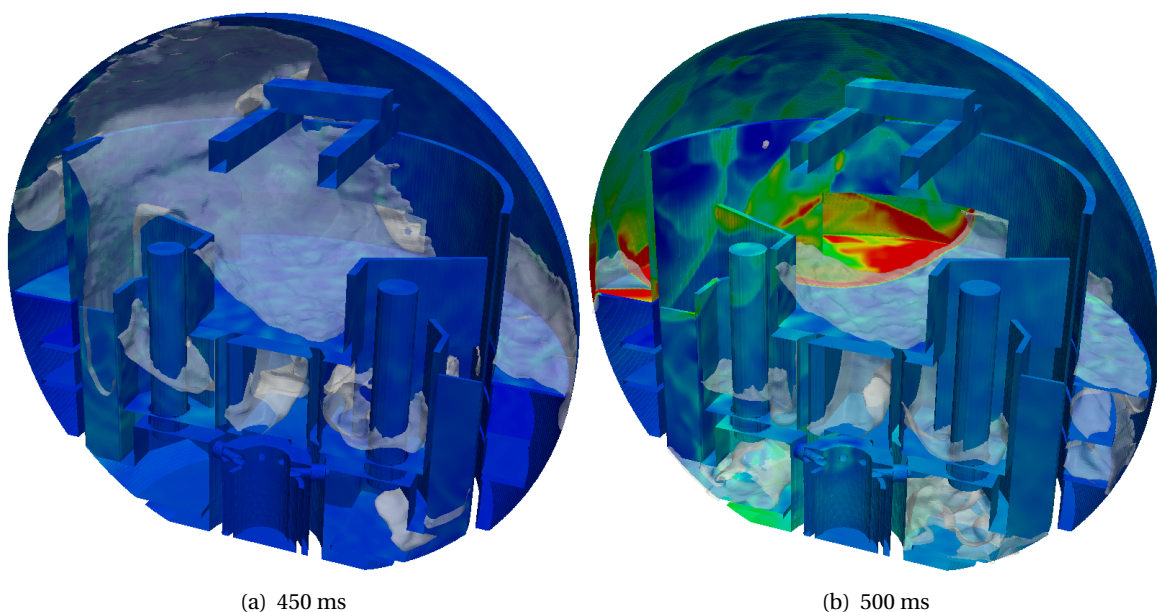
Figure 5.4: Wall pressure including semi-transparent flame contour; $\widehat{X}_{H_2} = 12.5$ %, $\Delta X_{H_2} = 5$ %, $b = 0.5$ (stratified); Rainbow color scale (appendix A) from 2.5 to 30 bar
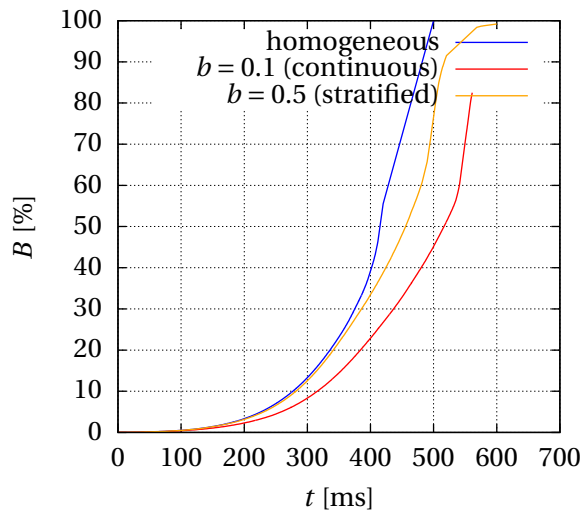
Figure 5.5: Temporal evolution of the burnout B for different mixture cases

with temporally continuous pressure signals at discrete points in space (fig. 5.9) yields a sufficiently detailed picture of the sequence of events. For all cases, the simulated overall time period is 0.7 s.

Figure 5.6 visualizes the explosion process for the homogeneous mixture consisting of 15 % of hydrogen in air. Approximately over the first 200 ms after ignition, the flame spreads slowly in the containment dome without any noticeable pressure increase. Progressive flame acceleration is accompanied by moderate pressure oscillations (242 ms). The flame starts to interact with enclosing geometry and enters the right steam generator tower from the top. Leading to overpressures higher than 1 bar, the explosion already transitioned from a slow to a fast deflagration (342 ms). As a consequence of further acceleration, a distinct precursor shock develops when the flame reaches the reactor adjacent room on the right (394 ms). Peak pressure is on the order of 15 bar. Triggered by reflection of the precursor shock, local coupling of the flame and leading shock occurs shortly after (405 ms). The detonation seems to originate from this event. It should be mentioned that, in general, the detonation origin is not exactly located in the cutting plane. In the next picture (415 ms), the stable detonation wave propagates to the left through the low-level reactor rooms. Before the flame fronts' coalescence in the left steam generator tower (between 415 ms and 425 ms), the largely diverging overpressure of downwards-oriented deflagrative combustion and upwards-oriented detonative combustion can clearly be seen. It is further possible to distinguish the corresponding propagation velocities of both combustion waves. The commonly made assumption of a detonation as the worst-case combustion regime agrees with these observations. Hazardous pressure loads, higher than 30 bar, are affecting the structure over a wide region close to the left steam generator tower (425 ms). Just as well, the simulation demonstrates the benefit of using a single solver framework to describe regime-switching flame propagation.

A different sequence of events appears for inhomogeneous mixtures. From a global point of view, the explosion process is quite similar for both cases ($b = 0.1$ in fig. 5.7 and $b = 0.5$ in fig. 5.8). A temporal shift, as already indicated by the burnout diagram 5.5, is not surprising given the lower average hydrogen concentration of 12.5 %. The phenomenology of flame acceleration in the upper part of the containment coincides with the homogeneous

case. The steam generator towers emerge as the main path of flame propagation between upper and lower part of the containment. Comparably late (537 ms for $b = 0.1$ and 491 ms for $b = 0.5$), a local explosion emanates from the rich region in the containment dome. At this point in time, the deflagration wave has already penetrated the low-level reactor rooms. When the strong blast wave catches up with the downwards-propagating flame, local coupling occurs in the outer corridors on the left (542 ms for $b = 0.1$ and 501 ms for $b = 0.5$) and in the refueling bay (553 ms for $b = 0.1$ and 505 ms for $b = 0.5$). Decoupling follows shortly after, as soon as the lean mixture is reached (559 ms for $b = 0.1$ and 505 ms for $b = 0.5$). No stable detonation wave can be detected in the lower part of the containment although a strong pressure build-up is present. In the last picture (559 ms for $b = 0.1$ and 519 ms for $b = 0.5$), distinct pressure waves, propagating through the hot combustion products in the containment dome, stand out. It can be summarized that DDT is basically possible also in the gradient cases at lower average hydrogen concentrations. However, the detonation quenches in regions with insufficient local hydrogen concentration. The DDT limit is usually several percent of hydrogen below the detonation transmission limit [58]. The conclusions of this paragraph might be different for the reverse situation with ignition in the lean region, e.g. at ignition location 2 (cf. fig. 5.2).

Supplementary temperature fields of all three cases are given in appendix C. Since the flame contour is already superimposed in the pressure fields, the corresponding temperature fields are not directly included here. Nevertheless, some interesting observations can be made in figs. C.1, C.2 and C.3: As long as gas-dynamic effects do not play a role, the temperature of the burned mixture is more or less given by the adiabatic flame temperature. The temperature rises by several hundred degrees if strong pressure waves occur. For example, strong blast waves propagating in the containment dome after DDT can clearly be identified. Moreover, both inhomogeneous mixtures are characterized by a vertical post-flame temperature stratification following roughly the initial concentration profiles. Adiabatic flame temperatures of three characteristic hydrogen concentration levels at elevated thermodynamic initial conditions are calculated as 1163.6 K (10 %), 1351.1 K (12.5 %) and 1536.0 K (15 %) using CANTERA [95].

Temporally continuous pressure signals at all probing locations (tab. 5.1) are depicted in fig. 5.9. Two configurations are opposed to each other: Homogeneous mixture (left column) and stratified inhomogeneous mixture with $b = 0.5$ (right column). The second inhomogeneous mixture with a continuous concentration gradient ($b = 0.1$) shows a temporally delayed but quite similar behavior and is therefore not directly included here. The corresponding pressure profiles are appended in fig. C.4. It is possible to draw conclusions on the underlying combustion regime from this and previous data.

The Adiabatic Isochoric Complete Combustion (AICC) reference pressure is calculated from a zero-dimensional thermodynamic balance and is additionally plotted in fig. 5.9. For elevated thermodynamic initial conditions, CANTERA [95] predicts AICC pressure values of 10.25 bar (12.5 %) and 11.49 bar (15 %). Both values lie clearly above the design pressure of the steel liner in Konvoi-type plants, namely 6.3 bar following Liang et al. [164]. According to the conservative simulation setup imposing a completely closed (i.e. no mass transfer to the environment) and adiabatic (i.e. no heat losses to the environment) boundary, all pressure signals have to converge to the AICC value after the system settles. Figure 5.9 thus verifies global mass and energy conservation in the model.

(a) 33 ms

(b) 242 ms

(c) 342 ms

(d) 365 ms

(e) 382 ms

(f) 394 ms

(g) 405 ms

(h) 415 ms

(i) 425 ms
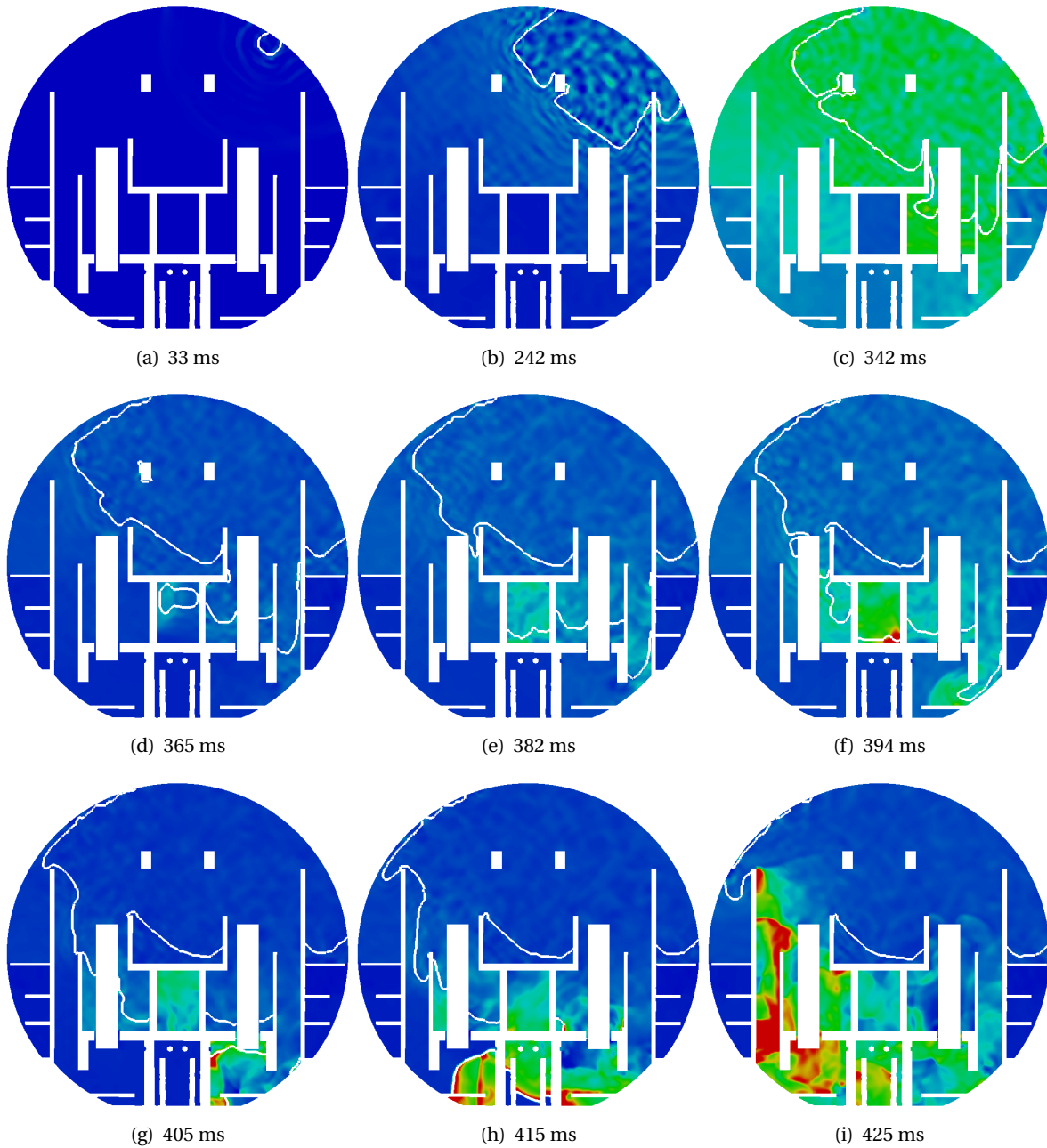
Figure 5.6: Pressure field including flame contour; $\widehat{X}_{H_2} = 15\,\%$, $\Delta X_{H_2} = 0\,\%$ (homogeneous); Rainbow color scale according to appendix A: First row from 2.5 to 5 bar, second row from 2.5 to 15 bar, third row from 2.5 to 30 bar

(a) 34 ms

(b) 249 ms

(c) 345 ms

(d) 438 ms

(e) 485 ms

(f) 537 ms

(g) 542 ms

(h) 553 ms

(i) 559 ms
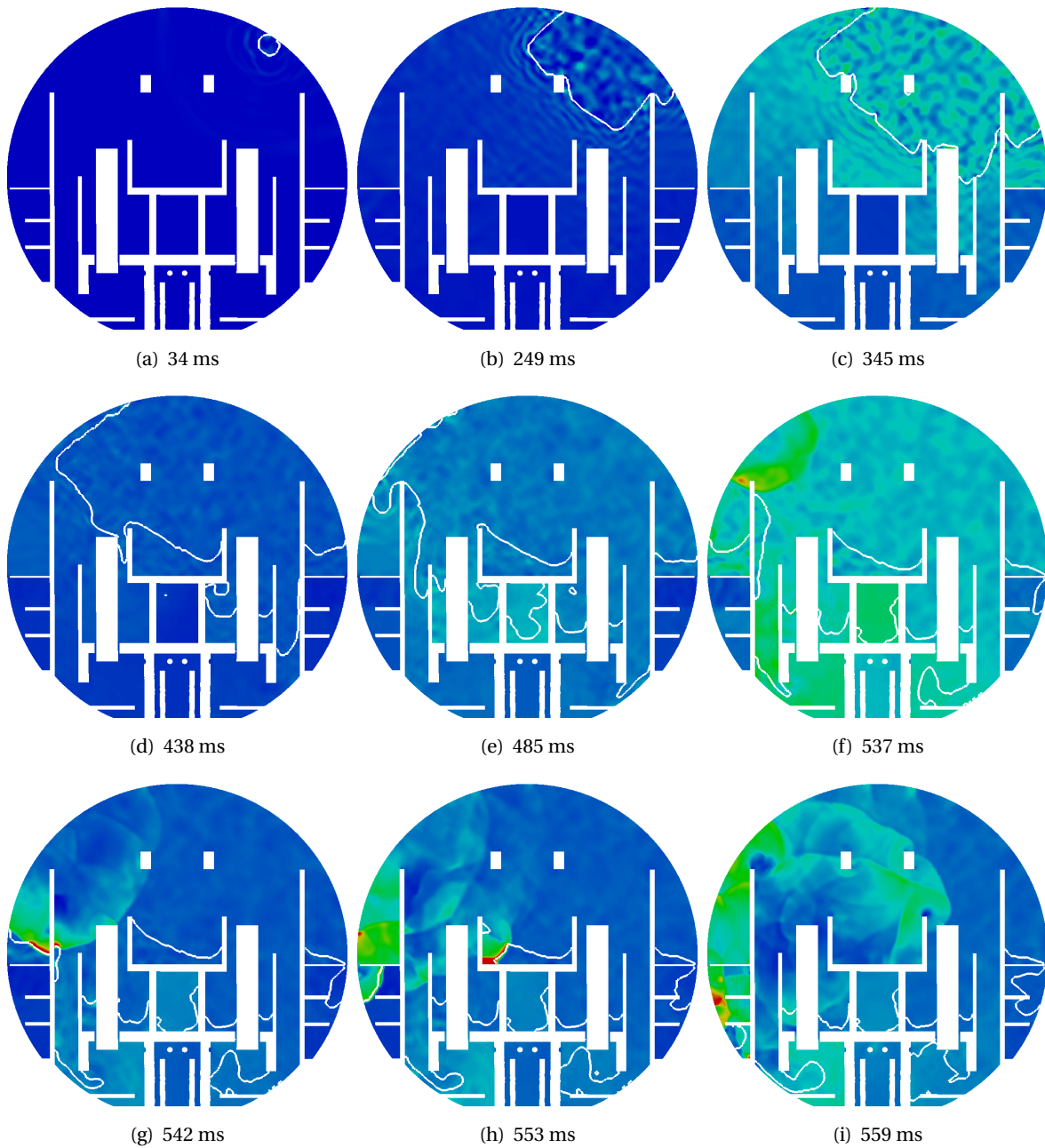
Figure 5.7: Pressure field including flame contour; $\widehat{X}_{H_2} = 12.5\,\%$, $\Delta X_{H_2} = 5\,\%$, $b = 0.1$ (continuous); Rainbow color scale according to appendix A: First row from 2.5 to 5 bar, second row from 2.5 to 15 bar, third row from 2.5 to 30 bar

(a) 34 ms

(b) 249 ms

(c) 338 ms

(d) 418 ms

(e) 447 ms

(f) 491 ms

(g) 501 ms

(h) 505 ms

(i) 519 ms
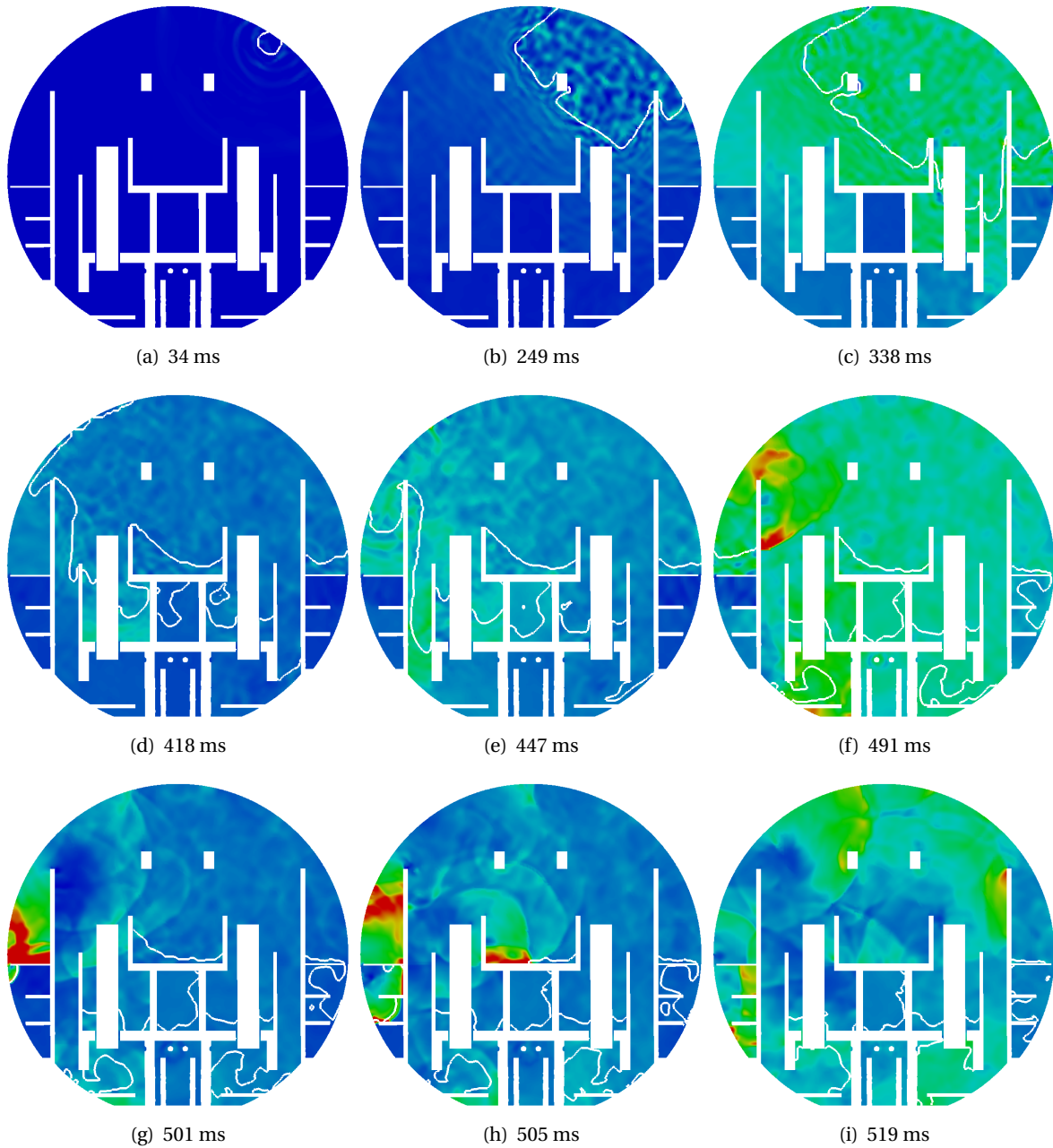
Figure 5.8: Pressure field including flame contour; $\widehat{X}_{H_2} = 12.5\,\%$, $\Delta X_{H_2} = 5\,\%$, $b = 0.5$ (stratified); Rainbow color scale according to appendix A: First row from 2.5 to 5 bar, second row from 2.5 to 15 bar, third row from 2.5 to 30 bar

Via the homogeneous case, the fundamentally different character of deflagrative and detonative flame propagation is evident from comparing the pressure signals of sensor 4 (reactor adjacent room on the left) and the remaining sensors which are not passed by a detonation. Aside from shocks, pressure increases gradually in case of a deflagration whereas a sharp pressure rise is caused by a detonation wave. Pressure peaks at the remaining sensors (at later times) are caused by secondary reflections in the already burned mixture, but remain below the detonation-associated peak value. In the gradient case, pronounced pressure peaks are present only in the containment dome. Pressure profiles follow the AICC reference more closely at all remaining sensors. As already mentioned, no stable detonation wave is sustained in the lower part of the containment where the mixture is 5 % of hydrogen leaner. As can be seen from the comparison of sensor 1 (unobstructed dome) and sensor 5 (obstructed bottom of the reactor) in both cases, the delay between distinct pressure peaks in the burned mixture is mainly controlled by spatial dimensions. The large dome diameter of 56 m leads to high-amplitude low-frequency oscillations in the upper part of the containment. Convergence to the AICC value is faster in the lower part of the containment due to the dissipating effect of frequent reflection and intersection of pressure waves.

Considering the highly dynamic load behavior and the occuring peak values (more than twice the AICC pressure), the containment might fail in the generic cases examined. Radioactive material would be released to the environment. To complete the safety analysis chain in sec. 1.1, the next step would be to evaluate the structural integrity of the containment based on the given pressure loads. A detailed structural assessment, e.g. based on finite element analysis, seems to be inevitable but is outside the scope of this work. To provide appropriate spatially and temporally resolved input, the benefit of doing costly CFD explosion simulations becomes clear. Structural finite element analysis encompasses also higher oscillation modes. The superposition of different effects makes the output more difficult to interpret. A simple structural response model is the single-degree-of-freedom oscillator, cf. Baker et al. [14] for instance. It describes the first harmonic of a structural element which is represented by lumped parameters for mass, stiffness and damping. The model is well suited to understand the basic effects of transient pressure loads on the deformation of a structural element. Using the blast loaded elastic oscillator model (damping neglected), two regimes can be distinguished: impulsive and quasi-static response. If the load duration is clearly shorter than the response time of the wall (impulsive regime), structural response is dominated by the impulse (temporal integration of the overpressure profile) rather than peak pressure. However, peak pressure starts to play the main role if the load duration is clearly longer than the response time of the wall (quasi-static regime). Both parameters are important in the transition regime between both asymptotic limits.

It has to be pointed out that the fuel concentration was intentionally chosen high enough to provoke DDT in the simulations. From the presented study, it cannot directly be concluded that DDT is likely to occur in core meltdown scenarios, especially if safety measures like passive auto-catalytic recombiners are properly working. Despite some simplifications and impossible validation of the reactor simulations, the solver can be valuable for worst-case assessment or the identification of precarious configurations during the design phase already. A step towards deterministic DDT simulations on full reactor scale has been made.
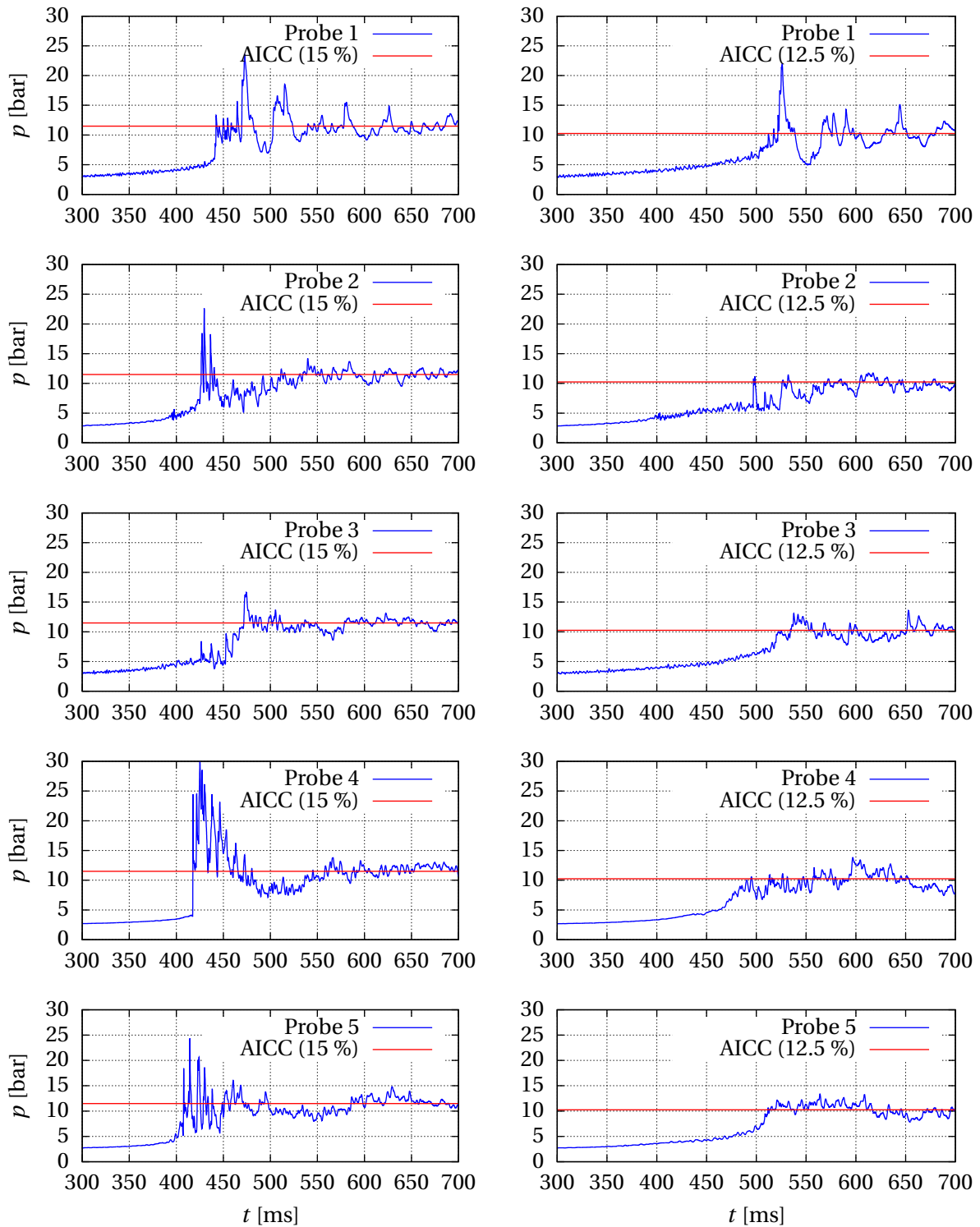
Figure 5.9: Transient pressure recordings at probing locations 1 to 5 compared to AICC pressure; Left column: $\widehat{X}_{H_2} = 15\,\%$, $\Delta X_{H_2} = 0\,\%$ (homogeneous); Right column: $\widehat{X}_{H_2} = 12.5\,\%$, $\Delta X_{H_2} = 5\,\%$, $b = 0.5$ (stratified)

5.3 Further influencing factors

Additional insight is available from earlier studies of Hasslberger et al. [102]. In the referenced work, several generic accident scenarios assuming globally lean hydrogen-air mixtures were investigated. The Konvoi-type reactor geometry was the same as described in sec. 5.1. As the simulations revealed, the sequence of events in terms of flame acceleration and DDT is very sensitive to the input parameters. In each of the three comparisons, only one input parameter (mixture distribution, ignition location or thermodynamic initial conditions) is varied. The most relevant findings are summarized:

- In terms of mixture composition, a different comparison was made by Hasslberger et al. [102] than in this work. In [102], homogeneous and inhomogeneous mixtures (with continuous concentration gradients defined by a stratification factor of $b = 0.1$ and a maximum concentration difference of $\Delta X_{H_2} = 10$ %) were compared at the same average hydrogen concentration. Thermodynamic initial conditions and ignition location were identical in both cases. It could be shown that mixture inhomogeneity can promote flame acceleration and ultimately DDT at a given average fuel concentration.

- Taking the same thermodynamic initial conditions and homogeneous mixture as a basis, initial flame acceleration is stronger for ignition in the lower part of the containment (ignition location 2 in fig. 5.2). Whereas widely unperturbed propagation of the flame is observed for ignition in the dome (ignition location 1 in fig. 5.2), the flame starts to interact with turbulence-inducing geometry at an earlier stage for ignition in the low-level reactor rooms. Additionally, perturbation of the flame by pressure waves, which are reflected off the walls, starts earlier in the bottom ignition case.

- At ambient thermodynamic initial conditions (1.013 bar, 293 K), the overall explosion process progresses slower than for elevated initial conditions (2.5 bar, 373 K) like in this work. The homogeneous mixture and ignition location were identical in both cases. The lower detonation limit is shifted to higher average hydrogen concentrations around 15 % for ambient initial conditions. Such critical values are subject to high uncertainties given the simplified geometrical model and the limitations of the CFD solver.

6 Summary

6.1 Motivation

In the framework of a research project funded by the German Federal Ministry of Economic Affairs and Energy (BMWi), a CFD combustion solver has been enhanced for the purpose of *nuclear safety analysis*. New numerical techniques and models aim at the prediction of large-scale hydrogen explosions like in the Fukushima-Daiichi core meltdown accident. A particular focus is placed on the hazardous Deflagration-to-Detonation Transition (DDT) phenomenon which is associated with extreme pressure loads on the confining structure. The developed tool can equally be used to support experimental studies or to identify precarious configurations during the design process of new facilities. Thus, the work is of academic interest and of practical relevance at the same time. The code shall eventually be delivered to Germany's nuclear safety agency GRS gGmbH and advance the state-of-the-art in hazard analysis. In doing so, interfaces to other codes for preceding fuel dispersion simulations as well as subsequent structural assessment have to be developed. Such coupling strategies are not part of this work but are presently under investigation in a follow-up project with nuclear industry. Independent of the specific motivation of this work, the methodology is not limited to nuclear safety but is potentially applicable to other technical problems like pulsed detonation engines (for which DDT has to be computed in each engine cycle, see e.g. [228]) or chemical and process industry.

6.2 CFD modeling

Contrary to the state-of-the-art in *large-scale* explosion modeling, the entire combustion process is computed within a single solver framework. Consequently, the use of empirical transition criteria (with limited validity) to select between multiple regime-optimized solvers can be avoided. A robust model is therefore necessary to cover all underlying regimes from slow (quasi-) laminar deflagration shortly after weak ignition to stable detonation propagation after possible occurrence of DDT. The multi-scale problem poses several challenges which are met by the following main features of the solver:

- The finite-volume solver is implemented in the open-source CFD package Open-FOAM which is able to handle topologically complex unstructured meshes.

- Due to the mixed parabolic-hyperbolic nature of the explosion problems, the computational methodology is built on the Favre-averaged unsteady compressible Navier-Stokes equations. Conservation equations for the total internal energy and for the hydrogen mixture fraction (because of potential mixture inhomogeneity) complete the system of governing equations. The ideal gas law is used as an equa-

tion of state. Turbulence closure is achieved through the well-established k-ω-SST model.

- A hybrid flame-tracking shock-capturing scheme is introduced to combine the advantages of different numerical techniques. On the one hand, explicit tracking of the flame by means of a geometrical Volume-of-Fluid method minimizes grid dependency of flame propagation which is one of the key issues on under-resolved industry-scale meshes. The underlying algorithm is executed iteratively to assure conservatism. On the other hand, a density-based solver architecture, in conjunction with an approximate Riemann solver (Harten-Lax-van Leer with Contact scheme) for the calculation of convective fluxes, ensures second-order accurate reproduction of gas-dynamic effects, essentially shocks.

- According to their mathematical behavior, hybrid temporal discretization is explicit with respect to convective terms and implicit with respect to diffusive terms. Dynamic time stepping adjusts the time step size to the accelerating flow. The limiting CFL criterion utilizes the maximum characteristic wave velocity (convective flow velocity + speed of sound) in the domain.

- Besides the kinematic propagation of the flame by a tracking algorithm, chemical reaction is modeled by a coupling of two source terms, one accounting for flamelet-like combustion and one for volumetric reaction (including auto-ignition). Dynamic and non-local effects of turbulence-chemistry interaction are included by solving an additional flame wrinkling evolution equation. Not only turbulence-induced, but also instabilities-induced flame wrinkling is taken into account via Dinkelacker's burning velocity correlation combined with an effective Lewis number approach. Flame quenching effects are additionally considered. To avoid the runtime-evaluation of numerically stiff source terms (of the Arrhenius type), required quantities of chemical kinetics are provided to the solver in the form of correlations and look-up tables, respectively.

- In order to reduce overall computational cost, adaptive mesh refinement locally increases mesh resolution according to the highly unsteady evolution of explosions. A combined refinement criterion is applied to dynamically refine the turbulent flame brush as well as relevant phenomena ahead of the flame (primarily precursor shocks and regions of enhanced turbulence production). Likewise, the algorithm based on isotropic cell division includes unrefinement in the completely burned region.

6.3 Large-scale validation

Due to the under-resolved nature of the simulations, there is a strong influence of subgrid models, especially for gas-dynamics, turbulence and chemical reaction. It is indispensable to validate the overall model by means of experimental data. The largest ever conducted indoor DDT experiments in the RUT facility (Kurchatov Institute, Moscow region) have been chosen because of their industry-scale geometrical dimensions and detailed instrumentation. Investigated DDT mixtures are close to the safety-relevant lower detonation limit which was measured at 12.5 % of hydrogen in air. For very lean mixtures ($\lesssim$ 15 % with Lewis numbers far smaller than unity), intrinsic flame instabilities, e.g. of thermal-diffusive nature, are a major contributor to flame acceleration.

As the simulations showed, the methodology is, in principle, able to capture the essential phenomena behind flame acceleration and DDT in obstructed channels. In contrast to very successful simulations of DDT by shock focusing (RUT configuration 22 with 14 % of hydrogen), prediction of DDT in the vicinity of the flame (RUT configuration 16 with 12.5 % of hydrogen) is less reliable. The reason is probably related to the difficulties in adequately resolving or modeling flame instabilities like the Richtmyer-Meshkov instability or the local explosion of unburned pockets enclosed in burned mixture in the vicinity of the turbulent flame brush. Additionally, a less challenging test case in a near-stoichiometric mixture (RUT configuration 09 with 25.5 % of hydrogen in air) involves direct detonation initiation and propagation. The code successfully reproduces key safety characteristics such as the detonation propagation velocity and associated pressure loads. Since homogeneous mixtures are generally not realistic for accident scenarios, the effect of mixture inhomogeneity was discussed by means of a generic case. The conclusion that inhomogeneous mixtures can promote flame acceleration and eventually DDT corresponds well to laboratory-scale experiments in the GraVent facility.

The intentionally coarse spatial discretization demonstrates the method's applicability to large-scale accident scenarios. Using appropriate sub-grid models and advanced numerical techniques (primarily flame tracking and adaptive mesh refinement), it is possible to predict flame acceleration and DDT at reasonable accuracy without access to high performance computing facilities. Reduction of grid dependency and minimization of computational cost are intrinsically tied to each other.

Another possibility to massively speed up the simulations is by dimensionality reduction. However, even if the geometry exhibits a strong two-dimensional character, inexpensive two-dimensional simulations must be assessed non-conservative. Flame acceleration and ultimately DDT propensity is systematically underestimated compared to three-dimensional simulations. Additional analysis indicates that the different evolution of flame surface area is responsible for this behavior. Splitting up the interaction on modeled microscopic (e.g. by turbulent eddies or flame instabilities) and resolved macroscopic level (e.g. by the jet behavior due to obstacles), their relative contribution provides further insight into the relevant mechanisms behind flame acceleration. Effective microscopic flame surface area is roughly one order of magnitude higher than the resolved macroscopic area.

6.4 Large-scale application

Following the motivation of this work, the developed solver was finally applied to a full-scale Konvoi-type nuclear reactor, i.e. a standardized German pressurized water reactor design. The geometrical model includes essential plant components (reactor pressure vessel, steam generators, pressurizer, polar crane etc.) and internal concrete structures. Because of the large free gas volume of approximately 75,000 m^3, massively parallelized computations were executed on the SuperMUC high performance cluster. Three generic DDT scenarios in globally lean hydrogen-air mixtures were examined. Unlike the homogeneous mixture, both inhomogeneous mixtures exhibit a one-dimensional vertical concentration gradient (of varying steepness) to imitate more realistic initial conditions. Weak ignition was assumed in the fuel-rich region at the top of the containment.

As expected, a strong sensitivity of the explosion process on mixture composition was observed. The sequence of events is highly three-dimensional which underscores the point of performing extensive CFD simulations for this kind of analysis. The steam generator towers emerge as the main path of flame propagation between the containment dome and low-level reactor rooms. Pressure loads on the confining structure show a profoundly dynamic behavior depending on the position in the containment. While distinct pressure oscillations appear in the unobstructed dome, faster convergence to static loads occurs in the more obstructed bottom of the reactor.

The simulations represent an extrapolation to some extent, especially regarding the mesh density and thermodynamic initial conditions. Despite some simplifications and impossible direct validation of the reactor simulations, the solver can be valuable for worst-case assessment in the context of nuclear safety analysis. A step towards deterministic DDT simulations on full reactor scale has been made.

7 Outlook

While keeping the framework of the numerical methodology, it is advisable to extend the combustion model to more complex mixtures including *steam* and *carbon monoxide*. Steam is generally present in the context of nuclear safety and carbon monoxide can be produced in large amounts during the ex-vessel phase of a core meltdown accident (Molten Corium Concrete Interaction). Whereas non-flammable steam mainly acts as an inert diluent (thermodynamic or physical effect) [145, 169], carbon monoxide is another flammable gas which changes not only fluid properties but has a strong influence on chemical kinetics (chemical effect) [149]. All required reactivity parameters like laminar burning velocity or ignition delay times have to be corrected for. Regarding the mixture composition, the current binary system (hydrogen, air) must be replaced by a ternary (hydrogen, carbon monoxide, air) or quaternary system (hydrogen, carbon monoxide, steam, air). Its dynamic evolution might be implemented by transport equations for one or two additional mixture fractions. Experimentalists are encouraged to provide appropriate validation data on laboratory and large scale.

Another possibility to extend the solver's capabilities is via the *distributed porosity concept* to include the effect of small-scale obstacles on sub-grid level. Even when using a high performance cluster, all geometrical details can usually not be represented by an industry-scale computational mesh. Simulation domains covering a full-scale nuclear reactor are a predestined example of that dilemma. The methodology originally dates back to Patankar and Spalding [204] and has been applied in explosion context e.g. by Arntzen [6]. The general idea is to assign volume as well as area porosities to computational cells, depending on the type of expression. For instance, an entirely blocked cell corresponds to zero porosity and an entirely unblocked cell corresponds to unity porosity. A porosity-based modification of the governing equations then allows to account for effects like drag, turbulence production and flame wrinkling which are caused by unresolved obstacles on sub-grid level.

Following the promising results in this work, it appears reasonable to devote additional effort to the modeling of unresolved *intrinsic flame instabilities*. Katzy et al. [123] conduct detailed experimental investigations on the development of thermal-diffusive and hydrodynamic instabilities during the early stage of flame propagation at vanishing or low turbulence intensity. The goal is to incorporate such phenomena in a sub-grid model without the need to actually resolve them. Modeling approaches with a similar background, i.e. comparably slow deflagration of lean hydrogen-air mixtures, are presented by Bauwens et al. [18] and Yáñez et al. [284].

As performance monitoring revealed, an unresolved issue concerns the solver architecture. Both essential numerical techniques, adaptive mesh refinement and explicit flame tracking, involve unequal processor loads in a parallel environment. *Dynamic redistribution* of processor sub-domains holds the potential to further increase the solver's efficiency. Besides, there is room for improvement in terms of a *fully parallelized workflow*

(including not only parallel execution of the CFD solver itself but also parallelized data input and output as well as pre- and post-processing) which is currently missing.

Bibliography

[1] Agbaglah, G., Delaux, S., Fuster, D., Hoepffner, J., Josserand, C., Popinet, S., Ray, P., Scardovelli, R. and Zaleski, S.: Parallel simulation of multiphase flows using octree adaptivity and the volume-of-fluid method. *Comptes Rendus Mecanique*, 339:194–207, 2011.

[2] Ahn, H. T. and Shashkov, M.: Multi-material interface reconstruction on generalized polyhedral meshes. *Journal of Computational Physics*, 226:2096–2132, 2007.

[3] Amdahl, G. M.: Validity of the single processor approach to achieving large scale computing capabilities. *Proceedings of the Spring Joint Computer Conference*, pp. 483–485. ACM, 1967.

[4] Anderson, D. A., Tannehill, J. C. and Pletcher, R. H.: Computational Fluid Mechanics and Heat Transfer. Hemisphere Publishing, 1984.

[5] Anderson, J.: Modern Compressible Flow. 3rd ed. McGraw–Hill, 2004.

[6] Arntzen, B.: Modelling of turbulence and combustion for simulation of gas explosions in complex geometries. PhD thesis, NTNU Trondheim, 1998.

[7] Aslam, T. D.: A level-set algorithm for tracking discontinuities in hyperbolic conservation laws: I. Scalar equations. *Journal of Computational Physics*, 167:413–438, 2001.

[8] Aslam, T., Bdzil, J. and Stewart, D.: Level set methods applied to modeling detonation shock dynamics. *Journal of Computational Physics*, 126:390–409, 1996.

[9] Auban, O., Zboray, R. and Paladino, D.: Investigation of large–scale gas mixing and stratification phenomena related to LWR containment studies in the PANDA facility. *Nuclear Engineering and Design*, 237:409–419, 2007.

[10] Aung, K., Hassan, M. and Faeth, G.: Flame stretch interactions of laminar premixed hydrogen/air flames at normal temperature and pressure. *Combustion and Flame*, 109:1–24, 1997.

[11] Austin, J.: The Role of Instability in Gaseous Detonation. PhD thesis, California Institute of Technology, 2003.

[12] Azatyan, V.: Problems of combustion, explosion, and gas detonation in the theory of nonisothermal chain processes. *Russian Journal of Physical Chemistry A*, 88:747–758, 2014.

[13] Bak, P., Chen, K. and Tang, C.: A forest-fire model and some thoughts on turbulence. *Physics letters A*, 147:297–300, 1990.

[14] Baker, W. E., Cox, P., Kulesz, J., Strehlow, R. and Westine, P.: Explosion hazards and evaluation: vol. 5. Elsevier, 2012.

[15] Baraldi, D., Kotchourko, A., Lelyakin, A., Yanez, J., Middha, P., Hansen, O., Gavrikov, A., Efimenko, A., Verbecke, F., Makarov, D. et al.: An inter-comparison exercise on CFD model capabilities to simulate hydrogen deflagrations in a tunnel. *International Journal of Hydrogen Energy*, 34:7862–7872, 2009.

[16] Barr, P. and Ashurst, W. T.: Interface scheme for turbulent flame propagation. Technical report, Sandia National Laboratories, Livermore, CA, USA, 1984.

[17] Bartlmä, F.: Gasdynamik der Verbrennung. Springer, 1975.

[18] Bauwens, C. R., Chaffee, J. and Dorofeev, S.: Vented explosion overpressures from combustion of hydrogen and hydrocarbon mixtures. *International Journal of Hydrogen Energy*, 36:2329–2336, 2011.

[19] Beccantini, A. and Studer, E.: The reactive Riemann problem for thermally perfect gases at all combustion regimes. *International Journal for Numerical Methods in Fluids*, 64:269–313, 2010.

[20] Bechtold, J. and Matalon, M.: The dependence of the Markstein length on stoichiometry. *Combustion and Flame*, 127:1906–1913, 2001.

[21] Bell, J. B., Colella, P. and Glaz, H. M.: A second-order projection method for the incompressible Navier-Stokes equations. *Journal of Computational Physics*, 85:257–283, 1989.

[22] Berthoud, G.: Vapor explosions. *Annual Review of Fluid Mechanics*, 32:573–611, 2000.

[23] Bielert, U., Klug, M. and Adomeit, G.: Application of front tracking techniques to the turbulent combustion processes in a single stroke device. *Combustion and Flame*, 106:11–28, 1996.

[24] Biello, D.: The world really could go nuclear: September 2015. `https://www.scientificamerican.com/article/the-world-really-could-go-nuclear/`. Last accessed November 29, 2016.

[25] Bird, R., Stewart, W. and Lightfoot, E.: Transport Phenomena. 2nd ed. John Wiley & Sons, 2001.

[26] Boeck, L., Hasslberger, J. and Sattelmayer, T.: Flame acceleration in hydrogen-air mixtures with concentration gradients. *Combustion Science and Technology*, 186:1650–1661, 2014.

[27] Boeck, L., Msalmi, S., Koehler, F., Hasslberger, J. and Sattelmayer, T.: Criteria for DDT in hydrogen-air mixtures with concentration gradients. *Tenth International Symposium on Hazards, Prevention, and Mitigation of Industrial Explosions*, Bergen, Norway, 2014.

[28] Boeck, L.: Deflagration-to-Detonation Transition and Detonation Propagation in H_2-Air Mixtures with Transverse Concentration Gradients. PhD thesis, Technische Universität München, 2015.

[29] Boeck, L., Primbs, A., Hasslberger, J., Ettner, F. and Sattelmayer, T.: Influence of concentration gradients on detonation velocities in hydrogen–air mixtures. *First International Conference on Combustion and Explosion*, Ramsau, Austria, 2013.

[30] Boeck, L., Berger, F., Hasslberger, J. and Sattelmayer, T.: Detonation propagation in hydrogen–air mixtures with transverse concentration gradients. *Shock Waves*, 26: 181–192, 2016.

[31] Boeck, L., Mével, R. and Sattelmayer, T.: Models for shock-induced ignition evaluated by detailed chemical kinetics in the context of deflagration-to-detonation transition. *Eleventh International Symposium on Hazards, Prevention, and Mitigation of Industrial Explosions*, Dalian, China, 2016.

[32] Borghi, R.: On the Structure and Morphology of Turbulent Premixed Flames. In: Casci, C. (editor): Recent Advances in the Aerospace Sciences, pp. 117–138. Plenum Press, 1985.

[33] Borghi, R.: Turbulent combustion modelling. *Progress in Energy and Combustion Science*, 14:245–292, 1988.

[34] Bradley, D., Lau, A. and Lawes, M.: Flame stretch rate as a determinant of turbulent burning velocity. *Philosophical Transactions of the Royal Society of London, Series A*, 338:359–387, 1992.

[35] Bray, K.: Methods of Including Realistic Chemical Reaction Mechanisms in Turbulent Combustion Models. In: Warnatz, J. and Jaeger, W. (editors): Complex Chemical Reaction Systems, vol. 47 in: Springer Series in Chemical Physics, pp. 356–375. Springer, 1986.

[36] Bray, K. and Moss, J.: A unified statistical model of the premixed turbulent flame. *Acta Astronautica*, 4:291–319, 1977.

[37] Bray, K., Libby, P. A. and Moss, J.: Unified modeling approach for premixed turbulent combustion – Part I: General formulation. *Combustion and Flame*, 61:87–102, 1985.

[38] Breitung, W. and Kotchourko, A.: Numerische Simulation von turbulenten Wasserstoffverbrennungen bei schweren Kernreaktorunfällen. Technical report, FZK-Nachrichten 28, 1996.

[39] Breitung, W. and Royl, P.: Procedure and tools for deterministic analysis and control of hydrogen behavior in severe accidents. *Nuclear Engineering and Design*, 202: 249–268, 2000.

[40] Breitung, W., Chan, C., Dorofeev, S., Eder, A., Gerland, B., Heitsch, M., Klein, R., Malliakos, A., Shepherd, J., Studer, E. and Thibault, P.: Flame acceleration and deflagration-to-detonation transition in nuclear safety. Technical report, OECD/NEA/CSNI/R7, 2000.

[41] Breitung, W., Baumann, W., Bielert, U., Burgeth, B., Dorofeev, S., Kaup, B., Kotchourko, A., Necker, G., Redlinger, R., Royl, P., Starflinger, J., Stern, G., Travis, J., Veser, A. and Xu, Z.: Innovative Methoden zu Analyse und Kontrolle des Wasserstoffverhaltens bei Kernschmelzunfällen. Technical report, Forschungszentrum Karlsruhe, Institut für Kern- und Energietechnik, 2005.

[42] Breitung, W., Dorofeev, S., Kotchourko, A., Redlinger, R., Scholtyssek, W., Bentaib, A., L'Heriteau, J.-P, Pailhories, P., Eyink, J., Movahed, M., Petzold, K.-G., Heitsch, M., Alekseev, V., Denkevits, A., Kuznetsov, M., Efimenko, A., Okun, M., Huld, T. and Baraldi, D.: Integral large scale experiments on hydrogen combustion for severe accident code validation-HYCOM. *Nuclear Engineering and Design*, 235:253 – 270, 2005.

[43] Brent, R. P.: An algorithm with guaranteed convergence for finding a zero of a function. *The Computer Journal*, 14:422–425, 1971.

[44] Brähler, T. and Koch, M.: Analysis and Validation of Hydrogen Combustion Models of ASTEC. Technical report, Lehrstuhl Energiesysteme und Energiewirtschaft, Ruhr-Universität Bochum, 2011.

[45] Brouillette, M.: The Richtmyer-Meshkov instability. *Annual Review of Fluid Mechanics*, 34:445–468, 2002.

[46] Browne, S., Ziegler, J. and Shepherd, J.: Numerical solution methods for shock and detonation jump conditions. Technical report, GALCIT Report FM2006.006, 2008.

[47] Candel, S. M. and Poinsot, T. J.: Flame stretch and the balance equation for the flame area. *Combustion Science and Technology*, 70:1–15, 1990.

[48] Cant, R. and Mastorakos, E.: An Introduction to Turbulent Reacting Flows. Imperial College Press, 2008.

[49] Cant, R., Pope, S. and Bray, K.: Modelling of flamelet surface-to-volume ratio in turbulent premixed combustion. *Symposium (International) on Combustion*, vol. 23, pp. 809–815, 1991.

[50] Černe, G., Petelin, S. and Tiselj, I.: Numerical errors of the volume-of-fluid interface tracking algorithm. *International Journal for Numerical Methods in Fluids*, 38:329–350, 2002.

[51] Chapman, D.: On the rate of explosion in gases. *Philosophical Magazine*, 47:90–104, 1899.

[52] Chorin, A. J.: Flame advection and propagation algorithms. *Journal of Computational Physics*, 35:1–11, 1980.

[53] Ciccarelli, G. and Dorofeev, S.: Flame acceleration and transition to detonation in ducts. *Progress in Energy and Combustion Science*, 34:499–550, 2008.

[54] Ciccarelli, G., Johansen, C. T. and Parravani, M.: The role of shock–flame interactions on flame acceleration in an obstacle laden channel. *Combustion and Flame*, 157:2125–2136, 2010.

[55] Clavin, P.: Dynamic behavior of premixed flame fronts in laminar and turbulent flows. *Progress in Energy and Combustion Science*, 11:1–59, 1985.

[56] Colin, O., Pires da Cruz, A. and Jay, S.: Detailed chemistry–based auto–ignition model including low temperature phenomena applied to 3–D engine calculations. *Proceedings of the Combustion Institute*, 30:2649–2656, 2005.

[57] Coward, H. F. and Jones, G. W.: Limits of flammability of gases and vapors. Technical report, DTIC, 1952.

[58] Cross, M. and Ciccarelli, G.: DDT and detonation propagation limits in an obstacle filled tube. *Journal of Loss Prevention in the Process Industries*, 36:380–386, 2015.

[59] Daudey, N. and Champasith, A.: Accidental hydrogen release inside a nuclear power plant: CFD modelling and consequence analysis. *Tenth International Symposium on Hazards, Prevention, and Mitigation of Industrial Explosions*, Bergen, Norway, 2014.

[60] Deiterding, R.: Parallel Adaptive Simulation of Multi-dimensional Detonation Structures. PhD thesis, Technische Universität Cottbus, 2003.

[61] Dimmelmeier, H., Eyink, J. and Movahed, M.-A.: Computational validation of the EPR combustible gas control system. *Nuclear Engineering and Design*, 249:118–124, 2012.

[62] Dinkelacker, F., Hoelzler, S. and Leipertz, A.: Studies with a turbulent-flame-speed-closure model for premixed turbulent flame calculations. *17th International Colloquium on the Dynamics of Explosions and Reactive Systems*, Heidelberg, Germany, 1999.

[63] Dinkelacker, F., Manickam, B. and Muppala, S.: Modelling and simulation of lean premixed turbulent methane/hydrogen/air flames with an effective Lewis number approach. *Combustion and Flame*, 158:1742–1749, 2011.

[64] Dorofeev, S.: Flame acceleration and explosion safety applications. *Proceedings of the Combustion Institute*, 33:2161–2175, 2011.

[65] Dorofeev, S., Sidorov, V., Dvoinishnikov, A. and Breitung, W.: Deflagration to detonation transition in large confined volume of lean hydrogen–air mixtures. *Combustion and Flame*, 104:95 – 110, 1996.

[66] Dorofeev, S., Sidorov, V., Kuznetsov, M., Matsukov, I. and Alekseev, V.: Effect of scale on the onset of detonations. *Shock Waves*, 10:137–149, 2000.

[67] Dorofeev, S., Kuznetsov, M., Alekseev, V., Efimenko, A. and Breitung, W.: Evaluation of limits for effective flame acceleration in hydrogen mixtures. *Journal of Loss Prevention in the Process Industries*, 14:583–589, 2001.

[68] Döring, W.: Über den Detonationsvorgang in Gasen. *Annalen der Physik*, 43:421–436, 1943.

[69] Drinovac, P.: Experimentelle Untersuchungen zu katalytischen Wasserstoffrekombinatoren für Leichtwasserreaktoren. PhD thesis, Rheinisch–Westfälische Technische Hochschule Aachen, 2006.

[70] Driscoll, J. F.: Turbulent premixed combustion: Flamelet structure and its effect on turbulent burning velocities. *Progress in Energy and Combustion Science*, 34:91–134, 2008.

[71] Dukowicz, J. K. and Baumgardner, J. R.: Incremental remapping as a transport/advection algorithm. *Journal of Computational Physics*, 160:318–335, 2000.

[72] Dyadechko, V. and Shashkov, M.: Moment-of-fluid interface reconstruction. *Los Alamos report LA-UR-05-7571*, 2006.

[73] Dzieminska, E. and Hayashi, A. K.: Auto-ignition and DDT driven by shock wave–boundary layer interaction in oxyhydrogen mixture. *International Journal of Hydrogen Energy*, 38:4185–4193, 2013.

[74] Eder, A.: Brennverhalten schallnaher und überschall–schneller Wasserstoff–Luft Flammen. PhD thesis, Technische Universität München, 2001.

[75] Efimenko, A. A. and Dorofeev, S. B.: CREBCOM code system for description of gaseous combustion. *Journal of Loss Prevention in the Process Industries*, 14:575–581, 2001.

[76] Einfeldt, B.: On Godunov–type methods for gas dynamics. *SIAM Journal on Numerical Analysis*, 25:294–318, 1988.

[77] Einstein, A.: Die Grundlage der allgemeinen Relativitätstheorie. *Annalen der Physik*, 49:769–822, 1916.

[78] Emami, S., Mazaheri, K., Shamooni, A. and Mahmoudi, Y.: LES of flame acceleration and DDT in hydrogen–air mixture using artificially thickened flame approach and detailed chemical kinetics. *International Journal of Hydrogen Energy*, 40:7395–7408, 2015.

[79] Ettner, F.: Effiziente numerische Simulation des Deflagrations–Detonations–Übergangs. PhD thesis, Technische Universität München, 2013.

[80] Ettner, F., Vollmer, K. and Sattelmayer, T.: Einfluss von Mischungsgradienten und seitlichem Massenverlust auf die Flammenbeschleunigung und die Detonation in Kanälen. GRS-Abschlussbericht Vorhaben Nr. 1501338, Technische Universität München, 2011.

[81] Ettner, F., Vollmer, K. and Sattelmayer, T.: Mach reflection in detonations propagating through a gas with a concentration gradient. *Shock Waves*, 23:201–206, 2013.

[82] Ettner, F., Vollmer, K. and Sattelmayer, T.: Numerical simulation of the deflagration-to-detonation transition in inhomogeneous mixtures. *Journal of Combustion*, http://dx.doi.org/10.1155/2014/686347 2014.

[83] Explosion Dynamics Laboratory (EDL), California Institute of Technology: Shock and Detonation Toolbox. http://www.galcit.caltech.edu/EDL/public/cantera/html/SD_Toolbox/. Last accessed November 29, 2016.

[84] Favre, A.: Equations des gaz turbulents compressibles. *Journal de Mécanique*, 4:361–390, 1965.

[85] Ferziger, J. and Peric, M.: Computational Methods for Fluid Dynamics. 3rd ed. Springer, 2002.

[86] Friedrich, A., Grune, J., Necker, G., Sempert, K., Stern, G., Veser, A., Kuznetsov, M., Kotchourko, A., Breitung, W. and Jordan, T.: Kriterien für Flammenbeschleunigung und Detonationsübergang in Wasserstoff–Luft–Gemischen mit Konzentrationsgradienten und partiellem Einschluss. GRS-Abschlussbericht Vorhaben Nr. 1501346, Pro-Science GmbH, Karlsruher Institut für Technologie, Karlsruhe, 2011.

[87] Fuster, D., Bagué, A., Boeck, T., Le Moyne, L., Leboissetier, A., Popinet, S., Ray, P., Scardovelli, R. and Zaleski, S.: Simulation of primary atomization with an octree adaptive mesh refinement and VOF method. *International Journal of Multiphase Flow*, 35:550–565, 2009.

[88] Gaathaug, A. V., Vaagsaether, K. and Bjerketvedt, D.: Experimental and numerical investigation of DDT in hydrogen–air behind a single obstacle. *International Journal of Hydrogen Energy*, 37:17606–17615, 2012.

[89] Gamezo, V. N., Ogawa, T. and Oran, E. S.: Deflagration-to-detonation transition in H_2-air mixtures: Effect of blockage ratio. *AIAA Paper*, 440:5–8, 2009.

[90] Gamezo, V., Desbordes, D. and Oran, E.: Two–dimensional reactive flow dynamics in cellular detonation waves. *Shock Waves*, 9:11–17, 1999.

[91] García, J., Baraldi, D., Gallego, E., Beccantini, A., Crespo, A., Hansen, O., Høiset, S., Kotchourko, A., Makarov, D., Migoya, E. et al.: An intercomparison exercise on the capabilities of CFD models to reproduce a large-scale hydrogen deflagration in open atmosphere. *International Journal of Hydrogen Energy*, 35:4435–4444, 2010.

[92] Gerlinger, P.: Numerische Verbrennungssimulation. Springer, 2005.

[93] Glassman, I.: Combustion. Academic press, 1997.

[94] Golovitchev, V., Nordin, N., Jarnicki, R. and Chomiak, J.: 3–D Diesel spray simulations using a new detailed chemistry turbulent combustion model. *Society of Automotive Engineers*, 2000.

[95] Goodwin, D.: Cantera: an object–oriented software toolkit for chemical kinetics, thermodynamics and transport processes: 2009. `http://code.google.com/p/cantera`. Last accessed November 29, 2016.

[96] Gorchkov, V., Kiyanda, C., Short, M. and Quirk, J.: A detonation stability formulation for arbitrary equations of state and multi-step reaction mechanisms. *Symposium (International) on Combustion*, 31:2397–2405, 2007.

[97] Grune, J., Sempert, K., Haberstroh, H., Kuznetsov, M. S. and Jordan, T.: Experimental investigation of hydrogen–air deflagrations and detonations in semi-confined flat layers. *Journal of Loss Prevention in the Process Industries*, 26:317–323, 2013.

[98] Grune, J., Sempert, K., Kuznetsov, M. S. and Jordan, T.: Experimental investigation of fast flame propagation in stratified hydrogen–air mixtures in semi-confined flat layers. *Journal of Loss Prevention in the Process Industries*, 26:1442–1451, 2013.

[99] Harvie, D. J. and Fletcher, D. F.: A new volume of fluid advection algorithm: the stream scheme. *Journal of Computational Physics*, 162:1–32, 2000.

[100] Hasslberger, J., Ettner, F., Boeck, L. and Sattelmayer, T.: 2D and 3D flame surface analysis of flame acceleration and deflagration–to–detonation transition in hydrogen–air mixtures with concentration gradients. *24th International Colloquium on the Dynamics of Explosions and Reactive Systems*, Taipei, Taiwan, 2013.

[101] Hasslberger, J., Boeck, L. and Sattelmayer, T.: Numerical simulation of deflagration-to-detonation transition in large confined volumes. *Tenth International Symposium on Hazards, Prevention, and Mitigation of Industrial Explosions*, Bergen, Norway, 2014.

[102] Hasslberger, J., Katzy, P., Boeck, L. and Sattelmayer, T.: Massively parallelized simulation of deflagration-to-detonation transition in a Konvoi-type pressurized water reactor. *24th International Conference on Nuclear Engineering*, Charlotte, NC, USA, 2016.

[103] He, L.: A scaling analysis of the critical conditions for a deflagration-to-detonations transition. *Combustion Theory and Modelling*, 4:107–122, 2000.

[104] Heidari, A., Ferraris, S., Wen, J. X. and Tam, V.: Numerical simulation of large scale hydrogen detonation. *International Journal of Hydrogen Energy*, 36:2538–2544, 2011.

[105] Heidari, A. and Wen, J. X.: Flame acceleration and transition from deflagration to detonation in hydrogen explosions. *International Journal of Hydrogen Energy*, 39: 6184–6200, 2014.

[106] Heidari, A. and Wen, J. X.: Numerical simulation of flame acceleration and deflagration to detonation transition in hydrogen-air mixture. *International Journal of Hydrogen Energy*, 39:21317–21327, 2014.

[107] Hernández, J., López, J., Gómez, P., Zanzi, C. and Faura, F.: A new volume of fluid method in three dimensions – Part I: Multidimensional advection method with face-matched flux polyhedra. *International Journal for Numerical Methods in Fluids*, 58: 897–921, 2008.

[108] Hirt, C., Amsden, A. A. and Cook, J.: An arbitrary Lagrangian-Eulerian computing method for all flow speeds. *Journal of Computational Physics*, 14:227–253, 1974.

[109] Hirt, C. and Nichols, B. D.: Volume of fluid (VOF) method for the dynamics of free boundaries. *Journal of Computational Physics*, 39:201–225, 1981.

[110] Hsu, W.-S., Chen, H.-P. and Lin, H. C.: Hydrogen behavior in a large-dry pressurized water reactor containment building during a severe accident. *Tenth International Symposium on Hazards, Prevention and Mitigation of Industrial Explosions*, Bergen, Norway, 2014.

[111] Hyman, J. M.: Numerical methods for tracking interfaces. *Physica D: Nonlinear Phenomena*, 12:396–407, 1984.

[112] Iaccarino, G., Ooi, A., Durbin, P. and Behnia, M.: Reynolds averaged simulation of unsteady separated flow. *International Journal of Heat and Fluid Flow*, 24:147–156, 2003.

[113] Ivey, C. and Moin, P.: Conservative volume of fluid advection method on unstructured grids in three dimensions. *Center for Turbulence Research Annual Research Briefs*, pp. 179–192, 2012.

[114] Jasak, H.: Numerical solution algorithms for compressible flow. Lecture Notes, University of Zagreb, 2006.

[115] Jasak, H. and Gosman, A.: Automatic resolution control for the finite-volume method, Part 2: Adaptive mesh refinement and coarsening. *Numerical Heat Transfer: Part B: Fundamentals*, 38:257–271, 2000.

[116] Jasak, H. and Rusche, H.: Dynamic mesh handling in OpenFOAM. *Proceeding of the 47th Aerospace Sciences Meeting Including the New Horizons Forum and Aerospace Exposition*, Orlando, FL, USA, 2009.

[117] Jemison, M., Loch, E., Sussman, M., Shashkov, M., Arienti, M., Ohta, M. and Wang, Y.: A coupled level set-moment of fluid method for incompressible two-phase flows. *Journal of Scientific Computing*, 54:454–491, 2013.

[118] Jofre, L., Lehmkuhl, O., Castro, J. and Oliva, A.: A PLIC-VOF implementation on parallel 3D unstructured meshes. *Fifth European Conference on Computational Fluid Dynamics, ECCOMAS*, 2010.

[119] Jones, W. and Launder, B.: The prediction of laminarization with a two-equation model of turbulence. *International Journal of Heat and Mass Transfer*, 15:301–314, 1972.

[120] Jouguet, E.: Sur la propagation des réactions chimiques dans les gaz. *Journal de Mathématiques Pures et Appliquées*, 1:347–425, 1905.

[121] Joulin, G. and Mitani, T.: Linear stability analysis of two-reactant flames. *Combustion and Flame*, 40:235–246, 1981.

[122] Kaiser, T. L.: Under-resolved simulation of detonations in inhomogeneous hydrogen-air mixtures. Master's thesis, Technische Universität München, 2013.

[123] Katzy, P., Boeck, L., Hasslberger, J. and Sattelmayer, T.: Application of high-speed OH-PLIF technique for improvement of lean hydrogen-air combustion modeling. *24th International Conference on Nuclear Engineering*, Charlotte, NC, USA, 2016.

[124] Kee, R. J., Rupley, F. M., Miller, J. A., Coltrin, M. E., Grcar, J. F., Meeks, E., Moffat, H. K., Lutz, A. E., Dixon-Lewis, G., Smooke, M. D., Warnatz, J., Evans, G. H., Larson, R. S., Mitchell, R. E., Petzold, L. R., Reynolds, W. C., Caracotsios, M., Stewart, W. E., Glarborg, P., Wang, C. and Adigun, O.: The Chemkin thermodynamic database: 2000.

[125] Kee, R., Coltrin, M. and Glarborg, P.: Chemically Reacting Flow. John Wiley & Sons, 2003.

[126] Keenan, J., Makarov, D. and Molkov, V.: Towards the implementation of Rayleigh-Taylor instability into the multi-phenomena deflagration model. *Proceedings of the Seventh International Seminar on Fire and Explosion Hazards*, 2013.

[127] Keenan, J., Makarov, D. and Molkov, V.: Rayleigh-Taylor instability: Modelling and effect on coherent deflagrations. *International Journal of Hydrogen Energy*, 39: 20467–20473, 2014.

[128] Kellenberger, M. and Ciccarelli, G.: Propagation mechanisms of supersonic combustion waves. *Proceedings of the Combustion Institute*, 35:2109–2116, 2015.

[129] Keppeler, R. and Pfitzner, M.: Modelling of Landau-Darrieus and thermo-diffusive instability effects for CFD simulations of laminar and turbulent premixed combustion. *Combustion Theory and Modelling*, 19:1–28, 2015.

[130] Kerner, A., Stück, F. and Weiss, F.-P.: Der Unfall von Tschernobyl 1986. *atw*, 2:80–87, 2011.

[131] Kessler, D., Gamezo, V. and Oran, E.: Numerical simulation of deflagration-to-detonation transition in methane-air mixtures on large scale. *Proceedings of the Seventh International Seminar on Fire and Explosion Hazards*, 2013.

[132] Kessler, D., Gamezo, V. and Oran, E.: Simulations of flame acceleration and deflagration–to–detonation transitions in methane–air systems. *Combustion and Flame*, 157:2063–2077, 2010.

[133] Kessler, D., Gamezo, V. and Oran, E.: Multilevel detonation cell structures in methane-air mixtures. *Proceedings of the Combustion Institute*, 33:2211–2218, 2011.

[134] Kessler, D., Gamezo, V. and Oran, E.: Gas–phase detonation propagation in mixture composition gradients. *Philosophical Transactions of the Royal Society of London, Series A*, 370:567–596, 2012.

[135] Ketterl, S.: A conservative geometrical volume-of-fluid method with iterative interface reconstruction supporting unstructured meshes. Master's thesis, Technische Universität München, 2014.

[136] Khokhlov, A., Oran, E. and Thomas, G.: Numerical simulation of deflagration-to-detonation transition: The role of shock–flame interactions in turbulent flames. *Combustion and Flame*, 117:323–339, 1999.

[137] Kim, J. and Hong, S.-W.: Analysis of hydrogen flame acceleration in APR1400 containment by coupling hydrogen distribution and combustion analysis codes. *Progress in Nuclear Energy*, 78:101–109, 2015.

[138] Kirmeß, O.: Numerische Simulation instationärer, turbulenter Flammenausbreitung in Rohren. PhD thesis, Rheinisch–Westfälische Technische Hochschule Aachen, 1996.

[139] Klein, M.: Direkte Numerische Simulation des primären Strahlzerfalls in Einstoffzerstäuberdüsen. PhD thesis, Technische Universität Darmstadt, 2002.

[140] Klein, R., Breitung, W., Coe, I., He, L., Olivier, H., Rehm, W. and Studer, E.: Models and criteria for prediction of deflagration-to-detonation transition (DDT) in hydrogen-air-steam systems under severe accident conditions. Forschungszentrum Jülich, 2000.

[141] Kogarko, S. and Zeldovich, Y.: Detonation of gaseous mixtures. *Doklady Akademiya Nauk SSSR*, 63:553–556, 1948.

[142] Kolmogorov, A.: Local structure of turbulence in incompressible viscous fluid at very large Reynolds number. *Doklady Akademiya Nauk SSSR*, 30:299–303, 1941.

[143] Kolmogorov, A.: A refinement of previous hypotheses concerning the local structure in turbulence in viscous incompressible fluid at high Reynolds number. *Journal of Fluidmechanics*, 177:133–166, 1962.

[144] Konnov, A.: Remaining uncertainties in the kinetic mechanism of hydrogen combustion. *Combustion and Flame*, 154:507–528, 2008.

[145] Koroll, G. and Mulpuru, S.: The effect of dilution with steam on the burning velocity and structure of premixed hydrogen flames. *Symposium (International) on Combustion*, vol. 21, pp. 1811–1819, 1988.

[146] Kotchourko, A.: Safety of hydrogen as an energy carrier: Compilation report on SBEPs results of the 4th period. Technical report, HySafe network, 2007.

[147] Kotchourko, A., Breitung, W., Veser, A. and Dorofeev, S.: Tube experiments and numerical simulation on turbulent hydrogen-air combustion. *21st International Symposium on Shockwaves*, Great Keppel Island, Australia, 1997.

[148] Kuczera, B.: Das schwere Tohoku-Seebeben in Japan und die Auswirkungen auf das Kernkraftwerk Fukushima-Daiichi. *International Journal for Nuclear Power*, 56:4–5, 2011.

[149] Kumar, R., Koroll, G., Heitsch, M. and Studer, E.: Carbon monoxide–hydrogen combustion characteristics in severe accident containment conditions. Technical report, OECD/NEA/CSNI/R10, 2000.

[150] Kunkelmann, C.: Numerical Modeling and Investigation of Boiling Phenomena. PhD thesis, Technische Universität Darmstadt, 2011.

[151] Kuo, K.: Principles of Combustion. John Wiley & Sons, 1986.

[152] Kuznetsov, M. S., Grune, J., Friedrich, A., Sempert, K., Breitung, W. and Jordan, T.: Hydrogen–air deflagrations and detonations in a semi-confined flat layer. *Proceedings of the Sixth International Seminar on Fire and Explosion Hazards*, 2010.

[153] Kuznetsov, M. S., Jordan, T. and Grune, J.: Combustion regimes in a stratified layer of hydrogen-air mixture. *Proceedings of the International Congress on Advances in Nuclear Power Plants*, 2011.

[154] Kuznetsov, M., Yanez, J., Grune, J., Friedrich, A. and Jordan, T.: Hydrogen combustion in a flat semi-confined layer with respect to the Fukushima Daiichi accident. *Nuclear Engineering and Design*, 286:36–48, 2015.

[155] Landau, L. D.: On the theory of slow combustion. *Acta Physicochimica URSS*, 19:77–85, 1944.

[156] Laney, C.: Computational Gasdynamics. Cambridge University Press, 1998.

[157] Law, C.: Combustion Physics. Cambridge University Press, 2006.

[158] Le Métayer, O., Massoni, J. and Saurel, R.: Modelling evaporation fronts with reactive Riemann solvers. *Journal of Computational Physics*, 205:567–610, 2005.

[159] Lee, J.: The Detonation Phenomenon. Cambridge University Press, 2008.

[160] Lee, J. and Moen, I.: The mechanisms of transition from deflagration to detonation in vapor cloud explosions. *Progress in Energy and Combustion Science*, 6:359–389, 1980.

[161] Leer, B. van: Towards the ultimate conservative difference scheme. V. A second-order sequel to Godunov's method. *Journal of Computational Physics*, 32:101–136, 1979.

[162] LeVeque, R. J.: High-resolution conservative algorithms for advection in incompressible flow. *SIAM Journal on Numerical Analysis*, 33:627–665, 1996.

[163] Lewis, B. and Elbe, G. von: Combustion, Flames and Explosion of Gases. Academic Press, 1987.

[164] Liang, Z., Sonnenkalb, M., Bentaib, A., Sangiorgi, M. et al.: Status report on hydrogen management and related computer codes. Technical report, OECD/NEA/CSNI/R8, 2014.

[165] Liberman, M., Ivanov, M., Kiverin, A., Kuznetsov, M., Chukalovsky, A. and Rakhimova, T.: Deflagration–to–detonation transition in highly reactive combustible mixtures. *Acta Astronautica*, 67:688–701, 2010.

[166] Liberman, M., Kiverin, A. and Ivanov, M.: On detonation initiation by a temperature gradient for a detailed chemical reaction model. *Physics Letters A*, 375:1803–1808, 2011.

[167] Liefvendahl, M. and Troëng, C.: Parallelization and load balancing of a dynamic mesh method for moving boundary CFD. *Proceedings of the Open Source CFD International Conference*, Berlin, Germany, 2008.

[168] Liovic, P., Rudman, M., Liow, J.-L., Lakehal, D. and Kothe, D.: A 3D unsplit-advection volume tracking algorithm with planarity-preserving interface reconstruction. *Computers and Fluids*, 35:1011–1032, 2006.

[169] Liu, D. and MacFarlane, R.: Laminar burning velocities of hydrogen-air and hydrogen-air steam flames. *Combustion and Flame*, 49:59–71, 1983.

[170] López, J. and Hernández, J.: Analytical and geometrical tools for 3D volume of fluid methods in general grids. *Journal of Computational Physics*, 227:5939–5948, 2008.

[171] López, J., Hernández, J., Gómez, P. and Faura, F.: A volume of fluid method based on multidimensional advection and spline interface reconstruction. *Journal of Computational Physics*, 195:718–742, 2004.

[172] Ma, H., Woosley, S., Malone, C., Almgren, A. and Bell, J.: Carbon deflagration in type Ia supernova. I. Centrally ignited models. *The Astrophysical Journal*, 771:58, 2013.

[173] Maas, U. and Pope, S. B.: Simplifying chemical kinetics: Intrinsic low-dimensional manifolds in composition space. *Combustion and Flame*, 88:239–264, 1992.

[174] Magnussen, B. and Hjertager, B.: On mathematical modeling of turbulent combustion with special emphasis on soot formation and combustion. *Proceedings of the Combustion Institute*, 16:719–729, 1976.

[175] Magnussen, B. F.: The eddy dissipation concept: A bridge between science and technology. *ECCOMAS Thematic Conference on Computational Combustion*, pp. 21–24, 2005.

[176] Makarov, D., Verbecke, F., Molkov, V., Kotchourko, A., Lelyakin, A., Yanez, J., Baraldi, D., Heitsch, M., Efimenko, A. and Gavrikov, A.: An intercomparison of CFD models to predict lean and non-uniform hydrogen mixture explosions. *International Journal of Hydrogen Energy*, 35:5754–5762, 2010.

[177] Manninen, M., Silde, A., Lindholm, I., Huhtanen, R. and Sjövall, H.: Simulation of hydrogen deflagration and detonation in a BWR reactor building. *Nuclear Engineering and Design*, 211:27–50, 2002.

[178] Marić, T., Marschall, H. and Bothe, D.: voFoam – A geometrical volume of fluid algorithm on arbitrary unstructured meshes with local dynamic adaptive mesh refinement using OpenFOAM. *arXiv preprint arXiv:1305.3417*, 2013.

[179] Marić, T., Marschall, H. and Bothe, D.: lentFoam – A hybrid level set/front tracking method on unstructured meshes. *Computers and Fluids*, 113:20–31, 2015.

[180] Martín-Valdepeñas, J., Jiménez, M., Martín-Fuertes, F. and Fernández, J.: Improvements in a CFD code for analysis of hydrogen behaviour within containments. *Nuclear Engineering and Design*, 237:627–647, 2007.

[181] Mavriplis, D. J.: Revisiting the least-squares procedure for gradient reconstruction on unstructured meshes. *AIAA Paper*, 3986, 2003.

[182] Menter, F.: CFD best practice guidelines for CFD code validation for reactor-safety applications. Technical report, Fifth EURATOM Framework Programme, European Commission, 2002.

[183] Menter, F. and Esch, T.: Elements of industrial heat transfer predictions. *16th Brazilian Congress of Mechanical Engineering (COBEM)*, 2001.

[184] Menter, F.: Two–equation eddy–viscosity turbulence models for engineering applications. *AIAA Journal*, 32:1598–1605, 1994.

[185] Menter, F.: Review of the shear-stress transport turbulence model experience from an industrial perspective. *International Journal of Computational Fluid Dynamics*, 23:305–316, 2009.

[186] Menter, F., Kuntz, M. and Langtry, R.: Ten years of industrial experience with the SST model. *Turbulence, Heat and Mass Transfer*, 4:625–632, 2003.

[187] Merziger, G., Mühlbach, G., Wille, D. and Wirth, T.: Formeln und Hilfen zur Höheren Mathematik. Binomi Verlag, 2007.

[188] Meshkov, E. E.: Instability of the interface of two gases accelerated by a shock wave. *Fluid Dynamics*, 4:101–104, 1969.

[189] Michel, J.-B., Colin, O. and Angelberger, C.: On the formulation of species reaction rates in the context of multi–species CFD codes using complex chemistry tabulation techniques. *Combustion and Flame*, 157:701–714, 2010.

[190] Middha, P. and Hansen, O. R.: Predicting deflagration to detonation transition in hydrogen explosions. *Process Safety Progress*, 27:192–204, 2008.

[191] Molkov, V., Makarov, D. and Schneider, H.: LES modelling of an unconfined large-scale hydrogen–air deflagration. *Journal of Physics D: Applied Physics*, 39:4366, 2006.

[192] Mooney, K., Papper, J. and Voskuilen, T.: Performance evaluation of existing and new VoF simulation techniques: solving, interface treatment, and dynamic meshes. *Ninth OpenFOAM Workshop*, pp. 23–26, Zagreb, Croatia, 2014.

[193] Moser, V.: Simulation der Explosion magerer Wasserstoff–Luft–Gemische in groß-skaligen Geometrien. PhD thesis, Rheinisch–Westfälische Technische Hochschule Aachen, 1997.

[194] Mosso, S., Garasi, C. and Drake, R.: A smoothed two-and three-dimensional inter-face reconstruction method. *Computing and Visualization in Science*, 12:365–381, 2009.

[195] Movahed-Shariat-Panahi, M.: Recommendation for maximum allowable mesh size for plant combustion analyses with CFD codes. *Nuclear Engineering and Design*, 253:360–366, 2012.

[196] Nettleton, M. A.: Gaseous Detonations: Their Nature, Effects and Control. Springer Science & Business Media, 2012.

[197] Neumann, J. von: Theory of Detonation Waves. In: Taub, A. (editor): John von Neumann, Collected Works. Macmillan, 1942.

[198] Noh, W. F. and Woodward, P.: SLIC (simple line interface calculation). *Proceedings of the Fifth International Conference on Numerical Methods in Fluid Dynamics*, pp. 330–340, 1976.

[199] Noll, B., Schütz, H. and Aigner, M.: Numerical simulation of high–frequency flow instabilities near an airblast atomizer. *ASME Turbo Expo*, New Orleans, LA, USA, 2001.

[200] O'Conaire, M., Curran, H., Simmie, J., Pitz, W. and Westbrook, C.: A comprehensive modeling study of hydrogen oxidation. *International Journal of Chemical Kinetics*, 36:603–622, 2004.

[201] OECD group of experts: State-of-the-art report on containment thermal-hydraulics and hydrogen distribution. Technical report, OECD/NEA/CSNI/R16, 1999.

[202] OECD group of experts: ISP-49 on hydrogen combustion. Technical report, OECD/NEA/CSNI/R9, 2011.

[203] Oran, E. and Gamezo, V.: Origins of the deflagration–to–detonation transition in gas–phase combustion. *Combustion and Flame*, 148:4–47, 2007.

[204] Patankar, S. and Spalding, D.: A Calculation Procedure for the Transient and Steady-State Behavior of Shell-and-Tube Heat Exchangers. McGraw-Hill, New York, 1974.

[205] Pedersen, H. H., Enstad, G. A., Wingerden, M. van, Olsen, K. L., Kalvatn, I. B., Somoe, K., Wilkins, B., Middha, P. and Wingerden, K. van: Investigation of concentration effects on the flame acceleration in vented channels. *Ninth International Symposium on Hazards, Prevention and Mitigation of Industrial Explosions*, Cracow, Poland, 2014.

[206] Peters, N.: Turbulent Combustion. Cambridge University Press, 2000.

[207] Poinsot, T. and Veynante, D.: Theoretical and Numerical Combustion. 2nd ed. R.T. Edwards, 2005.

[208] Poinsot, T., Veynante, D. and Candel, S.: Diagrams of premixed turbulent combustion based on direct numerical simulation. *Symposium (International) on Combustion*, 23:613–619, 1990.

[209] Poinsot, T., Veynante, D. and Candel, S.: Quenching processes and premixed turbulent combustion diagrams. *Journal of Fluid Mechanics*, 228:561–606, 1991.

[210] Polifke, W., Flohr, P. and Brandt, M.: Modeling of inhomogeneously premixed combustion with an extended TFC model. *Journal of Engineering for Gas Turbines and Power*, 124:58–65, 2002.

[211] Pope, S.: PDF methods for turbulent reactive flows. *Progress in Energy and Combustion Science*, 19:119–192, 1985.

[212] Pope, S.: Turbulent Flows. Cambridge University Press, 2000.

[213] Popinet, S.: An accurate adaptive solver for surface-tension-driven interfacial flows. *Journal of Computational Physics*, 228:5838–5866, 2009.

[214] Popinet, S. and Zaleski, S.: A front-tracking algorithm for accurate representation of surface tension. *International Journal for Numerical Methods in Fluids*, 30:775–793, 1999.

[215] Poruba, C.: Turbulente Flammenausbreitung in Wasserstoff–Luft–Gemischen. PhD thesis, Technische Universität München, 2003.

[216] Press, W. H., Teukolsky, S. A., Vetterling, W. T. and Flannery, B. P.: Numerical Recipes in C++ – The Art of Scientific Computing. Cambridge University Press, 2002.

[217] Reinecke, M., Hillebrandt, W., Niemeyer, J., Klein, R. and Gröbl, A.: A new model for deflagration fronts in reactive fluids. *arXiv preprint astro-ph/9812119*, 1998.

[218] Reynolds, O.: On the dynamical theory of incompressible viscous fluids and the determination of the criterion. *Philosophical Transactions of the Royal Society of London, Series A*, 186:123–164, 1895.

[219] Richtmyer, R. D.: Taylor instability in shock acceleration of compressible fluids. *Communications on Pure and Applied Mathematics*, 13:297–319, 1960.

[220] Rider, W. J. and Kothe, D. B.: Reconstructing volume tracking. *Journal of Computational Physics*, 141:112–152, 1998.

[221] Rogovin, M.: Three Mile Island: A report to the commissioners and to the public. Technical report, Nuclear Regulatory Commission, 1979.

[222] Rosas, C., Davis, S., Engel, D., Middha, P., Wingerden, K. van and Mannan, M.: Deflagration to detonation transitions (DDTs): Predicting DDTs in hydrocarbon explosions. *Journal of Loss Prevention in the Process Industries*, 30:263–274, 2014.

[223] Rudman, M.: Volume-tracking methods for interfacial flow calculations. *International Journal for Numerical Methods in Fluids*, 24:671–691, 1997.

[224] Sathiah, P., Haren, S. van, Komen, E. and Roekaerts, D.: The role of CFD combustion modeling in hydrogen safety management – Part II: Validation based on homogeneous hydrogen–air experiments. *Nuclear Engineering and Design*, 252:289–302, 2012.

[225] Sathiah, P., Komen, E. and Roekaerts, D.: The role of CFD combustion modeling in hydrogen safety managemen – Part I: Validation based on small scale experiments. *Nuclear Engineering and Design*, 248:93–107, 2012.

[226] Scardovelli, R. and Zaleski, S.: Direct numerical simulation of free-surface and interfacial flow. *Annual Review of Fluid Mechanics*, 31:567–603, 1999.

[227] Scardovelli, R. and Zaleski, S.: Analytical relations connecting linear interfaces and volume fractions in rectangular grids. *Journal of Computational Physics*, 164:228–237, 2000.

[228] Schauer, F., Stutrud, J. and Bradley, R.: Detonation initiation studies and performance results for pulsed detonation engine applications. Technical report, DTIC, 2001.

[229] Schmid, H.-P.: Ein Verbrennungsmodell zur Beschreibung der Wärmefreisetzung von vorgemischten turbulenten Flammen. PhD thesis, Universität Karlsruhe, 1995.

[230] Schmid, H.-P., Habisreuther, P. and Leuckel, W.: A model for calculating heat release in premixed turbulent flames. *Combustion and Flame*, 113:79–91, 1998.

[231] Schmidt, H. and Klein, R.: A generalized level-set/in-cell-reconstruction approach for accelerating turbulent premixed flames. *Combustion Theory and Modelling*, 7:243–267, 2003.

[232] Schneider, P. and Eberly, D. H.: Geometric Tools for Computer Graphics. Morgan Kaufmann, 2002.

[233] Schneider, T.: Verfolgung von Flammenfronten und Phasengrenzen in schwachkompressiblen Strömungen. PhD thesis, Rheinisch–Westfälische Technische Hochschule Aachen, 2000.

[234] Schranner, F. S., Domaradzki, J. A., Hickel, S. and Adams, N. A.: Assessing the numerical dissipation rate and viscosity in numerical simulations of fluid flows. *Computers and Fluids*, 114:84–97, 2015.

[235] Sethian, J. and Smereka, P.: Level set methods for fluid interfaces. *Annual Review of Fluid Mechanics*, 35:341–372, 2003.

[236] Shepherd, J. and Lee, J.: On the Transition from Deflagration to Detonation. In: Hussaini, M., Kumar, A. and Voigt, R. (editors): Major Research Topics in Combustion, pp. 439–487. Springer, 1992.

[237] Sherman, M. P., Tieszen, S. and Benedick, W. B.: FLAME facility: The effect of obstacles and transverse venting on flame acceleration and transition to detonation for hydrogen-air mixtures at large scale. Technical report, Nuclear Regulatory Commission, Washington DC, USA, Division of Systems Research; Sandia National Laboratories, Albuquerque, NM, USA, 1989.

[238] Shirani, E., Jafari, A. and Ashgriz, N.: Turbulence models for flows with free surfaces and interfaces. *AIAA Journal*, 44:1454–1462, 2006.

[239] Shu, C.-W.: High-order finite difference and finite volume WENO schemes and discontinuous Galerkin methods for CFD. *International Journal of Computational Fluid Dynamics*, 17:107–118, 2003.

[240] Sieren, F.: Atomkraftwerk – Made in China: September 2016. `http://www.handelsblatt.com/politik/international/sierens-welt/sierens-welt-atomkraftwerk-made-in-china/14584974.html`. Last accessed November 29, 2016.

[241] Smiljanovski, V.: Ein numerisches Verfahren zur Berechnung schneller Vormischflammen und der Deflagrations–Detonations–Transition (DDT). PhD thesis, Rheinisch–Westfälische Technische Hochschule Aachen, 1996.

[242] Smiljanovski, V., Moser, V. and Klein, R.: A capturing–tracking hybrid scheme for deflagration discontinuities. *Combustion Theory and Modelling*, 1:183–215, 1997.

[243] Sonnenkalb, M.: Unfallanalysen für DWR vom Typ KONVOI (GKN-2) mit dem Integralcode MELCOR 1.8.4. A-2954, GRS, 2001.

[244] Spalding, D.: Mixing and chemical reaction in steady confined turbulent flames. *Symposium (International) on Combustion*, 13:649–657, 1971.

[245] Sundar, H., Sampath, R. S. and Biros, G.: Bottom-up construction and 2:1 balance refinement of linear octrees in parallel. *SIAM Journal on Scientific Computing*, 30:2675–2708, 2008.

[246] Sussman, M. and Puckett, E. G.: A coupled level set and volume-of-fluid method for computing 3D and axisymmetric incompressible two-phase flows. *Journal of Computational Physics*, 162:301–337, 2000.

[247] Tang, K., Beccantini, A. and Corre, C.: Combining discrete equations method and upwind downwind-controlled splitting for non-reacting and reacting two-fluid computations: Two dimensional case. *Computers and Fluids*, 103:132–155, 2014.

[248] Taylor, B., Kessler, D., Gamezo, V. and Oran, E.: Numerical simulations of hydrogen detonations with detailed chemical kinetics. *Proceedings of the Combustion Institute*, 34:2009–2016, 2013.

[249] Taylor, G.: The formation of a blast wave by a very intense explosion. I. Theoretical discussion. *Philosophical Transactions of the Royal Society of London, Series A*, 201:159–174, 1950.

[250] Thije-Boonkkamp, J.: The Conservation Equations for Reacting Gas Flow. Eindhoven University of Technology, 1993.

[251] Thomas, G.: Some observations on the initiation and onset of detonation. *Philosophical Transactions of the Royal Society of London, Series A*, 370:715–739, 2012.

[252] Thomas, G. O., Ward, S. M., Williams, R. L. and Bambrey, R. J.: On critical conditions for detonation initiation by shock reflection from obstacles. *Shock Waves*, 12:111–119, 2002.

[253] Toro, E.: Riemann Solvers and Numerical Methods for Fluid Dynamics: A Practical Introduction. Springer, 1999.

[254] Toro, E., Spruce, M. and Speares, W.: Restoration of the contact surface in the HLL-Riemann solver. *Shock Waves*, 4:25–34, 1994.

[255] Tragsdorf, I.: Entwicklung und Untersuchung von Katalysatorelementen für innovative Wasserstoff–Rekombinatoren. Reihe Energietechnik Nr. 36, Forschungszentrum Jülich, 2005.

[256] Trouvé, A. and Poinsot, T.: The evolution equation for the flame surface density in turbulent premixed combustion. *Journal of Fluid Mechanics*, 278:1–31, 1994.

[257] Tryggvason, G., Bunner, B., Esmaeeli, A., Juric, D., Al-Rawahi, N., Tauber, W., Han, J., Nas, S. and Jan, Y.-J.: A front-tracking method for the computations of multiphase flow. *Journal of Computational Physics*, 169:708–759, 2001.

[258] Tryggvason, G., Scardovelli, R. and Zaleski, S.: Direct Numerical Simulations of Gas–Liquid Multiphase Flows. Cambridge University Press, 2011.

[259] Turns, S.: An Introduction to Combustion. 2nd ed. McGraw–Hill, 2000.

[260] Urtiew, P. A. and Oppenheim, A. K.: Experimental observations of the transition to detonation in an explosive gas. *Philosophical Transactions of the Royal Society of London, Series A*, pp. 13–28, 1966.

[261] Utschick, M.: Sicherheitskriterien der vorgemischten Verbrennung wasserstoffhaltiger Brennstoffe in Gasturbinen. PhD thesis, Technische Universität München, 2016.

[262] Vaidyanathan, G.: Nuclear power must make a comeback for climate's sake: December 2015. https://www.scientificamerican.com/article/nuclear-power-must-make-a-comeback-for-climate-s-sake/. Last accessed November 29, 2016.

[263] Velikorodny, A., Studer, E., Kudriakov, S. and Beccantini, A.: Combustion modeling in large scale volumes using EUROPLEXUS code. *Journal of Loss Prevention in the Process Industries*, 35:104–116, 2015.

[264] Vincent, S., Larocque, J., Lacanette, D., Toutant, A., Lubin, P. and Sagaut, P.: Numerical simulation of phase separation and a priori two-phase LES filtering. *Computers and Fluids*, 37:898–906, 2008.

[265] Visser, D. C., Houkema, M., Siccama, N. B. and Komen, E. M. J.: Validation of a FLUENT CFD model for hydrogen distribution in a containment. *Nuclear Engineering and Design*, 245:161–171, 2012.

[266] Vollmer, K.: Einfluss von Mischungsgradienten auf die Flammenbeschleunigung und die Detonation in Kanälen. PhD thesis, Technische Universität München, 2015.

[267] Vollmer, K., Ettner, F. and Sattelmayer, T.: Deflagration-to-detonation transition in hydrogen-air mixtures with a concentration gradient. *Combustion Science and Technology*, 184:1903–1915, 2012.

[268] Vukadinovic, V., Habisreuther, P., Zarzalis, N. and Suntz, R.: Influence of pressure on Markstein number effect in turbulent flame front propagation. *ASME Turbo Expo*, San Antonio, TX, USA, 2013.

[269] Wardle, K. E. and Weller, H. G.: Hybrid multiphase CFD solver for coupled dispersed/segregated flows in liquid-liquid extraction. *International Journal of Chemical Engineering*, http://dx.doi.org/10.1155/2013/128936 2013.

[270] Warnatz, J., Maas, U. and Dibble, R.: Verbrennung: Physikalisch–Chemische Grundlagen, Modellierung und Simulation, Experimente, Schadstoffentstehung. Springer, 1997.

[271] Weimer, W.: Gabriel zerstört Eon und RWE: September 2015. `http://www.handelsblatt.com/politik/deutschland/whatsright/whats-right-gabriel-zerstoert-eon-und-rwe/12307932.html`. Last accessed November 29, 2016.

[272] Welch, J. E., Harlow, F. H., Shannon, J. P. and Daly, B. J.: The MAC method – A computing technique for solving viscous, incompressible, transient fluid-flow problems involving free surfaces. Technical report, Los Alamos Scientific Laboratories, University of California, NM, USA, 1965.

[273] Weller, H., Tabor, G., Jasak, H. and Fureby, C.: A tensorial approach to computational continuum mechanics using object-oriented techniques. *Computers in Physics*, 12: 620–631, 1998.

[274] Weller, H.: The development of a new flame area combustion model using conditional averaging. Technical report, Thermo–Fluids Section Report TF/9307, Imperial College London, 1993.

[275] Weller, H., Marooney, C. and Gosman, A.: A new spectral method for calculation of the time-varying area of a laminar flame in homogeneous turbulence. *Symposium (International) on Combustion*, vol. 23, pp. 629–636, 1991.

[276] Weller, H., Tabor, G., Gosman, A. and Fureby, C.: Application of a flame–wrinkling LES combustion model to a turbulent mixing layer. *Symposium (International) on Combustion*, 27:899–907, 1998.

[277] White, F.: Viscous Fluid Flow. 3rd ed. McGraw–Hill, 2006.

[278] Wilcox, D.: Turbulence Modeling for CFD. DCW Industries, 2006.

[279] Williams, F.: Combustion Theory. 2nd ed. Benjamin/Cummings Publishing Company, 1985.

[280] Xiao, J., Travis, J. R. and Kuznetsov, M.: Numerical investigations of heat losses to confinement structures from hydrogen-air turbulent flames in ENACCEF facility. *International Journal of Hydrogen Energy*, 40:13106–13120, 2015.

[281] Yang, X. and James, A. J.: Analytic relations for reconstructing piecewise linear interfaces in triangular and tetrahedral grids. *Journal of Computational Physics*, 214: 41–54, 2006.

[282] Yáñez, J., Kotchourko, A. and Lelyakin, A.: KYLCOM model for the calculation of under-resolved hydrogen combustion problems. *Proceedings of the Sixth International Seminar on Fire and Explosion Hazards*, 2010.

[283] Yáñez, J., Kotchourko, A., Lelyakin, A., Gavrikov, A., Efimenko, A., Zbikowski, M., Makarov, D. and Molkov, V.: A comparison exercise on the CFD detonation simulation in large–scale confined volumes. *International Journal of Hydrogen Energy*, 2010.

[284] Yáñez, J., Kotchourko, A. and Lelyakin, A.: Hydrogen deflagration simulations under typical containment conditions for nuclear safety. *Nuclear Engineering and Design*, 250:678–686, 2012.

[285] Youngs, D. L.: Time-dependent multi-material flow with large fluid distortion. *Numerical Methods for Fluid Dynamics*, 24:273–285, 1982.

[286] Youngs, D. L.: An interface tracking method for a 3D Eulerian hydrodynamics code. *Atomic Weapons Research Establishment*, 44/92:35, 1984.

[287] Yu, S. and Navarro-Martinez, S.: Modelling of deflagration to detonation transition using flame thickening. *Proceedings of the Combustion Institute*, 35:1955–1961, 2015.

[288] Zalesak, S. T.: Fully multidimensional flux-corrected transport algorithms for fluids. *Journal of Computational Physics*, 31:335–362, 1979.

[289] Zbikowski, M., Makarov, D. and Molkov, V.: LES model of large scale hydrogen–air planar detonations: Verification by the ZND theory. *International Journal of Hydrogen Energy*, 33:4884–4892, 2008.

[290] Zbikowski, M., Makarov, D. and Molkov, V.: Numerical simulations of large–scale detonation tests in the RUT facility by the LES model. *Journal of Hazardous Materials*, 181:949–956, 2010.

[291] Zeldovich, Y.: On the theory of the propagation of detonation in gaseous systems. Translation from: Zhurnal Eksperimental'noi i Teoreticheskoi Fiziki, 10:542-568, 1940. Technical Memorandum 1261, National Advisory Committee for Aeronautics, USA, 1960.

[292] Zeldovich, Y., Librovich, V., Makhviladze, G. and Sivashinsky, G.: On the development of detonation in a non–uniformly preheated gas. *Acta Astronautica*, 15:313–321, 1970.

[293] Zhang, X. and Shu, C.-W.: Positivity-preserving high order finite difference WENO schemes for compressible Euler equations. *Journal of Computational Physics*, 231: 2245–2258, 2012.

[294] Zimont, V., Polifke, W., Bettelini, M. and Weisenstein, W.: An efficient computational model for premixed turbulent combustion at high Reynolds numbers based on a turbulent flame speed closure. *Transactions of the ASME*, 120:526–532, 1998.

[295] Zimont, V. and Lipatnikov, A.: A numerical model of premixed turbulent combustion of gases. *Chemical Physics Reports*, 14:993–1025, 1995.

A   Contour plots color scale

As depicted in fig. A.1, the identical blue-to-red rainbow color scale (HSV color space) is used in all contour plots.

Min   Max
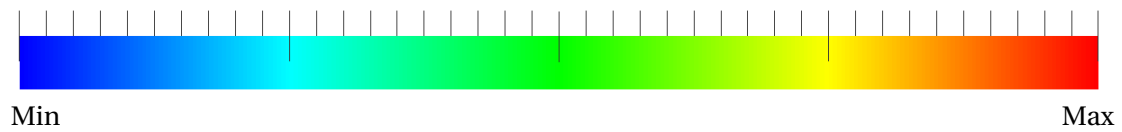
Figure A.1: Blue-to-red rainbow color scale

B Derivation of the parabolic model for volumetric reaction

The parabolic source term formulation for volumetric reaction can be derived by starting from the ansatz

$$\alpha(t) = 0.5 + 0.5\tanh(At) \tag{B.1}$$

and its temporal derivative [187]

$$\dot{\alpha}(t) = 0.5A\cosh^{-2}(At). \tag{B.2}$$

Solving ansatz B.1 for t gives

$$t = \frac{1}{A}\mathrm{artanh}(2\alpha - 1) \tag{B.3}$$

which can be reformulated to

$$t = \frac{1}{2A}\ln\frac{\alpha}{1-\alpha} \tag{B.4}$$

by using [187]

$$\mathrm{artanh}(x) = 0.5\ln\frac{1+x}{1-x}. \tag{B.5}$$

Inserting eq. B.4 in eq. B.2 and applying the addition theorem [187]

$$\cosh^2(x) = 0.5(\cosh(2x) + 1) \tag{B.6}$$

as well as the definition [187]

$$\cosh(x) = 0.5(e^x + e^{-x}) \tag{B.7}$$

finally yields

$$\dot{\alpha}(\alpha) = 2A\alpha(1-\alpha), \tag{B.8}$$

i.e. the source term formulation in reaction progress space.

The constant A can now be determined by requiring

$$\alpha(t = 0.5\,t_{\mathrm{exo}}) = 0.5 + 0.5\tanh(0.5A t_{\mathrm{exo}}) \overset{!}{=} 0.99, \tag{B.9}$$

meaning that t_{exo} is the time span in which α rises from 0.01 to 0.99. This discrete clipping is necessary due to the asymptotic behavior of the hyperbolic tangent towards infinity. It is then straightforward to obtain

$$A = \frac{\ln(99)}{t_{\mathrm{exo}}} = \frac{B}{t_{\mathrm{exo}}} \approx \frac{4.5951}{t_{\mathrm{exo}}}. \tag{B.10}$$

C Supplementary Konvoi simulation data

The cutting plane of the subsequent temperature fields is identical to the corresponding pressure fields discussed in sec. 5.2.

The probing locations of the subsequent pressure profiles are specified in tab. 5.1 and visualized in fig. 5.2.

(a) 33 ms (b) 242 ms (c) 342 ms

(d) 365 ms (e) 382 ms (f) 394 ms

(g) 405 ms (h) 415 ms (i) 425 ms
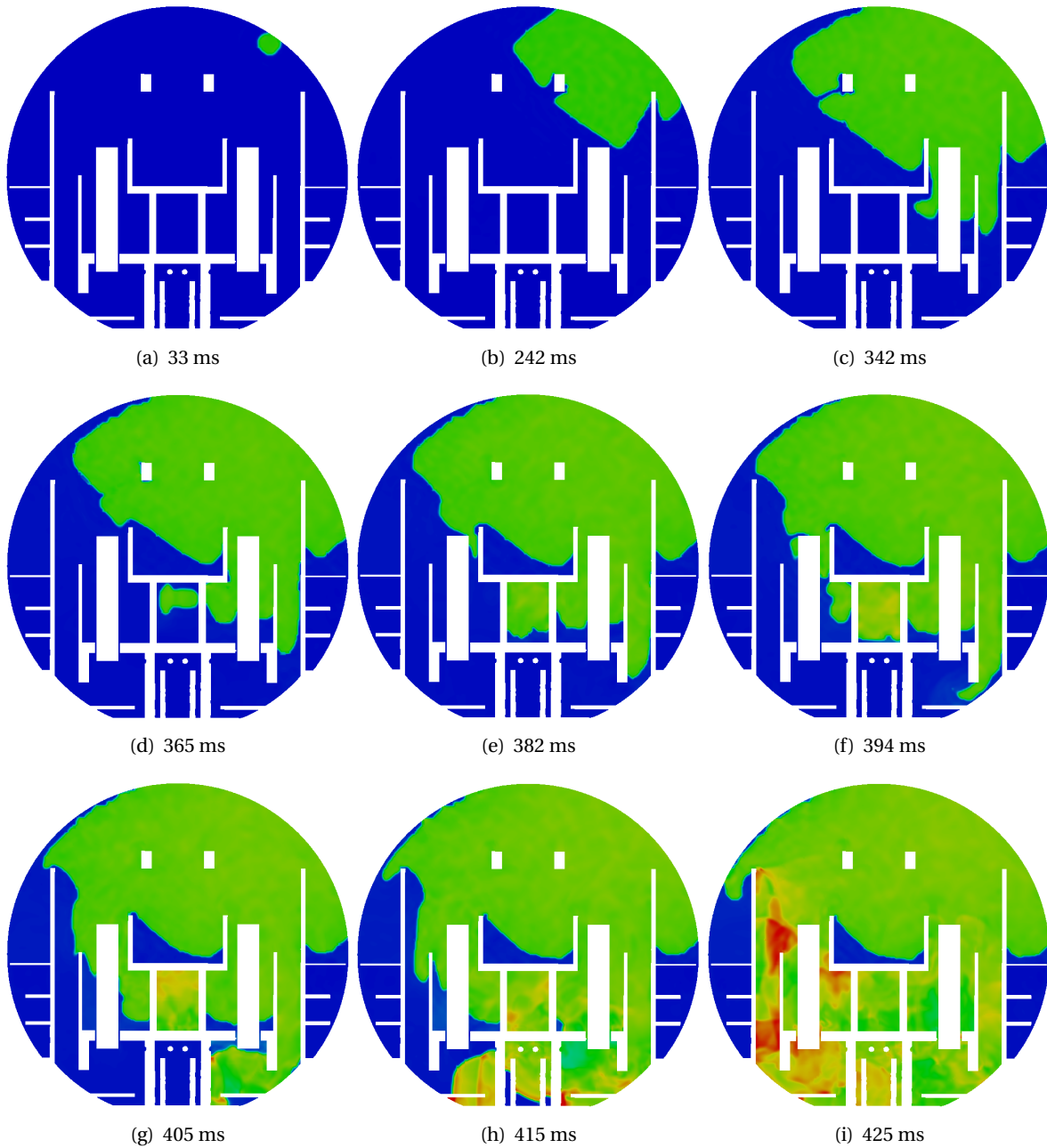
Figure C.1: Temperature field; $\widehat{X}_{\text{H}_2} = 15\,\%$, $\Delta X_{\text{H}_2} = 0\,\%$ (homogeneous); Rainbow color scale (appendix A) from 370 to 2500 K

(a) 34 ms   (b) 249 ms   (c) 345 ms

(d) 438 ms   (e) 485 ms   (f) 537 ms

(g) 542 ms   (h) 553 ms   (i) 559 ms
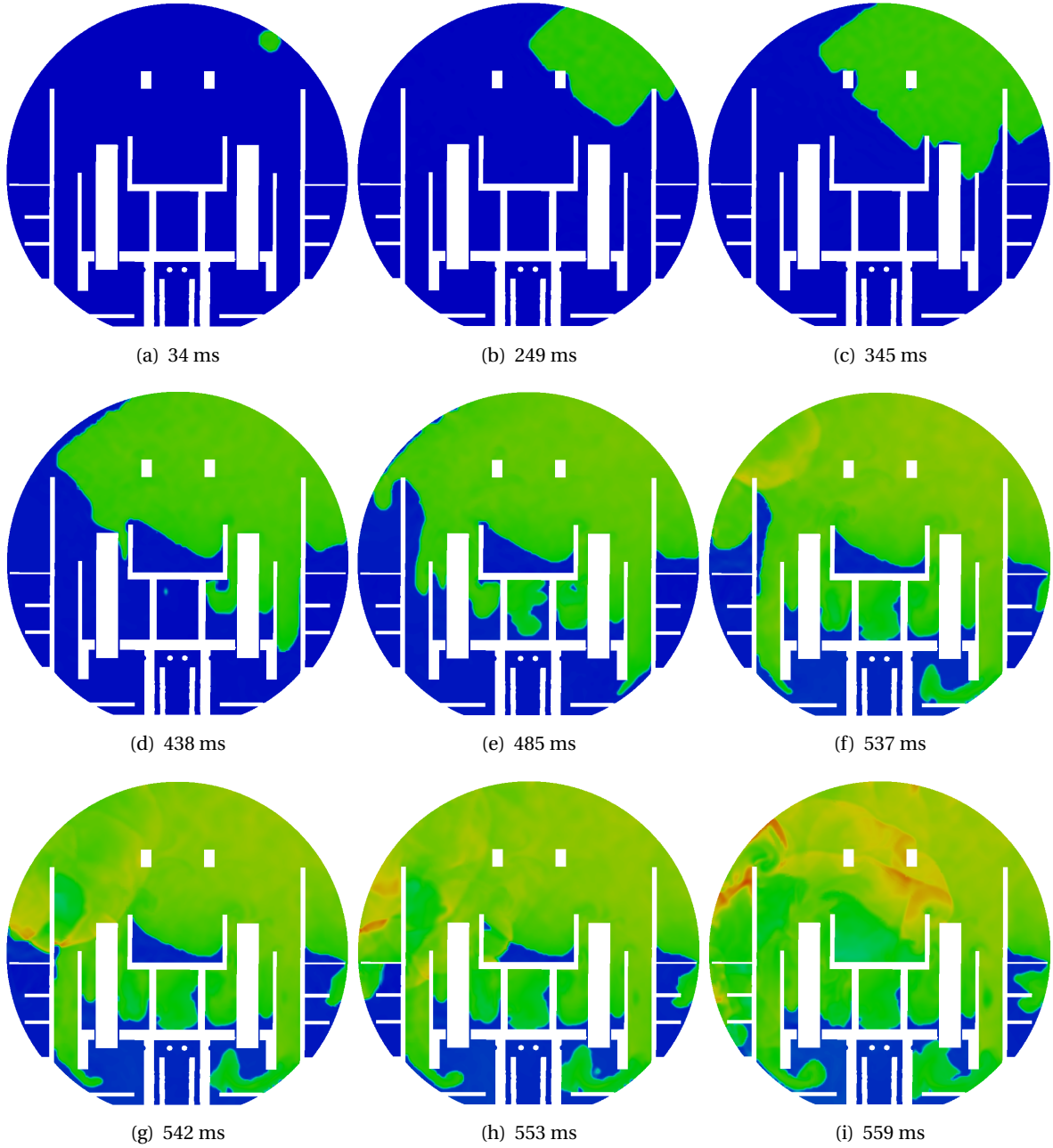
Figure C.2: Temperature field; $\widehat{X}_{H_2} = 12.5\,\%$, $\Delta X_{H_2} = 5\,\%$, $b = 0.1$ (continuous); Rainbow color scale (appendix A) from 370 to 2500 K

(a) 34 ms   (b) 249 ms   (c) 338 ms

(d) 418 ms   (e) 447 ms   (f) 491 ms

(g) 501 ms   (h) 505 ms   (i) 519 ms
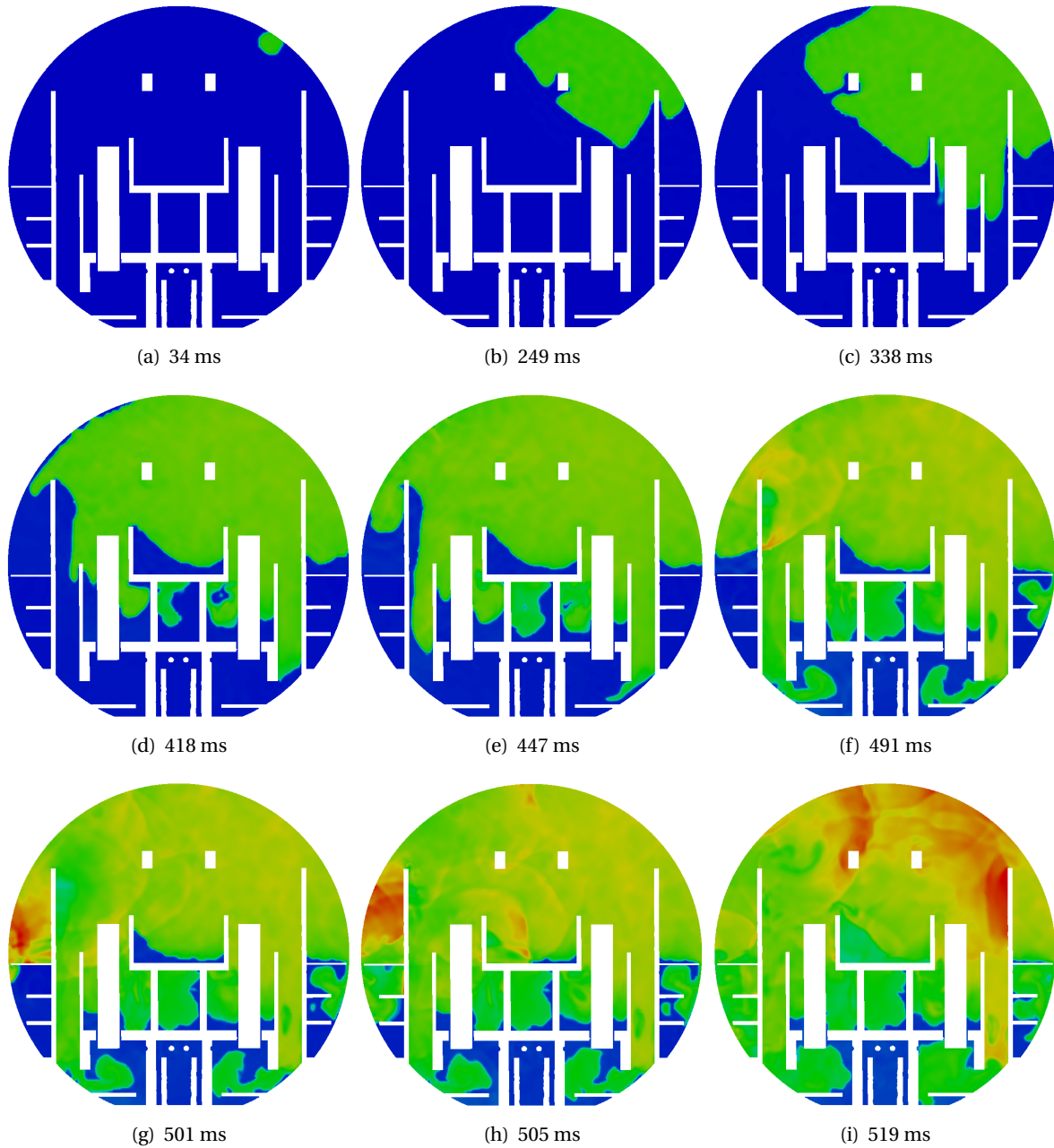
Figure C.3: Temperature field; $\widehat{X}_{H_2} = 12.5\,\%$, $\Delta X_{H_2} = 5\,\%$, $b = 0.5$ (stratified); Rainbow color scale (appendix A) from 370 to 2500 K
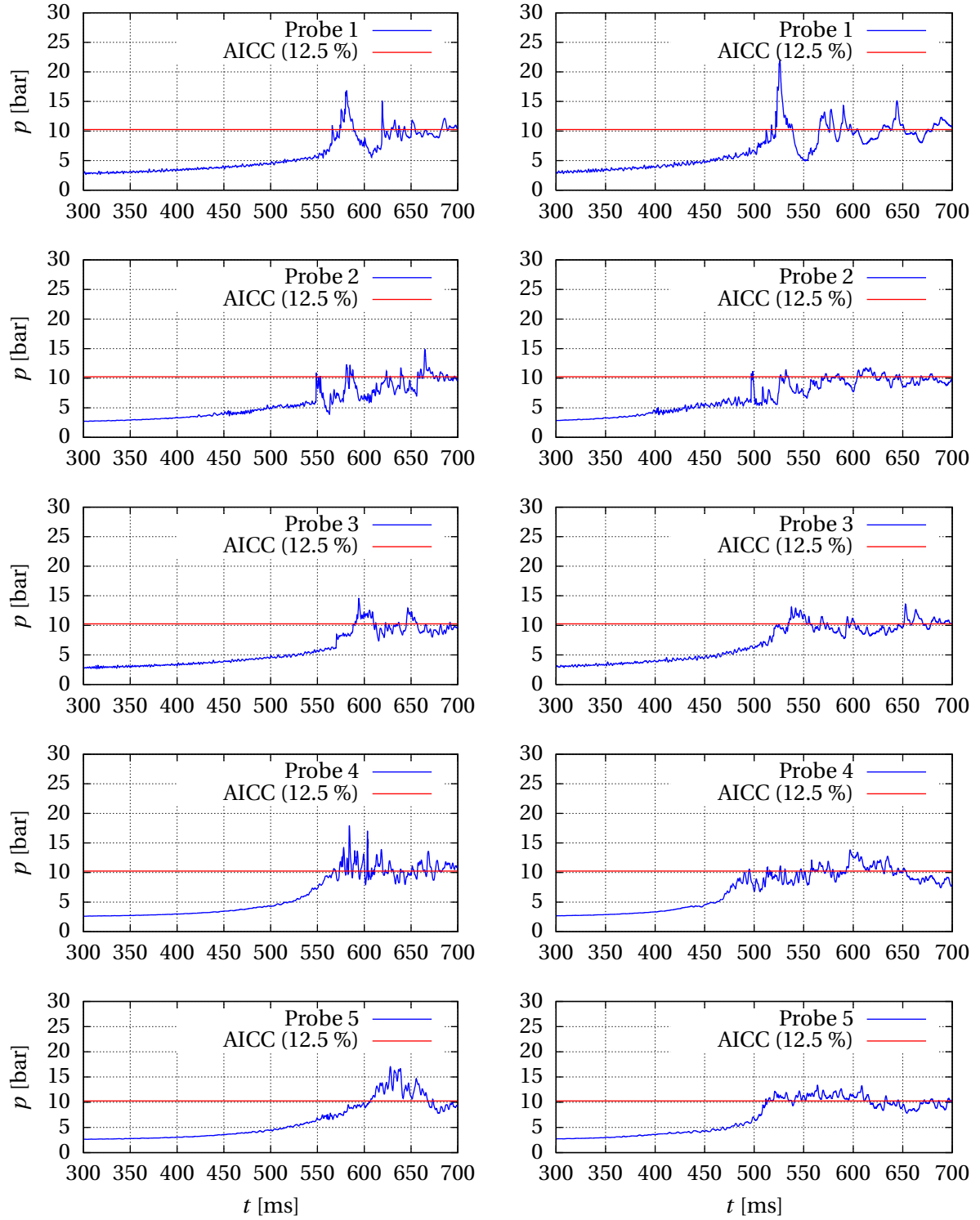
Figure C.4: Transient pressure recordings at probing locations 1 to 5 compared to AICC pressure; Left column: $\widehat{X}_{H_2} = 12.5$ %, $\Delta X_{H_2} = 5$ %, $b = 0.1$ (continuous); Right column: $\widehat{X}_{H_2} = 12.5$ %, $\Delta X_{H_2} = 5$ %, $b = 0.5$ (stratified)